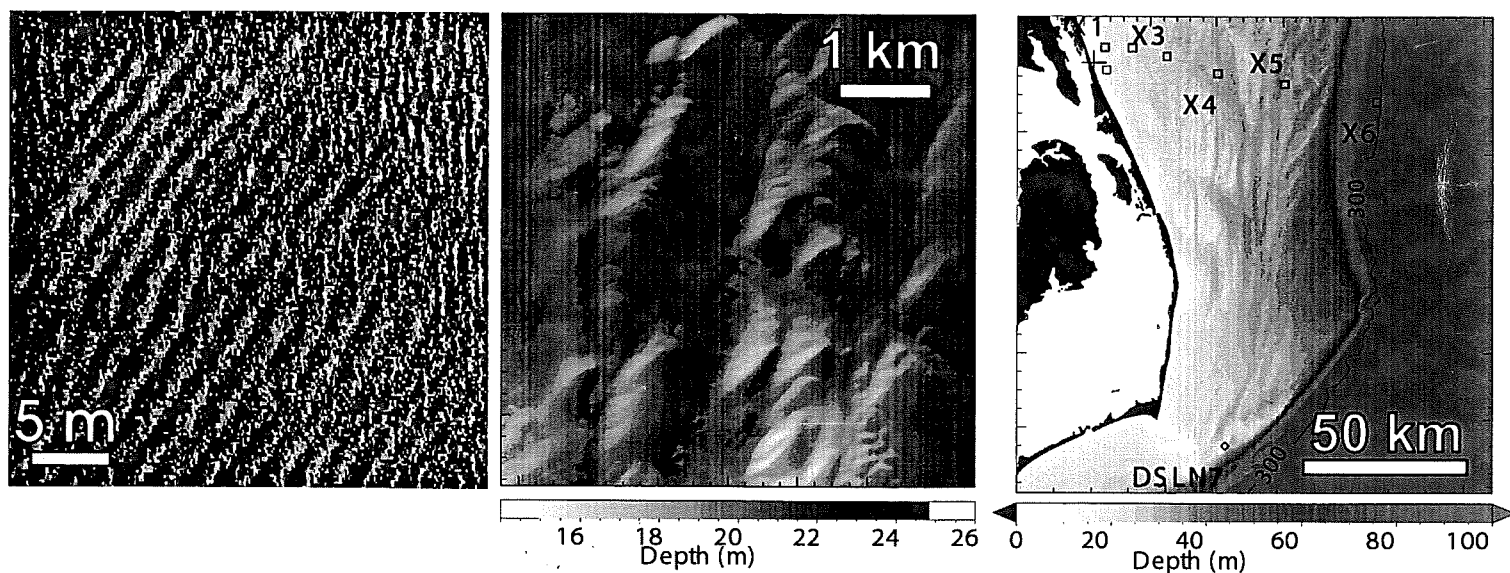


Naval Postgraduate School, Department of Oceanography
Monterey, California, September 2001.



Swell across the continental shelf



a doctoral dissertation by Fabrice Ardhuin

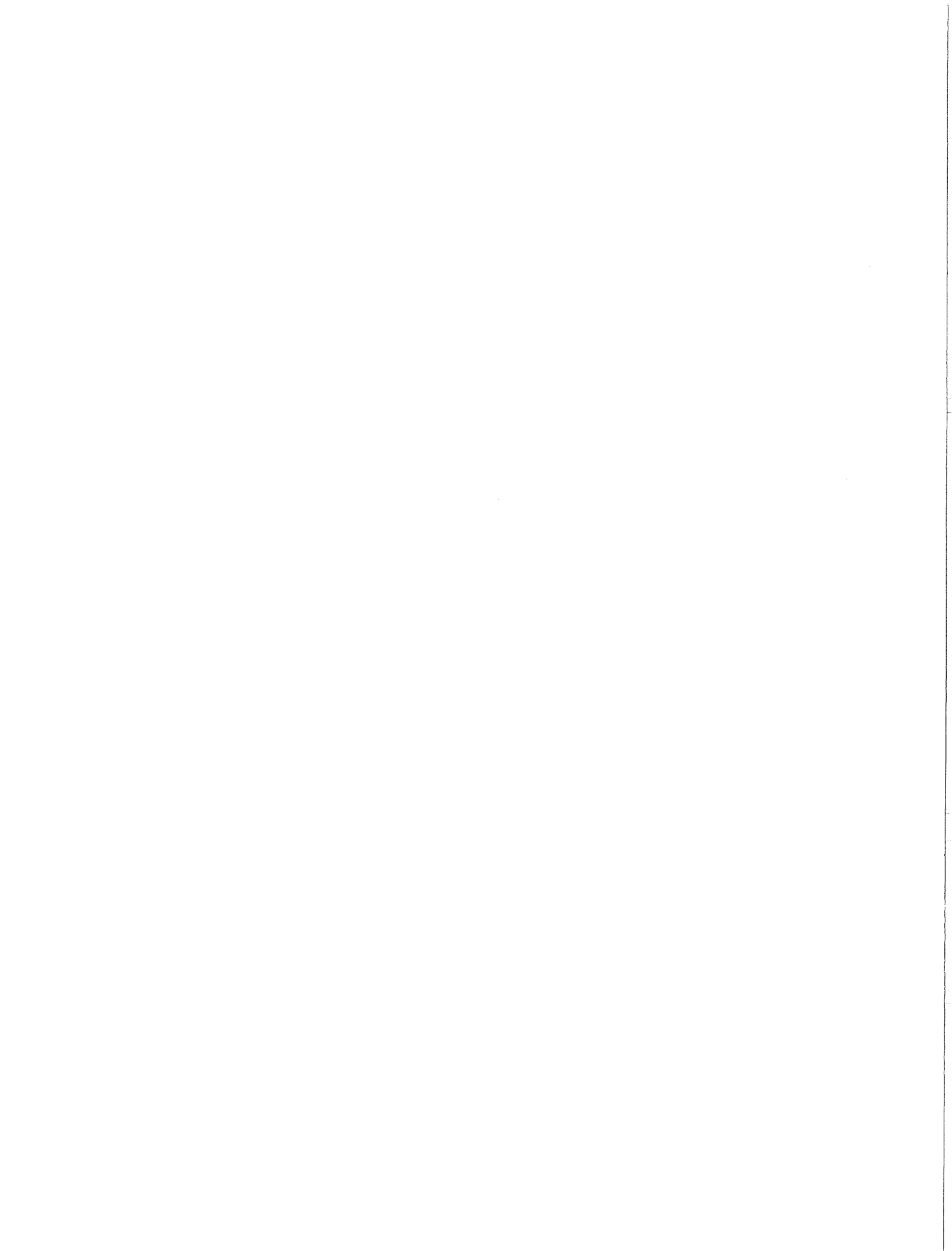
Comme nous les vagues passent
toutes semblables, chacune différente,
mais toutes interagissent
et laissent une trace.

A ceux qui nous ont quitté, et à ceux qui viendront

Waves come and go, like us,
all alike and each different,
but all interacting
so their memory lives on.

To all that have gone and all that will come

Monterey, 1 September 2001



REPORT DOCUMENTATION PAGE

Form Approved OMB No. 0704-0188

Public reporting burden for this collection of information is estimated to average 1 hour per response, including the time for reviewing instruction, searching existing data sources, gathering and maintaining the data needed, and completing and reviewing the collection of information. Send comments regarding this burden estimate or any other aspect of this collection of information, including suggestions for reducing this burden, to Washington Headquarters Services, Directorate for Information Operations and Reports, 1215 Jefferson Davis Highway, Suite 1204, Arlington, Va 22202-4302, and to the Office of Management and Budget, Paperwork Reduction Project (0704-0188) Washington DC 20503.

1. AGENCY USE ONLY (<i>Leave blank</i>)	2. REPORT DATE September 2001	3. REPORT TYPE AND DATES COVERED Ph.D. Dissertation	
4. TITLE AND SUBTITLE SWELL ACROSS THE CONTINENTAL SHELF		5. FUNDING NUMBERS	
6. AUTHORS Arduin, Fabrice			
7. PERFORMING ORGANIZATION NAME(S) AND ADDRESS(ES) Naval Postgraduate School Monterey CA 93943-5000		8. PERFORMING ORGANIZATION REPORT NUMBER	
9. SPONSORING/MONITORING AGENCY NAME(S) AND ADDRESS(ES) Service Hydrographique et Oc'eanographique de la Marine, Brest, France U.S. Office of Naval Research, Coastal Dynamics Program, Arlington, VA		10. SPONSORING/MONITORING AGENCY REPORT NUMBER	
11. SUPPLEMENTARY NOTES The views expressed in this thesis are those of the author and do not reflect the official policy or position of the Department of Defense or the U.S. Government.			
12a. DISTRIBUTION/AVAILABILITY STATEMENT Approved for public release; distribution is unlimited.		12b. DISTRIBUTION CODE	
13. ABSTRACT(<i>maximum 200 words</i>) The transformation of surface gravity waves propagating through shallow regions is investigated with extensive field data from the North Carolina continental shelf. A spectral energy balance equation is derived for a bidimensional bottom topography with random small-scale irregularities, in which bottom friction is introduced heuristically with a parameterized source term, and solved numerically using a hybrid Eulerian-Lagrangian scheme. This new model named CREST (Coupled Rays with Eulerian Source Terms) determines accurately refraction of waves by subgrid-scale depths variations using precomputed rays, allowing applications to large coastal areas with relatively coarse grids. Hindcasts of swell events during field experiments show large variations in wave heights caused by refraction and bottom friction. Widespread observations of sand ripples confirm that the bottom roughness is enhanced by wave-generated vortex ripples, thus sheltering the shore from offshore swells by dissipating wave energy in the bottom boundary layer. Resulting wave height attenuation up to 70 % (84 % of the wave energy) was observed in moderately energetic conditions. Bragg scattering of waves by wavelength-scale bottom features significantly increases (up to a factor two) the directional spread of waves.			
14. SUBJECT TERMS Waves, Modeling, Bragg Scattering, Sand Ripples, Boundary Layer, Continental Shelf		15. NUMBER OF PAGES 150	
		16. PRICE CODE	
17. SECURITY CLASSIFICATION OF REPORT Unclassified	18. SECURITY CLASSIFICATION OF THIS PAGE Unclassified	19. SECURITY CLASSIFICATION OF ABSTRACT Unclassified	20. LIMITATION OF ABSTRACT UL

THIS PAGE INTENTIONALLY LEFT BLANK

Approved for public release; distribution is unlimited
SWELL ACROSS THE CONTINENTAL SHELF

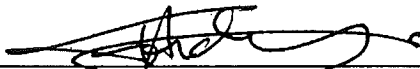
Fabrice Ardhuin
Ingénieur de l'Armement
M.S., Ecole Polytechnique, 1997
M.Res., Université Paul Sabatier, 1998
Submitted in partial fulfillment of the
requirements for the degree of

DOCTOR OF PHILOSOPHY IN OCEANOGRAPHY

from the

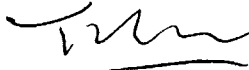
**NAVAL POSTGRADUATE SCHOOL
September 2001**

Author:

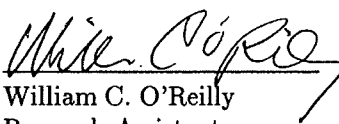


Fabrice Ardhuin

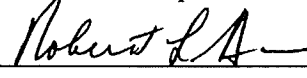
Approved by:



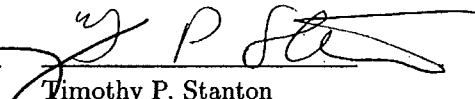
Thomas H. C. Herbers
Associate Professor
of Oceanography
Dissertation Supervisor



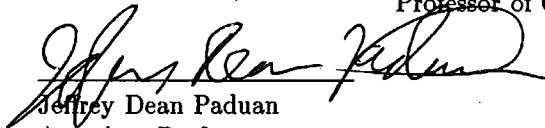
William C. O'Reilly
Research Assistant
Professor of Oceanography



Robert L. Haney
Professor of Meteorology

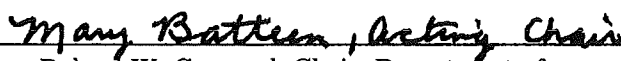


Timothy P. Stanton
Research Associate
Professor of Oceanography



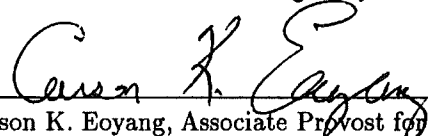
Jeffrey Dean Paduan
Associate Professor
of Oceanography

Approved by:



Roland W. Garwood, Chair, Department of
Oceanography

Approved by:



Carson K. Eoyang, Associate Provost for Academic affairs

THIS PAGE INTENTIONALLY LEFT BLANK

ABSTRACT

The transformation of surface gravity waves propagating through shallow regions is investigated with extensive field data from the North Carolina continental shelf. A spectral energy balance equation is derived for a bidimensional bottom topography with random small-scale irregularities, in which bottom friction is introduced heuristically with a parameterized source term, and solved numerically using a hybrid Eulerian-Lagrangian scheme. This new model named CREST (Coupled Rays with Eulerian Source Terms) determines accurately refraction of waves by subgrid-scale depths variations using precomputed rays, allowing applications to large coastal areas with relatively coarse grids. Hindcasts of swell events during field experiments show large variations in wave heights caused by refraction and bottom friction. Widespread observations of sand ripples confirm that the bottom roughness is enhanced by wave-generated vortex ripples, thus sheltering the shore from offshore swells by dissipating wave energy in the bottom boundary layer. Resulting wave height attenuation up to 70 % (84 % of the wave energy) was observed in moderately energetic conditions. Bragg scattering of waves by wavelength-scale bottom features significantly increases (up to a factor two) the directional spread of waves.

RESUME

La transformation d'ondes de gravité de surface est étudiée au moyen d'une équation d'évolution pour les densités spectro-angulaires, établie à partir des équations de conservation de la quantité de mouvement et de la masse, dans le cas d'un fond lisse avec une topographie irrégulière. L'effet de la rugosité du fond est introduit de manière empirique. Un modèle numérique hybride Eulerien-Lagrangien est présenté pour résoudre cette équation. Entre autres avantages ce nouveau modèle, dénomé Crêtes (Couplage de Rayons par Termes de Source Euleriens) permet d'utiliser des maillages non-structurés pour le terme de source, tandis que les effets de la réfraction et du levage causés par les variations de profondeur aux échelles sous-maille sont précisément pris en compte grâce aux rayons précalculés. Ainsi ce modèle peut être appliqué à de vastes zones côtières avec des maillages relativement lâches.

Des observations de rides de sable sur le plateau continental de Caroline du Nord, combinées à des simulations numériques d'épisodes houleux observés au cours de campagnes à la mer, montrent que les variations de la hauteur des vagues à la traversée d'un plateau continental large, peu profond et sableux, sont essentiellement causés par la réfraction et la friction au fond, pour laquelle les rides créées par les vagues jouent un rôle déterminant. Ces rides protègent la côte des houles d'amplitude moyenne, avec, pour les cas décrits ici, une atténuation maximale de 70 % de la hauteur de vague, soit 84 % de l'énergie.

Les propriétés directionnelles de la houle sont modifiées par la présence d'irrégularités bathymétriques d'échelle horizontale comparable à la longueur d'onde de la houle. Cette interaction houle-topographie est décrite ici par la théorie de la diffusion de Bragg pour des vagues aléatoires, et représentée par un terme de source, ou plus précisément d'échange, dans l'équation d'évolution des densités spectro-angulaires. Sur le plateau Nord-Carolinien cette diffusion peut augmenter l'étalement angulaire des vagues d'un facteur deux, contrariant le rétrécissement du spectre angulaire causé par la réfraction. Ces prévisions correspondent aux observations, malgré la persistance d'une erreur résiduelle qui peut être attribuée en grande partie aux incertitudes sur les conditions à la limite au large, mais qui peut aussi être la trace d'autres phénomènes non représentés dans le modèle.

TABLE OF CONTENTS

ABSTRACT	v
RESUME	vii
ACKNOWLEDGMENT	xv
I. INTRODUCTION	1
A. Motivation and objectives	1
B. Statistical description of waves	2
C. The energy balance equation	5
D. Wave-bottom scattering	8
E. Energy dissipation in the bottom boundary layer	10
1. Bottom drag	10
2. Bedform dynamics	10
3. Parameterization	12
F. Numerical wave models	15
II. THE CREST WAVE MODEL	17
A. Numerical schemes	19
1. Model domain and boundary conditions	19
2. Precomputations	21
3. Integration in time	23
B. Source term	25
C. Model tests	25
D. Model implementation and field data	28
E. Hindcasts	30
1. October storm	30
2. Hurricane Gordon	32
F. Discussion	40
1. Movable bed model	40
2. Model efficiency	40
G. Summary	41
III. WAVE-BOTTOM BRAGG SCATTERING	43
A. Scattering theory for heterogeneous random waves	43
1. General formulation	43
2. First order solution	47
3. Second order solution	47
4. Third order solution	48
5. Energy balance	49
6. Conditions of validity	50
7. Extensions of the present theory	51
B. Random waves over sinusoidal bars	51
1. Stochastic source term approach	53
2. Comparison with deterministic theory for normal incidence	54
3. Oblique incidence and finite numbers of bars	56
4. Bottom slope effects	58

C.	Hindcast of wave scattering on a natural shelf	59
1.	Wave data	59
2.	Bottom topography	59
3.	Numerical model	62
4.	Hindcast	64
D.	Summary	70
IV.	OBSERVATIONS OF WAVE-GENERATED RIPPLES	71
A.	Experiment	71
B.	Surficial sediments	74
C.	Sidescan sonar images of bedforms	76
D.	Evaluation of ripple parameterizations	81
E.	Summary and discussion	86
V.	VALIDATION OF THE ENERGY BALANCE EQUATION	87
A.	Introduction	87
B.	Swell observations during DUCK94 and SHOWEX	88
1.	Instruments and data analysis	88
2.	Wave conditions	90
3.	Dataset reduction	94
C.	Hindcasts organization	94
1.	The CREST wave model	94
2.	Bathymetry and model grid	94
3.	Boundary conditions	96
4.	Bottom sediments and small scale topography.	96
5.	Source terms	98
D.	Model-data comparisons	102
1.	Mean direction	103
2.	Directional spread	103
3.	Wave heights	105
4.	Model errors and offshore boundary	112
E.	Summary and practical implications	112
VI.	CONCLUSIONS AND PERSPECTIVES	115
	APPENDIX A: DERIVATION OF THE ENERGY BALANCE (3.47)	119
	LIST OF REFERENCES	125

LIST OF FIGURES

1.1	Wave spectra	4
1.2	Wave-bottom interactions	7
1.3	Resonance condition for Bragg scattering	8
1.4	The three boundary layer regimes	11
1.5	Schematic of ripples	12
1.6	Examples of dissipation factors f_e as a function of the Shields number ψ_{rms}	14
2.1	Numerical scheme of CREST	18
2.2	Treatment of the boundary condition	20
2.3	Model tests with an alongshore uniform shelf	26
2.4	Comparison of semi-implicit and explicit schemes	27
2.5	Bottom topography and model grid	29
2.6	Wind and wave conditions, October 1994	31
2.7	Hindcasts, October 1994	33
2.8	Hindcasts of H_s and $\bar{\theta}$, October 19, 1994	34
2.9	Ripples and dissipation factors, October 1994	35
2.10	Wind and wave conditions, November 1994	36
2.11	Hindcasts of H_s and $\bar{\theta}$, November 18, 1994	38
2.12	Ripples and dissipation factors, November 1994	39
3.1	Random waves and irregular bottom: definition sketch.	44
3.2	Values of $\chi(kH)$, as defined by (3.49).	50
3.3	Wave scattering by sinusoidal bars	52
3.4	Resonant wavenumbers for sinusoidal bars.	53
3.5	Reflection of waves by sinusoidal bars	55
3.6	Comparison of stochastic and deterministic theories	57
3.7	High resolution (10 m) bottom topography	60
3.8	Bottom elevation spectra	61
3.9	Model grid	63
3.10	Wave spectrum and Bragg scattering source term	64
3.11	Directional properties across the shelf	66
3.12	Realistic test of the Bragg scattering source term	67
3.13	Sensitivity to the wavenumber cut-off	68
4.1	Topography and SHOWEX sidescan sonar surveys	72
4.2	SHOWEX observed wave conditions and ripples	73
4.3	Example grain size distributions	74
4.4	Spatial variations of D_{50} and ripple coverage	75
4.5	Extraction of ripple parameters from sidescan images	77
4.6	Examples of unusual ripple patterns	79
4.7	Time evolution of ripple directions and wavelengths	80
4.8	Cross-shelf distribution of ripple directions and wavelengths	81
4.9	Wave forcing conditions during ripple formation	83
4.10	Ripple wavelength λ versus crest-normal ripple direction θ_r	85
5.1	Bathymetry and instrument locations during DUCK94 and SHOWEX.	89
5.2	Tracks of North Atlantic hurricanes	91
5.3	Wind and wave conditions during DUCK94.	92

5.4	Wind and wave conditions during SHOWEX.	93
5.5	Model grid.	95
5.6	Distribution of median grain sizes.	97
5.7	Bottom elevation spectra	99
5.8	Dissipation factors	100
5.9	Model errors on the mean direction θ_p at the peak frequency	104
5.10	Nearshore versus offshore directional spread	106
5.11	Model errors on the directional spread $\sigma_{\theta,p}$ at the peak frequency	107
5.12	Relative error on the directional spread $\sigma_{\theta,p}$ as a function of the peak frequency	108
5.13	Model errors in predictions of the significant wave heights H_s	110
5.14	Relative error of H_s predictions as a function of the Shields number.	111
6.1	Singing sands, lake Huron, 28 April 2001	118

LIST OF TABLES

4.1	Ripples at sites of sediment sample collection	84
5.1	Wave-measuring instruments during DUCK94 and SHOWEX	90

ACKNOWLEDGMENT

I thank all those that have contributed to my lucky encounter with professor Herbers, the spark that initiated the work presented here, and much more now under way, from my parents Claude and Gérard, to professors Haney and Thornton, all the way through my professors at the lycées Jean Durand and Pierre de Fermat, and at Ecole Polytechnique, and many friends, including Lise Labroue. Professors Herbers, O'Reilly and Drake deserve a large part of the credit for the ideas developed below and already published or in press elsewhere, but more importantly I appreciate their deep knowledge of the physics of ocean waves, skills with wave models and data, and undaunted interest for what many physicist only view as 'dirt'. Working day by day with professor Herbers I had the unique opportunity to experience his true kindness, and generosity with his time and all available means and relations. I can only wish that our collaborations will go on for as long as waves will hold mysteries for us. I truly enjoyed working at NPS, and Duck, N. C., without mentioning countless airports and planes, thanks to the support and presence of Paul Jessen, Mark Orzech, Richard Dentzman, the dedicated librarians of the Dudley Knox Library, in particular Susan Miller, and stimulating discussions, at NPS and elsewhere, with Ad Reniers, Hendrik Tolman, Denis Morichon, Timothy Stanton, Yehuda Agnon, Edith Gallagher, Luigi Cavaleri, Robert Jensen, and Igor Lavrenov. I also wish to apologize to the many authors whose work was not mentioned in the present dissertation or in the journal papers, as their foreign language makes them little known in the English-language scientific community, and I wish to congratulate professor Lavrenov for his efforts in translating his latest book in English, and allowing Russian and eastern European science to get the recognition it deserves. The National Ocean Service, National Data Buoy Center, USACE Field Research Facility, and Robert Jensen, thank you so much again, are acknowledged for providing freely bathymetric and wave data, and maintaining their valuable databases.

I am forever indebted to the french taxpayers for my tuition and salary while a student Ecole Polytechnique, Université Paul Sabatier, and the Naval Postgraduate School, where I enjoyed being one of the best paid graduate students in the world and strived to prove worthy of it, and I thank the Service Hydrographique and Océanographique de la Marine, and in particular Mr Ingénieur Général Souquière, for their support before and throughout the Ph.D. program. I must thank again Denis, Ad and Edie for putting up with my workaholic routine in the last year of my work, with surfing lessons, parties, and nice runs on the beach... not so nice after 21 miles. Finally, and foremost, I have special thanks to Fanny who maybe wished I did not go to California in the first place, but accepted to be my wife, with unflagging love and support through these three years of waiting, flying across the ocean, and parting again.

I. INTRODUCTION

A. Motivation and objectives

Surface gravity waves, in oceans, lakes, or ponds, often simply called ‘waves’, are one of the earliest observed and studied among the many phenomena that physicists refer to as waves. Waves inspired many of the greatest mathematicians, physicists, and oceanographers from the 19th and 20th centuries, from Boussinesq, Laplace, Stokes, and Rayleigh, to Hasselmann, Munk, Phillips, Sverdrup, and Zakharov, to name only a few. Because of their simple yet rich nature (waves are generally dispersive and weakly non-linear), and the natural homogeneity of water bodies and the atmosphere above, waves were the natural testing ground for many theories and ideas, from Fourier analysis, initially developed for heat conduction, to Fermi-Pasta-Ulam recurrences or weak turbulence theory. In the view of this enormous body of knowledge, one may think that everything about waves is already perfectly known, but this is not the case. In particular the generation of waves by wind, and the resulting highly non-linear breaking waves are still the subject of active research. As waves propagate away from the area where they were generated by wind, they evolve into regular swell that can radiate across large ocean basins with little energy loss, until they reach the coast and finally dissipate in the surf zone, or reflect from a cliff. Both seabed geology and topography strongly influence the evolution of swell, across continental shelves, shallow marginal seas, or lakes, in a way that is still poorly understood.

The goal of the present dissertation is to determine these effects quantitatively, from theory and wave measurements in the field, using a numerical model. The mathematical model and adapted numerical techniques to represent swell evolution proposed here will hopefully not only improve conceptual understanding of the physical processes, but also lead to more accurate predictions and hindcasts of swells near the shore.

In the marine environment all human activities depend on such wave predictions, from fishing, shipping and naval or amphibious operations, to the development of coastal regions and the offshore industry. Preparation for D-day during the second world war was the driving force behind some of the first attempts at systematic wave prediction using available theory (Sverdrup & Munk, 1947). Just like waves are driven by the wind, so were wave models pushed by the advent of operational weather forecasting and its refinements over the last sixty years. Observations and predictions of rising sea level and storm frequency, both associated with global warming, are increasing the challenge posed by ocean waves, and continue to call for better wave predictions. Current wave models used for engineering design or operational predictions already provide immensely valuable information, but some important physical processes at play in the evolution of waves in shallow water are still poorly known. Models therefore rely on empirical relations that are derived from limited data sets, and thus cannot be used with confidence in untested situations.

The dissipation of wave energy due to friction on a sandy bottom offers an interesting example. Based on the ideas used for ocean currents and air flows, Hasselmann & Collins (1968) proposed that this bottom friction may follow a quadratic drag law and they derived the corresponding effect for random waves. Data from the 1968 JOint North Sea Project (JONSWAP, Hasselmann *et al.*, 1973), off the coast of Sylt in the North Sea, provided a real-life test of their theory. The theory failed to explain the observed wave dissipation variations, even after accounting for the dominant tidal currents. Lacking a reliable physics-based bottom drag formulation, most wave models today use a simple parameterization of bottom friction based on the quadratic drag law for waves in the presence of dominant tidal currents, with a tunable coefficient. This coefficient is usually set at the average measured value during JONSWAP, although its variations span two decades in the JONSWAP dataset. It is a tribute to human engineering genius that this parameterization generally gives reasonable results, even in the absence of significant currents. However this crude

representation of bottom friction certainly lacks the reliability and accuracy of theories based on first principles foundation on which one may like to build a multi-billion dollar harbor, or plan for the next D-Day. Fortunately a better understanding of the bottom friction is now available, as the thin bottom boundary layer where energy dissipation takes place has been studied theoretically, in the laboratory, in numerical experiments, and, to a lesser degree, in the field. However even the most elaborate boundary layer models (e.g. Reichardt, 1951; Weber 1991*b*) need some information on the roughness that depends on the bottom geology and bedforms. The strong effect of wave generated sand ripples on bottom drag was already measured in 1963 in the laboratory (Zhukovets, 1963), but the introduction of this effect in wave forecasting models (Graber & Madsen 1988; Graber, Beardsley & Grant, 1989; Tolman, 1994) had to await the first parameterizations of movable sand bottom roughness by Grant & Madsen (1982), and Madsen *et al.* (1990). Before the present work no field data was available to demonstrate the importance of sand ripples for wave evolution and test these parameterizations. This slow progress should not overshadow successes in other areas of wave research, such as depth-induced breaking, but it illustrates how science may be hindered by the lack of good public data and the fragmentation of the research community into very small groups, despite international federating efforts such as the meetings of the WAVE Model Development and Implementation (WAMDI) group, and the Waves In Shallow Environments (WISE) group.

The SHOaling Waves Experiment (SHOWEX), conducted in 1999 and funded by the U.S. Office of Naval Research, provided a much needed impetus to take a fresh look at the physics and the parameterizations of waves in shallow water. It provided a rich dataset of wave measurements, bathymetric and geological surveys, that is used in the present dissertation. The numerical wave model developed in chapter II was first validated with data from a previous experiment (DUCK94), showing the effect of sand ripples on bottom friction, but the theoretical results on wave scattering by irregular small scale topography (chapter III), could not have been tested without the high-resolution bathymetric surveys performed during SHOWEX. The presence of sand ripples, analyzed in chapter IV, was determined for the first time on a large scale by sidescan sonar surveys conducted during SHOWEX, providing a unique combination of wave measurements and bedform images. The wide range of wave conditions during this three-month long experiment, including major hurricanes and northeaster storms, allowed for a comprehensive statistical validation of the representation of sand ripples and wave-topography scattering in the wave model, in chapter V. Perspectives arising from that data set and the new numerical model are presented in chapter VI, with a summary of the main results of this dissertation.

Before getting into these new developments the non-expert reader may consult, for an in-depth introduction, the following overview of related wave theories, models, and observations.

B. Statistical description of waves

Waves at the air-water interface modify the surface elevation, and the pressure and velocity below and above the surface. Wave motion is characterized by oscillations around a position of equilibrium, a ‘horizontal’ sea surface, under the action of gravity that tends to restore the equilibrium. In the presence of wind or steep wave fronts, surface tension may act as another restoring force for very short (capillary) waves (figure 6.1). This latter force will be neglected in the present work where the focus is on long period waves (frequency f less than 0.25 Hz), in the absence of wind. The position of the surface is defined by the function $z = \zeta(\mathbf{x}, t)$ where \mathbf{x} is the horizontal position vector, z is the vertical coordinate, pointing upward, with $z = 0$ the equilibrium position of the surface, and t is time. Assuming irrotational wave motion, a very good approximation in general, the horizontal velocity vector \mathbf{u} and vertical velocity w can be expressed as gradients of a velocity potential $\phi(\mathbf{x}, z, t)$: $\mathbf{u} = \nabla\phi$, where ∇ is the horizontal gradient operator, and $w = \partial\phi/\partial z$. The pressure perturbation $p(\mathbf{x}, z, t)$ can be given in terms of ϕ and ζ using Bernoulli’s equation (e.g. § III.A). The

wave motion is therefore completely described by $\phi(\mathbf{x}, z, t)$, which obeys Laplace's equation, and $\zeta(\mathbf{x}, t)$.

Since the objective of the present work is to describe the evolution of such waves over distances that are generally much larger than the wavelength, it is not practical to determine accurately ζ and ϕ everywhere. Instead a statistical representation of the sea surface will be preferred (see Komen *et al.*, 1994). The probability distribution of the sea surface elevation ζ at any horizontal location is generally very nearly Gaussian as the result of the superposition of many different waves with different frequencies and directions, propagating at different speeds, except in very shallow water where the wave height is of the same order as the water depth (Elgar & Guza, 1985). As a result of this property the joint probability distribution of the surface elevation can be determined from the surface elevation covariance function

$$\langle \zeta(\mathbf{x}_1, t_1) \zeta(\mathbf{x}_2, t_2) \rangle. \quad (1.1)$$

A similar covariance can be used to describe the velocity potential.

The three-dimensional Fourier transform of (1.1) with respect to the two horizontal space and the time coordinates yields the (vector) wavenumber-frequency spectrum $E(\mathbf{k}, f)$. Since wave properties usually evolve slowly in space and time, the Fourier transform, a decomposition in sinusoidal waves, is advantageously replaced by a decomposition of ζ and ϕ in slowly modulated sinusoidal waves, that may be based on the evolutionary spectral theory of Priestley (1965), giving a spectrum $E(\mathbf{k}, f, \mathbf{x}, t)$ that is also a slow function of horizontal space and time, (see Komen *et al.*, 1994, and chapter III). This spectrum can be evaluated by applying a three-dimensional Fourier Transform to time series of surface elevation maps, $\zeta(\mathbf{x}, t)$, or related quantities such as the surface slope, obtained by continuously imaging the sea surface in a small region with a dwelling aircraft (Dugan *et al.*, 1996).

A projection of this three-dimensional spectrum into two, or just one, dimensions is more readily accessible from simpler measurements. In linear theory, a very good approximation for waves in general and swell in particular, the wave frequency f and wavenumber magnitude $k = |\mathbf{k}|$ are related (in the absence of currents) by the dispersion relation $f/(2\pi) = gk \tanh(kh)$, where g is the apparent gravity acceleration and h is the water depth. Therefore the projection of the three-dimensional spectrum into a two-dimensional wavenumber $E(\mathbf{k})$ or frequency-direction $E(f, \theta)$ spectrum loses only the information on the weak non-linear effects. The wavenumber spectrum can be estimated, more or less directly and for different ranges of wavelengths depending on the platform, by surface imaging instruments such as scanning altimeters (e.g. Hwang *et al.*, 2000), Real Aperture Radars (Jackson, Walton & Baker, 1985), and Synthetic Aperture Radars (e.g. Komen *et al.*, 1994). In-situ measurements of velocity, pressure, or surface elevation with coherent arrays can provide estimates of $E(f, \theta)$ (e.g. Davis & Regier, 1977; Long & Hasselmann, 1979; Pawka, 1983; Herbers & Guza, 1990). $E(f, \theta)$ is convenient for practical use as f is conserved during wave propagation (in the absence of currents and neglecting non-linear effects) whereas k is modified by depth shoaling. An example spectrum is given in figure 1.1, using data from a coherent array of pressure sensors in 8 m depth at the U. S. Army Corps Field Research Facility in Duck, North Carolina. These estimates are more precise as one increases the number of sensors in the array. Most analysis methods for this type of data involve the cross and auto-correlations between the various measurements, assuming uniform statistics over the length of individual records. Alternative analysis techniques have been proposed to give higher resolution in the directional spectra by reducing the frequency resolution. Such a technique developed by Donelan, Drennan & Magnusson (1996) gives interesting results but interpretation is made difficult by the unfounded hypothesis that for any given time and frequency band the wave field is dominated by one wave group coming from a well-defined direction.

The projection of $E(f, \theta)$ on the frequency axis (the frequency spectrum, see figure 1.1b) can be evaluated from the time series of surface elevation (as measured by an infrared laser mounted on a tower) or pressure at a fixed sub-surface elevation, for example at the sea floor. It is the most

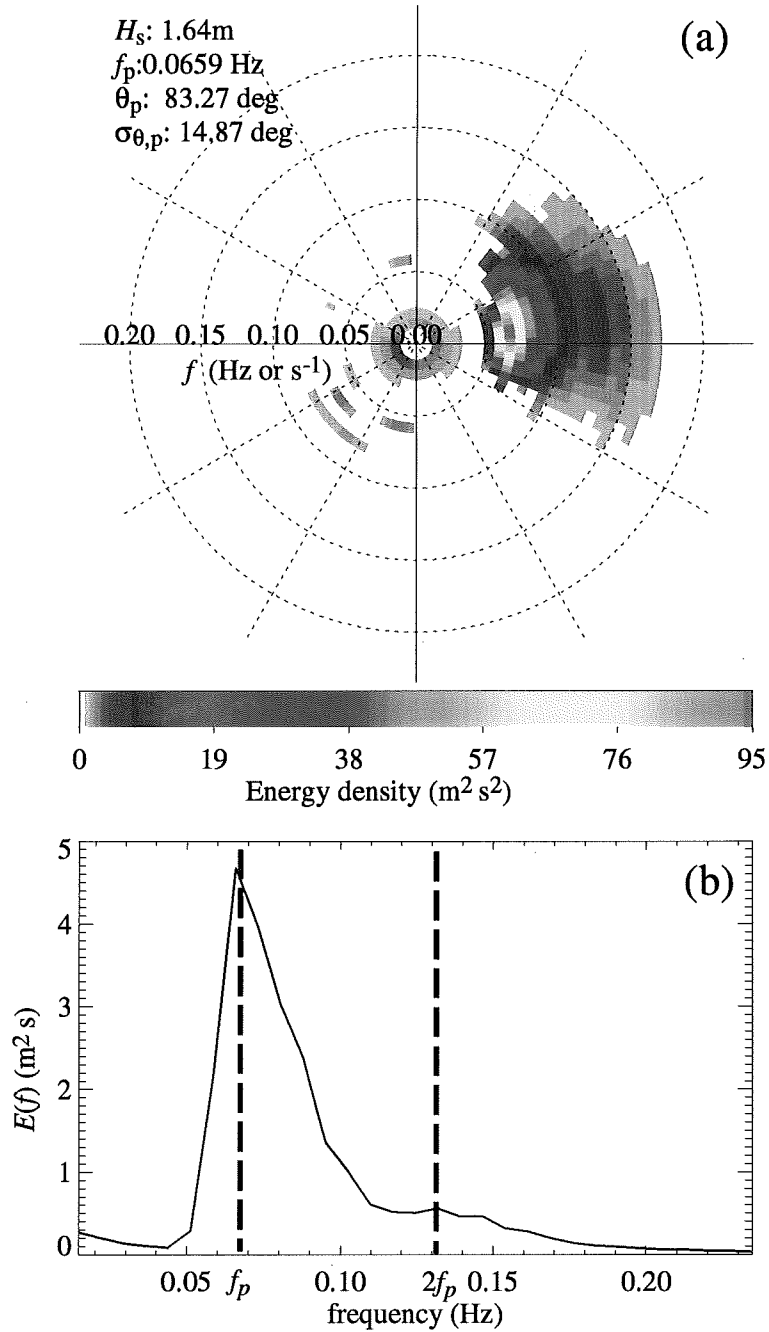


Figure 1.1: Wave spectra

(a) Example frequency-direction wave spectrum, determined from pressure array measurements in 8 m depth at Duck, NC, October 19, 1994, 7:00–10:00 EST. (b) Corresponding frequency spectrum, in which the first harmonic peak at $f = 2f_p$ is probably due to non-linear effects, which are enhanced in shallow water and for large amplitude waves such as these (see § II.E.1 for more information on this event).

common in-situ measure of the sea state but it gives no information on the directional properties of waves.

The main wave properties are often quantified with a few parameters. The most common are the significant wave height H_s , defined as four times the square root of the elevation variance (the area under the curve in figure 1.1.b), the peak frequency f_p at which the spectrum $E(f)$ is maximum, or its reciprocal, the peak period $T_p = 1/f_p$. In the limit of a narrow frequency spectrum, H_s is equal to the average height $H_{1/3}$ of the highest one third of the waves. H_s is indirectly determined from the shape of satellite radar altimeter pulses (e.g. Rao *et al.*, 1990), back-scattered by the sea surface, providing the only wave measurement available globally that is used for operational wave forecasting.

The elevation variance density spectra E defined above in wavenumber-frequency, wavenumber, frequency-direction, or frequency spaces are commonly called wave energy spectra. However they must be multiplied by the water density ρ and gravity g to have units of energy. For the example spectrum shown in figure 1.1.a, the onshore energy flux, that is the average rate (over many waves) at which wave energy is released on the nearby beach per meter of coastline, is 13 kW. This estimate illustrates how powerful waves are, even after losing 75% of their energy across the shelf because of bottom friction (see chapters II and V).

Between coherent arrays providing detailed directional information, and single sensors giving simple frequency spectra, intermediate self-contained devices have been developed to measure some representative directional properties of waves. The directional properties of the wave spectrum are usually summarized with a mean direction for the entire spectrum, $\bar{\theta}$, for each frequency, $\bar{\theta}(f)$, or at the peak only, θ_p , as indicated on figure 1.1. The corresponding directional spread σ_θ , $\sigma_\theta(f)$, or $\sigma_{\theta,p}$, gives a measure of the half-width of the directional distribution of the wave energy (Kuik, van Vledder & Holthuijsen, 1988). In the present dissertation σ_θ is equal to the standard deviation in radians if the directional distribution is narrow, and reaches a maximum value of $2^{1/2}$ radians (that is 81 degrees) for an isotropic distribution. These simple parameters can be determined from the first Fourier components of the directional distribution at each frequency. Both the first and second Fourier components can be estimated from collocated tri-axis acceleration time series (as measured by a Directional Waverider buoy), or any combination of three independent scalar quantities related to these by linear wave theory, such as the heave, pitch, and roll of a floating platform (Longuet-Higgins, Cartwright & Smith, 1963; Long, 1980), or pressure p and horizontal velocity components u and v . A ‘cloverleaf’ curvature buoy (Cartwright & Smith, 1964), was designed to provide more Fourier components, but proved delicate to use.

Moored surface-following buoys can be used in any water depth for accurate measurement of the dominant swells (e.g. O’Reilly *et al.*, 1996), but these large Lagrangian sensors do not resolve short, nonlinear waves, and are suspected to miss extremely large (so-called ‘freak’) waves by sliding off their top. Bottom-mounted pressure and p - u - v gauges are more accurate but limited to shallow areas ($\simeq 20$ m, depending on the frequency of interest) because of the vertical exponential attenuation of the wave signal over a height equal to the wavelength.

The directional information given by the first two Fourier components measured by all these instruments can be used to estimate a full frequency-direction spectrum. The Maximum Entropy Method (Lygre & Krogstad, 1986), used in the present work, gives an estimate that is constrained to fit the data exactly but the construction of a directional distribution from only four parameters calls for caution in interpreting the resulting estimates.

C. The energy balance equation

The evolution of the wave spectrum $E(\mathbf{k}, \mathbf{x}, t)$, can be described with a spectral energy balance (Gelci, Cazalé & Vassal, 1957). Neglecting the effects of currents, it is given by (e.g.

Whitham 1974):

$$\frac{\partial E}{\partial t} + \nabla_{\mathbf{x}} \cdot (\mathbf{C}_g E) + \nabla_{\mathbf{k}} \cdot (\mathbf{C}_k E) = S \quad (1.2)$$

where $\nabla_{\mathbf{x}}$ and $\nabla_{\mathbf{k}}$ are horizontal divergence operators in geographical and wavenumber space respectively, and \mathbf{C}_g (the group speed) and \mathbf{C}_k are the corresponding energy transport velocities. The source term $S(\mathbf{k}, \mathbf{x}, t)$ is the net rate of energy transfer to component \mathbf{k} resulting from interactions between wave components, or interactions with the bottom, the atmosphere, or other flows in the water column such as internal waves. The effects of currents can be added by replacing the energy spectrum by the action spectrum $N = 2\pi E/f$, and replacing S with the corresponding action source term (e.g. Bretherton and Garret, 1969; Komen et al, 1994).

The spectral energy balance can also be formulated from a Lagrangian point of view:

$$\frac{dE}{dt} = S \quad (1.3)$$

where the left-hand side is the rate of change of E following a wave component along its ray trajectory. (1.2) and (1.3) are equivalent for waves that obey a dispersion relation of the form $f = W(\mathbf{k}, \mathbf{x}, t)$ where f is the wave component frequency. However, in contrast to the Eulerian balance (1.2), the along-ray conservation of spectral densities for $S = 0$ is valid only in \mathbf{k} -space (Longuet-Higgins, 1957). In both cases the left hand sides represent the advection of wave energy accounting for refraction (the turning of wave crests around shoals and depressions) and shoaling (the increase in energy when the group speed decreases).

The stochastic representation outlined above, generally referred to as weakly non-linear and ‘phase averaged’, assumes that phases of spectral wave components are uncorrelated. This is appropriate for waves in intermediate and deep water where nonlinearity is weak and phases are randomized by dispersion (Benney & Saffman, 1966). This simplification is not applicable in very shallow water, inside or very near the surf zone, where waves are weakly dispersive and non-linearity is enhanced. The reader may follow Freilich & Guza (1984) and Herbers & Burton (1997) for spectral approximations used in this regime, or Osborne *et al.* (1998), for a different approach based on inverse-scattering theory.

The energy balance (1.2) or (1.3) provides a simple prognostic equation for the evolution of the wave spectrum. In shallow to intermediate water depths, surface gravity waves are affected by sea bed features with a wide range of scales (figure 1.2). Wave refraction over large scale (nominally 1 to 10 km) bottom features can induce dramatic variations in wave energy along the coast that are readily observed (e.g. Munk and Traylor, 1947). The effects of refraction on the evolution of wave spectra are generally well understood, and accurately represented in the left-hand sides of (1.2–1.3) by geometrical optics models (e.g. Longuet-Higgins, 1957; Mei, 1989; O’Reilly & Guza, 1993; §II.A).

However the ray trajectories followed by wave groups, predicted by the geometrical optics approximation, may be modified by the strong non-linearity of steep waves (Willebrand, 1975). This effect will be neglected in the present work as it is weak for the low steepness swell observed outside storm wave-generation regions. The present analysis is focused on swell, with small surface slopes in light wind conditions, so that generation of waves by the wind, dissipation of energy due to wave breaking, and mutual interaction of different wave trains can be neglected. These processes that control wave evolution in deep water are usually represented in the right-hand side source terms of (1.2–1.3), by the sum of three parameterized source terms, S_{in} for the wind energy input, S_{dis} for the wave breaking dissipation, and S_{nl} for the non-linear wave-wave interactions. Although the latter is never completely absent even without wind, it can be discarded here as it modifies the wave spectrum on a time scale of the order of $(\varepsilon^4 f_p)^{-1}$ where ε is the mean wave slope, and f_p is the peak frequency (Hasselmann, 1962). This time scale for the lowest order interactions is generally much longer (of the order of 20 days for 0.1 Hz swell with $\varepsilon = 0.05$) than the propagation time of swell over the regions of interest in the present work (about three hours for 0.1 Hz swell crossing the North Carolina continental shelf). Higher order interactions are even weaker (Krasitskii, 1994).

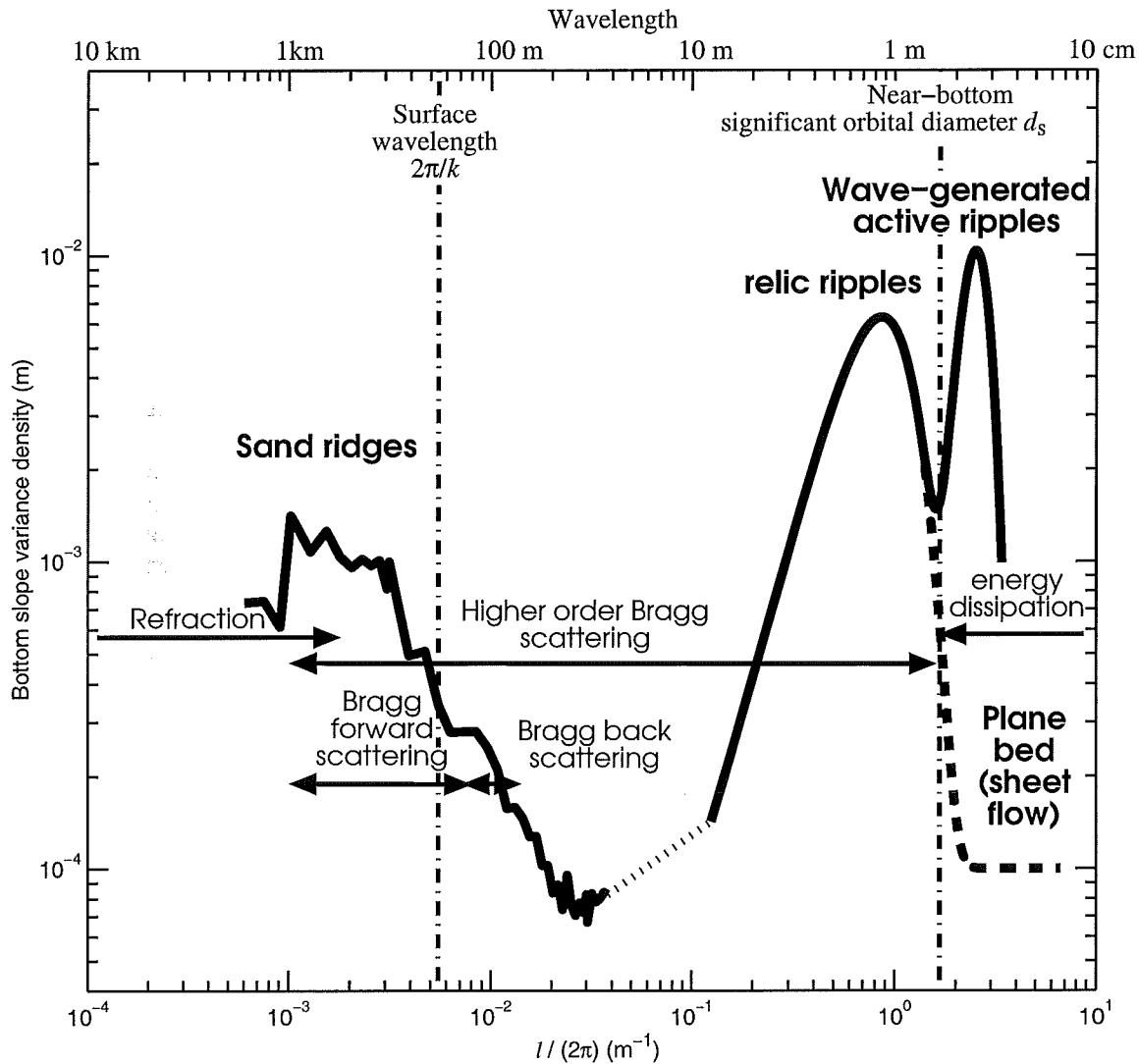


Figure 1.2: Wave-bottom interactions

Summary of the effects of different bottom undulation scales (the bottom x -axis coordinate $2\pi/l$ is the reciprocal bottom wavelength), for typical moderate swell motion scales (wavelength $k/2\pi$ and significant near-bed orbital displacement diameter d_s , indicated by vertical dash-dotted lines). The thick curve is a typical bottom slope spectrum for the North Carolina shelf derived from bathymetry surveys for bottom wavelengths larger than 40 m. A variety of bedforms of wavelengths less than 10 m can be generated by the waves depending on the forcing conditions. Of particular interest are steep and active vortex ripples (solid curve, with wavelengths and heights estimated from sidescan sonar surveys) maintained by the wave orbital motion. They strongly enhance the turbulent dissipation of wave energy on the shelf. These ripples become relic in benign wave conditions, or are obliterated in strong forcing conditions, turning the sea bed into a sheet flow layer with lower drag (dashed curve).

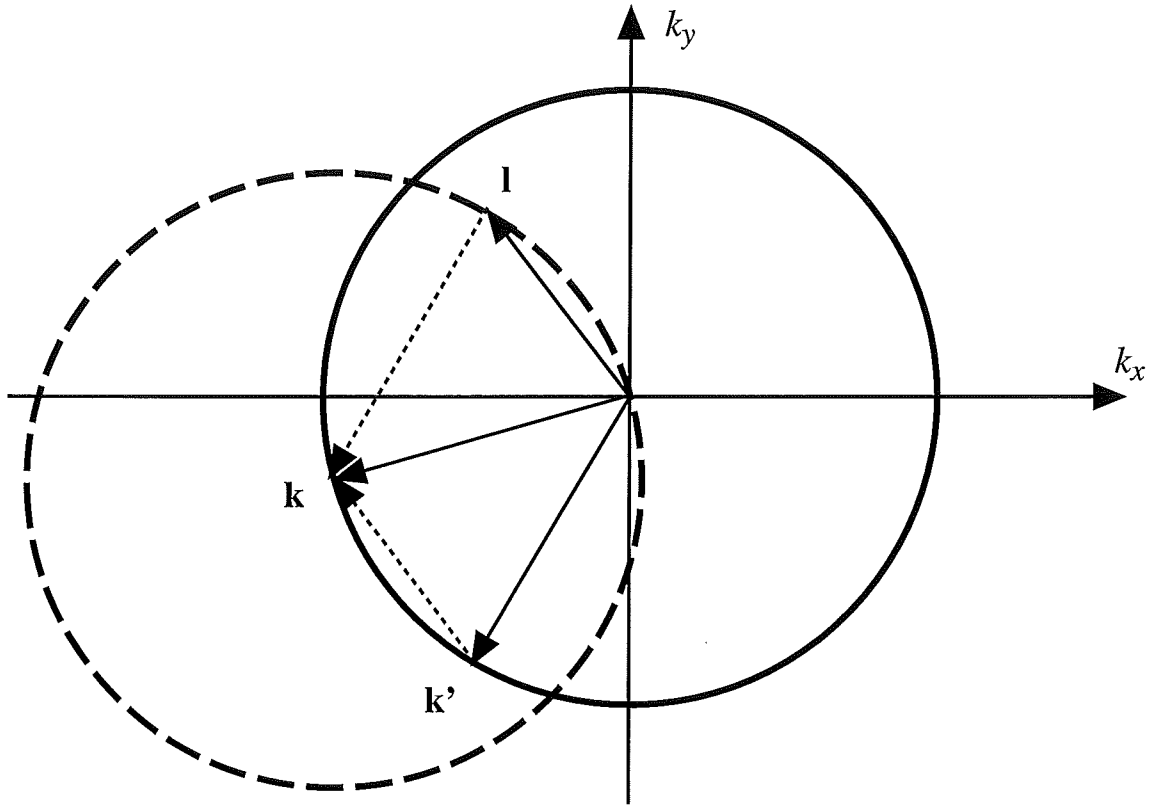


Figure 1.3: Resonance condition for Bragg scattering

The interaction between a surface wave with wavenumber k' and a bottom component with wavenumber l excites a surface wave with the sum wavenumber $k = k' + l$. For fixed k , the resonant k' and l lie on the solid and dashed circles, respectively.

Swell evolution is therefore determined primarily by wave-bottom interaction processes. Small scale (one half to several wavelengths) bottom features can scatter waves, and bottom irregularities shorter than the typical orbital diameter of the wave motion at the bottom, can be considered as roughness elements that are responsible for the dissipation of wave energy in the bottom boundary layer (figure 1.2). These latter two effects are discussed in the next two sections together with their representation as source terms in the right hand sides of (1.2–1.3).

D. Wave-bottom scattering

Hasselmann (1966) proposed a statistical theory for the evolution of random surface gravity waves over an irregular bottom assuming spatially homogeneous conditions (i.e. uniform surface wave and bottom elevation spectra). At the lowest order, two wave components with the same radian frequency ω but different wavenumber vectors k and k' exchange energy in a resonant triad interaction with the bottom component that has the difference wavenumber $l = k - k'$ (figure 1.3). This Bragg scattering process is potentially important for the directional properties of the waves. Long (1973) applied Hasselmann's theory to swell in the North Sea with some assumptions about the unknown statistical properties of the bottom topography. His results suggested that back scattering of surface waves from bottom undulations with wavelengths close to half the surface wavelength

($\mathbf{k} \approx -\mathbf{k}'$, $l \approx 2k$) could explain the swell energy decay observed during the JONSWAP experiment (Hasselmann *et al.*, 1973), but subsequent bathymetric surveys (Richter, Schmalfeldt & Siebert, 1976) showed that the amplitude of seabed undulations at the site of the JONSWAP experiment was too small to cause significant back scattering. Ewing & Pitt (1982) observed reflected waves increasing in height away from a rocky coast, qualitatively consistent with wave-bottom Bragg scattering. Yet the importance of wave scattering by natural seabeds has remained unknown in general. It is believed to be weak, and the lack of detailed bathymetric data has prevented further investigations (Komen *et al.*, 1994).

Using a different deterministic approach, Davies (1979) derived an analytical solution for the weak reflection of a monochromatic wave train propagating at normal incidence over a patch of sinusoidal bars, that was subsequently verified in laboratory experiments (Heathershaw 1982; Davies & Heathershaw, 1984). Davies' theory does not account for the decay of the incident wave, losing energy to the reflected component, and therefore overestimates strong reflections, in particular at resonance where $l = 2k$. Mei (1985) derived a more accurate energy conserving solution, valid close to resonance, that was confirmed by experiments (Hara & Mei, 1987). The more general case of oblique incidence was considered by Mei (1985), Dalrymple & Kirby (1986) and Kirby (1993). Mei (1985) further generalized his theory to bars superimposed on a sloping bottom. Kirby (1986*a*; 1986*b*) subsequently showed that Mei's (1985) generalized theory can also be derived from modified mild slope equations. Other related developments include non-linear effects in a long wave approximation (Benjamin, Boczar-Karakiewicz & Pritchard, 1987), higher order Bragg scattering (Mitra & Greenberg, 1984; Belzons, Rey & Guazzelli, 1991; Liu & Yue, 1998; Agnon & Sheremet, 2000), extended mild slope equations for steep topography (Athanasoulis & Belibakis, 1999), and investigations of Anderson localization of waves on a random bottom (Devillard, Dunlop & Souillard, 1988; Belzons, Guazzelli & Parodi, 1988). Implications for sediment transport and the formation of multiple sand bar systems just outside the surf zone were discussed by Heathershaw (1982) and Mei (1985).

Whereas Hasselmann's (1966) stochastic theory gives an energy balance equation that is an efficient tool for predicting the spectral evolution of random waves, it is restricted to homogeneous wave and bottom topography properties, and has not been verified experimentally. In contrast, Mei's (1985) deterministic theory is more general and has been verified for simple cases, but it has not been applied yet to a natural sea bed because it requires a numerical solution to an elliptic equation that is prohibitively expensive for large domains. Kirby (1986*a*) discussed these two complementary theories but could not reconcile them for the case of monochromatic waves traveling over a sinusoidal bottom. Indeed, Hasselmann's theory assumes that the wave energy spectrum is continuous across the resonance manifold in order to determine its long-term evolution, and thus cannot be applied to monochromatic waves (see Hasselmann, 1962, and Komen *et al.*, 1994, for detailed discussions of the continuum approximation in random wave scattering theory).

In chapter III we examine the effects of wave-bottom scattering from natural seabed topography by extending Hasselmann's (1966) theory to a heterogeneous wave field and sea bed topography. Hasselmann's scattering source term is re-derived on a gently sloping bottom with slowly varying wave and bottom spectral properties, correcting for an apparent error in the wave-bottom coupling coefficients given by Hasselmann (1966) and Long (1973), and further reducing the likely importance of Bragg scattering during JONSWAP. In § III.B this result is verified through comparisons with analytic results of deterministic theories for waves propagating over a finite patch of sinusoidal bars, and the consequences of introducing a large-scale bottom slope are investigated. The effects of Bragg scattering on swell propagation across the North Carolina continental shelf are illustrated in § III.C with an implementation of the scattering source term in the spectral wave prediction model CREST (chapter II) using measured wave spectra and high-resolution bathymetric data. Extensive comparisons with field data are performed in chapter V.

E. Energy dissipation in the bottom boundary layer

1. Bottom drag

In addition to the relatively well understood energy conserving wave-bottom interaction processes, wave evolution across continental shelves and in shallow marginal seas is also believed to be strongly affected by non-conservative bottom boundary layer processes (e.g. Shemdin *et al.*, 1980; Bouws and Komen, 1983; Weber, 1988; Young & Gorman, 1995; Herbers, Hendrickson & O'Reilly, 2000).

For sea beds composed of non-cohesive sandy sediments, the dissipation of wave energy in the bottom boundary layer was shown, in laboratory experiments, to be strongly dependent on the presence of sand ripples formed by the near-bed wave orbital motion (e.g. Zhukovets, 1963; Nielsen, 1992). Neglecting currents unrelated to the waves, the bottom boundary layer can be classified in three regimes, based on the ratio of friction and buoyant forces acting on a sand grain, and represented by the maximum Shields number ψ_{\max} (often denoted θ'_{\max})

$$\psi_{\max} = \frac{f'_w u_{\max}^2}{(s-1)gD}, \quad (1.4)$$

where f'_w is a skin friction factor, s is the specific density of the sand grains, D is their diameter, and g is the acceleration of gravity (Shields, 1936). For small values of ψ_{\max} , the bottom morphology does not change, thus retaining the history of past wave events and biological activity. In this 'relic roughness' regime wave energy dissipation is minimal as bottom velocities are small and turbulence is weak.

In the following the magnitude of the wave energy dissipation will be measured by the dissipation factor f_e , an averaged drag coefficient that gives the energy dissipation from a representative bottom velocity cubed. f_e increases dramatically as surficial sediments, intermittently set in motion by the wave orbital flow, organize into ripples that increase bottom roughness. This transition occurs when ψ_{\max} increases past a threshold value ψ_c (typically 0.03–0.1 for well-sorted quartz sand) (e.g. Nielsen, 1981). These 'active ripples' sharply increase the turbulent dissipation of wave energy, as vortices are shed by the orbital flow at the ripple crests. According to experiments by Madsen, Mathisen & Rosengaus (1990) with random waves, f_e is maximum when $\psi_{\text{rms}} \simeq 1.2\psi_c$, where ψ_{rms} is computed from the root mean square bottom velocity amplitude using a formulation similar to (1.4). Example swell conditions with this maximum drag are a peak period $T_p=12$ s, and significant wave height $H_s = 1.5$ m in 25 m depth over well sorted quartz sand with grain size $D = 0.15$ mm. For larger values of ψ_{\max} (larger wave height or frequency), f_e gradually decreases as ripple crests are eroded by stronger flow.

For very large values of ψ_{\max} , of the order of $10\psi_c$ (Li and Amos, 1999), a layer of sediment, called 'sheet flow', moves with the water column, washing out ripples, giving a relatively weaker energy dissipation in the bottom boundary layer. Both the thickness of this 'sheet flow' layer and the dissipation factor f_e increase with ψ . These three flow regimes, relic roughness, active ripples, and sheet flow, are illustrated in figure 1.4.

2. Bedform dynamics

Since small-scale bedforms on the sandy sea floor play an important role in the transformation of waves across the shelf, we give here a brief review of studies on their properties. Bedforms not only affect waves but also have a strong impact on the transport of sediments, either as a result of their migration or because of their influence on the flow that shapes them. Their presence, formation, and evolution have been observed extensively in nearshore environments (e.g. Hunt, 1882; Forel, 1888; Dingler, 1974; Vincent & Osborne, 1993; Gallagher, Elgar & Thornton, 1998; Traykovski *et al.*, 1999). In the absence of mean currents, waves can generate ripples that are symmetric in

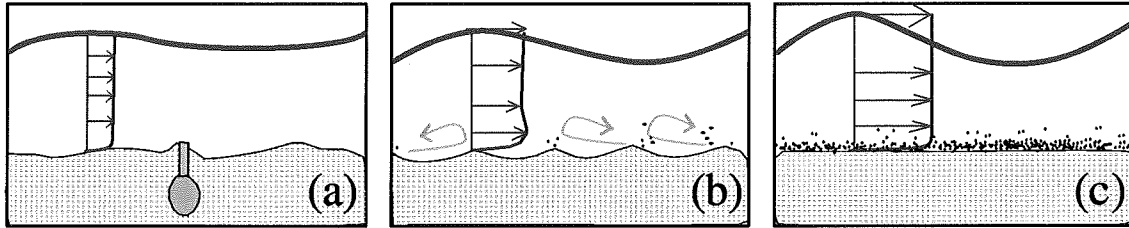


Figure 1.4: The three boundary layer regimes

(a) relic roughness. (b) active ripples. (c) sheet flow. In each the wavelength and water depth should be much larger than indicated, typically 100 m, versus 1 m for the bottom ripples. The horizontal arrows indicate the velocity profile under the wave crests (the flow reverses under the troughs). Curved arrows in (b) represent vortices generated in the lee of the ripple crests, to the right under wave crests and to the left under wave troughs.

cross-section. The formation of such wave ripples was first investigated in the laboratory by Darwin (1883) using a rotating bath. He noted the important role of the vortices generated in the lee of the ripples, further observed by Ayrton (1910), eroding the ripple troughs and building up the crests. Such bedforms, termed ‘vortex ripples’ by Bagnold (1946), exert a much larger drag on the flow than friction on sand grains. Vortex ripples occasionally have been called ‘orbital ripples’ because their wavelength is related to the near-bed orbital diameter of the wave motion, or ‘megaripples’ when they exceed some large wavelength, although they should not be confused with nearshore short-crested megaripples generated by different processes (Gallagher *et al.*, 1998).

Based on dimensional analysis and numerical morphodynamic modeling Andersen (1999) and Andersen & Fredsøe (1999) found that the wave flow over ripples is essentially governed by two nondimensional parameters, λ/d and η/λ , where λ and η are the ripple wavelength and height, and d is the diameter of the bottom orbital excursion of water parcels (figure 1.5). Sediment motions are governed by two additional parameters, the ratio w_s/u_{\max} of the settling velocity of sand grains w_s and the maximum near-bed orbital velocity u_{\max} , and the maximum ratio of friction and buoyant forces acting on a sand grain, represented by the Shields number ψ_{\max} (1.4). When ψ_{\max} is larger than a critical value ψ_c the flow is able to move sand grains. If the bed is initially flat, ‘rolling-grain ripples’ will form as a result of an instability of the flat bed. In this case each grain creates a region of weaker flow (‘shadow’) in its lee, and grains tend to group and form ripples with larger shadows (Blondeaux, 1990; Vittori & Blondeaux, 1990; Andersen, 1999, 2001). These rolling-grain ripples eventually evolve into vortex ripples (Sherer, Melo & Marder, 1999; Faraci & Foti, 2001). The height η of vortex ripples is generally closely related to λ . The ripples are steepest for $1 < \psi_{\max}/\psi_c < 4$, when the vortices created in the lee of the crests maintain η/λ values between 0.1 and 0.15.

Numerical model simulations of the morphodynamics of one-dimensional ripples under sinusoidal waves confirm that the vortex forming in the lee of the crest with a size of the order of the orbital diameter d exerts a strong shear on the lee-side slope of the ripples that tends to build up the crests together with the flow on the upstream slope of the ripple (Andersen, 1999). If two ripples are initially closer than a minimal stable wavelength λ_m , the vortex in the lee of the upstream ripple will erode the downstream ripple and one ripple may disappear creating a defect in the regular spacing of the bed that will allow λ to grow. Conversely, ripples that initially are much farther apart than λ_m will promote the generation of ripples in the troughs, dividing λ by a factor two. Values of λ_m were found to be related to the orbital diameter with $\lambda_m = 0.4d$ when $w_s/u_{\max} < 0.07$ and $\lambda_m = 0.63d$ when $w_s/u_{\max} > 0.07$. The transition for $w_s/u_{\max} = 0.07$ corresponds to a shift in the principal mode of sediment transport from suspended load to bed load, and the evolution from two-dimensional to three-dimensional ripple patterns (Nielsen, 1979). The movement of defects in the three-dimensional ripple pattern should tend to reduce the average crest distance to λ_m (Ander-

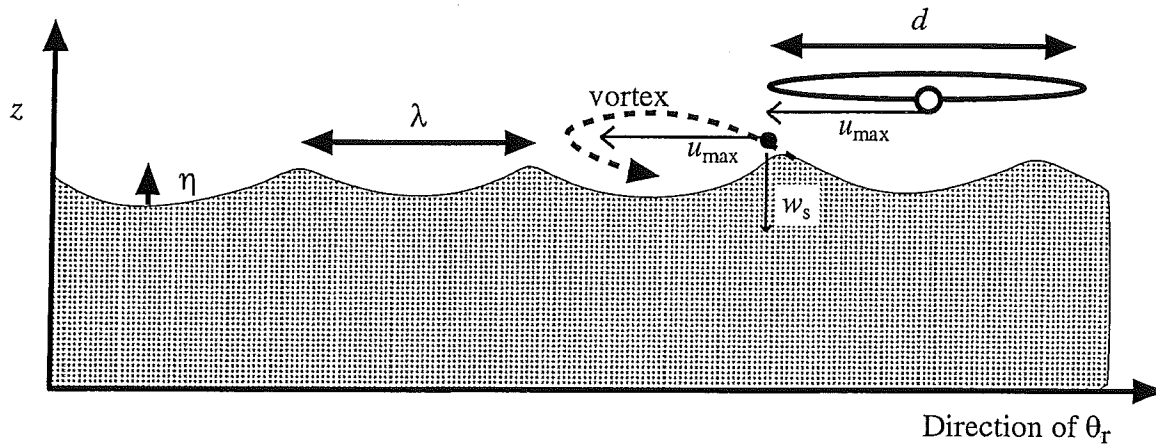


Figure 1.5: Schematic of ripples

Definition of ripple and wave forcing parameters. The cartoon corresponds to the passing of a wave trough, propagating to the right. Turbulent eddies are generated in the lee of the ripple crests. The wave flow (represented by the free-stream velocity u_{\max}) and the vortex return flow (dashed arrow) converge at the ripple crest, building up the ripple profile. The velocity of a water particle (open circle) at the top of the boundary layer is indicated by u_{\max} , and its trajectory is a flat ellipsis. The velocity of a suspended sand grain (filled circle) is a combination of the surrounding flow velocity, comparable to u_{\max} , and its settling velocity w_s .

sen and Fredsøe, 1999). Other classifications and characterizations of wave-generated ripples have been proposed based on empirical evidence (e.g. Morigridge, Davies & Willis, 1994; Wiberg & Harris, 1994) but they generally failed to reconcile all laboratory and field observations.

In the field ripples may be affected by the presence of wave groups (e.g. Madsen *et al.*, 1990), the mixture of grain sizes (e.g. Wallbridge *et al.*, 1999), and the directional distribution of the waves (Willis *et al.*, 1993), although experiments support simple parameterizations using 'equivalent parameters', e.g. the median grain size D_{50} , and the velocity u_s , orbital diameter d_s and Shields number ψ_s based on the significant wave height H_s (e.g. Traykovski *et al.*, 1999).

The presence and characteristics of wave-formed ripples on the North Carolina continental shelf is verified in chapter IV with simultaneous wave and bottom morphology measurements acquired in 1999 during the SHOaling Waves EXperiment (SHOWEX). These observations were motivated by earlier analysis of wave data (Herbers, Hendrickson & O'Reilly, 2000), and numerical modeling studies (chapters II) of strong damping of swell propagating across the shelf. The new data presented in chapter IV includes sediment samples, repeat sidescan sonar images of the bottom, and three-month-long observations of wave frequency-directional spectra. The analyzed ripples direction and wavelength, in relation with preceding wave forcing conditions and sediment properties, are reconciled with the parameterization of Andersen & Fredsøe (1999) and previous observations by Traykovski *et al.* (1999).

3. Parameterization

The representation of sand bedforms in wave models (e.g. Graber & Madsen, 1988; Tolman, 1994) usually involve a 'ripple roughness predictor' which, based on the wave conditions and sediment nature, determines the flow regime, the type of bottom features (e.g. Clifton, 1976; Wiberg & Harris, 1995) and their equivalent sand grain roughness k_N (e.g. Grant & Madsen, 1982; Madsen *et al.* 1990; Li & Amos 1998). This roughness predictor is combined with a hydrodynamic model of the bottom

boundary layer flow that predicts the corresponding wave energy dissipation. Most hydrodynamic models parameterize turbulence with a vertical profile of the eddy viscosity (Kajiura, 1968; Grant & Madsen, 1979; Weber, 1991*a*, 1991*b*; see Wiberg, 1995, for a review). The use of a single roughness length for spectral waves was validated in laboratory experiments by Mathisen and Madsen (1999). The general parameterization of (non-linear) spectral dissipation term (the bottom friction ‘source’ term) in terms of the wave spectrum was considered by Weber (1991) and simplified for practical application using a narrow spectrum approximation that was also used by Madsen (1994).

Grant & Madsen (1982) provided the first comprehensive parameterization of the interaction of waves with a mobile sandy bed (i.e. relic roughness, active ripples and sheet flow). The present dissertation considers a later parameterization proposed by Tolman (1994) that combines a ripple roughness predictor proposed by Madsen *et al.* (1990), with Grant and Madsen’s (1979) hydrodynamic model, extended to spectral waves by Madsen, Poon & Graber (1988) based on a narrow spectrum approximation. For the sheet flow regime Tolman used Wilson’s (1989) extrapolation of river flows to oscillatory boundary layers. The source term S is expressed as a quasi-linear function of the energy density E with a directionally isotropic (negative) growth rate λ :

$$S(f, \theta) = \lambda(f) \times E(f, \theta) \quad (1.5)$$

$$\lambda(f) = -f_e u_{b,rms} \frac{(2\pi f)^2}{2g \sinh^2(kh)} \quad (1.6)$$

where g is the gravity acceleration, h is the local water depth, k is the wavenumber magnitude, and f_e is the local dissipation factor representing the ripples or sheet flow effect depending on sediment and wave characteristics. The sediment parameters are a representative grain size D , specific density $s = \rho_s/\rho$, where ρ_s and ρ are the densities of sediments and water respectively, and the critical Shields number for sediment motion ψ_c . The wave parameters are a representative orbital velocity $u_{b,rms}$ and a horizontal displacement $a_{b,rms}$ at the top of the bottom boundary layer, evaluated using (11) and (25) in Madsen *et al.*’s (1988) model:

$$u_{b,rms}^2 = \int_{\mathbf{k}} \frac{8\pi^2 f^2}{\sinh^2(kh)} E(\mathbf{k}) d\mathbf{k}, \quad (1.7)$$

$$a_{b,rms}^2 = \int_{\mathbf{k}} \frac{2}{\sinh^2(kh)} E(\mathbf{k}) d\mathbf{k}. \quad (1.8)$$

For a linear profile of eddy viscosity, Grant and Madsen (1979) determined the skin friction factor f'_w , giving the Shields number $\psi_{rms} = f'_w u_{b,rms}^2 / [g(s-1)D]$, and total friction factor f_w (ratio of bulk stress and $u_{b,rms}^2$) as implicit functions of the grain size D and equivalent grain roughness of the bedforms k_N , respectively:

$$\frac{z_0}{l} = \sqrt{\frac{2}{f'_w \text{ or } f_w} \frac{D \text{ or } k_N}{30\kappa a_{b,rms}}}, \quad (1.9)$$

$$f'_w \text{ or } f_w = \frac{\kappa^2}{2 \left[\ker^2 \left(2\sqrt{z_0/l} \right) + \text{kei}^2 \left(2\sqrt{z_0/l} \right) \right]} \quad (1.10)$$

where z_0/l is a nondimensional roughness length, κ is Von Karman’s constant ($\kappa = 0.4$ for clear water), and \ker and kei are the zeroth order Kelvin functions.

The dissipation factor f_e is assumed equal to the total (skin friction and form drag) friction factor f_w (e.g. Nielsen, 1992), determined by solving iteratively (1.9,b). The equivalent grain roughness k_N of the bedforms is parameterized as a function of ψ_{rms} , ψ_c , $a_{b,rms}$, and $u_{b,rms}$. For $\psi_{rms}/\psi_c < 1.2$ (i.e. in the ‘relic roughness’ regime), k_N is taken to be 0.01 m and f_e is limited to a maximum value of 0.30 (Jonsson, 1980). Beyond $1.2\psi_c$, in the ‘active ripple/sheet flow’ regime,

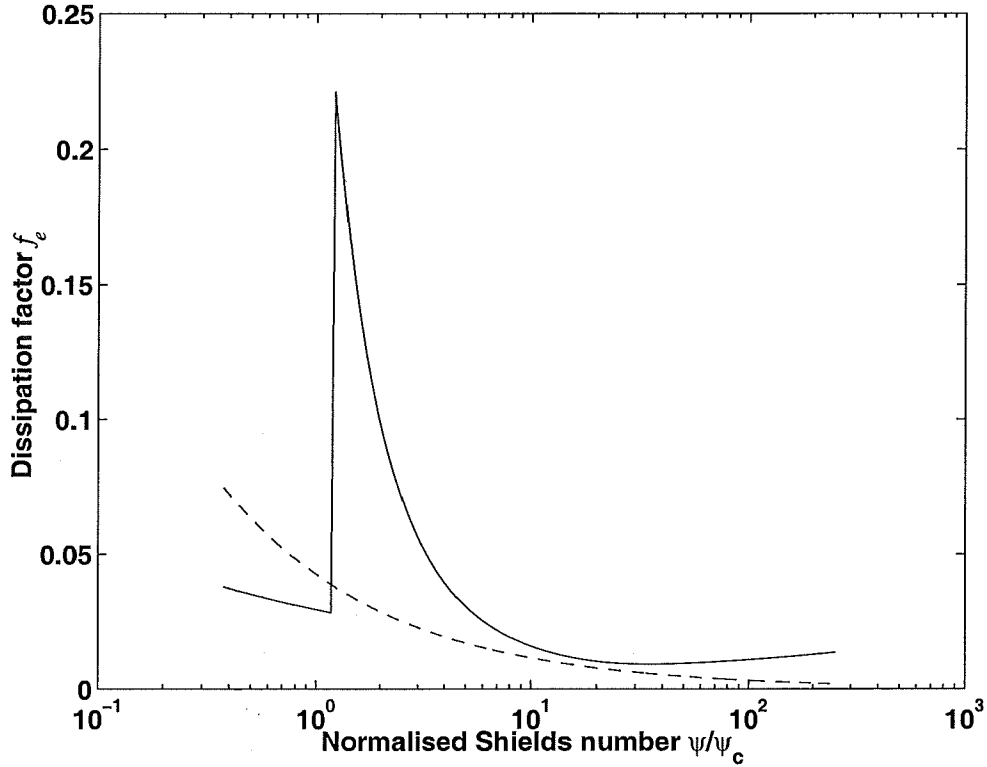


Figure 1.6: Examples of dissipation factors f_e as a function of the Shields number ψ_{rms} . The solid line is Tolman's (1994) parameterization for a representative grain size $D = 0.15$ mm, and wave period $T = 14$ s. The dashed line shows corresponding values of f_e using the JONSWAP parameterization.

k_N is the sum of a ripple roughness k_r and a sheet flow roughness k_s . Madsen *et al.* (1990) gave empirical values of k_r for random waves in laboratory experiments and Wilson (1989) extrapolated to waves values of k_s measured for river flows:

$$k_r = a_{\text{b,rms}} \times 1.5 \left(\frac{\psi_{\text{rms}}}{\psi_c} \right)^{-2.5}, \quad (1.11)$$

$$k_s = 0.57 \frac{u_{\text{b,rms}}^{2.8}}{[g(s-1)]^{1.4}} \frac{a_{\text{b,rms}}^{-0.4}}{(2\pi)^2}. \quad (1.12)$$

The first evaluation of Tolman's (1994) parameterization against field data is performed in § II.E, followed by a systematic evaluation using all swell-dominated data sets from DUCK94 and SHOWEX in chapter V. Slight modifications to Tolman's (1994) formulation are proposed in chapter V, with empirically calibrated coefficients that improve the accuracy of swell hindcasts on the North Carolina continental shelf.

Also considered in § II.E and V is the simpler empirical 'JONSWAP' parameterization of bottom dissipation used in many operational wave prediction models. It assumes that f_e is inversely proportional to $u_{\text{b,rms}}$ so that the attenuation coefficient $\Gamma = gf_e u_{\text{b,rms}}/2$ is constant and the source term is given by:

$$S(f, \theta) = -\Gamma \left[\frac{2\pi f}{g \sinh(kh)} \right]^2 E(f, \theta) \quad (1.13)$$

An average value $\Gamma = 0.038 \text{ m}^2\text{s}^{-3}$ was inferred from the JONSWAP North Sea experiment (Hasselmann *et al.*, 1973), despite a wide scatter of the attenuation coefficient Γ (from 0.0019 to 0.160 m^2s^{-3}). This parameterization has encountered some success (Bouws and Komen, 1983), and replaced quadratic drag formulations proposed previously (Hasselmann and Collins, 1968). The reason for this success over sandy bottoms, in spite of very few physical arguments, probably comes from the fact that this parameterization gives dissipation factors f_e that decrease as a function of the Shields number (figure 1.6), following the movable-bed model for relic roughness and sheet flow conditions, although it clearly misses the amplification of f_e in active ripple generation conditions.

F. Numerical wave models

Most numerical models for the evolution of surface gravity waves across ocean basins, marginal seas, and continental shelves that account for non-conservative processes (e.g. wave generation by winds, wave breaking, and bottom friction) are based on implementations of the spectral energy balance (1.2), or a similar wave action balance, with finite difference schemes. These models are efficient in deep water applications where large spatial and temporal scales of wave evolution allow for relatively coarse grids (e.g. The SWAMP group, 1984; Komen *et al.*, 1994).

In shallow water accurate representation of refraction may require grid resolution of the order of 100 m. If the region of interest is small (less than 100 km^2), a high resolution Eulerian model is feasible and gives good results (Booij, Ris & Holthuijsen, 1999), but the computational cost is presently too large for larger shelf areas, even in a steady state formulation. Additionally, finite difference approximations in these models cause numerical diffusion, artificially spreading wave energy in time, \mathbf{x} , and \mathbf{k} space, in a way unrelated to the physical evolution of a wave spectrum over bottom topography. High-order finite difference schemes and piecewise ray methods, using local ray trajectories to estimate the advection terms of (1.2), have been developed to mitigate this effect (Sobey, 1986; Young, 1988; Lavrenov & Onvlee, 1995; Benoit, Marcos & Becq, 1996).

Lagrangian wave prediction models based on (1.3) usually assume a source term S equal to zero. This approach is suitable for narrow shelf regions where propagation distances are too short for significant wave generation or decay (O'Reilly & Guza, 1991). Lagrangian models avoid the numerical diffusion of finite difference schemes, but the ray trajectories are highly sensitive to topography details. The scattering of rays over rough bottom topography causes physical diffusion of wave energy that may broaden wave spectra in shallow water. The accurate representation of these fine scale bathymetry effects in a ray model requires averaging over a large number of rays, whether the rays be computed from initially parallel directions (forward refraction, e.g. Bouws and Battjes, 1982) or from fixed points (back-refraction, e.g. O'Reilly & Guza, 1993). Back-refraction models are not based on finite area elements, unlike forward refraction and finite-difference schemes in Eulerian models, and thus have different conservation properties. For example finite-difference schemes are generally constrained to conserve energy fluxes through the model domain, but the energy fluxes obtained through spatial interpolation in a back-refraction model balance exactly only in the limit of high spatial and wavenumber resolution. Nevertheless if a detailed bathymetry is available, a back-refraction ray model with high wavenumber resolution gives a potentially more accurate representation of wave propagation than finite difference schemes.

Cavaleri and Malanotte-Rizzoli (1981) included wind input and dissipation source terms in a ray model. Their model parameterizes the source terms for each individual wave component, and solves the energy balance equation independently for each ray, without any coupling. Lavrenov (Personal communication, 2000) used a similar approach but restricted the source terms to those that only depend on the energy at the same wavenumber, such as the damping of waves by sea ice, so that rays are indeed independent. In chapter II we present a new model that includes coupling between rays through a source term that is parameterized in terms of the full energy spectrum.

II. THE CREST WAVE MODEL

In this chapter, published in a slightly different form in the *Journal of Physical Oceanography* (Ardhuin, Herbers & O'Reilly, 2001), a new numerical model is presented for solving the spectral energy balance (1.3). The source term $S(\mathbf{k}, t)$ is evaluated at each point of a coarse Eulerian grid, and subsequently interpolated from this grid onto ray trajectories. The energy balance (1.3) is integrated along a full spectrum of rays traced backward from each grid point to the model boundary. Spectral components are advected from the model boundary along the precomputed rays while being modified by the interpolated source terms, until they reach a grid point where all components are combined into a full spectrum $E(\mathbf{k}, t)$ from which $S(\mathbf{k}, t)$ can be evaluated (figure 2.1). The advection and source term computations are performed simultaneously for the entire model domain. This hybrid Eulerian-Lagrangian model essentially couples a Lagrangian energy advection scheme with an Eulerian source term computation scheme. The formulation of the source term computations is not constrained in any way by the advection scheme and thus can be adapted from existing third-generation models.

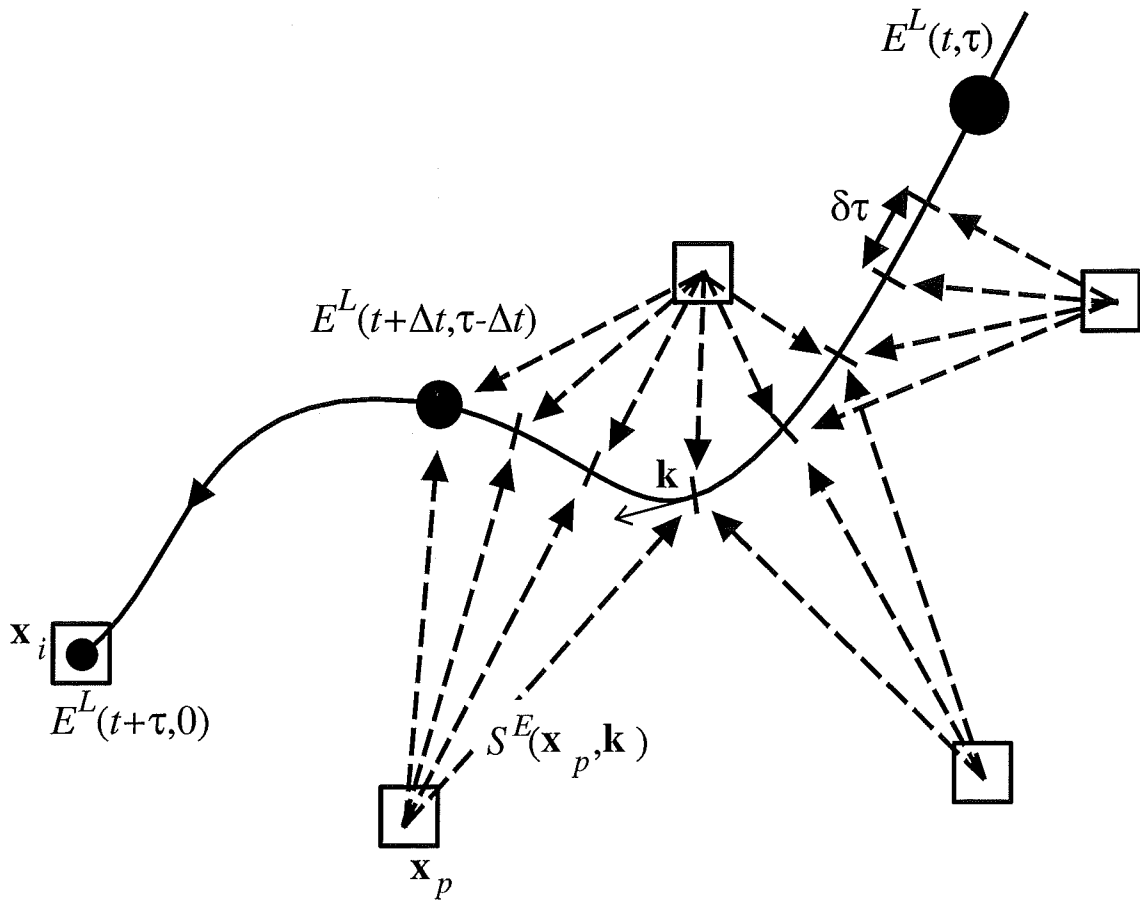


Figure 2.1: Numerical scheme of CREST

The Lagrangian energy balance is integrated from t to $t + \Delta t$ along a single ray (solid curve) using a spatially interpolated source term. Filled circles symbolize the magnitude of the energy density, and dashed arrows indicate the interpolation of the source term from the Eulerian grid (squares) onto the ray at increments $\delta\tau$. See §II.A for further details.

A. Numerical schemes

The model consists of two parts. First wave rays are traced backwards from fixed Eulerian grid points, with positions \mathbf{x}_i , to the model boundary. Second, these trajectories are used to integrate (1.3) in time, using an ensemble average over a large number of rays. Along each ray, arriving at \mathbf{x}_i with a wavenumber vector \mathbf{k} , we define a Lagrangian energy density $E^L(t, \tau)$ as the energy density ‘upstream’ of \mathbf{x}_i at time t , where τ is the energy advection time from the local ray position to the grid point \mathbf{x}_i (figure 2.1). The spectral densities E^L are averaged over ensembles of rays within finite bands \mathbf{k}_j of the arrival wavenumbers \mathbf{k} at \mathbf{x}_i . The full Eulerian energy density spectrum $E^E(\mathbf{x}_i, \mathbf{k}, t)$ at \mathbf{x}_i is evaluated by combining the average Lagrangian density predictions $E^L(t, 0)$ at \mathbf{x}_i for all bands \mathbf{k}_j . A source term $S(\mathbf{x}_i, \mathbf{k}_j, t)$ is determined at each grid point from the full Eulerian spectrum E^E and other local parameters (e.g. wind stress and bottom roughness). S is then interpolated in \mathbf{x} and \mathbf{k} space to yield an approximate source term $\tilde{S}(t, \tau)$ at the local ray positions and wavenumbers which in turn modifies $E^L(t, \tau)$ along the rays (figure 2.1). Rays and grid are thus coupled at $\tau = 0$ only.

The entire set of interpolation coefficients, representing the influence of the topography on waves is precomputed once, and stored in files. Using these files and a time series of wave spectra at the model open boundaries the energy balance equation is integrated in time.

Although the Lagrangian energy balance (1.3) holds only for energy density in wavenumber (\mathbf{k}) space, the propagation of waves is formulated more conveniently using wave frequency f and direction θ as variables. In the following f and θ are used throughout in ray calculations, grid discretization and result displays, but the energy density in \mathbf{k} space is used in the energy balance calculations.

1. Model domain and boundary conditions

The model domain covers a region of known bottom topography. From an arbitrary set of N_{gp} grid points (hereinafter called ‘model grid’) with locations $(\mathbf{x}_i)_{i=1, N_{\text{gp}}}$ a triangular mesh is generated using Delauney’s tessellation technique. The outermost points of the mesh form the model boundary, which is therefore a polygon. Additional interior polygons can be added to the boundary in order to represent islands in the model domain (figure 2.2). Ray trajectories are traced backward in time from the grid points \mathbf{x}_i until they cross a boundary. For each \mathbf{x}_i , rays are computed for a large number of frequencies f_j and arrival directions θ_l . Depending on the geographical region covered by the model domain, rays can be trapped in shallow water and end at the coast, or reach a deep water region where they become straight, or cross the model boundary in a region of intermediate depth. In all cases a ray is terminated when it crosses a triangle side connecting two boundary grid points, and the Lagrangian energy density carried by the ray into the model domain is approximated by a linear interpolation of the spectral densities at these two grid points (figure 2.2).

The boundary condition for the model is therefore fully prescribed by the spectral densities at the grid points along the boundary, for directions toward the inside of the boundary. On the open part of the boundary, spectra may be estimated from deep water wave measurements or obtained by nesting the model within a larger scale wave model. On the closed coastal part of the boundary, the energy entering the domain may be set equal to zero (i.e. wave energy impinging on the coast is dissipated in the surf zone) or, in the case of a steep coastline, determined by partially reflecting the shoreward energy flux. In order to reduce the scattering of rays over large propagation distances, the model domain can be subdivided into subdomains that are coupled through their common boundaries. This technique reduces memory requirements by shortening the rays, at the expense of some local numerical diffusion, as the energy that is transmitted through the boundary is interpolated from boundary grid points (e.g. ray d in figure 2.2).

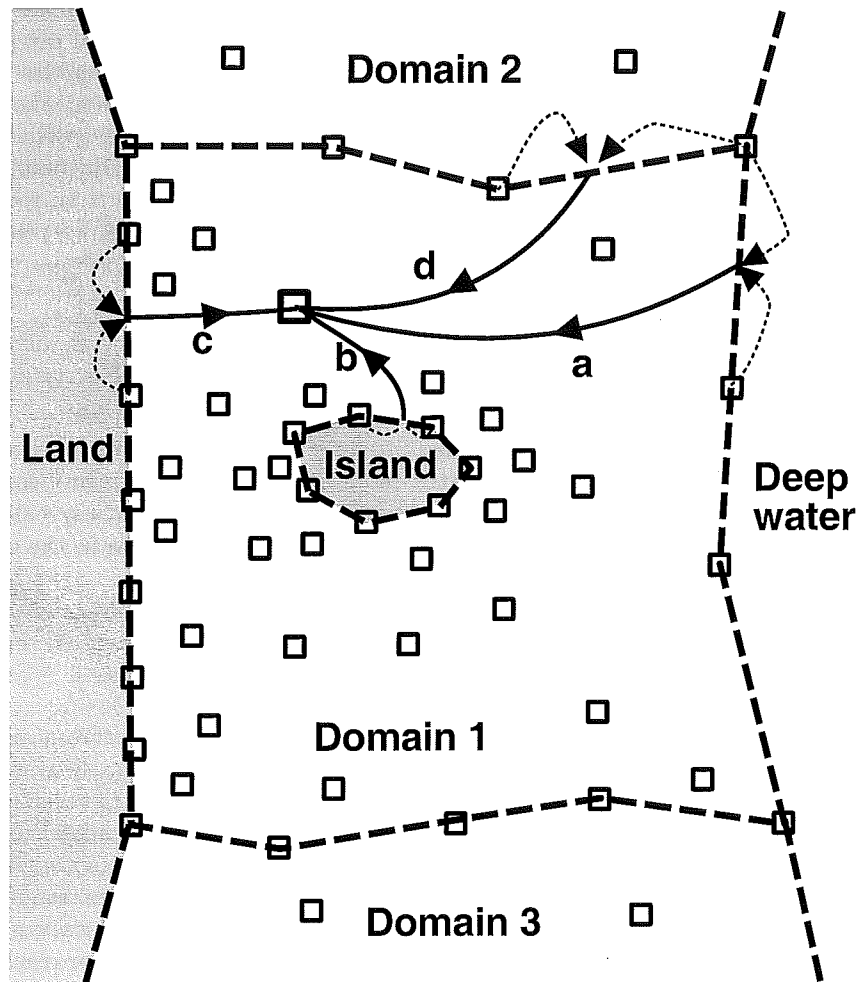


Figure 2.2: Treatment of the boundary condition

In this schematic squares represent grid points. The boundaries (dashed lines) separate and couple adjacent model subdomains. Examples are shown of rays transporting energy into the model domain from four different types of boundaries (a: shelf break, b: island, c: coast, d: internal boundary between model subdomains) to a given grid point (large square). In cases a and d energy is advected through the boundary, whereas in cases b and c energy is reflected from the boundary. In all cases, the energy is interpolated (dotted arrows) at the boundary from the adjacent two boundary grid points.

2. Precomputations

a. Rays

In applications presented here the model domain is small enough to neglect the curvature of the earth, and use local Cartesian (x, y) coordinates. The geometry of wave rays is determined by Fermat's geometrical optics principle that the integral of the phase speed C along a curve is minimum when this curve is a ray, which yields Snell's law¹ when bottom contours are parallel. The ray equations are:

$$\frac{dx}{ds} = \cos(\theta) \quad (2.1)$$

$$\frac{dy}{ds} = \sin(\theta) \quad (2.2)$$

$$\frac{d\theta}{ds} = \frac{1}{C} \frac{dC}{dh} \left[\frac{dh}{dx} \cdot \sin(\theta) - \frac{dh}{dy} \cdot \cos(\theta) \right] \quad (2.3)$$

with s a curvilinear coordinate along the ray, h the water depth, and θ the angle between the x axis and the tangent to the ray. Wave energy is transported along the ray with the group velocity C_g and the frequency f is conserved. In the linear approximation we have:

$$(2\pi f)^2 = gk \tanh(kh) \quad (2.4)$$

$$C = \sqrt{\frac{g}{k} \tanh(kh)} \quad (2.5)$$

$$C_g = C \left(\frac{1}{2} + \frac{kh}{\sinh(2kh)} \right) \quad (2.6)$$

where $k = |\mathbf{k}|$ is the wavenumber magnitude.

Along the ray the local depth and bottom slopes are evaluated from a biquadratic fit to the bathymetry grid (Dobson, 1967). The wavenumber magnitude k is computed from f using (2.5) and used to determine C , C_g and $\frac{dC}{dh}$. With these parameters (2.1)–(2.3) are integrated using an error-controlled Cash-Karp Runge-Kutta scheme (Press *et al.*, 1992) with a variable step size.

Along each ray the position and direction (\mathbf{x}^m, θ^m) are computed at small distance intervals $\delta s = \int_{\tau^m}^{\tau^m + \delta\tau} C_g d\tau$ that correspond to a fixed advection time step $\delta\tau$. A $\delta\tau$ was chosen for each frequency such that $\delta s = 200$ m in deep water. The result of the ray computation is a series of positions and directions (\mathbf{x}^m, θ^m) for each of the rays with m ranging from 0 at the initial grid point to M at the domain boundary, with typical values $M \sim 1000$ in the implementation presented in §II.D.

M , \mathbf{x}^M and θ^M give the time lag, position and direction at the end of the ray, needed to specify the boundary condition. Although waves can travel along the same ray in both directions, the rays are used here only to advect energy from the boundaries to the grid points.

¹The dutch mathematician Willebrord Snel discovered the law of refraction in 1621, but it was only published in 1703 in *Dioptrica*, by Christiaan Huygens, in which Snell is given the Latin name Snellius, which is often misspelt in English as 'Snell'. The French philosopher René Descartes gave Snell's law in *La dioptrique*, an appendix to his famous *Discours de la méthode pour bien conduire sa raison et chercher la verité dans les sciences*, published in Leiden in 1637, but it was apparently taken from Snel's work although he repeated Snel's experiments in 1626 or 1627. Snel's law is wrongly attributed to Descartes in the French scientific literature.

Source: the MacTutor history of mathematics archive, University of St Andrews, Scotland, <http://www-groups.dcs.st-andrews.ac.uk/history>

b. Interpolation of boundary conditions and source term

At each position \mathbf{x}^m along a ray, a local source term estimate $\tilde{S}(\mathbf{x}^m)$ is given by the linear interpolation in space of source term predictions at the three grid points \mathbf{x}_i of the local triangle. Since the source term is computed only at discrete directions θ_l , another linear interpolation, with weights w_l^m , is performed over the two directions θ_l that enclose the local direction θ^m of the ray. The same procedure is used for deriving an estimate \tilde{E}_B of the energy density $E^L(\tau^M)$ at the boundary:

$$\tilde{S}(\mathbf{x}^m) = \sum_{i,l} \alpha_i^m w_l^m S(\mathbf{x}_i, \theta_l) \quad (2.7)$$

$$\tilde{E}_B = \sum_{i,l} \beta_i w_l^M E^E(\mathbf{x}_i, \theta_l) \quad (2.8)$$

where the spatial weighting coefficients α_i^m and β_i are nonzero only for the three grid points \mathbf{x}_i on the vertices of the local triangle, and the two points of the boundary segment crossed by the ray, respectively.

In order to resolve the refraction of a single wave component and interpolate accurately the source term onto the ray, a small time step $\delta\tau$ is required that is of the order of 10 to 100 s for typical swell group velocities ($C_g = O(10 \text{ m s}^{-1})$) and scales ($O(1 - 10 \text{ km})$) of bottom features. This time step is too small for an efficient time integration of the energy balance equation (1.3). This integration is performed here with a fixed larger time step Δt (10 minutes in the calculations presented here), that resolves the typically slower evolution of the wave energy and source terms in space, and temporal changes of the offshore boundary conditions. The source term \tilde{S} (2.7) is averaged over an advection time interval Δt^n , that covers values of τ from $(n-1)\Delta t$ to $n\Delta t$:

$$\tilde{S}^n = \sum_{i,l} A_{il}^n S(\mathbf{x}_i, \theta_l) \quad (2.9)$$

$$\text{with } A_{il}^n = \frac{\delta\tau}{\Delta t} \sum_{i'=i, l'=l, m} \alpha_{i'}^m w_{l'}^m \quad (2.10)$$

where the summation over m includes all ray segments that fall within the time step Δt^n . In the applications presented here the timestep index n ranges from 0 at the grid point to 10-50, depending on the location of the grid point, the frequency of the waves, and the complexity of the topography. Higher frequency waves and rough topography require more timesteps than low frequency waves and smooth topography, because the group velocity decreases with increasing frequency and bending of rays over rough topography lengthens the propagation path.

c. Finite bandwidth approximation

So far we have considered the evolution of the spectral energy density $E^L(t, \tau)$ along a single ray. Since individual ray trajectories are highly sensitive to the underlying bathymetry, the energy balance equation is ensemble-averaged over a 'bundle' of rays originating from \mathbf{x}_i with frequencies and directions covering a small but finite bandwidth. The rays that form a bundle can be scattered and follow different paths away from \mathbf{x}_i , therefore the ray ensemble has a physical interpretation only at the grid points \mathbf{x}_i as a finite bandwidth average. The ensemble averaged energy density E^L and associated source term interpolation coefficients A_{il}^n are given by weighed averages of single-ray values:

$$E^L(t, \tau) = \sum_r b_r E_r^L(t, \tau) \quad (2.11)$$

$$A_{il}^n = \sum_r b_r A_{il}^{r,n} \quad (2.12)$$

where the summation is over all the rays in the bundle, and b_r is the fraction of the finite bandwidth attributed to the individual ray r .

Different rays from the same bundle may reach the boundary during different timesteps, so that the ensemble average ‘boundary energy’ \tilde{E}_B^n must be defined for each time step n :

$$\tilde{E}_B^n = \sum_{i,l} B_{il}^n E^E(\mathbf{x}_i, \theta_l) \quad (2.13)$$

$$B_{il}^n = \sum_{r,v=i,l'=l} b_r \beta_{il}^r w_{il}^{r,M} \quad (2.14)$$

where the summation is restricted to those rays that reach the boundary during time step n .

Averaging over finite frequency-direction bands not only accounts for the scattering of rays by refraction over bottom irregularities, but also has the advantage of avoiding the ‘garden sprinkler effect’ of Eulerian models formulated for a discrete spectrum (e.g. SWAMP group, 1984). A large number of ray computations (of the order of 1000 for applications presented here) may be needed to obtain a stable ensemble average but these time-consuming computations can be performed in parallel for different bundles and grid points.

The results of the precomputation are the ensemble averaged interpolation coefficients A_{il}^n and B_{il}^n . These coefficients are written to files that are used in the time-integration scheme described below.

3. Integration in time

The energy balance equation (1.3), averaged over ray ensembles, is a unidimensional time evolution equation that can be integrated using standard finite difference schemes. However, a more accurate formulation is possible for linear or quasi-linear source terms. The total source term S is split into a (quasi-)linear part λE and a residual term R that includes constant and non-linear (in E) contributions:

$$\frac{dE}{dt} = \lambda E + R \quad (2.15)$$

For λ and R constants, (2.15) has an exact solution for the evolution of E over one time step:

$$E(t + \Delta t) = E(t) \exp(\lambda \Delta t) + R \left[\frac{\exp(\lambda \Delta t) - 1}{\lambda} \right] \quad (2.16)$$

For λ and R varying slowly in time and space an approximate solution is obtained by replacing λ and R in (2.16) with average values. The interpolation of the total source term $\lambda E + R$ is more accurate with this formulation, provided that the gradients of λ , in \mathbf{k} -space, \mathbf{x} -space and time are smaller than those of E (see § II.C). For fully non-linear source terms (i.e. $\lambda = 0$) (2.16) reduces to a first order Euler scheme.

λ and R are assumed to be known functions Ω and Θ of the local wave spectrum that can be adopted from parameterizations in existing Eulerian models. λ and R are interpolated from the Eulerian grid onto the rays using the precomputed coefficients A_{il}^n . The complete integration scheme

is given by:

Source term evaluation (on the grid) :

$$\lambda(t) = \Omega(E^E(t)) \quad (2.17)$$

$$R(t) = \Theta(E^E(t)) \quad (2.18)$$

Interpolations (grid to rays coupling) :

$$\tilde{E}_B^n(t) = \sum_{i,l} B_{il}^n E^E(\mathbf{x}_i, \theta_l, t) \quad (2.19)$$

$$\tilde{\lambda}^n(t) = \left[\sum_{i,l} A_{il}^n \lambda(\mathbf{x}_i, \theta_l, t) E^E(\mathbf{x}_i, \theta_l, t) \right] / \sum_{i,l} A_{il}^n E^E(\mathbf{x}_i, \theta_l, t) \quad (2.20)$$

$$\tilde{R}^n(t) = \sum_{i,l} A_{il}^n R(\mathbf{x}_i, \theta_l, t) \quad (2.21)$$

Prognostic equation (along the rays) :

$$E^L(t + \Delta t, (n-1)\Delta t) = E_B^n(t) + E^L(t, n\Delta t) \exp(\tilde{\lambda}^n(t) \Delta t) \\ + \tilde{R}^n(t) \left[\frac{\exp(\tilde{\lambda}^n(t) \Delta t) - 1}{\tilde{\lambda}^n(t)} \right] \quad (2.22)$$

Rays to grid coupling (at $\tau = 0$) :

$$E^E(t + \Delta t) = \begin{cases} E^L(t + \Delta t, 0) \\ \text{or} \\ E_B(t + \Delta t) \end{cases} \quad (2.23)$$

where the frequency variable f_j is omitted. Variables \mathbf{x}_i , and θ_l are written explicitly only in the interpolations (2.19)–(2.21). In (2.20) the weighting of λ by the corresponding energy density E^E allows the conservation of the source term λE in the interpolation. The prognostic equation (2.22) applies the interpolated boundary condition and source term to the Lagrangian energy balance to determine E^L at the next time step. The Eulerian spectrum E^E is advanced to time $t + \Delta t$ with (2.23), closing the set of equations. For grid points \mathbf{x}_i located on model domain boundaries, the spectral densities E^E , for waves traveling into the model domain, are prescribed by the boundary condition E_B . On the deep water boundary E_B is set equal to the observed deep water spectrum. At other external boundaries E_B is set equal to zero. At internal boundaries E^E , for waves traveling into one domain, is prescribed by E^E , for waves traveling out of the other domain. For all other components and interior grid points E^E follows from E^L . Each equation can be evaluated in parallel for all the ray ensembles and all grid points, and different frequency bands are only coupled by the source term.

The accuracy of this scheme depends on the relative size of the Eulerian (T_E) and Lagrangian (T_L) time scales of wave evolution. For $T_E \ll T_L$ (e.g. a sudden and uniform change in forcing conditions over the entire model grid) the dominant source of error is the low order time integration scheme. If $T_E \gg T_L$ (e.g. strong energy dissipation at a fixed location, with quasi-stationary boundary conditions and source term) the largest errors may result from spatial interpolation of the source term. Large errors occur if either T_E or T_L are comparable to, or smaller than, Δt . For all cases presented in §II.E, Δt is small compared to both T_E and T_L . An alternative predictor-corrector scheme was tested, giving results that are indistinguishable from those of the scheme used here.

B. Source term

In the present chapter the source term is restricted to the energy dissipation caused by bottom friction. The detailed parameterization, that represents the rate of change of the energy of the spectral components, is taken from Tolman (1994), as presented in chapter I and discussed again in chapter V. The numerical scheme of the present model assumes that this source term varies smoothly on the scale of the Eulerian grid. This assumption may be violated in the case of bottom friction, and the spatial interpolation of the source term onto ray trajectories may cause large errors in the transition region from the ‘relic roughness’ to the ‘active ripple’ regime where f_e increases by one order of magnitude (figure 1.6). Tolman (1995) proposed a subgrid model of the source term that accounts for subgrid variations of the Shields number ψ resulting from variations over each grid cell of the water depth h , grain size D , critical Shields number for sediment motion ψ_c , significant wave height H_s , and peak wave period T_p . For simplicity these five random variables were assumed to be Gaussian and independent. Because no quantitative information on the spatial variability of sediment characteristics was available, a simpler subgrid model was implemented here. If uniform sediment properties are assumed then both D and ψ_c are uniform within each grid cell, leaving only three random variables h , H_s and T_p . In model simulations of swell evolution on the North Carolina shelf, using observed incident wave conditions, most of the subgrid variability of the source term resulted from the subgrid variations of water depths h rather than the wave parameters H_s and T_p , and H_s was correlated with h . This predominance of the depth variability was also noted by Tolman (1995) and used in his computations.

In the present subgrid model spatial variations in the water depth h are represented by forming a histogram of depths for a grid cell that consists of the triangles surrounding the grid point \mathbf{x}_i , using ten depth bins that span the mean ± 2 standard deviations of h . A corresponding linear theory shoaling correction of the wave spectrum is added to account for correlations of H_s with h . A subgrid-averaged value of λ is obtained by averaging estimates of λ (1.6) for each depth bin, based on the corresponding shoaling-corrected wave spectrum, weighted by the depth histogram values.

There is no strong justification for neglecting the subgrid variability of the sediment properties and simplifying sediment description by using the median grain size D_{50} and a constant critical Shields number $\psi_c = 0.05$. This problem is further discussed in chapter IV where we show evidence of significant changes in sediment properties over short distances ($O(100\text{ m})$) on the North Carolina continental shelf.

C. Model tests

The error in the ray computation is controlled by the variable time step, but other errors are introduced by the discretization in frequency and direction and the ray ensemble average. The accuracy of the propagation scheme was tested by applying the model, with the source term set equal to zero, to an idealized shelf with parallel depth contours, for a uniform and stationary off-shore boundary condition (figure 2.3a). The mean wave directions and directional distributions of energy predicted by the model agree closely with analytical (Snel’s law) results (figure 2.3 a,c), demonstrating that ray integration and discretization errors are small.

The model formulation assumes that the source term varies on scales comparable to or larger than the spacing of the grid. This condition is required for a valid interpolation. The accuracy of the interpolation scheme was tested by computing the source term directly at 20 additional grid points located along a ray segment (for 0.07 Hz waves) that covers a full source term integration time step $\Delta t = 600$ s. Source term estimates interpolated onto this ray segment with (2.20),(2.21) in a hindcast of wave evolution across the North Carolina shelf (§II.E), are compared with direct estimates at the additional grid points in figure 2.4. Results (averaged over a time step Δt) show that the linear spatial interpolations give a good approximation of subgrid variations in the source

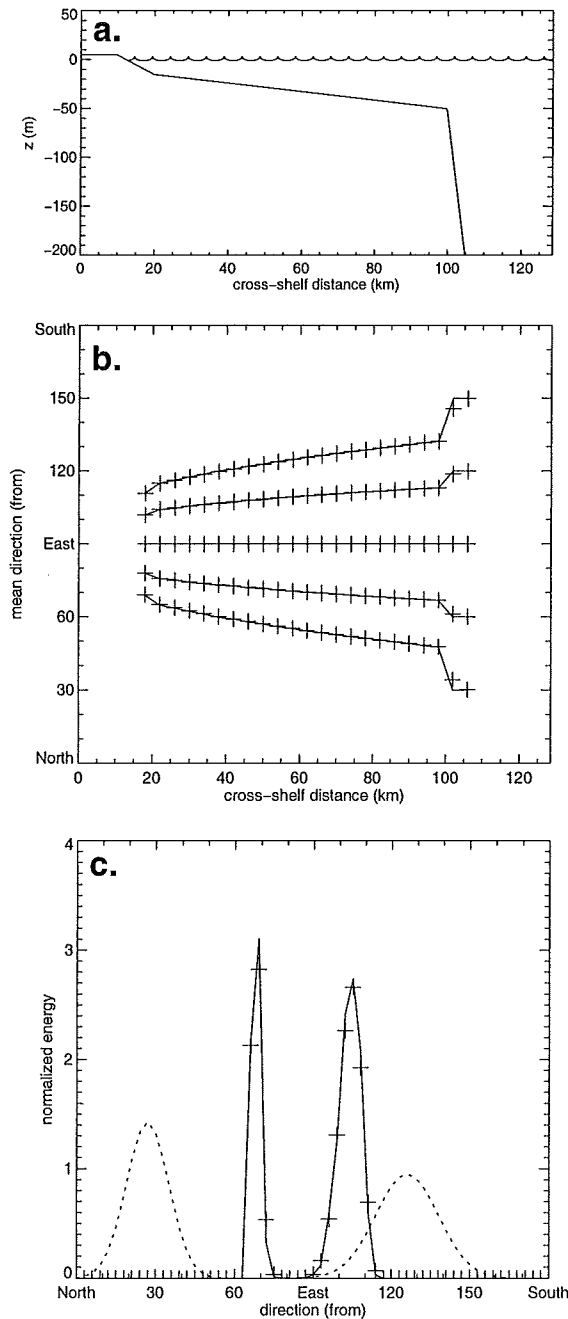


Figure 2.3: Model tests with an alongshore uniform shelf

The offshore wave energy is distributed uniformly over a narrow (0.0655-0.0685 Hz) frequency band. (a) Cross-shelf depth profile. (b) Predicted (+) and analytical (solid line) mean wave direction versus cross-shelf distance. Results are shown for narrow offshore directional distributions (standard deviation of 10 degrees) with mean wave directions varying between 30° and 150° . (c) An example directional distribution predicted by the model (+) in 20 m depth for a given offshore bimodal distribution (dotted line) is compared to the analytical solution (solid line).

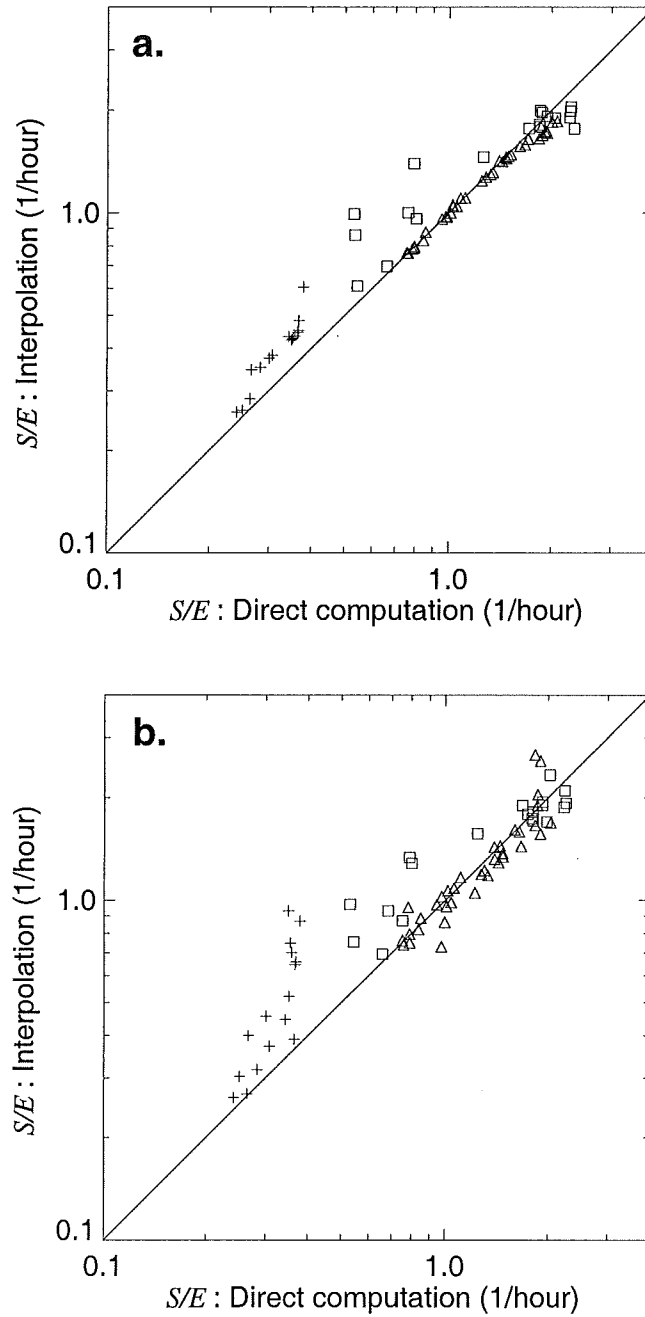


Figure 2.4: Comparison of semi-implicit and explicit schemes

Interpolated versus directly computed values of S/E (inverse of the bottom dissipation e-folding time), using (a) a quasi-linear source term implementation that interpolates λ (1.6), and (b) a non-linear implementation of the same source term that interpolates S (1.5). The source term estimates are averages over a 10 minute time step. Symbols represent different boundary layer regimes within the grid cell: relic ripples (+), active ripples (Δ), and a transition from relic to active ripples (squares).

term. That is, the source term gradients are rather well resolved by the grid. The interpolation is most accurate when the ripple regime is the same at all the neighboring grid points. Overall, a quasi-linear implementation of the movable bed source term (i.e. $\lambda = S/E$, $R = 0$ in (2.15)) (figure 2.3a), yields smaller errors than a non-linear implementation of the same source term (i.e. $\lambda = 0$, $R = S$ in (2.15)) (figure 2.3b).

D. Model implementation and field data

The hybrid Eulerian-Lagrangian model (§II.A) with a movable bed bottom dissipation source term (§II.B) was implemented for the North Carolina shelf region between $35^\circ N$ and $37^\circ N$ (figure 2.5). During the DUCK94 experiment a 100 km cross shelf transect of nine bottom mounted pressure sensors was deployed extending from 12 m depth (site A) to 87 m depth (site I) (figure 2.5; Herbers *et al.*, 2000). The instrument deployed at site H in 49 m depth was located within 2 km of 3-m discus buoy 44014 operated by the National Data Buoy Center (NDBC). Between site A and the shore a pressure sensor array was operated in 8 m depth by the Army Corps of Engineers Field Research Facility, Duck, North Carolina. Other instruments on the inner shelf included current meters, thermistors and conductivity sensors in depths ranging from 4 m to 26 m. Data from these instruments show that outside the surf zone the depth-averaged currents are mostly wind-driven with speeds usually in the range 10 to 20 cm s⁻¹, and occasional stronger currents (> 50 cm s⁻¹) in storm conditions (Lentz *et al.*, 1999). These currents are generally much weaker than both the wave speeds and the near-bed orbital velocities of energetic swell in shallow water. The effects of currents on the propagation of swell and on the wave bottom boundary layer are neglected here.

Bathymetry data was derived from the National Ocean Service digital database and additional bathymetric surveys conducted during the DUCK94 experiment (Herbers *et al.*, 2000). These data sets were merged and linearly interpolated onto a regular 6" longitude by 6" latitude grid, using a standard Delauney tessellation technique (2.5). This grid was then linearly transformed into a Cartesian x (west-east) and y (south-north) coordinate grid (resolution 152 and 185 m respectively) that is used in the Lagrangian ray integrations (2.1)–(2.3). Errors introduced by neglecting the curvature of the earth, are small for the size (128 by 211 km) of our domain (O'Reilly & Guza, 1993).

The Eulerian model grid, much coarser than the bathymetry grid, consists of 329 grid points arranged in triangles that vary in size from 5 km on the inner shelf to 10 km on the outer shelf (figure 2.5). Slightly coarser grids gave similar results, suggesting that the resolution chosen here is adequate. The model domain was made as small as possible while covering the shelf region through which most of the wave energy, measured by the pressure sensors, has propagated. The model boundaries were chosen to be the 11 m isobath (except around the 8 m array, where a grid point is collocated with the array), the 400 m isobath, and the $35^\circ 12' N$ and $37^\circ 58' N$ parallels. Swell energy enters the model domain only through the deep water boundary where the spectrum $E_B(f_j, \theta_l, t)$ is assumed to be spatially uniform. The model domain is subdivided into a main subdomain, around sites A to I and additional subdomains (figure 2.5). This allows for the representation of waves coming from high incidence angles, and reduces the memory required to store all the interpolation coefficients, including those for trapped rays, to one gigabyte. Trapped rays are not necessary for the applications presented in §II.E, since energy enters the model domain only through the deep water boundary, but were implemented for applications with other source terms (chapters III and V) and reflective boundaries. The use of subdomains, described in §II.A, introduces some numerical diffusion for waves propagating across the internal boundaries, but these waves, with high incidence angles, generally carry a small fraction of the total energy in the present applications.

For each grid point \mathbf{x}_i , rays are initially traced for 162 frequencies, at arrival direction intervals of 0.25° . For each frequency the arrival directions are subsequently bisected (O'Reilly & Guza, 1993), until neighboring rays have directions and positions at the boundary within 2° and 5

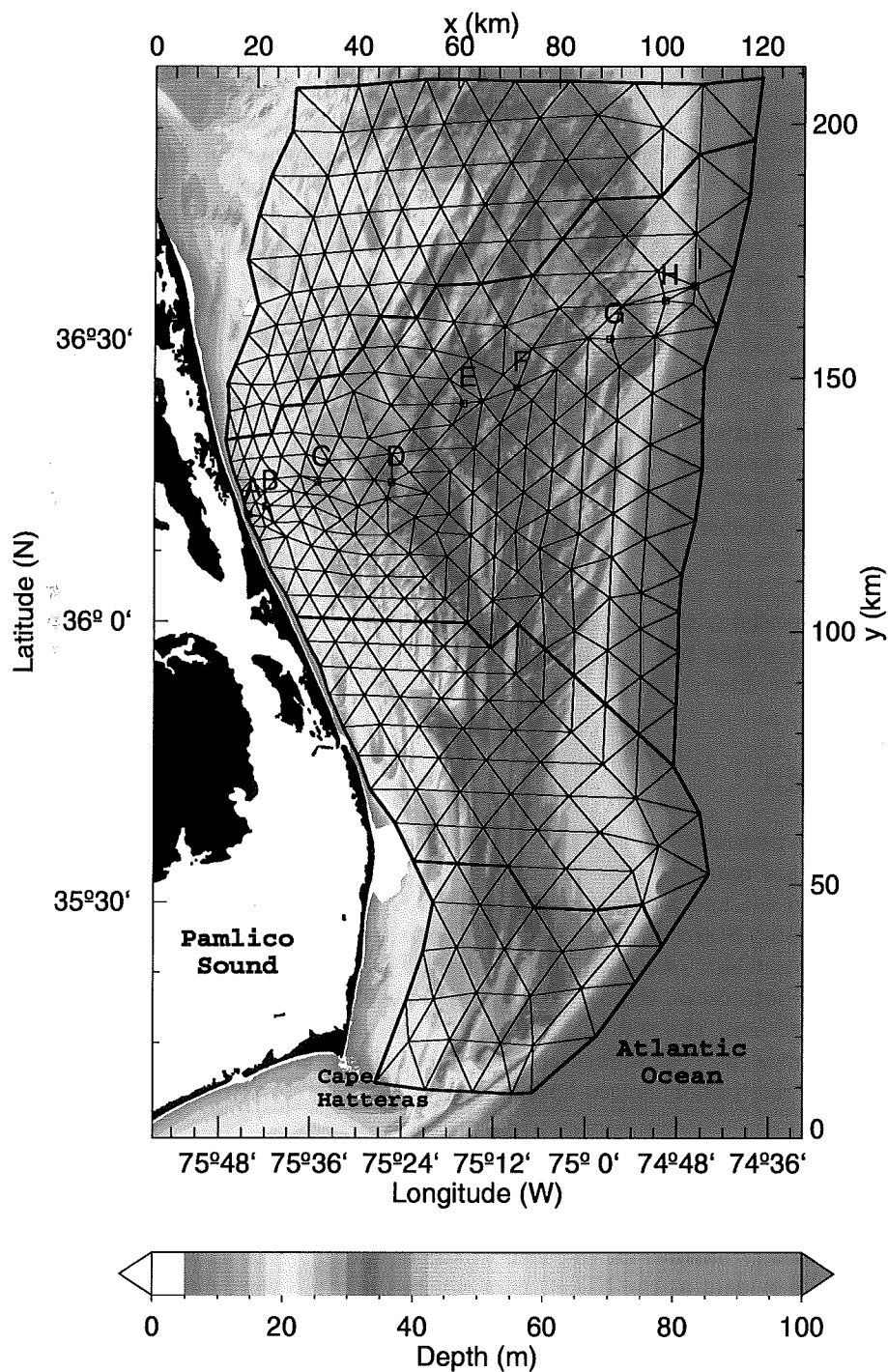


Figure 2.5: Bottom topography and model grid

The grid points where the source term is evaluated are the nodes of the triangular mesh. A linear interpolation is applied in each triangle to approximate the source term along the rays (figure 1). The entire model domain is subdivided into subdomains separated by thicker lines. Grid points denoted with dots labeled A to I are the locations of pressure sensors deployed during the DUCK94 field experiment.

km of one another, respectively. If the number of rays for a 3° sector exceeds 500 the bisection is stopped. The rays are grouped in 19×120 bundles, that represent finite bandwidths of the spectrum $E^E(x_i, f_j, \theta_l, t)$ with 19 frequencies f_j spaced exponentially with a 5% increment from 0.05 Hz to 0.12 Hz, and 120 directions θ_l spaced linearly over a full circle with a 3 degree resolution. The number of rays per bundle varies from $N_f \times 13$ (initial number of rays before bisecting) to $N_f \times 500$ (an upper limit set for broadly scattered bundles), where N_f is the number of frequencies per frequency band. N_f decreases from 9 for 0.05 Hz to 3 for 0.12 Hz.

Wave frequency spectra $E(f_j, t)$, integrated over directions, are estimated from the measured bottom pressure records at sites A-I, using a linear theory depth correction. The offshore frequency-direction spectrum $E_B(f_j, \theta_l, t)$ is estimated by combining the frequency spectrum obtained from the pressure sensor at site H, with directional distributions estimated from the nearby NDBC buoy cross-spectra using the Maximum Entropy Method (Lygre & Krogstad, 1986). This spectrum is back-refracted from site H to deep water, assuming parallel bottom contours, and neglecting the time lag between site H and the offshore model boundary. Although the offshore conditions generally varied slowly on time scales of several hours, this spectrum is determined at 10 minute intervals, in order to match the model time step Δt . Frequency-directional wave spectra on the inner shelf were estimated from the 8 m depth array near site A (Herbers, Elgar & Guza, 1999).

Based on core samples collected in 1997 on the inner shelf (Rebecca Beavers, Duke University, personal communication, 1999), and earlier geological data covering the entire shelf (Milliman *et al.*, 1972; Swift and Sears, 1974) we crudely approximate the bottom sediments in the entire area encompassed by the model with a thick uniform layer of fine quartz sand ($s = 2.65$), with a representative grain size $D = 0.15$ mm and a critical Shields number $\psi_c = 0.05$. These approximations are further discussed in chapter IV.

E. Hindcasts

Hindcasts are presented for two time periods in 1994, October 17 through 21 and November 16 through 19, that are representative of fall weather patterns causing large waves on the North Carolina coast. Wind sea and swell were observed in October, generated by a storm that moved across the eastern United States into the North Atlantic, whereas in November large swells arrived from Hurricane Gordon which remained in the western Atlantic, south of Cape Hatteras (see figure 5.2 in chapter V). In both cases, the model was run both with and without the bottom dissipation source term. Runs without the source term isolate the effects of refraction and shoaling in the evolution of wave spectra, and the difference between runs with and without the source term can be used to assess energy dissipation caused by bottom friction.

1. October storm

On October 14 and 15 local winds from the north-east were strong enough to contribute significantly to the energy balance on the shelf at the dominant (8-10 s) wave periods (figure 2.6). Strong wind forcing is evident at the NDBC buoy where the mean wave direction $\bar{\theta}$ (defined here as the direction of the first-order moment vector $\int \int \mathbf{k}/k E(\mathbf{k}) dk_x dk_y$) follows the local wind direction. As wave generation is not represented in the present model, predictions are not expected to be accurate during the spin-up of this storm.

On October 15 the significant wave height observed at site H reached a maximum value $H_s = 5.3$ m (4.3 m in the restricted model frequency range), with a peak period $T_p = 11$ s (figure 2.6b). After October 16 local winds subsided and T_p shifted to 15 s, indicating a transition from wind sea to swell. Between October 15 and 18, H_s decreased to 2.3 m (time I) followed by an increase to 2.8 m on October 19 (time II), with a narrow, swell dominated spectrum (not shown). After October 19 H_s and T_p gradually decreased to 0.6 m and 10 s respectively.

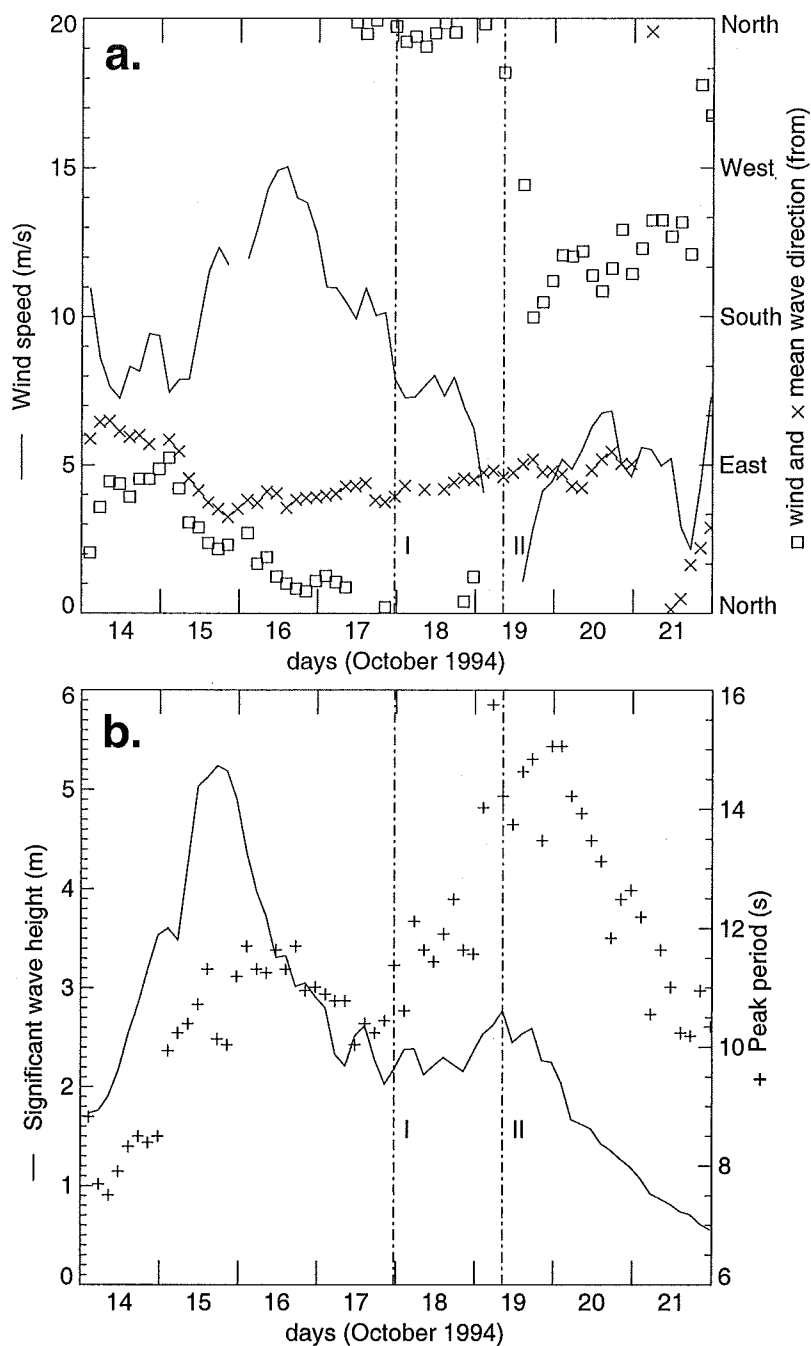


Figure 2.6: Wind and wave conditions, October 1994

Three-hour averages. (a) Wind speed (solid line), wind direction (squares), and mean wave direction (x) measured by NDBC buoy 44014 (near site H) (b) Significant wave height and peak period estimated from pressure sensor H (peak periods were replaced by the NDBC buoy values when smaller than 8 s). Vertical dash-dotted lines labeled 'I' (17 October at 23:30 EST) and 'II' (19 October at 08:30 EST) indicate times for which more detailed analyses are presented in figures 2.8, 2.9.

Model predictions are presented only for the swell-dominated period October 17 to 21. Predictions of H_s with bottom dissipation are generally in good agreement with observed H_s on the outer (e.g. figure 2.7a) and inner shelf (e.g. figure 2.7b). The model predicts the expected turning of $\bar{\theta}$ towards the shore-normal direction, owing to refraction by the large scale shelf slope (figure 2.8). The observed shift in $\bar{\theta}$, up to 25 degrees between the offshore buoy and the nearshore (8 m depth) array, is reproduced by the model (figure 2.7c). Observed and predicted $\bar{\theta}$ in 8 m depth differ by less than 5 degrees.

Model predictions without bottom dissipation show a small decrease in wave height across the shelf that is caused by refraction and shoaling effects (figure 2.7a,b). The model with movable bed friction predicts a strong attenuation of H_s across the shelf (figures 2.7b, 2.8) that is comparable to the observed attenuation. The observed and predicted decay across the outer shelf is negligible except for a slight (10%) decrease of H_s on October 19 when swell energy was maximum (time II in figure 2.7a). Strong decay of H_s is observed and predicted across the inner shelf, up to a factor 2 (equivalent to a 75% energy reduction) (figure 2.7b). The observed and predicted decrease of H_s across the shelf is generally smaller when H_s is smaller (e.g. compare times I and II in figures 2.7a,b). On October 21 when H_s was less than 0.5 m, the observed and predicted H_s (with and without bottom dissipation) are nearly uniform across the shelf.

Details of the representation of bottom friction in the model are illustrated in figure 2.9. The predicted variation of the dissipation factor f_e on the scale of the grid resolution confirms the importance of subgrid modeling of the movable bed (Tolman, 1995). Predicted boundary layer regimes (relic roughness or active ripples) are sensitive to the offshore wave conditions. On October 17 (time I in figures 2.6, 2.7), the model predicts relic roughness over most of the shelf with dissipation factors f_e close to the relic regime minimum ($f_e = 0.04$) and a sharp transition to active ripples ($0.08 < f_e < 0.18$) in depths shallower than 25 m (figure 2.9a). The boundary between active and relic ripples generally follows the depth contours. The corresponding local decay rate $|\lambda|$ proportional to $f_e u_b \sinh^{-2}(kh)$ (1.6) is enhanced not only by the large increase in f_e , but also by the increase of the bottom orbital velocity u_b in shallow water. Seaward of site D, predicted H_s with and without bottom dissipation are nearly equal to the observed H_s , whereas further inshore, predicted H_s with and without bottom dissipation diverge sharply and predictions of H_s with bottom dissipation reproduce the observed decay of H_s across the inner shelf (figure 2.9b). The strongly enhanced dissipation predicted by the movable bed model on the inner shelf is consistent with the observed variations in wave heights. However, the JONSWAP parameterization also gives reasonable predictions of H_s in this case.

On October 19 when the swell energy was maximum (time II in figures 2.6, 2.7), the movable bed model predicts active ripples on the entire shelf (figure 2.9c). The corresponding values of f_e are maximum close to the shelf break ($0.1 < f_e < 0.12$), and decrease inshore ($f_e = 0.04$ at site B). A strong decay of wave energy inshore of site G is evident in the difference between model predictions of H_s with and without bottom dissipation and these energy losses (on average 0.35 W m^{-2} over the entire shelf) are consistent with the observations (figure 2.9d). Inshore of site D the model with the source term underpredicts H_s (overpredicts decay) by about 25 to 50 cm. The JONSWAP parameterization on the other hand overpredicts H_s by 40 to 60 cm, as might be expected from figure 1.6.

2. Hurricane Gordon

Although the eye of Hurricane Gordon remained south of Cape Hatteras, local winds were strong ($10\text{-}15 \text{ m s}^{-1}$) on November 17 through the morning of November 18 (figure 2.10a). During the peak of this event (time III) when $H_s \simeq 10 \text{ m}$ and $T_p \simeq 15 \text{ s}$ (figure 2.10a), the local wind speed was about 13 m/s and the mean wave and wind direction differed by about 30 degrees. Estimated values of the wind energy input in the model frequency band (The WAMDI Group, 1988, (2.9)) are below 2 W m^{-2} on most of the shelf, while the predicted bottom dissipation rate is generally between

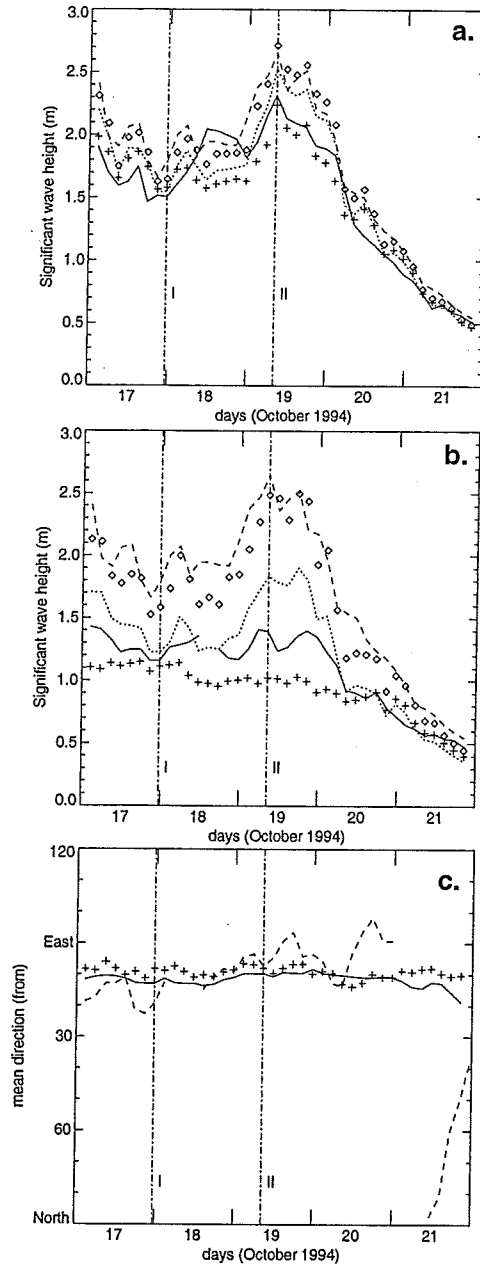


Figure 2.7: Hindcasts, October 1994

Three-hour averages of observed (solid line) and predicted (+: with movable-bed source term, \diamond : without) significant wave heights at sites F (a) and B (b) after the October storm. The dotted lines represent model results at the same sites based on the JONSWAP linear damping formulation. The offshore H_s is indicated with a dashed line. (c) The mean wave direction $\bar{\theta}$ measured at the 8 m depth array (solid line) is compared to the model prediction with the movable bed source term (+). The offshore $\bar{\theta}$ is indicated with a dashed line. Vertical dash-dotted lines labeled 'I' and 'II' indicate times for which more detailed analyses are presented in figures 2.8, 2.9.

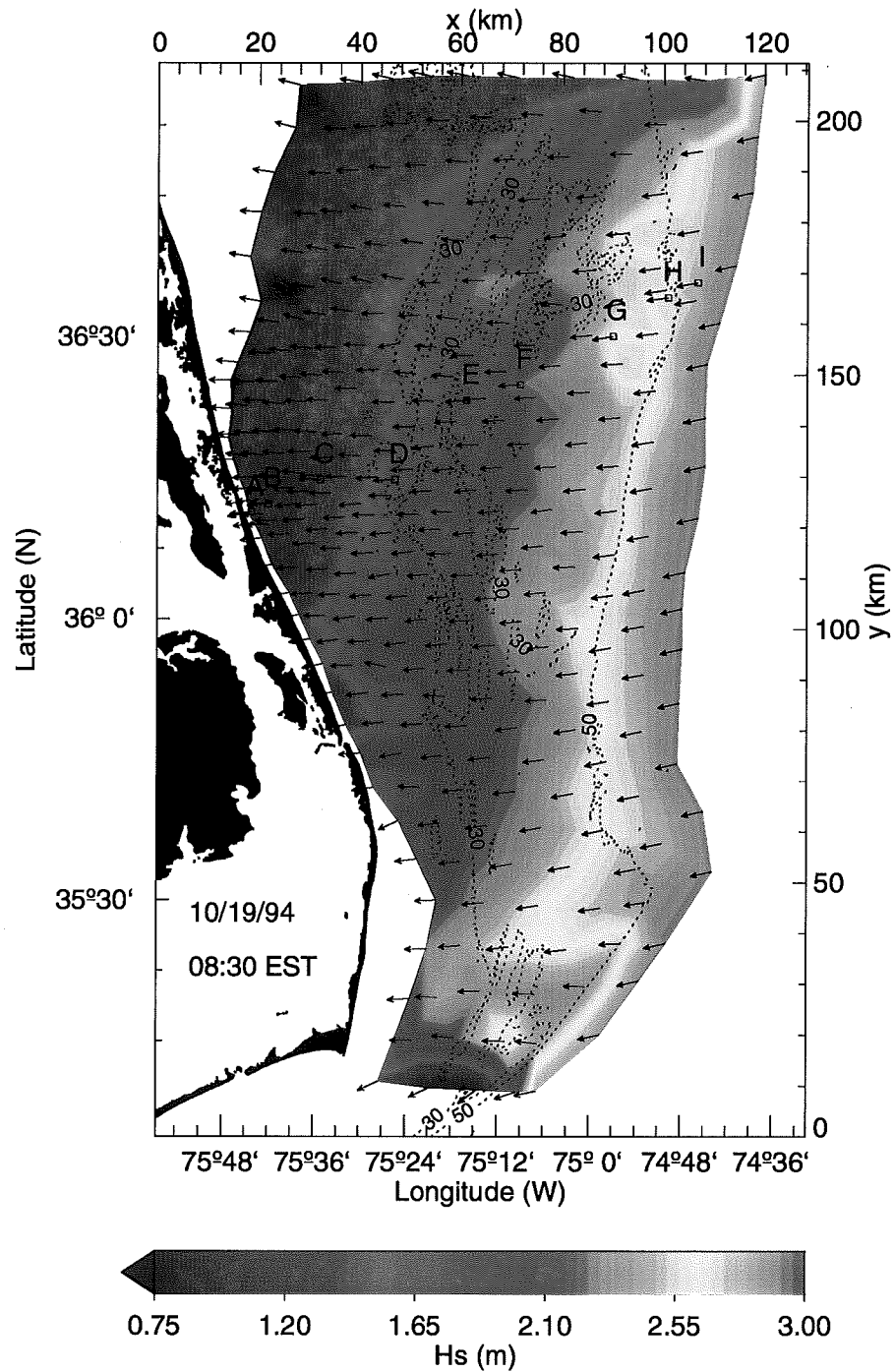


Figure 2.8: Hindcasts of H_s and $\bar{\theta}$, October 19, 1994
 Model predictions (with movable bed source term) of significant wave height (colors) and mean wave direction (arrows) at time II (figures 2.6, 2.7). Dotted lines indicate the 30 m and 50 m isobaths.

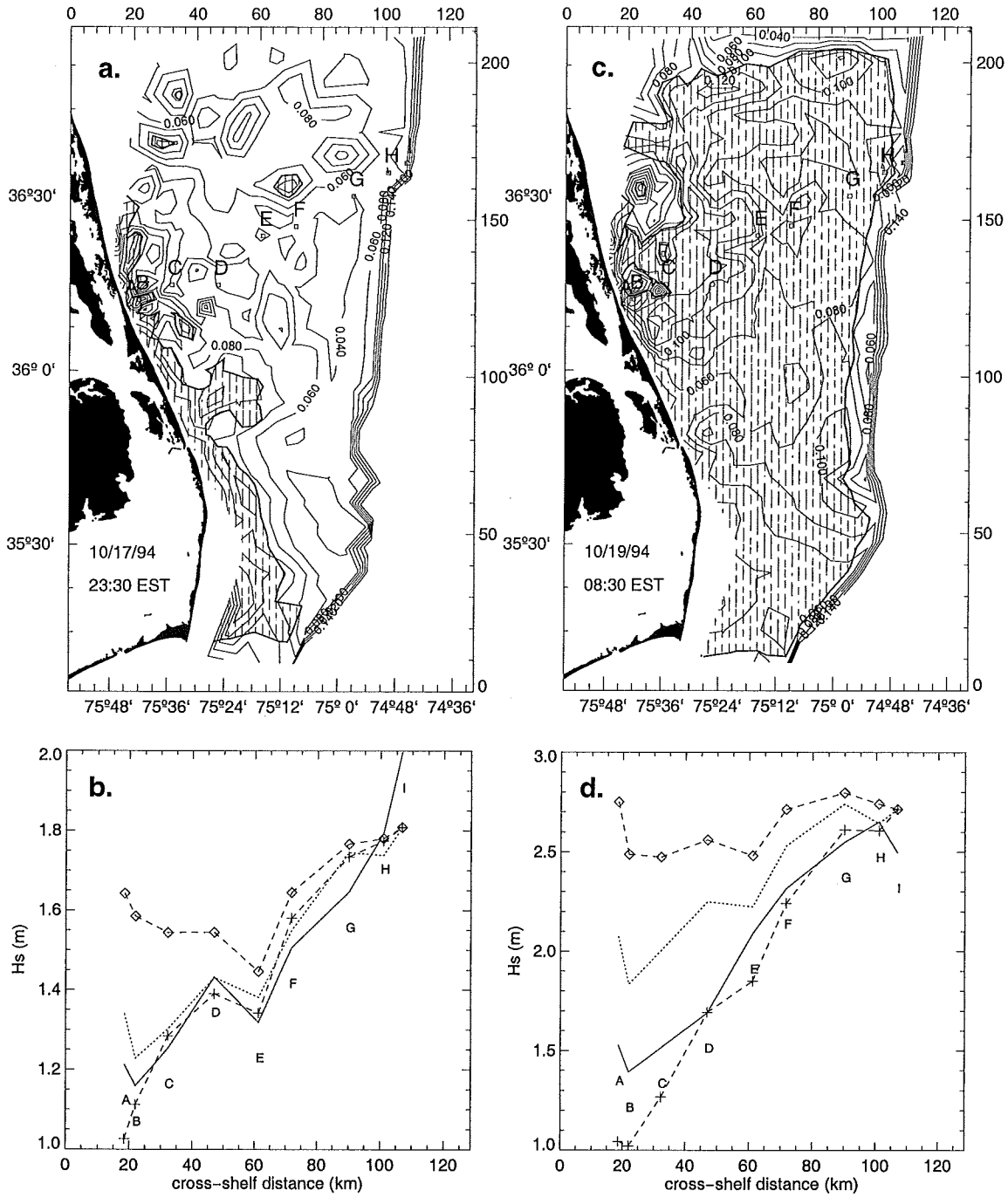


Figure 2.9: Ripples and dissipation factors, October 1994

(a) Ripple regime based on local mean water depth (hatched for active ripples, blank for relic roughness), and dissipation factor f_e (contour interval is 0.02) at time 'I' (figures 2.6, 2.7). (b) Observed (solid line) and predicted (\diamond : without bottom dissipation, $+$: with movable-bed source term, dotted: with JONSWAP source term) H_s at time I, as a function of cross-shelf distance. (c) Same as (a) for time II (figures 2.6, 2.7). (d) Same as (b) for time II.

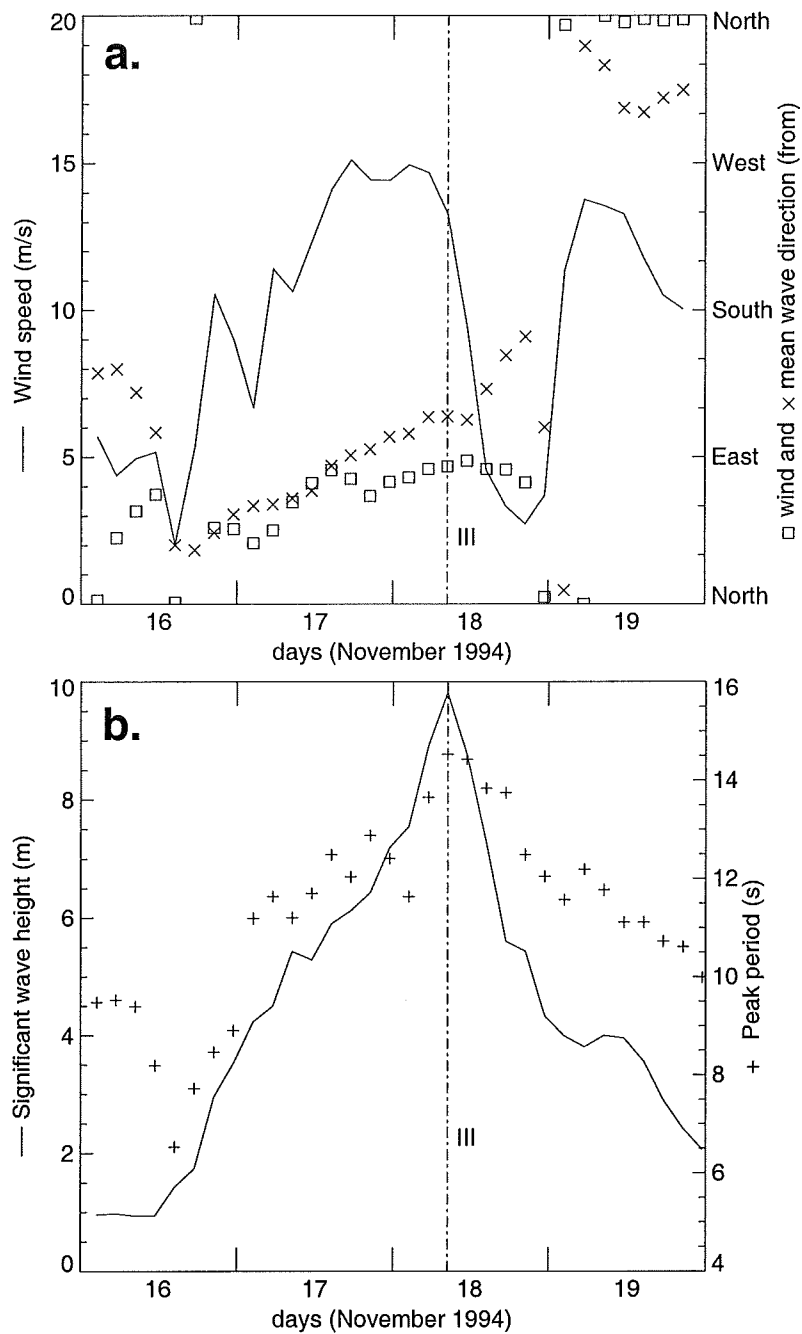


Figure 2.10: Wind and wave conditions, November 1994

Same format as figure 2.6). The vertical dash-dotted line labeled 'III' (18 November at 08:30 EST) indicates the time when H_s was maximum offshore.

2 and 10 W m^{-2} (both terms are maximum **near** the coast). Hence, although bottom dissipation appears to be the dominant source term, neglecting the wind input in this case may cause significant errors.

At time III the model predicts a gradual turning of the mean wave direction from 115° in deep water to 88° in 8 m depth (figure 2.11), in good agreement with the mean direction (88°) observed at the 8 m array (not shown). Model predictions without bottom dissipation yield a decrease in H_s from 8.5 m at site I near the shelf break to 7.4 m at site B on the inner shelf. This attenuation, associated with the time evolution of the storm and conservative shoaling and refraction processes, accounts for only part of the observed decrease of H_s to 5.8 m at site B. Including movable bed dissipation brings the model in better agreement with the observations (figure 2.12*b*). The predicted values of the dissipation factor f_e are about 10 times smaller than the values for the October event, owing to larger Shields numbers. On most of the shelf, f_e predictions vary between 0.01 and 0.02 (figure 2.12*a*), corresponding to sheet flow. Active ripples are predicted close to the shelf break in depths greater than 40 m. The representative bottom velocity u_b (a linear function of H_s for a given spectral shape) is 3 times larger than in the October event. In an absolute sense, the dissipation rate $|S|$ 1.5, proportional to $f_e u_b^3$, is a factor 3 larger than in the October event, but the relative decay rate $|\lambda|$ (1.6), proportional to $f_e u_b$, is a factor 3 smaller. As a result, the predicted relative decay of H_s across the shelf, due to bottom dissipation, is weaker for the Hurricane Gordon case than the October swell event (a 14% decrease compared to 36% in October, cf. figures 2.9*d* and 2.12*b*). The JONSWAP parameterization yields H_s predictions for Hurricane Gordon, that are close to both observed H_s and movable bed predictions (figure 2.12*b*).

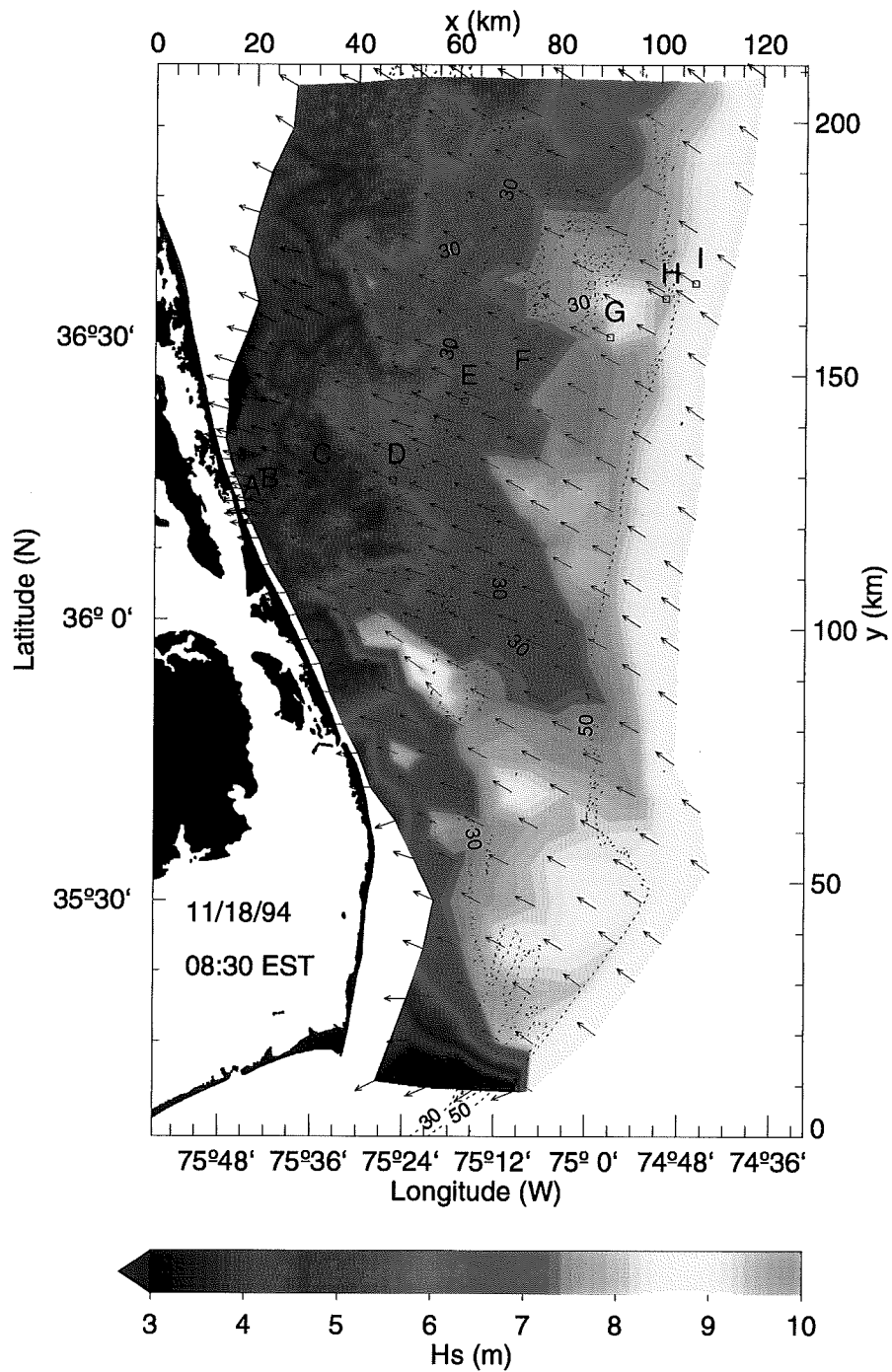


Figure 2.11: Hindcasts of H_s and $\bar{\theta}$, November 18, 1994

Model predictions (with moveable bed source term) of significant wave height (colors) and mean wave direction (arrows) at the peak of Hurricane Gordon (time 'III' in figure 2.10). Dotted lines indicate the 30 m and 50 m isobaths.

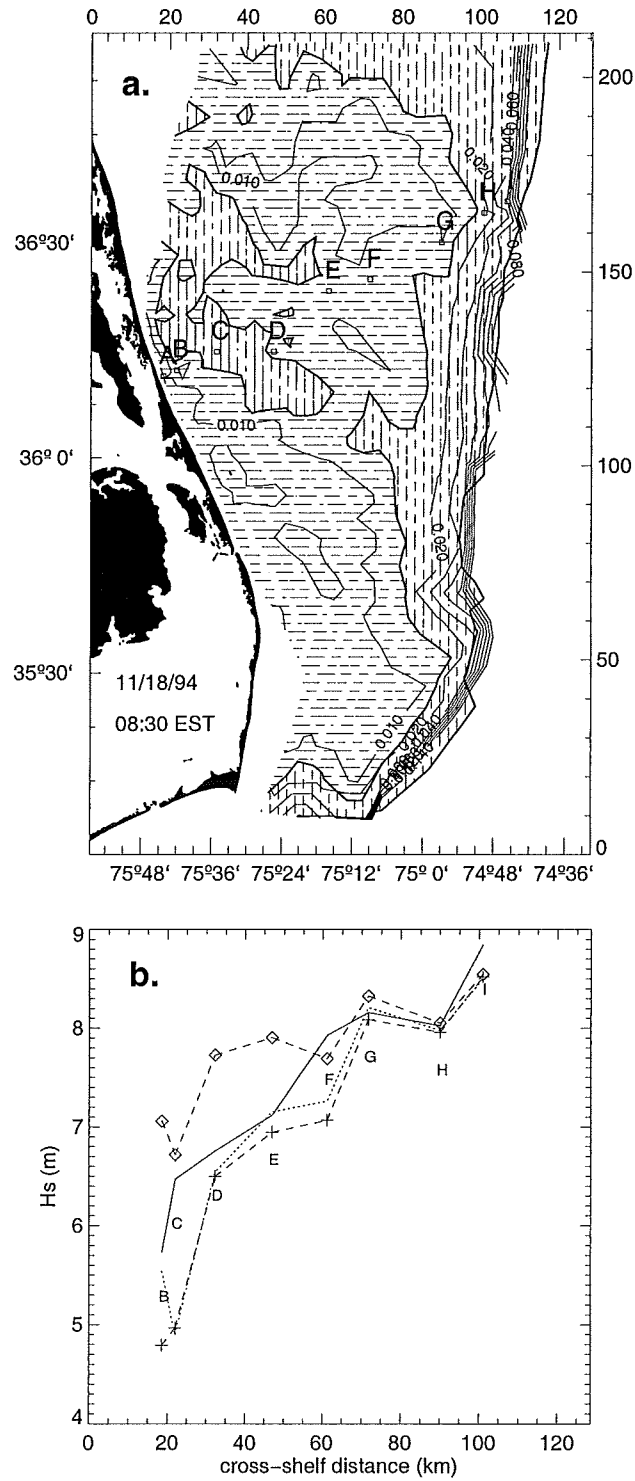


Figure 2.12: Ripples and dissipation factors, November 1994
 Time 'III' in figure 2.10. Same format as figure 2.9, with the addition of the $f_e = 0.01$ contour, and horizontal hatches for sheet flow conditions determined from the threshold criterion $\psi_{sf} = 0.172D^{-0.376}$ where D is in cm (Li and Amos, 1999).

F. Discussion

1. Movable bed model

The comparisons between observations and model predictions suggest that the observed decay of swell energy across the shelf is primarily the result of refraction and energy dissipation in the boundary layer over a movable sandy bed. Predicted wave frequency spectra (not shown) are also in good agreement with observed spectra, except at very low frequencies ($f < 0.06$ Hz) where energy levels are relatively low. The hindcast results suggest large spatial and temporal variations of the dissipation factor f_e as the seabed transitions through different roughness regimes (figure 1.6). Tests with different sand grain sizes in the range of probable values for the region (0.15 to 0.2 mm) indicated little sensitivity of the results. Although more accurate offshore wave data and detailed sediment distributions are needed for comprehensive tests of the bed roughness parameterization, the present results show a model tendency to overpredict swell damping, in particular in the active ripple regime (figures 2.7, 2.9*d*). The parameterization of the ripple roughness k_r was tuned to reproduce laboratory experiments with irregular but unidirectional waves (Madsen et al., 1990). Field conditions, with directionally spread waves, are likely to generate more irregular and less steep ripples, with smaller roughness k_r , than laboratory experiments (e.g. Nielsen, 1981). Therefore the estimates of k_r may be biased high. A reduction of k_r by 30% significantly improved the model accuracy (not shown).

The JONSWAP parameterization gives a relative decay in wave height H/H_{offshore} that is constant for a given dominant frequency. The observations presented here, all for swell with a peak period $T_p \simeq 15$ s, instead show a variable relative decay, in response to changes in the wave height (e.g. figure 2.7*b*). Equivalent values of Γ , the JONSWAP coefficient, were inferred from the movable-bed model hindcasts. At site F on the outer shelf, we find $0.025 \text{ m}^2\text{s}^{-3}$, $0.11 \text{ m}^2\text{s}^{-3}$, and $0.050 \text{ m}^2\text{s}^{-3}$ at times I, II and III respectively. For the same times at site B on the inner shelf, Γ values are $0.11 \text{ m}^2\text{s}^{-3}$, $0.095 \text{ m}^2\text{s}^{-3}$, and $0.057 \text{ m}^2\text{s}^{-3}$ respectively. These values generally fall between the JONSWAP average value $\Gamma = 0.038 \text{ m}^2\text{s}^{-3}$, and the one obtained from observations in the Great Australian Bight (Young & Gorman, 1995), $\Gamma = 0.152 \text{ m}^2\text{s}^{-3}$. Although the JONSWAP formulation with the widely used value $\Gamma = 0.038 \text{ m}^2\text{s}^{-3}$ gives reasonable wave height predictions in most conditions (figures 2.7, 2.9 and 2.12), it cannot reproduce the observed variations in swell decay, and significantly overestimates wave heights in active ripple conditions, as was also noticed by Weber (1991a). In contrast the constant roughness ($k_N = 4$ cm) proposed by Weber (1991) yields values of H_s that are still too high (by 30 cm) in the October 19 case, but too low (by 2.5 m) in the November 18 case (not shown). The movable bed model, adopted from Tolman (1994) without any adjustments, captures this variability, and fine tuning of all the empirical parameters, should further improve swell predictions. However, the movable bed parameterization requires site-specific sediment data that are not always available. Without such data, operational wave models may be better off with more robust dissipation models (e.g. Weber, 1991a; Tolman, 1994; Luo & Monbaliu, 1994; Young & Gorman, 1995).

2. Model efficiency

The new hybrid Eulerian-Lagrangian model CREST, presented here, was used to investigate the effects of a movable sandy sea bed on the transformation of swell across a continental shelf. Other physical processes such as wave generation, resonant non linear interactions between waves (see for example Herterich and Hasselmann, 1980) and resonant Bragg scattering of waves by bottom features (chapter III) can be incorporated as additional source terms in the energy balance equation. Hence the present model provides an alternative to the Eulerian finite difference scheme models commonly used for wave prediction. With $N_{\Delta t}$ a typical number of time steps for a ray bundle, and N_s a typical number of interpolation coefficients A_{il}^n and B_{il}^n for a given time step, the CREST wave

model requires memory space for storing the interpolation coefficients that is a factor $N_{\Delta t} \times N_s$ (of the order of 200 in the calculations presented here) larger than the space used for storing the spectrum. Thus CREST requires much more memory per grid point than an Eulerian model, that only needs to store the spectrum. The hybrid approach is attractive for applications where the spatial scales L_S of variations in the source terms are much larger than spatial scales L_R of refraction effects. An Eulerian model describing refraction with a finite difference scheme in space requires a grid resolving both L_R and L_S whereas the Eulerian grid in the present model needs to resolve only L_S because L_R is resolved by the precomputed rays. If L_S is much greater than L_R this property reduces drastically the number N_{gp} of grid points required for an accurate integration of the energy balance equation. Reducing N_{gp} has the added benefit that in coarser grids fewer grid points are used to interpolate of the source term for a given ray bundle, thus reducing the number N_s of interpolation coefficients per time step. The implementation of an Eulerian finite difference scheme with a resolution of about 500 m would have similar memory needs as the calculations presented here.

The considerable memory burden imposed by the storage of the ray information can be reduced by dividing the model domain into subdomains. The use of subdomains is clearly a compromise between a pure Lagrangian advection scheme and practical considerations. At the internal boundaries it re-introduces numerical diffusion in the advection and re-couples the rays to the grid for $\tau > 0$. Although not necessary in the application presented here it seems unavoidable for implementations of CREST on very large areas (e.g. $> 10^6$ km²). Further economy on the computer resources can also be achieved by specifying a maximum number of time steps along the rays after which the energy is interpolated from the neighboring grid point. This scheme also increases numerical diffusion. For one-timestep-long rays the numerical scheme becomes a finite bandwidth version of the piece-wise ray methods.

The representation by refraction alone of the effects of small scale bottom irregularities is cumbersome in the present model, and may not reflect the entire complexity of that process. A statistical representation of the interaction of waves with the smallest scale bathymetric features (e.g. the wave-bottom Bragg scattering source term described by Hasselmann (1966), and Long (1973) appears attractive because it would improve the physical description of wave-bottom interactions, and the rays computed on smoother bathymetry would be less scattered, thus requiring a smaller number N_s of interpolation coefficients. This improvement is described in chapter III.

The small number of grid points in CREST is also advantageous for complex source terms (e.g. quartet interactions between wave components) that are prohibitively expensive to evaluate accurately on a high-resolution grid. Furthermore the flexible model grid generated from any arbitrary set of points can be tailored to the bathymetry and shape of the model domain with higher resolution in the shallowest parts of the domain. In this respect CREST is similar to the TOMAWAC model (Benoit *et al.*, 1996).

For practical applications, computing ray trajectories is too expensive to allow a time-dependent ray geometry. This prevents the use of CREST in regions with strong temporal medium variations such as unsteady currents and tidal depth changes found in shallow estuaries and macrotidal seas, unless an approximate representation of these effects as source terms is found.

G. Summary

A non-stationary spectral wave model was developed using a hybrid Eulerian-Lagrangian scheme to examine the damping of swell propagating across a wide, shallow continental shelf. The model accurately represents refraction by advecting wave energy from deep water along a full spectrum of precomputed ray trajectories to a large number of grid points on the shelf. The source term in the energy balance is computed at each of these grid points, based on the complete frequency-directional spectrum. The source term is then interpolated from the Eulerian grid onto the rays, thus allowing for nonlinear coupling of wave components traveling along different rays. The energy bal-

ance is averaged over ensembles of rays to represent a finite spectral bandwidth. The (Lagrangian) computation of energy advection along rays and the (Eulerian) source term evaluation are carried out in parallel through the entire model domain. Source term formulations can be adapted from existing third-generation wave prediction models, whereas the finite difference propagation schemes of these models are replaced with a full Lagrangian ray method. This hybrid scheme avoids the numerical diffusion and 'garden sprinkler' problems of existing models that use finite difference schemes. The ray calculations and source term interpolation scheme add considerable computational effort, but both the ray trajectories and interpolation coefficients are precomputed for a given coastal region and model grid. The spectral energy balance is integrated in time with an efficiency comparable to existing finite-difference schemes.

The model was implemented with a source term restricted to energy dissipation in the bottom boundary layer over a movable sandy bed, as parameterized by Tolman (1994). The model was used to hindcast swell evolution across the North Carolina continental shelf for a range of wave conditions (significant wave heights between 0.5 and 10 m, and peak periods between 8 and 17 s) observed during two storms in 1994. Good agreement between observed and predicted variations of significant wave heights and mean wave directions across the shelf supports the hypothesis that refraction and movable bed bottom friction dominate the evolution of swell over a shallow sandy continental shelf.

III. WAVE-BOTTOM BRAGG SCATTERING

The energy balance (1.3) implicitly assumes that depth variations are small at scales comparable to the wavelength. Topographic features at those scales should therefore be excluded from refraction calculations but their effect on the waves can be represented in the energy balance in the form of Bragg scattering source terms. This stochastic representation of energy exchanges between wave components, was first developed by Hasselmann (1962) for wave-wave scattering, and later extended (Hasselmann, 1966) to wave scattering by external perturbations using a decomposition of the bottom elevation in Fourier modes. This theory is extended in the present chapter to heterogeneous wave and bottom properties, using decompositions in slowly modulated Fourier modes. Only the lowest order wave-bottom Bragg scattering process is considered. The present chapter reproduces with more details an article currently in press in the *Journal of Fluid Mechanics* (Ardhuin & Herbers, 2001).

A. Scattering theory for heterogeneous random waves

The present derivation of the energy balance equation for random waves propagating over an irregular sea floor uses a perturbation expansion of the wave energy, closely following Hasselmann's (1962) derivation of energy transfers in quartet wave-wave interactions, and a ray approximation of medium variations adapted from Mei (1989, ch. 3). The result is a local energy balance equation that incorporates refraction and shoaling by large scale depth variations, and a source term describing Bragg scattering by seabed topography with small horizontal scales (of the order of the surface wavelength).

1. General formulation

We consider weakly nonlinear random waves propagating over an irregular bottom with a slowly varying mean depth and random small scale topography. For the sake of simplicity we will neglect the effects of mean currents on wave propagation (see for example Bretherton & Garrett, 1969) and on wave scattering by bottom undulations (Kirby, 1988; Ting, Lin & Kuo, 2000). All variables are non-dimensionalized with a representative wavenumber k_0 , gravity acceleration g and water density ρ . The bottom elevation is represented by $z = -H(\mathbf{x}) + h(\mathbf{x})$, where h is a zero-mean small deviation from the gently sloping large scale bottom features represented by $-H(\mathbf{x})$, \mathbf{x} is the horizontal position vector, and z is the elevation relative to the mean water level. The vertical position of the ocean free surface is given by $\zeta(\mathbf{x}, t)$ with a zero mean value (figure 3.1). Assuming irrotational flow for an incompressible fluid, the horizontal velocity field \mathbf{u} is equal to $\nabla\phi$, the horizontal gradient of a velocity potential, and the vertical velocity w is equal to $\partial\phi/\partial z$. We further assume that ρ is constant. The governing equations for ϕ are

$$\nabla^2\phi + \frac{\partial^2\phi}{\partial z^2} = 0 \quad \text{for} \quad -H + h \leq z \leq \zeta, \quad (3.1)$$

$$\frac{\partial\phi}{\partial z} = \nabla\phi \cdot (\nabla h - \nabla H) \quad \text{at} \quad z = -H + h, \quad (3.2)$$

$$\frac{\partial^2\phi}{\partial t^2} + \frac{\partial\phi}{\partial z} = \nabla\phi \cdot \nabla\zeta - \nabla\phi \cdot \frac{\partial\nabla\phi}{\partial t} - \frac{\partial\phi}{\partial z} \frac{\partial^2\phi}{\partial t\partial z} \quad \text{at} \quad z = \zeta. \quad (3.3)$$

(3.1) is Laplace's equation, (3.2) is the 'free slip' bottom boundary condition, and the 'combined' surface boundary condition (3.3) is obtained by eliminating linear terms involving ζ from the dynamic

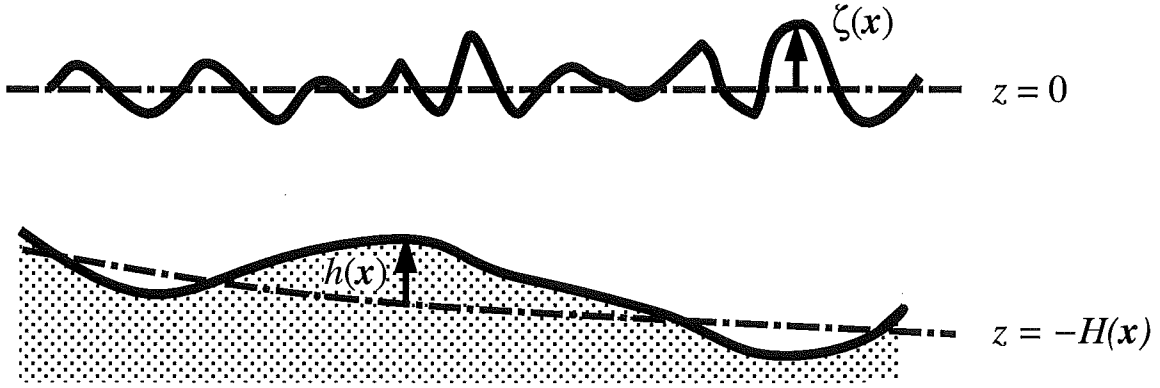


Figure 3.1: Random waves and irregular bottom: definition sketch.

(i.e. Bernoulli's equation) and kinematic conditions at the free surface (see for example Hasselmann, 1962). ζ is given by Bernoulli's equation,

$$\zeta + \frac{\partial \phi}{\partial t} = -\frac{1}{2} \left[|\nabla \phi|^2 + \left(\frac{\partial \phi}{\partial z} \right)^2 \right] \quad \text{at } z = \zeta. \quad (3.4)$$

Assuming that h varies on scales of the order of the surface wavelength, we introduce three small parameters: the wave slope $\varepsilon = k_0 a_0$, the small scale bottom slope $\eta = k_0 h_0$, and a measure β of the large scale bottom slope $|\nabla H|$. (3.1)–(3.3) are scaled as

$$\nabla^2 \phi + \frac{\partial^2 \phi}{\partial z^2} = 0 \quad \text{for } (-H + \eta h) \leq z \leq \varepsilon \zeta, \quad (3.5)$$

$$\frac{\partial \phi}{\partial z} = \nabla \phi \cdot (\eta \nabla h - \beta \nabla H) \quad \text{at } z = -H + \eta h, \quad (3.6)$$

$$\frac{\partial^2 \phi}{\partial t^2} + \frac{\partial \phi}{\partial z} = \varepsilon \nabla \phi \cdot \nabla \zeta - \varepsilon \nabla \phi \cdot \frac{\partial \nabla \phi}{\partial t} - \varepsilon \frac{\partial \phi}{\partial z} \frac{\partial^2 \phi}{\partial t \partial z} \quad \text{at } z = \varepsilon \zeta. \quad (3.7)$$

Following Keller (1958) we introduce slow space $\tilde{\mathbf{x}} = \alpha \mathbf{x}$ and time $\tilde{t} = \gamma t$ variables. h and ϕ are assumed to be semi-stationary random processes in horizontal space and time (for ϕ only), with evolution scales $(\alpha k_0)^{-1}$ and $\gamma^{-1} k_0^{-\frac{1}{2}}$ respectively (Priestley, 1965), that can be decomposed into Fourier modes with slowly varying amplitudes. Following Hasselmann (1962) we shall approximate h and ϕ with discrete sums, and take the limit to continuous integrals after deriving expressions for the evolution of the phase averaged wave energy. We write

$$h(\mathbf{x}) = \sum_{\mathbf{l}} B_{\mathbf{l}}(\tilde{\mathbf{x}}) e^{i\mathbf{l} \cdot \mathbf{x}}, \quad (3.8)$$

where \mathbf{l} are regularly spaced wavenumbers of bottom undulations and $B_{\mathbf{l}}$ are slowly varying amplitudes. Anticipating the effects of refraction, ϕ is decomposed as

$$\phi(\mathbf{x}, t) = \sum_{\mathbf{k}} \Phi_{\mathbf{k}}(\tilde{\mathbf{x}}, t, z) e^{iS_{\mathbf{k}}(\mathbf{x})}, \quad (3.9)$$

where \mathbf{k} are regularly spaced surface wavenumbers, and each \mathbf{k} -component has an amplitude $\Phi_{\mathbf{k}}$, an eikonal $S_{\mathbf{k}}$, and a local wavenumber

$$\mathbf{k}_r(\mathbf{k}, \beta \mathbf{x}) = \nabla S_{\mathbf{k}}(\mathbf{x}) \quad (3.10)$$

such that $\mathbf{k}_r = \mathbf{k}$ at the origin $\mathbf{x} = \mathbf{0}$. $\Phi_{\mathbf{k}}$ and \mathbf{k}_r are Lagrangian variables following a wave component along a ray trajectory. The spectral decomposition (3.9) for an evolutionary process is ‘unique’, in a sense defined by Priestley (1981, theorem 11.2.3), only for a finite region in space and time, and is used here only to evaluate local variations of $\Phi_{\mathbf{k}}$.

The slow spatial variations of $\Phi_{\mathbf{k}}$ can result from shoaling, refraction, and scattering processes, as well as non-stationary and non-uniform wave conditions. Since ϕ and h are real it follows that $\overline{\Phi_{\mathbf{k}}} = \Phi_{-\mathbf{k}}$ and $\overline{B_1} = B_{-1}$, where the overbar denotes the complex conjugate.

In the vicinity of $\mathbf{x} = \mathbf{0}$ the decomposition (3.9) reduces to a Fourier sum

$$\phi(\mathbf{x}, t) = \sum_{\mathbf{k}} \Phi_{\mathbf{k}}(\mathbf{0}, t, z) e^{i\mathbf{k}\cdot\mathbf{x}} + O(\alpha|\mathbf{x}|, \beta|\mathbf{x}|). \quad (3.11)$$

The simplified decomposition (3.11) will be used when no space differentiation is involved, taking advantage of the orthogonality of Fourier modes.

The goal of the present derivation is to determine from (3.1)–(3.4) the energy balance at $\tilde{\mathbf{x}} = \mathbf{0}$ for each \mathbf{k} -component of the wave spectrum (3.9). The solution depends on the relative magnitudes of the five small parameters: α , β , γ , η , and ε . Here we use

$$\alpha \approx \beta \approx \gamma \approx \eta^2 \approx \varepsilon^2 \ll 1. \quad (3.12)$$

The choice of a small scale bottom slope η much larger than the large scale slope β is usually well suited to sandy continental shelves, with the exception of the steeper beach and shelf break regions. This choice makes the present derivation a priori different from Mei’s (1985) theory in which $\beta \approx \eta$.

Following the method of Hasselmann (1962), the solution to (3.5)–(3.7) is obtained through a perturbation expansion in powers of ε ,

$$\phi = \phi_1 + \varepsilon\phi_2 + \varepsilon^2\phi_3 + \text{h. o. t.} \quad (3.13)$$

The boundary conditions (3.6) and (3.7) are expressed at $z = -H$ and $z = 0$, respectively, using Taylor series expansions of ϕ about $z = -H$ and $z = 0$, e.g. at the bottom,

$$\phi|_{z=-H+h} = \phi|_{z=-H} + \eta h \left. \frac{\partial \phi}{\partial z} \right|_{z=-H} + \eta^2 \frac{h^2}{2} \left. \frac{\partial^2 \phi}{\partial z^2} \right|_{z=-H} + \text{h. o. t.} \quad (3.14)$$

Each term in (3.13) will be found to be of the form

$$\phi_i = \sum_{\mathbf{k}, s} \frac{\cosh(k_r z + k_r H)}{\cosh(k_r H)} \Phi_{i, \mathbf{k}}^s(\tilde{\mathbf{x}}, t) e^{iS_{i, \mathbf{k}}(\mathbf{x})} + \text{bound wave terms}, \quad (3.15)$$

where k_r is the magnitude of the local wavenumber vector \mathbf{k}_r , s is a sign index (+ or –), $\Phi_{i, \mathbf{k}}^s$ is the amplitude of the free wave component (\mathbf{k}, s) that propagates in the direction of $s\mathbf{k}_r$, and $\overline{\Phi_{i, \mathbf{k}}^s} = \Phi_{i, -\mathbf{k}}^{-s}$.

The slowly evolving spectral statistics of free wave components can be expressed in terms of the covariances $F_{i, j, \mathbf{k}}^\Phi$ of the velocity potential amplitudes:

$$F_{i, j, \mathbf{k}}^\Phi = \left\langle \Phi_{i, \mathbf{k}}^+ \Phi_{j, -\mathbf{k}}^- + \Phi_{i, -\mathbf{k}}^- \Phi_{j, \mathbf{k}}^+ \right\rangle. \quad (3.16)$$

where the angular brackets denote an average over many realizations of the wave field, and in local space and time over a region that is large compared to the ‘fast’ scales k_0^{-1} of sea surface excursions but small compared to the slow scales $(\alpha k_0)^{-1}$ and $\gamma^{-1} (gk_0)^{-1/2}$ of spectral variations. The contribution of the complex conjugate pairs of components ($\mathbf{k}, +$) and ($-\mathbf{k}, -$) are combined in (3.16) so that $F_{i, j, \mathbf{k}}^\Phi$ is the covariance of waves propagating in the direction of \mathbf{k} . Note that the wavenumber separations $\Delta \mathbf{k}_r = (\Delta k_{r, x}, \Delta k_{r, y})$ in the sum (3.9) vary along rays owing to refraction.

In the limit of small wavenumber separation a continuous cross-spectrum can be defined at $\tilde{\mathbf{x}} = 0$ (e.g. Priestley, 1981 ch. 11)

$$F_{i,j}^{\Phi}(\mathbf{0}, \tilde{t}, \mathbf{k}) = \lim_{|\Delta \mathbf{k}| \rightarrow 0} \frac{F_{i,j,\mathbf{k}}^{\Phi}(\mathbf{0}, \tilde{t})}{\Delta k_x \Delta k_y}. \quad (3.17)$$

The definitions of all spectral densities are chosen so that the integral over the entire wavenumber plane yields the total covariance of ϕ_i and ϕ_j .

The slowly varying bottom elevation spectrum in discrete form is given by $F_1^B = \langle B_1 B_{-1} \rangle$ and in continuous form by

$$F^B(\tilde{\mathbf{x}}, \mathbf{l}) = \lim_{|\Delta \mathbf{l}| \rightarrow 0} \frac{F_1^B(\tilde{\mathbf{x}})}{\Delta l_x \Delta l_y}, \quad (3.18)$$

so that

$$\langle h^2(\tilde{\mathbf{x}}) \rangle = \int_{-\infty}^{+\infty} \int_{-\infty}^{+\infty} F^B(\tilde{\mathbf{x}}, \mathbf{l}) dl_x dl_y. \quad (3.19)$$

This definition differs by a factor 2 from the one chosen by Hasselmann (1966) and Long (1973).

The total wave energy at $\tilde{\mathbf{x}} = \mathbf{0}$, in non-dimensional form,

$$E(\mathbf{0}, \tilde{t}) = \left\langle \int_{-H+h}^{\zeta} \frac{1}{2} \left[|\nabla \phi|^2 + \left(\frac{\partial \phi}{\partial z} \right)^2 \right] dz \right\rangle + \frac{1}{2} \langle \zeta^2 \rangle, \quad (3.20)$$

can be written as

$$E(\mathbf{0}, \tilde{t}) = \int_{-\infty}^{\infty} \int_{-\infty}^{\infty} [\varepsilon^2 E_2(\mathbf{k}) + \varepsilon^3 E_3(\mathbf{k}) + \varepsilon^4 E_4(\mathbf{k})] dk_x dk_y + O(\varepsilon^5), \quad (3.21)$$

where

$$E_2(\mathbf{k}) = E_{1,1}(\mathbf{k}), \quad (3.22)$$

$$E_3(\mathbf{k}) = E_{2,1}(\mathbf{k}) + E_{1,2}(\mathbf{k}), \quad (3.23)$$

$$E_4(\mathbf{k}) = E_{2,2}(\mathbf{k}) + E_{3,1}(\mathbf{k}) + E_{1,3}(\mathbf{k}). \quad (3.24)$$

Here $E_{i,j}(\mathbf{k})$ is the $(i+j)^{\text{th}}$ order energy contribution from correlations between i^{th} and j^{th} order components with wavenumber \mathbf{k} . Since the average in (3.20) is over several wavelengths, correlations between wave components with different wavenumbers that result from reflections (i.e. standing wave patterns of nodes and antinodes) are averaged out and do not contribute to (3.21). For all (i,j) pairs $E_{i,j}(\mathbf{k}) = E_{j,i}(\mathbf{k})$. Hasselmann (1962) discarded odd-power energy terms E_3 and E_5 under the assumption that the sea surface is Gaussian. It was later found that this assumption is unnecessary (Benney & Saffman, 1966; Newell & Aucoin, 1971) as dispersion decorrelates the wave components during their propagation. Here additional terms involving correlations between two wave and one bottom component contribute to E_3 , but these terms are shown to be bounded in appendix A. The dynamically important growing terms will be found in the 4th order energy E_4 (3.24).

For freely propagating waves the potential and kinetic energy contributions to (3.20) are equal and $E_{i,j}$ is approximately given by the linear relation

$$E_{i,j}(\mathbf{0}, \tilde{t}, \mathbf{k}) = k F_{i,j}^{\Phi}(\mathbf{0}, \tilde{t}, \mathbf{k}) \tanh(kH). \quad (3.25)$$

Neglected in (3.25) are the contributions to the kinetic energy integral (3.20) from the z -intervals $[-H+h, -H]$ and $[0, \zeta]$. Although these contributions are $O(\varepsilon^4)$ and thus should be included in E_4 , their magnitude is bounded and thus their time derivative is $O(\varepsilon^6)$. All $O(\varepsilon^4)$ bounded terms resulting from the surface and bottom boundary conditions can be discarded in the following analysis of energy transfers within the wave spectrum (see Hasselmann, 1962, for a detailed discussion).

2. First order solution

Substitution of the first order wave field ϕ_1

$$\phi_1 = \sum_{\mathbf{k}, s} \frac{\cosh(k_r z + k_r H)}{\cosh(k_r H)} \Phi_{1,\mathbf{k}}^s(\tilde{\mathbf{x}}, t) e^{iS_{1,\mathbf{k}}(\mathbf{x})} \quad (3.26)$$

in the surface boundary condition (3.7) yields

$$\Phi_{1,\mathbf{k}}^s(\tilde{\mathbf{x}}, t) = \hat{\Phi}_{1,\mathbf{k}}^s(\tilde{\mathbf{x}}, \tilde{t}) e^{-is\omega t}, \quad (3.27)$$

where the radian frequency $\omega(k)$ is constant along rays, and is given by the linear dispersion relation (in non-dimensional form):

$$\omega(k) = [k_r \tanh(k_r H)]^{\frac{1}{2}}. \quad (3.28)$$

The slow space and time modulations of $\hat{\Phi}_{1,\mathbf{k}}^s$ and the associated variations of the energy spectrum $E_2(\mathbf{k}_r)$ are not constrained by the first order equations, but can be determined from the fourth order energy $E_4(\mathbf{k}_r)$ (3.24), that depends on both second and third order waves.

3. Second order solution

Substituting (3.13) in (3.5)-(3.7) and collecting terms of order ε and η yields the governing equations for the second order velocity potential ϕ_2

$$\nabla^2 \phi_2 + \frac{\partial^2 \phi_2}{\partial z^2} = 0 \quad \text{for} \quad -H \leq z \leq 0, \quad (3.29)$$

$$\frac{\partial \phi_2}{\partial z} = -h \frac{\partial^2 \phi_1}{\partial z^2} + \nabla \phi_1 \cdot \nabla h \quad \text{at} \quad z = -H, \quad (3.30)$$

$$\frac{\partial^2 \phi_2}{\partial t^2} + \frac{\partial \phi_2}{\partial z} = NL_2 \quad \text{at} \quad z = 0. \quad (3.31)$$

where NL_2 contains the non-linear terms in the surface boundary condition that force a bound wave solution ϕ_2^{nl} (Hasselmann, 1962, (47)). Note that refraction and shoaling terms associated with the large scale bottom slope ∇H are of higher order and do not contribute to the second order equations. Therefore ray curvature effects on ϕ_1 can be neglected, and we can use $\mathbf{k}_r \approx \mathbf{k}$ and $S_{\mathbf{k}}(\mathbf{x}) \approx \mathbf{k} \cdot \mathbf{x}$ in the vicinity of $\mathbf{x} = 0$. A general solution to Laplace's equation (3.29) is formed with a Fourier sum of free and bound wave components with amplitudes $\Phi_{2,\mathbf{k}}^s$ and $\Phi_{2,\mathbf{k}}^{\text{si},s}$:

$$\phi_2 = \sum_{\mathbf{k}, s} \left[\frac{\cosh(kz + kH)}{\cosh(kH)} \Phi_{2,\mathbf{k}}^s(t) + \frac{\sinh(kz + kH)}{\cosh(kH)} \Phi_{2,\mathbf{k}}^{\text{si},s}(t) \right] e^{i\mathbf{k} \cdot \mathbf{x}} + \phi_2^{\text{nl}}, \quad (3.32)$$

$\Phi_{2,\mathbf{k}}^{\text{si},s}$ follows from substituting the first order wave field (3.26), (3.27) in the right hand side of the bottom boundary condition (3.30).

$$\Phi_{2,\mathbf{k}}^{\text{si},s}(t) = - \sum_{\mathbf{k}', s} \frac{\mathbf{k} \cdot \mathbf{k}'}{k} B_{\mathbf{k}-\mathbf{k}'} \hat{\Phi}_{1,\mathbf{k}'}^s e^{-is\omega' t}, \quad (3.33)$$

where (ω', \mathbf{k}') obey the dispersion relation (3.28). The bound wave $\Phi_{2,\mathbf{k}}^{\text{si},s}$ effectively couples the bottom and surface waves. Substitution of (3.32) and (3.33) in (3.31) yields a forced harmonic oscillator equation for the free wave amplitude $\Phi_{2,\mathbf{k}}^s$,

$$\left(\frac{d}{dt^2} + \omega^2 \right) \Phi_{2,\mathbf{k}}^s(t) = \sum_{\mathbf{k}'} [k - \omega'^2 \tanh(kH)] \frac{\mathbf{k} \cdot \mathbf{k}'}{k} B_{\mathbf{k}-\mathbf{k}'} \hat{\Phi}_{1,\mathbf{k}'}^s(t). \quad (3.34)$$

Following the method of Hasselmann (1962), the time derivative of the energy density $E_{2,2}(\mathbf{k})$ of the second order waves in the limit of large t at $\tilde{\mathbf{x}} = \mathbf{0}$, can be written in the form (appendix A)

$$\frac{\partial E_{2,2}(\mathbf{k})}{\partial t} = K(k, H) \int_0^{2\pi} \cos^2(\theta - \theta') F^B(\mathbf{k} - \mathbf{k}') E_2(\mathbf{k}') d\theta', \quad (3.35)$$

where $\mathbf{k} = (k \cos \theta, k \sin \theta)$, $\mathbf{k}' = (k \cos \theta', k \sin \theta')$, and

$$K(k, H) = \frac{4\pi\omega k^4}{\sinh(2kH) [2kH + \sinh(2kH)]}. \quad (3.36)$$

4. Third order solution

Slow modulations of ϕ_1 yield third order terms in Laplace's equation. Substituting (3.13), (3.26), and (3.27) in (3.5)–(3.7), collecting terms of order ε^2 , $\varepsilon\eta$, η^2 , α , β , and γ , and using the approximations (in the vicinity of $\mathbf{x} = \mathbf{0}$) $\mathbf{k}_r = \mathbf{k} + O(\beta\mathbf{x})$, and $S_{\mathbf{k}}(\mathbf{x}) = \mathbf{k} \cdot \mathbf{x} + O(\alpha\mathbf{x}, \beta\mathbf{x})$, yields the following equations for the third order velocity potential ϕ_3

$$\begin{aligned} \nabla^2 \phi_3 + \frac{\partial^2 \phi_3}{\partial z^2} &= \overbrace{-i \sum_{\mathbf{k}, s} \mathbf{k} \cdot \nabla \left(\widehat{\Phi}_{1, \mathbf{k}}^s \frac{\cosh(k_r z + k_r H)}{\cosh(k_r H)} \right)}^{\text{I}} e^{i(\mathbf{k} \cdot \mathbf{x} - s\omega t)} \\ &\quad - \overbrace{i \sum_{\mathbf{k}, s} \nabla \cdot \left(\mathbf{k}_r \widehat{\Phi}_{1, \mathbf{k}}^s \frac{\cosh(k_r z + k_r H)}{\cosh(k_r H)} \right)}^{\text{II}} e^{i(\mathbf{k} \cdot \mathbf{x} - s\omega t)} \\ &\quad \text{for } -H \leq z \leq 0, \end{aligned} \quad (3.37)$$

$$\frac{\partial \phi_3}{\partial z} = - \overbrace{h \frac{\partial^2 \phi_2}{\partial z^2}}^{\text{III}} + \overbrace{\nabla \phi_2 \cdot \nabla h}_{\text{IV}} - i \overbrace{\sum_{\mathbf{k}, s} \mathbf{k} \cdot \nabla H \widehat{\Phi}_{1, \mathbf{k}}^s e^{i(\mathbf{k} \cdot \mathbf{x} - s\omega t)}}^{\text{V}} \quad \text{at } z = -H, \quad (3.38)$$

$$\frac{\partial^2 \phi_3}{\partial t^2} + \frac{\partial \phi_3}{\partial z} = i \overbrace{\sum_{\mathbf{k}, s} 2s\omega \frac{\partial \widehat{\Phi}_{1, \mathbf{k}}^s}{\partial t} e^{i(\mathbf{k} \cdot \mathbf{x} - s\omega t)}}^{\text{VI}} + NL_3 \quad \text{at } z = 0, \quad (3.39)$$

Note that third order terms involving ϕ_1 in the bottom boundary condition (3.38) vanish because $\partial^3 \phi_1 / \partial z^3 = 0$ and $\partial \phi_1 / \partial z = 0$ at $z = -H$. The right hand side forcing terms of (3.37–3.39) include Bragg scattering terms (III and IV), effects of spatial heterogeneities (I, II, and V), non-stationarity (VI), and third order nonlinear surface terms that are gathered here in the term NL_3 . This set of equations is linear in ϕ_3 . Therefore ϕ_3 is the sum of a homogeneous solution (absorbed in ϕ_1) and four particular solutions,

$$\phi_3 = \phi_3^{\text{sc}} + \phi_3^{\text{he}} + \phi_3^{\text{ns}} + \phi_3^{\text{nl}}, \quad (3.40)$$

where sc, he, ns and nl, stand for scattering, heterogeneity, non-stationarity, and non-linearity, respectively. Each solution satisfies (3.37)–(3.39) forced respectively by the scattering terms (III and IV) only, the heterogeneity terms (I, II and V) only, the non-stationarity term (VI) only, and the surface non-linearity terms (NL_3) only. Although ϕ_3^{nl} is resonantly forced, it contributes only bounded terms to E_4 (Hasselmann, 1962). Similarly, nonlinear contributions to the scattering terms III and IV (the $O(\varepsilon^2\eta)$ products involving ϕ_2^{nl} and bottom undulations) yield only bounded

contributions in E_4 . The remaining solutions ϕ_3^{sc} , ϕ_3^{he} , and ϕ_3^{ns} contribute growing terms, $E_{3,1}^{\text{sc}}$, $E_{3,1}^{\text{he}}$, and $E_{3,1}^{\text{ns}}$, to E_4 . Following the method used to obtain $\partial E_4^{2,2}/\partial t$, at $\tilde{\mathbf{x}} = \mathbf{0}$ we have (appendix A)

$$\frac{\partial [E_{3,1}^{\text{sc}}(\mathbf{k}) + E_{1,3}^{\text{sc}}(\mathbf{k})]}{\partial t} = -K(k, H) \int_0^{2\pi} \cos^2(\theta - \theta') F^B(\mathbf{k} - \mathbf{k}') E_2(\mathbf{k}) d\theta', \quad (3.41)$$

$$\frac{\partial [E_{3,1}^{\text{ns}}(\mathbf{k}) + E_{1,3}^{\text{ns}}(\mathbf{k})]}{\partial t} = -\frac{\partial E_2(\mathbf{k})}{\partial t}, \quad (3.42)$$

$$\frac{\partial [E_{3,1}^{\text{he}}(\mathbf{k}) + E_{1,3}^{\text{he}}(\mathbf{k})]}{\partial t} = -\mathbf{C}_g(\mathbf{k}) \cdot \nabla E_2(\mathbf{k}_r), \quad (3.43)$$

where $\mathbf{C}_g(\mathbf{k})$ is the group velocity of linear waves (A.27), and $E_2(\mathbf{k}_r)$ is a Lagrangian variable that describes energy evolution along the ray trajectory $[\mathbf{x}(\mathbf{k}, \beta r), \mathbf{k}_r(\mathbf{k}, \beta r)]$ of wave component \mathbf{k} , where r is the along-ray coordinate. $E_2(\mathbf{k}_r)$ is defined by

$$F_{1,1}^\Phi(\tilde{\mathbf{x}}, \tilde{t}, \mathbf{k}_r) = \lim_{|\Delta \mathbf{k}_r| \rightarrow 0} \frac{F_{1,1,\mathbf{k}}^\Phi(\tilde{\mathbf{x}}, \tilde{t})}{\Delta k_{r,x} \Delta k_{r,y}}, \quad (3.44)$$

$$E_2(\tilde{\mathbf{x}}, \tilde{t}, \mathbf{k}_r) = k_r F_{1,1}^\Phi(\tilde{\mathbf{x}}, \tilde{t}, \mathbf{k}_r) \tanh(k_r H). \quad (3.45)$$

Note that the advection term $\mathbf{C}_g(\mathbf{k}) \cdot \nabla E_2(\mathbf{k}_r)$ describes the divergence of the energy flux in Lagrangian coordinates, and thus incorporates refraction and shoaling effects. All other terms in (3.42)–(3.43) depend only on the energy at $\tilde{\mathbf{x}} = \mathbf{0}$ where the Lagrangian wavenumber \mathbf{k}_r is equal to the Eulerian wavenumber \mathbf{k} , and $E_2(\mathbf{k}_r) = E_2(\mathbf{k})$.

5. Energy balance

Combining (3.35), and (3.41)–(3.43), the rate of change of the fourth order spectrum (3.24) at $\tilde{\mathbf{x}} = \mathbf{0}$ is given by

$$\begin{aligned} \frac{\partial E_4(\mathbf{k})}{\partial t} &= -\frac{\partial E_2(\mathbf{k})}{\partial t} - \mathbf{C}_g(\mathbf{k}) \cdot \nabla E_2(\mathbf{k}_r) \\ &\quad + K(k, H) \int_0^{2\pi} \cos^2(\theta - \theta') F^B(\mathbf{k} - \mathbf{k}') [E_2(\mathbf{k}') - E_2(\mathbf{k})] d\theta', \end{aligned} \quad (3.46)$$

where $K(k, H)$ is given by (3.36).

To assure that E_4 is bounded for large t , that is $\partial E_4/\partial t = O(\varepsilon^5)$, the right-hand side terms of (3.46) must balance. Recognizing the first two of these terms as the total derivative of $E_2(\mathbf{k}_r)$ along a ray trajectory, and replacing E_2 by E , we obtain (using dimensional and unscaled variables from now on) the Lagrangian energy balance equation at $\tilde{\mathbf{x}} = \mathbf{0}$, accurate to order ε^4 :

$$\frac{dE(\mathbf{k}_r)}{dt} = S_{\text{Bragg}}(\mathbf{k}) + O(\varepsilon^5), \quad (3.47)$$

$$S_{\text{Bragg}}(\mathbf{k}) = 4\pi g^{\frac{1}{2}} H^{-\frac{9}{2}} \chi(kH) \int_0^{2\pi} \cos^2(\theta - \theta') F^B(\mathbf{k} - \mathbf{k}') [E(\mathbf{k}') - E(\mathbf{k})] d\theta', \quad (3.48)$$

with

$$\chi(kH) = \frac{(kH)^{\frac{9}{2}} [\tanh(kH)]^{\frac{1}{2}}}{\sinh(2kH) [2kH + \sinh(2kH)]}. \quad (3.49)$$

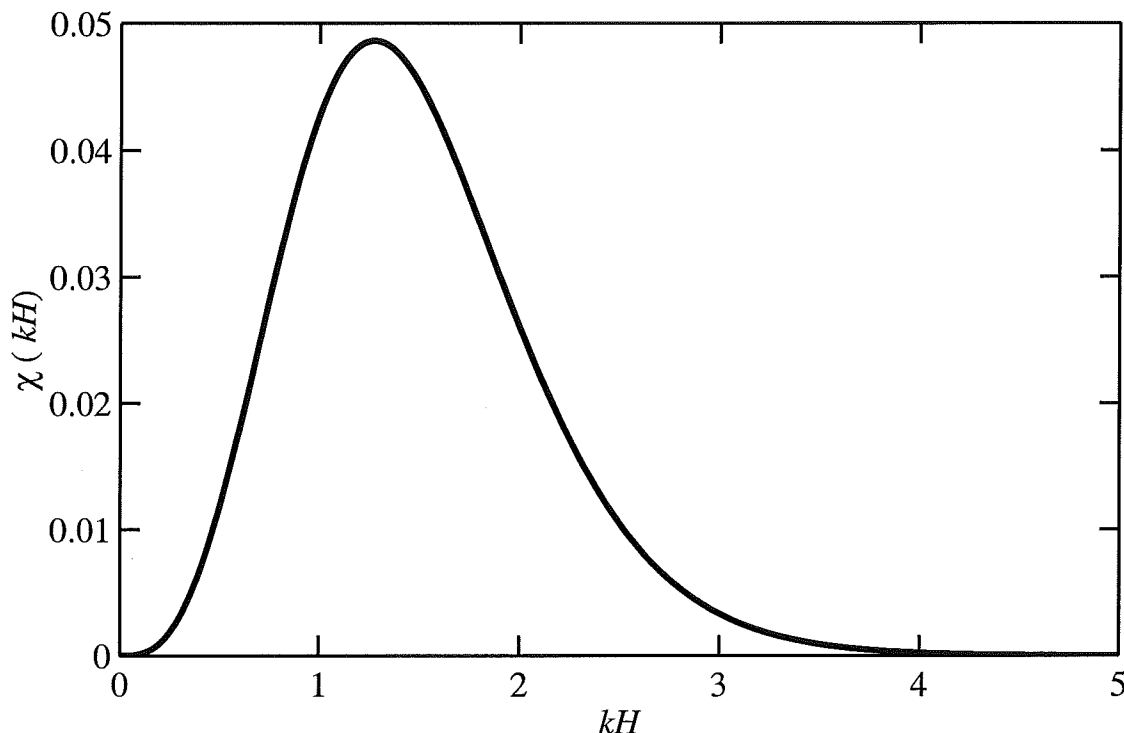


Figure 3.2: Values of $\chi(kH)$, as defined by (3.49).

(3.47) describes the net energy transfer at $\tilde{\mathbf{x}} = \mathbf{0}$ to a wave component with wavenumber \mathbf{k} (propagating in direction θ), resulting from triad interactions involving a wave of the same radian frequency ω and a different wavenumber \mathbf{k}' (direction θ'), and a bottom component with the difference wavenumber $\mathbf{l} = \mathbf{k} - \mathbf{k}'$ (figure 1.3). The energy transfer between components \mathbf{k} and \mathbf{k}' is proportional to the energy difference of the wave components and the bottom spectrum density at $\mathbf{l} = \mathbf{k} - \mathbf{k}'$. The factor $\cos^2(\theta - \theta')$ in (3.48) indicates that there is no energy transfer between waves propagating in perpendicular directions. The factor $\chi(kH)$ has a single maximum, approximately equal to 0.049 for the intermediate water depth $kH \approx 1.27$ (figure 3.2). In addition to directional and wavenumber dependencies, the scattering strength is proportional to $H^{-\frac{9}{2}}$, increasing strongly with decreasing water depth. Taking into account their different normalization of the bottom elevation spectrum, the present expression (3.48) of S_{Bragg} is 4 and 8 times smaller than the expressions given by Long (1973) and Hasselmann (1966), respectively.

6. Conditions of validity

The present theory is both a spectral generalization and higher-order energy conserving form of the solution given by Davies (1979) for sinusoidal bed undulations. Davies describes the generation of second order waves ϕ_2 , but uses constant amplitudes for ϕ_1 , and thus does not account for the associated energy losses of the primary waves. In the present theory the extension of the perturbation expansion to third order provides the balancing terms $E_{1,3}$ and $E_{3,1}$ (3.41), necessary for the conservation of the total energy in (3.47). Whereas Davies' theory assumes small reflected wave amplitudes, (3.47) can describe finite cumulative reflections over large distances and even complete localization of waves over rough bottom topography. However the present theory assumes

that significant wave amplitude variations occur over scales of $O(\alpha)$ wavelengths with $\alpha \approx \varepsilon^2$, and thus cannot accurately describe strong localized scattering that modify the wave amplitudes over scales of only a few wavelengths (see Mei, 1985, for a discussion of those effects over sinusoidal bottom topography, including in particular the importance of near-resonant interactions in that case).

It should be noted that the wavenumber spectrum $E(k) = \int_0^{2\pi} kE(\mathbf{k}) d\theta$ was assumed continuous in order to derive (3.47) in the limit of large times, removing the singularities for perfect resonance in (A.6), and reducing the bandwidth of important near-resonant interactions to a region of the spectrum where $E(\mathbf{k})$ can be considered constant. Thus (3.47) is not valid for monochromatic waves. Whereas the initial growth of the scattered energy is proportional to t^2 for resonant monochromatic waves, it is only proportional to t for waves with a continuous spectrum, because resonance becomes more selective with time, affecting a wavenumber bandwidth that narrows proportionally to t^{-1} .

Another consequence of the asymptotic large time limit taken in appendices A–D, is that the stochastic model (3.47) may not describe accurately wave evolution over natural sea beds which are often not homogeneous over scales of many wavelengths. The robustness of (3.47) for short propagation distances is examined in §3 through comparisons with deterministic models for wave evolution over a finite patch of sinusoidal bars. (3.47) includes wave-bottom interactions with $|\mathbf{k} - \mathbf{k}'| \ll k$, violating our scaling assumption $l \approx k$. This particular aspect is discussed in §3.4.

7. Extensions of the present theory

The present energy balance (3.47) may be extended to higher orders of η and/or ε by closing the energy Taylor expansion at E_6 , giving an evolution equation for $E_2 + E_4$. In the case of steeper waves, say $\alpha \approx \beta \approx \gamma \approx \eta^2 \approx \varepsilon^4$, it can be seen that all the energy transfer terms derived here (3.35, 3.41–3.43) are moved from E_4 to E_6 , joining the additional source term S_{n1} that represents resonant quartet wave-wave interaction (Hasselmann, 1962; Herterich and Hasselmann, 1980). Extensions to steeper waves and steeper topography, for example $\alpha \approx \beta \approx \gamma \approx \eta^4 \approx \varepsilon^4$, should yield at least two additional source terms, corresponding to higher order Bragg scattering (class II and III, see for example Liu & Yue, 1998).

Furthermore it can be expected that including higher order heterogeneity effects and non-linearity should introduce nonlinear effects on the left hand side of (3.47), as described by Willebrand (1975). For example in the present theory E_6 contains correlations between the tertiary waves ϕ_3^{n1} and the heterogeneity and non-stationarity terms ϕ_3^{he} and ϕ_3^{ns} . Thus it may be possible to derive a more complete energy balance equation with not only the source terms for the individual physical processes that contribute to the evolution of the wave spectrum, but also the cross-interactions of these processes that are usually neglected in wave prediction models (Komen *et al.*, 1994).

B. Random waves over sinusoidal bars

Following Davies (1979) we consider a simple seabed consisting of sinusoidal bars on an otherwise flat bottom for which analytical results exist that have been verified in laboratory experiments. Waves arriving from $x = -\infty$ at an incidence angle θ_I are partially reflected, in a direction $\theta_R = \pi - \theta_I$ by a patch of m sinusoidal bars of amplitude b , aligned with the y axis. The barred profile $h = b \sin(lx)$ covers the region $-L < x < L$ where $L = m\pi/l$ and l is the bar wavenumber (figure 3.3). The incident wave field is assumed to be a continuous spectrum $E_I(k)$ of unidirectional ($\theta = \theta_I$) waves. The total reflected energy E_R in the far field ($x \ll -L$) predicted by the stochastic and deterministic theories are compared for both normal and oblique incidence cases, in the limit of large m and for finite m .

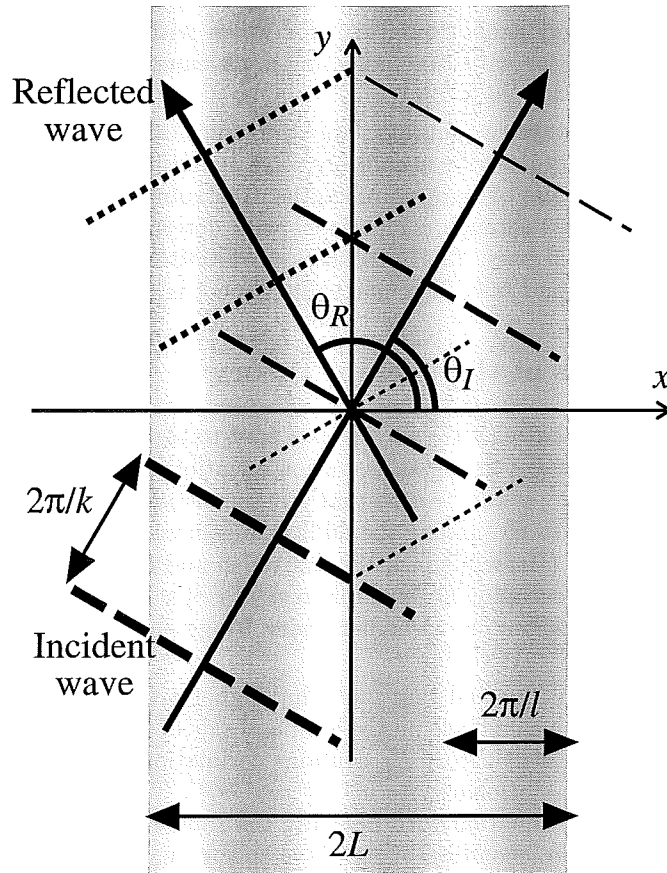


Figure 3.3: Wave scattering by sinusoidal bars
 Schematic of incident waves (dashed crests) and reflected waves (dotted crests) on a patch of sinusoidal bars (gray shades).

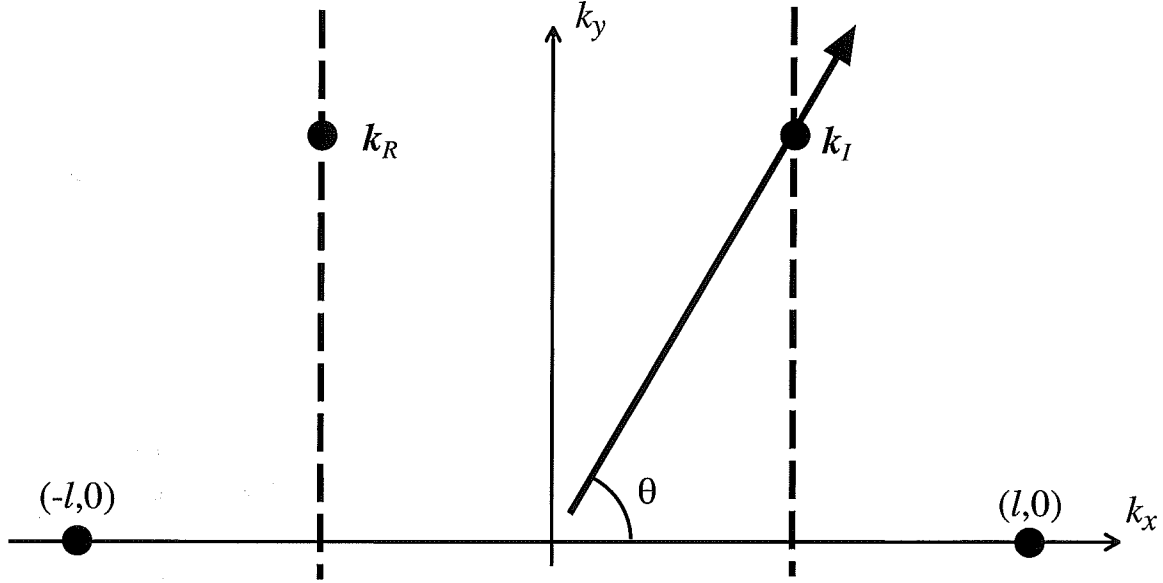


Figure 3.4: Resonant wavenumbers for sinusoidal bars.

Resonant triads for waves over sinusoidal bars represented on the wavenumber plane. The bar wavenumbers are fixed at $(l, 0)$ and $(-l, 0)$ and all possible pairs of resonant surface wavenumbers \mathbf{k}_I and \mathbf{k}_R lie on the vertical dashed lines. For the wave direction θ shown here, the directional spectral density $E(\theta)$ (the integral of $kE(\mathbf{k})$ along the thick arrow) is affected by energy transfers in the resonant $(\mathbf{k}_I, \mathbf{k}_R, \mathbf{l})$ triad.

1. Stochastic source term approach

In a steady state uniform along the y -axis, the energy balance (3.47) for the bottom profile described above simplifies to

$$C_g \cos \theta \frac{dE(\mathbf{k})}{dx} = S_{\text{Bragg}}(\mathbf{k}). \quad (3.50)$$

In order to evaluate S_{Bragg} (3.48) we approximate the finite patch of sinusoidal bars as a subsection of a sinusoidal bottom extending to infinity, for which the bottom variance spectrum F^B is a double Dirac distribution

$$F^B(\mathbf{l}) = \frac{b^2}{4} [\delta(l, 0) + \delta(-l, 0)]. \quad (3.51)$$

Outside the barred section ($|x| > L$) F^B is set equal to zero. The singularity in (3.51) is removed in S_{Bragg} by integrating (3.50) over k for a fixed direction θ (Figure 3.4). Changing variables from (k, θ') to the corresponding resonant bottom wavenumber $(l_x, l_y) = k(\cos \theta - \cos \theta', \sin \theta - \sin \theta')$ we obtain

$$\frac{dE(\theta)}{dx} = \frac{8\pi}{\cos \theta} \int \int_{\mathbf{k} \cdot \mathbf{l} > 0} \frac{\cos^2(\theta - \theta') F_b(\mathbf{l}) [E(\mathbf{k} - \mathbf{l}) - E(\mathbf{k})] k^5}{[1 - \cos(\theta - \theta')] [2kH + \sinh(2kH)]^2} dl_x dl_y, \quad (3.52)$$

where

$$E(\theta) = \int_0^\infty kE(k \cos \theta, k \sin \theta) dk \quad (3.53)$$

is the directional spectrum integrated over all wavenumbers, and the Jacobian $J = 1/\{k[1 - \cos(\theta - \theta')]\}$ of the transform from (k, θ') to (l_x, l_y) is used. Note that the integration over \mathbf{l} is restricted to the half plane where $\mathbf{k} \cdot \mathbf{l} > 0$ (figure 3.4).

For $-\pi/2 < \theta < \pi/2$ (3.52) describes the evolution of an incident component with direction $\theta_I = \theta$. Only interactions in the neighborhood of the resonant triad $\mathbf{k}_I = l(1, \tan \theta)/2$, $\mathbf{k}_R = l(-1, \tan \theta)/2$, $\mathbf{l} = (l, 0)$ contribute to this integral (figure 3.4). For $\pi/2 < \theta < 3\pi/2$, (3.52) describes the evolution of a reflected component with direction $\theta_R = \theta$ resulting from the resonance of $\mathbf{k}_I = l(1, -\tan \theta)/2$, $\mathbf{k}_R = l(-1, -\tan \theta)/2$, $\mathbf{l} = (-l, 0)$. Substitution of (3.51) in (3.52) yields

$$\frac{dE_R}{dx} = -D_x [E(\mathbf{k}_I) - E(\mathbf{k}_R)] \quad \text{for} \quad -L < x < L, \quad (3.54)$$

where

$$D_x = \frac{\pi b^2 \cos^2(2\theta_I) l^5}{16 \cos^6 \theta_I [1 + \cos(2\theta_I)] \left[\frac{lH}{\cos \theta_I} + \sinh\left(\frac{lH}{\cos \theta_I}\right) \right]^2}. \quad (3.55)$$

For weak reflection ($E(\mathbf{k}_I) \gg E(\mathbf{k}_R)$) we can neglect changes in $E(\mathbf{k}_I)$. Integrating (3.54) from L to $-L$ yields

$$E_R = 2LD_x E(\mathbf{k}_I) \quad \text{for} \quad x < -L. \quad (3.56)$$

For unidirectional incident waves with a spectrum $E_I(\mathbf{k}) = \delta(\theta - \theta_I) E_I(k)/k$, the total reflected energy is given by

$$E_R = D l E_I(k_I), \quad (3.57)$$

where D is a non-dimensional coefficient

$$D = \frac{2LD_x}{lk_I} = \frac{m\pi^2 b^2 \cos^2(2\theta_I) l^2}{4 \cos^5 \theta_I [1 + \cos(2\theta_I)] \left[\frac{lH}{\cos \theta_I} + \sinh\left(\frac{lH}{\cos \theta_I}\right) \right]^2}. \quad (3.58)$$

For the particular case of normal incidence ($\theta_I = 0$) D reduces to

$$D = \frac{m\pi^2 b^2 l^2}{8 [lH + \sinh(lH)]^2}. \quad (3.59)$$

2. Comparison with deterministic theory for normal incidence

In Davies' (1979) theory for weak reflection of a normally incident monochromatic wave train by a patch of m sinusoidal bars with amplitude b , the ratio of the reflected and incident wave amplitudes is given by

$$\kappa_{\text{DH}} = \frac{2bk}{2kH + \sinh(2kH)} \frac{(-1)^m 2k \sin(2kL)}{l \left(\frac{2k}{l}\right)^2 - 1}. \quad (3.60)$$

Theoretical values of κ_{DH} have been verified experimentally by Heathershaw (1982; see also Davies & Heathershaw, 1984), even in cases with large reflection coefficients.

For random waves with a wavenumber spectrum $E_I(k)$ the reflected energy $E_{R,\text{DH}}$ is the convolution of $|\kappa_{\text{DH}}(k)|^2$ and $E_I(k)$,

$$E_{R,\text{DH}} = \int_0^\infty |\kappa_{\text{DH}}(k)|^2 E_I(k) dk. \quad (3.61)$$

The response function $|\kappa_{\text{DH}}|^2$ has a 'resonant lobe' of width π/L and height proportional to m^2 centered at the resonant wavenumber $k = l/2$, and narrower side lobes at higher and lower wavenumbers (figure 3.5, dotted curve). In the limit of large m (equivalent to the large t limit in the stochastic theory), $|\kappa_{\text{DH}}|^2$ approaches a Dirac distribution

$$|\kappa_{\text{DH}}|^2 \sim \frac{m\pi^2 l}{8} \left(\frac{2bk}{2kH + \sinh(2kH)} \right)^2 \left(\frac{2k}{l} \right)^2 \delta\left(\frac{l}{2}\right). \quad (3.62)$$

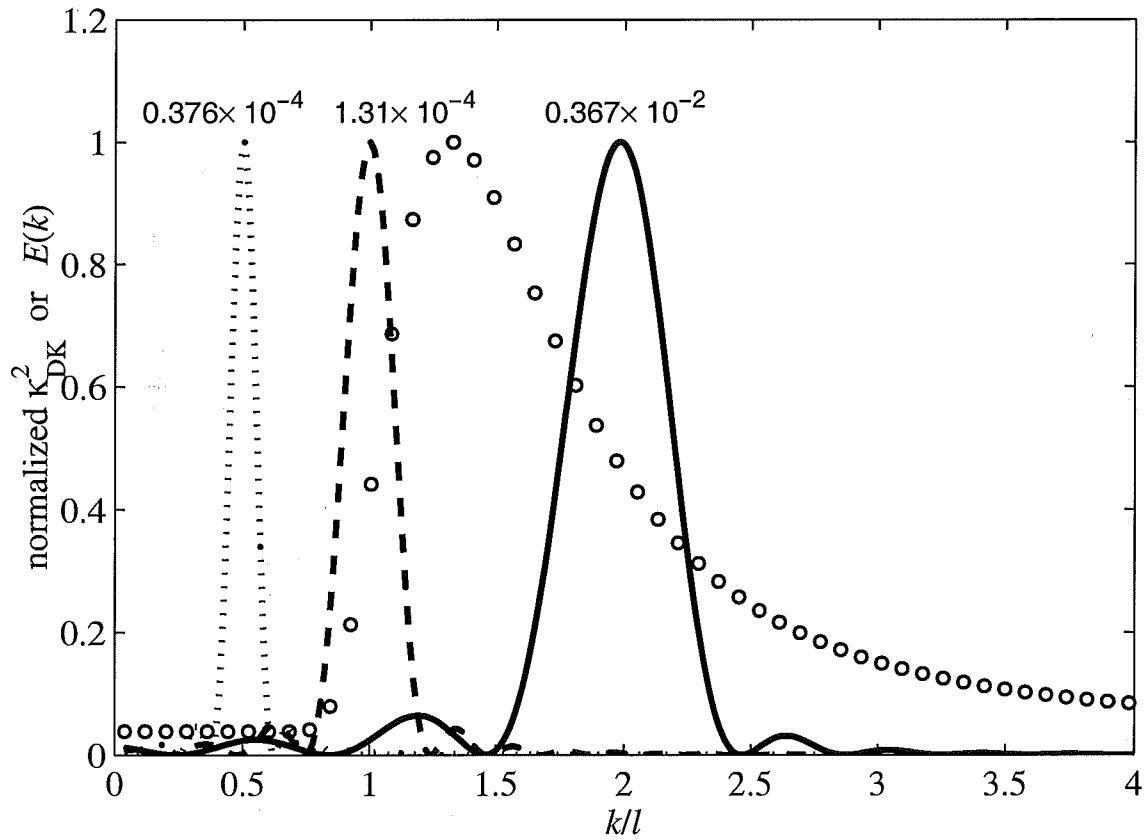


Figure 3.5: Reflection of waves by sinusoidal bars
 Response function $|\kappa_{DK}|^2$ for $H = 25$ m, $2\pi/l = 300$ m, $b = 0.05$ m, $m = 4$, and three incidence directions: $\dots\dots$, $\theta_I = 0^\circ$; $----$, $\theta_I = 60^\circ$; $—$, $\theta_I = 75.5^\circ$. (corresponding to resonant wavenumbers $k = l/2$, $k = l$, and $k = 2l$). The response functions are normalized by their maximum values indicated on the figure. For reference a generic wave spectrum is included (\circ , arbitrary units) with a Pierson-Moskowitz shape, a peak period of 14 s, and uniform infragravity energy levels. The total reflected energy is the convolution of $|\kappa_{DK}|^2$ and the wave spectrum.

Since $E_I(k)$ is continuous, the substitution of (3.62) in (3.61), yields

$$E_{R,DH} \sim \frac{m\pi^2 b^2 l^3}{8[lH + \sinh(lH)]^2} E_I\left(\frac{l}{2}\right), \quad (3.63)$$

which is identical to the stochastic theory prediction (3.57),(3.59). The exact agreement of the stochastic and (experimentally verified) deterministic theories in the limit of large m , where both are valid, confirms that the coupling factor χ (3.49), which differs by factors of 8 and 4 from previous publications (Hasselmann, 1966; Long 1973), is correct.

3. Oblique incidence and finite numbers of bars

Davies' (1979) theory for wave reflection from sinusoidal bars was generalized to oblique incidence and finite reflection coefficients by Mei (1985), using an approximation for weak detuning from resonance. Dalrymple & Kirby (1986) applied Mei's theory to a finite patch of bars and derived the amplitude reflection coefficient κ_{DK} (their equations 5 and 9). For normal incidence κ_{DK} is in good agreement with the experimental results of Davies & Heathershaw (1984), and reduces to κ_{DH} in the limit of small bar amplitude b . For oblique incidence no experimental verification exists but Mei's theory was verified numerically with solutions of Kirby's generalized mild slope equations (Kirby, 1993). Values of $|\kappa_{DK}|^2$ for a patch of four bars of wavelength $2\pi/l = 300$ m, and amplitude $b = 0.05$ m in 25 m depth, are shown in figure 3.5 as a function of k/l for different incidence angles θ_I . The interaction between the bottom undulations and the surface gravity waves is dominated by near-resonant triads, for which $|\kappa_{DK}|^2$ is maximum. The Bragg resonance condition $k = 2l/\cos\theta_I$ determines the wavenumber for which reflection is maximum, as a function of the incidence angle. For example, for the wave spectrum shown in figure 3.5, back scattering ($\theta_I \approx 0$, $\theta_R \approx 180^\circ$) is confined to the low wavelength (infragravity) part of the spectrum, and shorter swells are scattered forward (see the response functions for $\theta_I = 60^\circ$, $\theta_R = 120^\circ$ and $\theta_I = 75.5^\circ$, $\theta_R = 104.5^\circ$ in figure 3.5).

To determine the accuracy of the stochastic theory for a finite patch of bars, the total reflected energy E_R predicted by (3.57)–(3.58), valid only in the limit of large m , is compared to the 'exact' $E_{R,DK}$ predicted by the deterministic theory (3.61 where κ_{DH} is replaced by κ_{DK}), valid for arbitrary m . In these calculations $E_I(k)$ is taken to be a Pierson–Moskowitz (1964) spectrum with a peak period $T_p = 14$ s. A white background spectrum $E(k) = 0.04E_I(k_p)$ is added to represent contributions of longer wavelength infragravity waves (figure 3.5). The convolution integral (3.61) is computed numerically over the range $0.005 < k/l < 4$, for incidence angles $\theta_I = 0$, 60° and 75.5° . Other parameters are $H = 25$ m and $b = 0.05$ m. A small b value was chosen to have a small reflection coefficient ($\kappa_{DK} < 0.1$) because (3.57) neglects variations in the incident energy E_I and thus is valid only for weak reflections. The relative difference between stochastic and deterministic theories is shown in figure 3.6 as a function of m . This difference is sensitive to the variations of the wave spectrum across the resonant lobe and the relative magnitude of the side-lobes of the response function $|\kappa_{DK}|^2$. It vanishes in the limit $m \rightarrow \infty$ as the width of the resonant lobe and the height of the side-lobes go to zero. As m increases the predictions of both theories converge, as expected since both theories are valid for large m . For all three incidence angles $\theta_I = 0$, 60° and 75.5° , the difference in reflected wave energy predicted by the stochastic and deterministic theories is less than 25% for more than three bars. This rapid convergence not only provides a further consistency check of the coupling factor χ (3.49) for cases of oblique incidence, but also indicates that the stochastic Bragg scattering theory is surprisingly robust. Although formally valid only in the asymptotic limit of many bottom wavelengths, it yields reasonable estimates of energy transfers resulting from scattering by only a few bottom undulations.

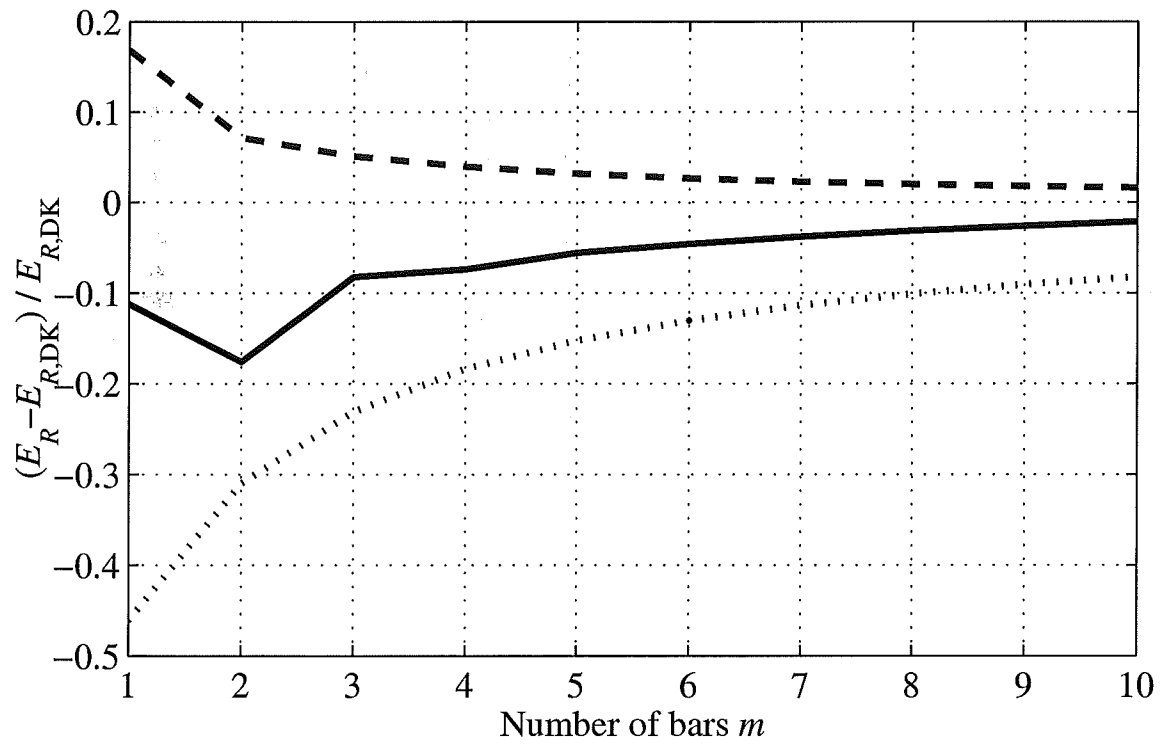


Figure 3.6: Comparison of stochastic and deterministic theories

Relative differences between the reflected energy predicted by the stochastic theory and the spectral form of the deterministic theory, (3.61, replacing κ_{DH} by κ_{DK}), as a function of the number of bars m . All other parameters are the same as those used in figure 3.5. The incident wave spectrum is shown in figure 3.5.

4. Bottom slope effects

The large time limit used to evaluate fourth order energy terms in appendices A–D requires implicitly that the large scale bottom slope does not significantly change the interaction over a distance Δr that allows waves to propagate across a sufficiently large number of bars m_a to approach the asymptotic limit of the energy transfer (figure 3.6). Wave refraction by the large-scale bottom slope changes the surface wavenumbers and thus introduces a detuning of near-resonant wave-bottom interactions. This detuning effect can be neglected only if changes in the surface wavenumbers are small compared to the width of the resonant lobe of the response function $|\kappa_{\text{DK}}|^2$ (figure 3.5).

For simplicity we consider a finite patch of m_a sinusoidal bars aligned with the y -axis, with wavenumber l , superimposed on a plane bottom with a downward slope β in a direction θ_b . The along-ray gradient of the resonance mismatch $u = (2k \cos \theta - l)/l$ is given by

$$\frac{\partial u}{\partial r} = \frac{2}{l} \left(\cos \theta \frac{\partial k}{\partial r} - k \sin \theta \frac{\partial \theta}{\partial r} \right). \quad (3.64)$$

Using Snell's law we have

$$\frac{\partial u}{\partial r} = \frac{-4\beta k^2 \cos \theta_b}{l[2kH + \sinh(2kH)]}. \quad (3.65)$$

For small bottom slopes the distance traveled by the waves across the bar field is $\Delta r \approx 2m_a\pi/(l \cos \theta)$, giving a change in the resonance mismatch

$$\Delta u \approx -\frac{2\pi m_a \beta \cos \theta_b}{\cos^3 \theta [2kH + \sinh(2kH)]}. \quad (3.66)$$

Detuning of resonant interactions by refraction can be neglected if $|\Delta u|$ is small compared with the (normalized) width of the resonant lobe $1/m_a$, that is

$$m_a |\Delta u| \ll 1. \quad (3.67)$$

(3.67) also follows from considering the phase difference between waves reflected by the first and m_a^{th} bars, which should be small compared to $\pi/2$ to allow the constructive interference that causes resonance.

(3.67) is a necessary condition for the application of the stochastic theory. For a given bottom slope β , (3.67) imposes a maximum incidence angle θ_{max} . For practical purposes we assume that the largest acceptable value of $m_a |\Delta u|$ is about 0.5, giving

$$\cos^3 \theta_{\text{max}} > \frac{4\pi m_a^2 \beta \cos \theta_b}{2kH + \sinh(2kH)}. \quad (3.68)$$

For example, considering 14 s period waves in 25 m depth with a bottom slope $\beta = 2 \times 10^{-4}$ at an angle $\theta_b = 60^\circ$, and taking $m_a = 2$, the source term (3.48) is expected to significantly overestimate the energy of scattered waves for incidence angles greater than $\theta_{\text{max}} \approx 83^\circ$, corresponding to a ratio $k/l = 4.3$.

It should be noted that (3.67) is consistent with the scaling of (3.1)–(3.4) requiring that bottom and surface elevations have comparable horizontal scales. This scaling is violated for large angle interactions (i.e. $k \gg l$ for θ close to 90°), even on a flat bottom. In the following the contribution of wave-bottom interactions to (3.48) is taken to be accurate for $\theta < \theta_{\text{max}}$ and is neglected for $\theta > \theta_{\text{max}}$. This crude truncation of the interactions is expected to give only qualitative results for the scattering of waves at large incidence angles. Sensitivity of predicted spectral evolution to the choice of the cut-off angle θ_{max} is examined for natural shelf topography in § 4.

C. Hindcast of wave scattering on a natural shelf

The effect of Bragg scattering on directional wave spectra evolution is illustrated here with a numerical model hindcast of swell evolution observed across the North Carolina shelf. The scattering source term S_{Bragg} (3.48) was implemented in the spectral model CREST (chapter II), that integrates the energy balance (3.47) in time using a hybrid Eulerian–Lagrangian numerical scheme. In addition to S_{Bragg} a bottom friction source term S_{fric} is included in the energy balance to account for energy dissipation in the boundary layer over a sandy movable bottom. Details of the model formulation, numerical scheme, treatment of boundary conditions, and parameterization of bottom friction are given in chapter II. S_{Bragg} is evaluated using bottom elevation spectra that were estimated from high-resolution bathymetry surveys. Processes not represented in the model such as wind generation, effects of currents, wave breaking, and non-linear effects, are expected to be negligible because at the time of the hindcast (21:00 Greenwich Mean Time, on October 20, 1994) local wind speeds (3 m s^{-1}), and current velocities ($\approx 20 \text{ cm s}^{-1}$, Lentz *et al.*, 1999) were weak, and the observed waves were long-period ($\approx 13 \text{ s}$) swell with low significant height ($\approx 1 \text{ m}$).

1. Wave data

Frequency-directional wave spectra were estimated from measurements on the outer and inner shelf near Duck, North Carolina (figure 3.7 *a*). An array of pressure sensors, located 1 km from the shoreline in 8 m depth, was operated by the Army Corps of Engineers Field Research Facility (FRF), in Duck, North Carolina, and a 3 m discus pitch and roll buoy located close to the shelf break, in 49 m depth, was operated by the National Data Buoy Center (NDBC). Standard techniques (Herbers *et al.*, 1999; §II.D) were used to obtain estimates of the frequency-directional wave spectra at both locations. The NDBC buoy wave spectrum was transformed across the shelf break to deep water using Snell’s law, assuming parallel depth contours, in order to obtain the offshore boundary condition for the model.

2. Bottom topography

Bathymetric data for most of the shelf was available from the National Ocean Service (NOS). In regions not covered by the NOS archives, water depths were measured during instrument deployment and recovery cruises in a series of experiments (DUCK94; Sandy Duck; SHOWEX) on the North Carolina continental shelf, using a single precision depth recorder. Additionally, high-resolution multibeam sonar bathymetric surveys were conducted during the SHOWEX experiment in November and December 1999, in two $6 \text{ km} \times 6 \text{ km}$ square regions of the inner shelf (labeled S_1 and S_2 in figure 3.7*a*). This data set was processed with the MB-System software (Caress & Chayes, 1995) to obtain 10 m resolution grids shown in figure 3.7 (*b,c*). The vessel motion and tide were carefully removed, although a slight but systematic measurement bias is still noticeable in the striped pattern of figure 3.7 (*c*), yielding an artificial ridge of spectral densities on the x -axis of figure 3.8 (*b*). Although the high-resolution bathymetry data was acquired five years after the wave data, comparisons with depth soundings, performed within a few months of the wave data collection, show good agreement, suggesting that bottom topographic features of scales larger than 500 m have not moved in regions S_1 and S_2 .

Bottom elevation spectra $F_1^B(l)$ and $F_2^B(l)$ (figure 3.8*a,b*) were estimated for regions S_1 and S_2 , respectively, based on bidimensional Fourier transforms of Hanning windowed $1.6 \text{ km} \times 1.6 \text{ km}$ square segments with 50 % overlap. The large scale bottom slope was previously removed from each segment using a bilinear fit. Spectra of the large scale shelf topography (not shown), computed from the entire bathymetry grid, are consistent with the spectral levels at small l shown in figure 3.8*a,b*. The bottom elevation spectra are not isotropic, showing a preferential north-east/south-west orientation of intermediate scales features (200–1000 m) that are most important for swell

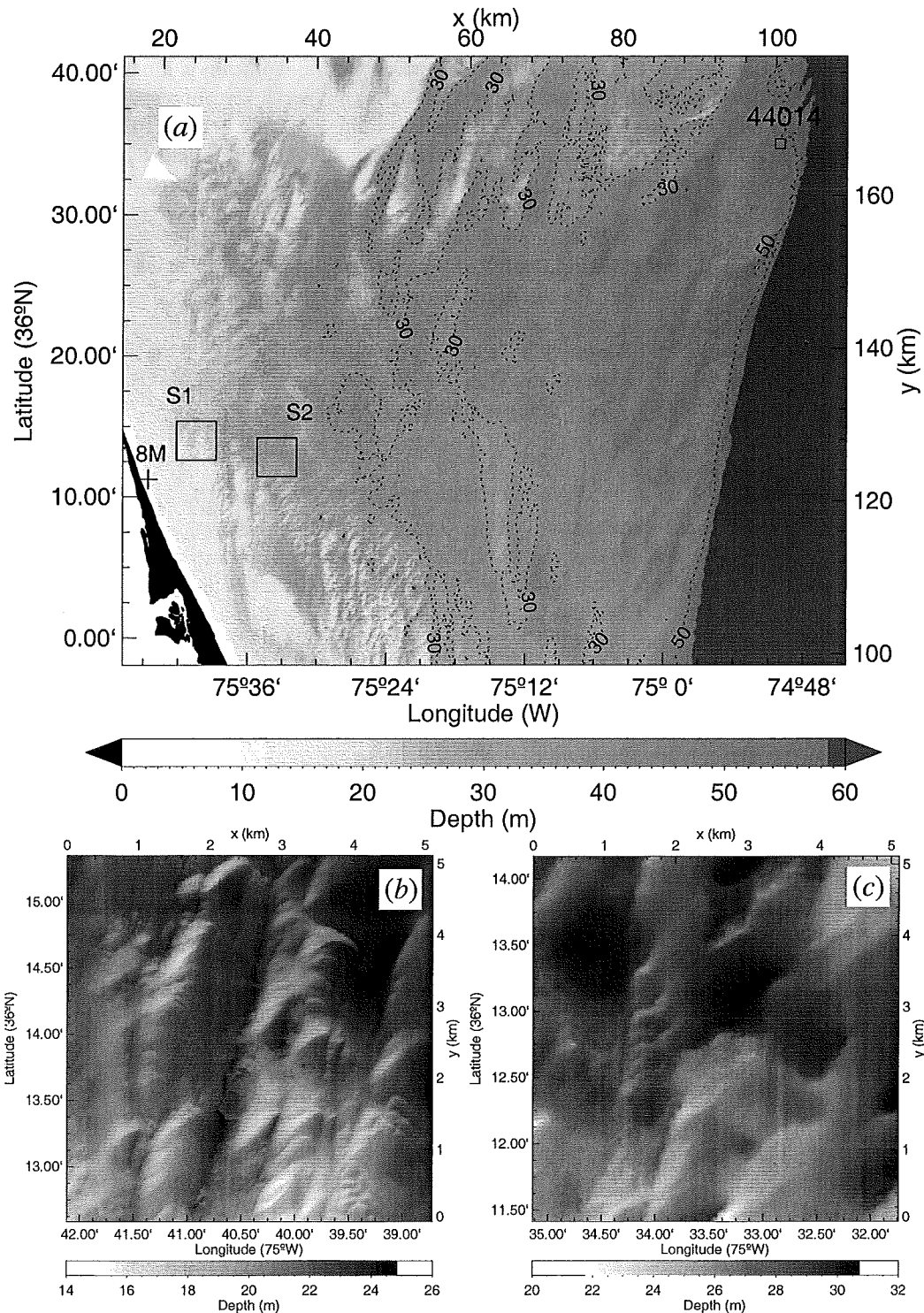


Figure 3.7: High resolution (10 m) bottom topography of the North Carolina continental shelf (*a*). The squares marked S1 and S2 are the regions enlarged in (*b*, *c*). Other symbols indicate locations of the FRF 8 m depth array (8M) and NDBC 3 m discus buoy (44014).

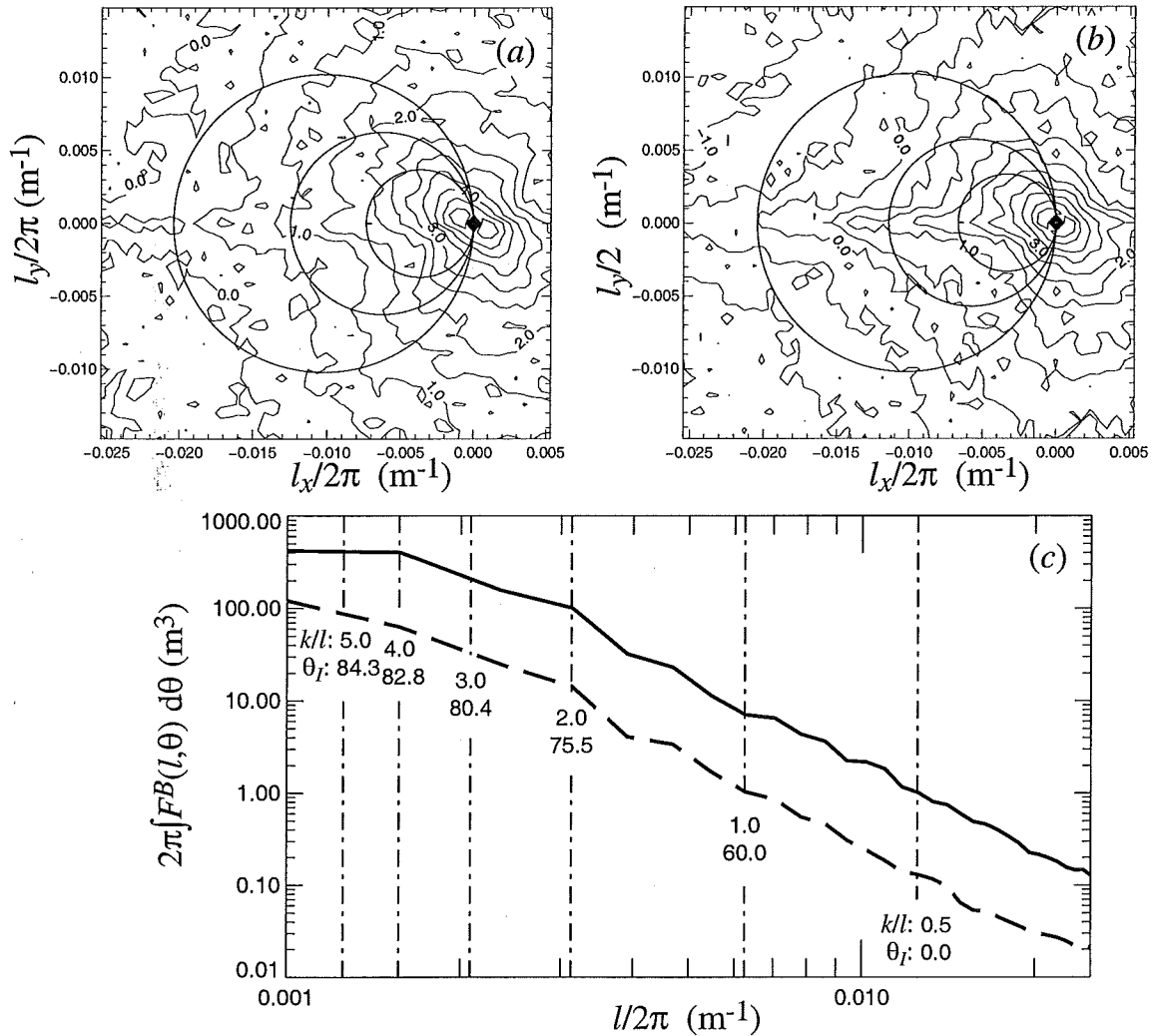


Figure 3.8: Bottom elevation spectra

Contour plots of the bottom variance spectra estimates for regions S1 (a) and S2 (b). The contour values are $\log_{10}(4\pi^2 F^B)$ with F^B in $\text{m}^4 \text{rad}^{-2}$, and the contour interval is 0.5. Circles indicate the bottom components that interact with waves arriving from the east with frequencies 0.05 (inner circle), 0.12 (middle circle) and 0.25 Hz (outer circle). Axes units are reciprocal wavelengths $l_x/(2\pi)$ and $l_y/(2\pi)$. (c) direction-integrated spectra for S1 (—) and S2 (---). The vertical lines indicate the bottom scales responsible for scattering 0.08 Hz swell, for various incidence angles θ_I .

scattering. It also appears that bottom spectral levels at these scales are about a factor 4 higher in region S_1 (15–25 m water depth, variance 1.4 m^2) than in the deeper region S_2 (20–40 m, variance 0.35 m^2 , see figure 3.8c). Lacking detailed topographic information in other regions, the bottom elevation spectrum used in model hindcasts is taken to be uniform over the entire continental shelf. Hindcasts are presented in §4 based on both estimates $F_1^B(\mathbf{l})$ and $F_2^B(\mathbf{l})$, illustrating the likely range of scattering effects.

3. Numerical model

The numerical wave model CREST used for the present calculations is described in chapter II with unchanged spatial and wavenumber grids. The model consists of a precomputation of wave rays and a Lagrangian time integration scheme for the energy balance (3.47). In contrast to more widely used finite-difference schemes (see for example the WAMDI group, 1988; Booij *et al.*, 1999) the Lagrangian approach avoids numerical diffusion that could cause an artificial broadening of the wave spectrum in shallow water (not related to physical scattering processes). The Eulerian model grid, shown in figure 3.9 is unstructured and much coarser than the bathymetry grid. It consists of 329 points \mathbf{x}_n distributed over a large portion of the shelf between latitudes 35 and 37° N. Wave rays are traced backwards from the Eulerian grid points to the model boundary, using a smoothed (2 km scale) bathymetry grid that resolves wave refraction over the large scale shelf topography. Along each ray the energy balance (3.47) is integrated in time. At the grid points the full wave spectrum $E(\mathbf{k})$ is evaluated using ensemble averages of rays within finite wavenumber bands $\mathbf{k}_{q,i}$ corresponding to 19 frequency bands f_q spaced exponentially with a 5% increment from 0.05 Hz to 0.12 Hz, and 120 direction bands θ_i spaced linearly over a full circle with a 3 degree resolution. The spectral source terms $S_{\text{fric}}(\mathbf{k})$, representing bottom friction (§II.B), and $S_{\text{Bragg}}(\mathbf{k})$, given by (3.48), are evaluated at the grid points based on the local spectrum $E(\mathbf{k})$ and other parameters. $S_{\text{fric}}(\mathbf{k})$ and $S_{\text{Bragg}}(\mathbf{k})$ are interpolated onto the ray trajectories to account for the energy losses (bottom friction), and exchanges with other wave components (scattering), of component \mathbf{k} during propagation. Details of the time integration and interpolation schemes can be found in §II.3.

The model was run here with uniform and steady offshore boundary conditions and a fixed integration time step $\Delta t = 10$ minutes, until a steady state was reached. To determine accurately the contribution of S_{Bragg} over the time step Δt , an implicit integration scheme was used. Omitting other source terms and propagation effects, (3.47) can be written in discretized form and for a given wavenumber magnitude k , as a set of linear equations

$$\frac{\partial E(k, \theta_i)}{\partial t} = 4\pi g^{\frac{1}{2}} H^{-\frac{9}{2}} \chi(kH) \sum_j L_{i,j}(k) E(k, \theta_j) \quad \text{for all } i, \quad (3.69)$$

where θ_i are the discretized directions with $\mathbf{k}_i = k(\cos \theta_i, \sin \theta_i)$ and the matrix $L(k)$ is given by

$$L_{i,j}(k) = \left[\cos^2(\theta_i - \theta_j) F^B(\mathbf{k}_i - \mathbf{k}_j) - \delta_{ij} \sum_n \cos^2(\theta_i - \theta_n) F^B(\mathbf{k}_i - \mathbf{k}_n) \right] \Delta\theta, \quad (3.70)$$

with $\delta_{ij} = 1$ for $i = j$ and 0 otherwise. As discussed below in §III.4, $F^B(\mathbf{l})$ is replaced by zero in (3.70) for k/l greater than $(k/l)_{\text{max}}$. Since L is real and symmetric, it can be diagonalized and represented as the matrix product $L = VDV^T$ where D is a diagonal matrix with the eigenvalues λ_i as diagonal elements, the columns of V are the corresponding normalized eigenvectors, and V^T is the transpose of V . Using this decomposition the solution of (3.69) can be given in the form

$$E(k, \theta_i, t + \Delta t) = \sum_j \sum_l V_{i,j}(k) \exp \left[4\pi g^{\frac{1}{2}} H^{-\frac{9}{2}} \chi(kH) \lambda_j(k) \Delta t \right] V_{l,j}(k) E(k, \theta_l, t). \quad (3.71)$$

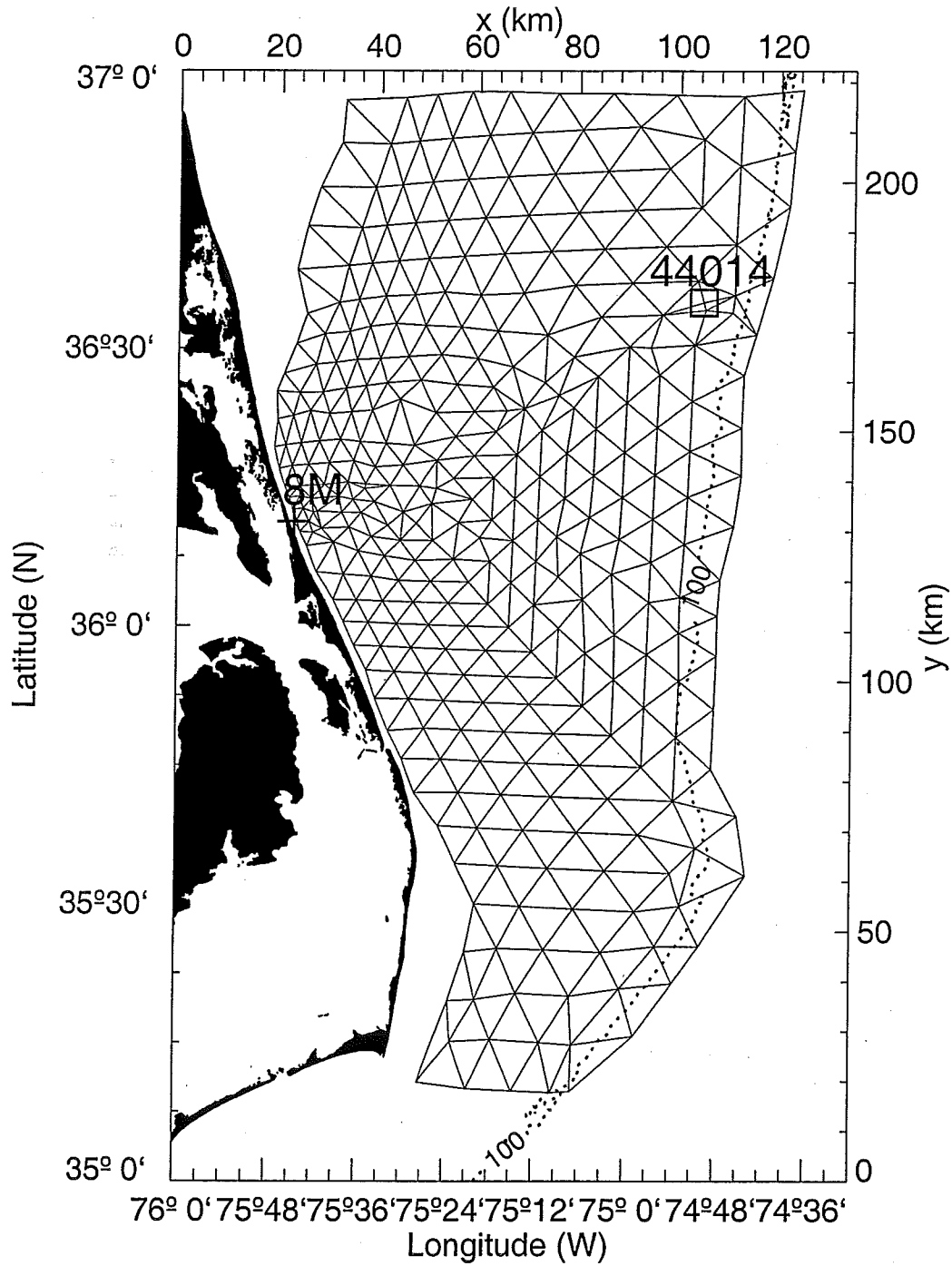


Figure 3.9: Model grid

The grid points where the source term is evaluated are the nodes of the triangular mesh. A linear interpolation is applied in each triangle to approximate the source term along the rays. The 100 m depth contour is indicated by the dotted line.

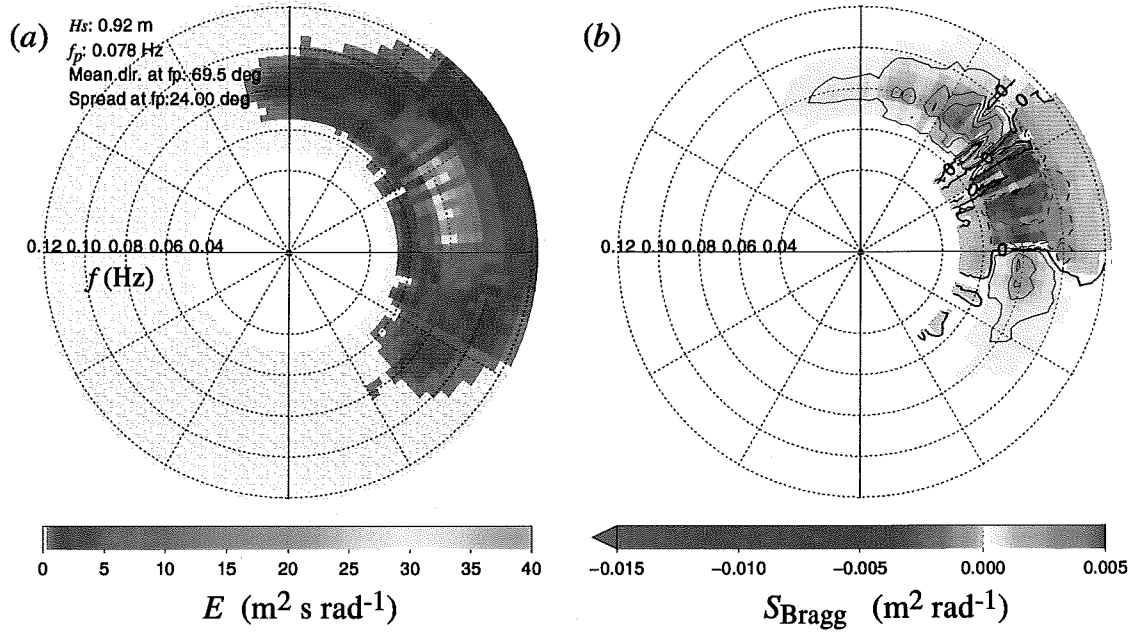


Figure 3.10: Wave spectrum and Bragg scattering source term

(a) Predicted wave spectrum E in region S_1 (figure 3.8) and (b) corresponding Bragg scattering source term S_{Bragg} , based on bottom spectrum F_1^B . Contours in (b) are solid for positive values (yellow to red color shades), heavy solid for $S_{\text{Bragg}} = 0$, and dashed for negative values (green to blue color shades).

The source term S_{Bragg} , R in (2.17), is given by the average change in $E(k, \theta_i, t)$ over a time step Δt

$$S_{\text{Bragg}}(k, \theta_i) = [E(k, \theta_i, t + \Delta t) - E(k, \theta_i, t)] / \Delta t. \quad (3.72)$$

The matrices $V(k)$ and eigenvalues $\lambda_i(k)$ are precomputed using Jacobi's algorithm (see for example Press *et al.*, 1992) for 500 values of k covering the entire range of wavenumbers in the model, and the resulting matrices V and D are interpolated on the spectral model grid. The high accuracy of the implicit numerical scheme was confirmed through comparisons with an explicit fifth order Cash-Karp Runge-Kutta scheme.

4. Hindcast

The model hindcast was performed both with and without the Bragg scattering source term, to isolate the scattering effects from other processes (refraction, shoaling and bottom friction), and using two different measured bottom elevation spectra (F_1^B (1) and F_2^B (1), figure 3.8) to estimate the possible variability of the scattering effects. Bottom components with wavelengths larger than 5 times the surface wavelength ($k/l > 5$) are excluded in the evaluation of S_{Bragg} because, as discussed in §3.4, the theory is not expected to be accurate for near-grazing angle interactions. Figure 3.10 shows an example wave spectrum predicted in region S_1 (20 m depth, figure 3.7), and the corresponding Bragg scattering source term. The source term has a 3-lobe shape with negative values near the peak θ_p of the directional wave spectrum, and positive maxima on both sides of the peak, at about $\theta_p \pm 30^\circ$. The interactions broaden the peak of the directional wave spectrum (forward-scattering) and cause weak, almost isotropic back-scattering. Sign reversals of S_{Bragg} within the main lobe (figure 3.10b) are caused by irregularities in the wave spectrum (figure 3.10a). Bragg

scattering tends to smooth the directional wave spectrum, with an evolution time-scale E/S_{Bragg} of the order of 10^3 and 10^4 s in 20 and 50 m depth, respectively.

The combined effect of Bragg scattering and refraction is shown in figure 3.11 with the predicted cross-shore evolution of the mean wave direction (from) at the peak frequency, $\bar{\theta}$, taken as the direction of the first-order moment vector

$$(a_1, b_1) = \int_0^\pi (\cos \theta, \sin \theta) E(f_p, \theta) d\theta, \quad (3.73)$$

and the corresponding directional spread,

$$\sigma_\theta = \{2 [1 - (a_1 \cos \bar{\theta} + b_1 \sin \bar{\theta}) / E(f_p)]\}^{\frac{1}{2}}. \quad (3.74)$$

σ_θ ranges from 0 for unidirectional waves, to 81 degrees for isotropic waves. Offshore propagating waves ($\pi < \theta < 2\pi$) are excluded in the analysis because the predicted back-scattering is weak, and reflection from the beach (Elgar, Herbers & Guza, 1994), not represented in the model, is apparent in the 8 m data (figure 3.11*b*).

The model without Bragg scattering predicts the expected turning of $\bar{\theta}$ towards the shore-normal direction, caused by refraction (figure 3.11*a*). The introduction of Bragg scattering shifts the mean wave direction by an additional 1 to 10 degrees to the north, because the bottom spectrum is not isotropic (figure 3.8). This effect is strongest for the hindcast which uses the bottom spectrum F_1^B with a larger variance. This small shift is not evident in the observations, suggesting that other processes, not represented in the model, may be important or the orientation of the bathymetric features in figure (3.8*a*) may not be representative of other parts of the shelf, but it is unlikely that the statistical nature of these features evolved significantly between 1994 when the wave data was collected and 1999 when the bottom bathymetry was surveyed, even if individual features may have moved. Besides, this effect is still apparent for waves observed in 1999 (see § V.D.1). The detailed directional spectra, shown in figure 3.12 demonstrate that rather than shifting the entire spectrum, Bragg scattering skews the directional spectrum to the north (figure 3.12*c, d*) by preferentially scattering waves that propagate in directions parallel to the crests of the larger bedforms (i.e. waves from the north-east, figures 3.8, 3.8).

Bragg scattering strongly affects the directional spread, causing a gradual increase of σ_θ across the shelf (figure 3.11*a*), that partly balances the reduction of the directional spread of the incident waves caused by refraction. Results based on bottom elevation spectra F_1^B and F_2^B are qualitatively similar but the increase in directional spread is much larger for the more 'energetic' bottom spectrum F_1^B (about a factor 2.5) than predicted for F_2^B (a factor 1.6). On the inner shelf, in 8 m depth, the observed σ_θ value of 14° is a factor 2 larger than the model prediction without Bragg scattering (7° , figure 3.11*b*), but falls in the range of model results with the source term S_{Bragg} based on bottom spectra F_1^B (18°) and F_2^B (12°).

The cut-off value $(k/l)_{\text{max}}$ of the ratio between surface and bottom wavenumbers was varied from 0.5 (no scattering) to 5, in order to examine the importance of different bottom topography scales in the scattering process (figure 3.13). Increasing $(k/l)_{\text{max}}$ from 0.5 (no scattering) to 1 (maximum scattering angle $\theta_{\text{max}} = 60^\circ$) does not change significantly the directional properties of the waves. These interactions, involving bottom components with wavelengths smaller than the surface wavelength, are weak because of the sharp roll-off of the bottom spectral levels at high wavenumbers. At the other end of the spectrum, results for $(k/l)_{\text{max}}$ values of 4 and 5 are nearly identical, indicating that larger bottom features also do not significantly affect directional properties. Although the bottom spectral levels are relatively high at these small values of l , the angular separation of the interacting wave components is small (11.5° for $k/l = 5$) and thus the energy transfers do not strongly modify a directional spectrum that is already broad. A range of interactions involving intermediate scale bottom components ($k/l = 1$ to 4) appears to dominate the scattering process (i.e. note the gradual shift of $\bar{\theta}$ and increase of σ_θ as $(k/l)_{\text{max}}$ increases from

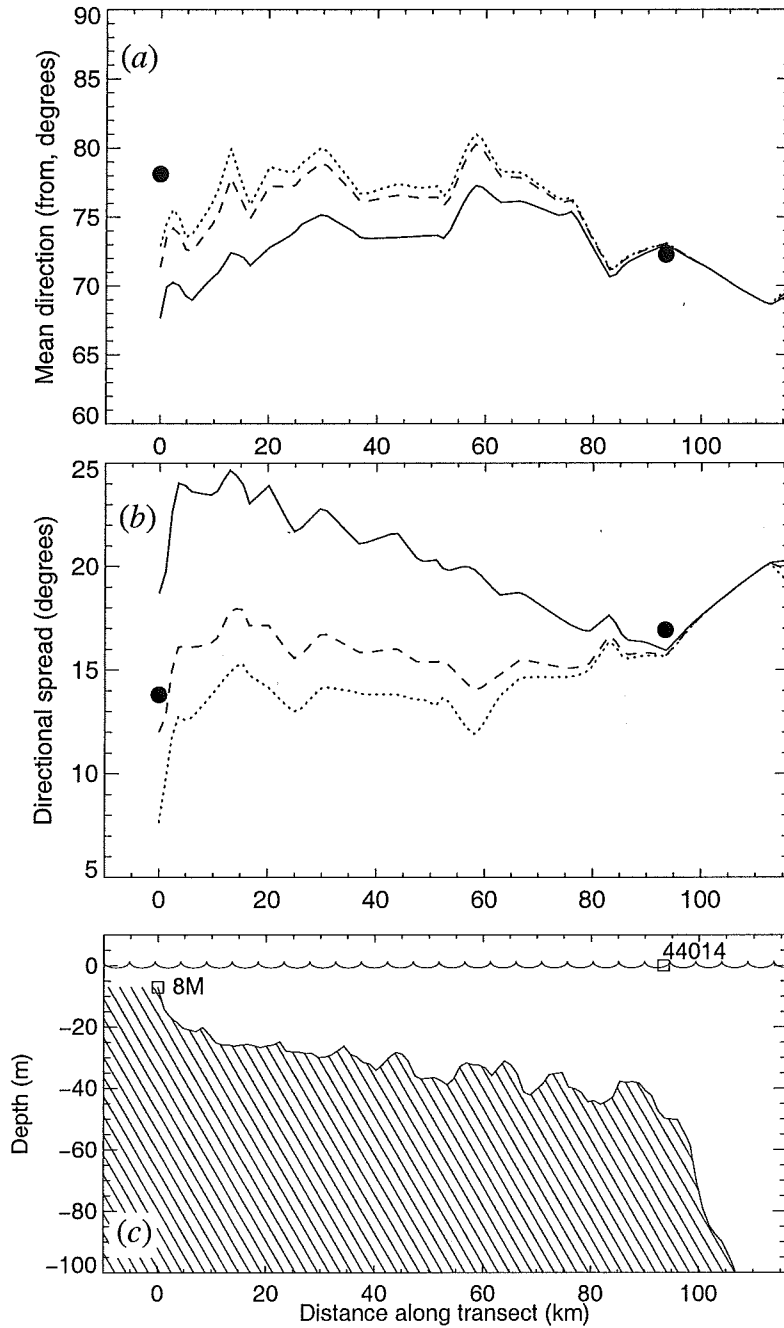


Figure 3.11: Directional properties across the shelf
 Measured (\bullet) and predicted (—, with Bragg scattering using F_1^B (1); ---, with Bragg scattering using F_2^B (1); \cdots , without Bragg scattering) variations of $\bar{\theta}$ (a) and σ_θ (b) at the peak frequency f_p . Results are shown for October 20, 2000, at 2100 GMT, along a cross-shelf transect (c) extending from the 8 m depth array to deep water offshore of NDBC buoy 44014. A maximum value of $k/l = 5$ was used in the scattering calculations.

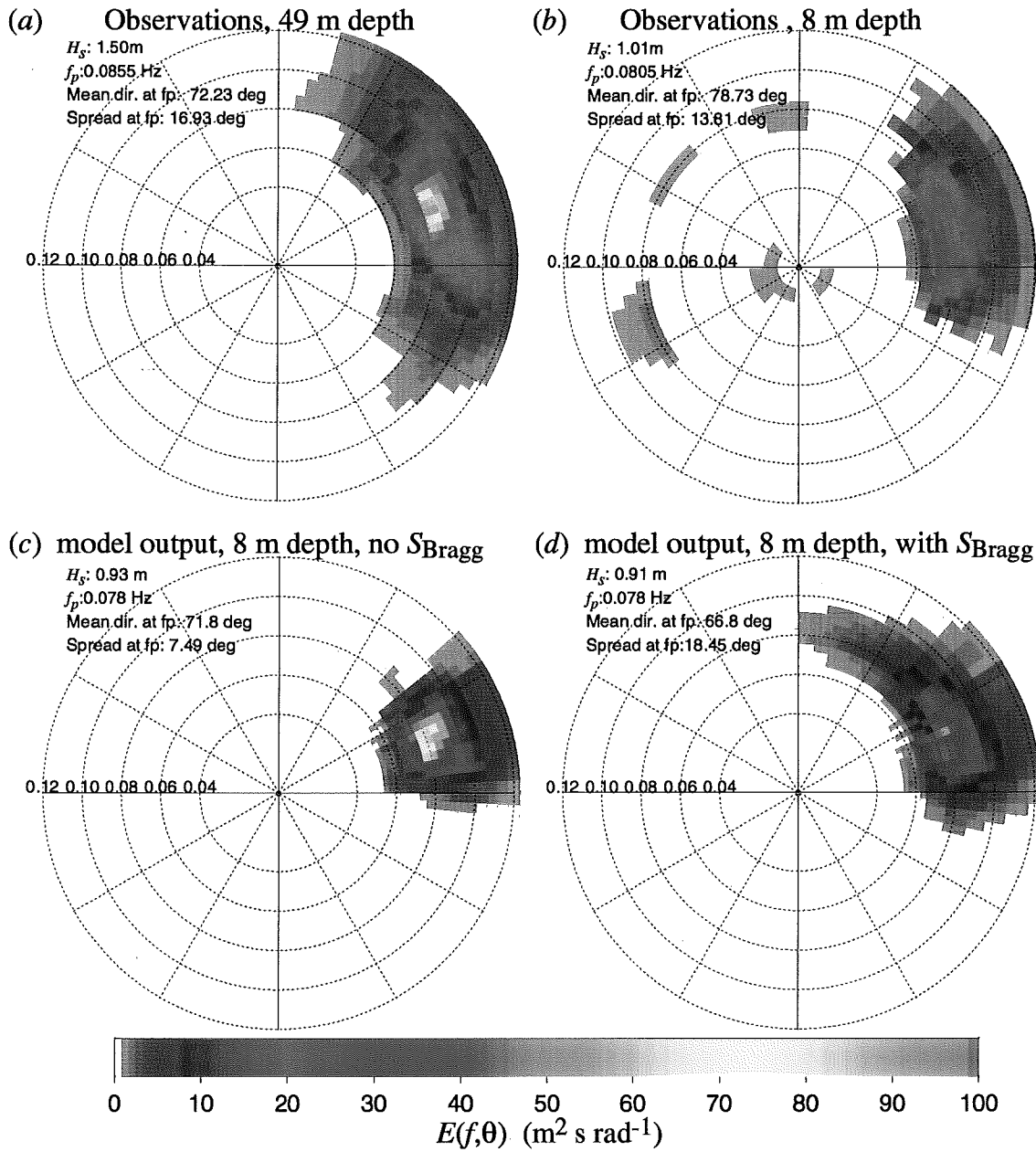


Figure 3.12: Realistic test of the Bragg scattering source term
 Observed wave spectra in (a) 49 and (b) 8 m depth, and predicted wave spectra in 8 m depth, (c) without Bragg scattering and (d) with Bragg scattering, based on the bottom spectrum F_1^B (figure 3.8a). Note that waves coming from the west in panel b are probably reflections from shore (at 1 km of the 8 m site).

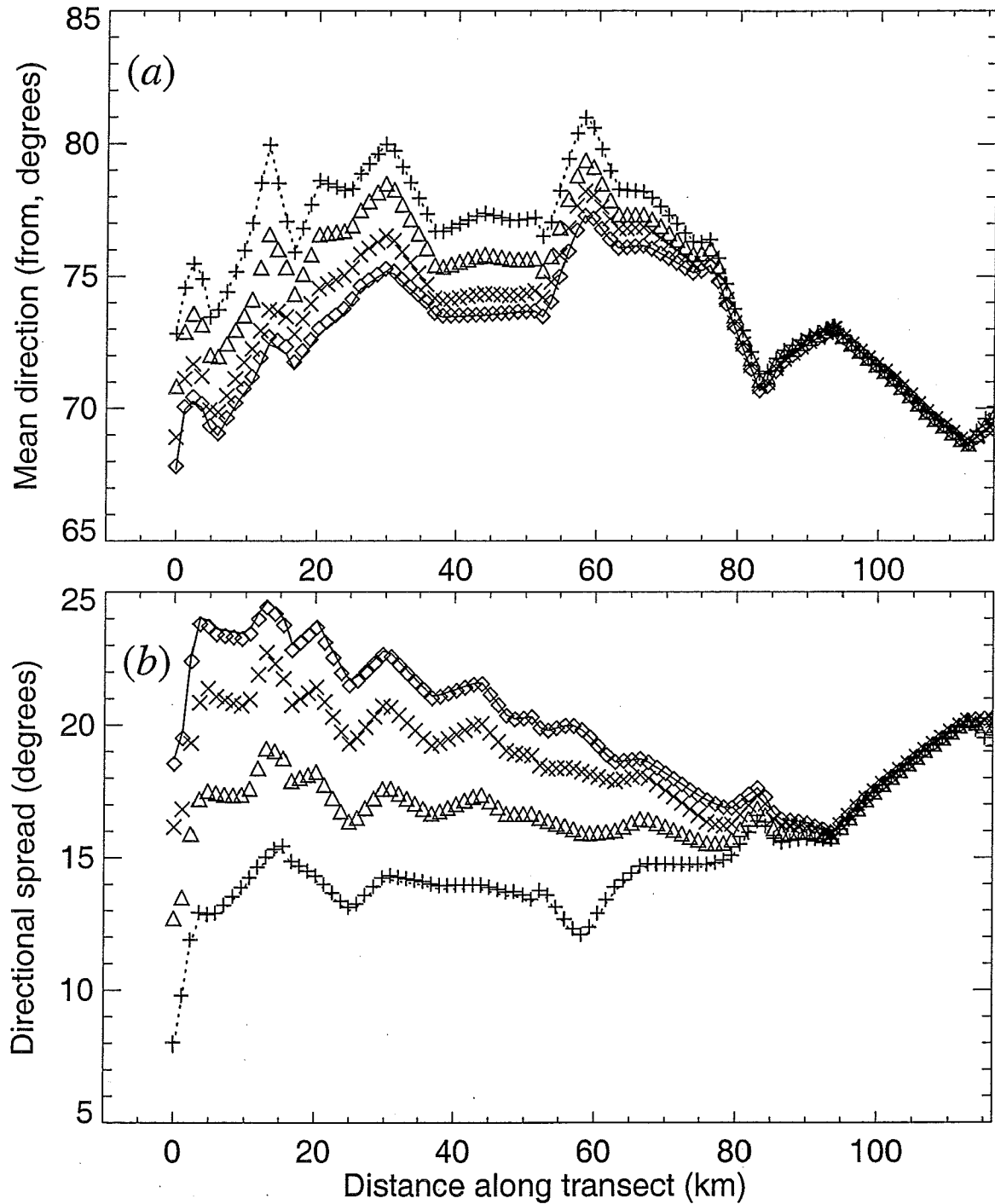


Figure 3.13: Sensitivity to the wavenumber cut-off
 Predicted variations of (a) $\bar{\theta}(f_p)$ and (b) $\sigma_{\theta}(f_p)$ across the shelf for six values of the cut-off parameter $(k/l)_{\max}$: —, 5; \diamond , 4; \times , 3; \triangle , 2; +, 1; \cdots , 0.5 (i.e. no Bragg scattering).

1 to 4 in figure 3.13). Predictions of σ_θ are insensitive to the bathymetry smoothing scale used in ray computations, with a typical 2 degrees difference between model runs using the original 150 m resolution grid, and the predictions presented here using a 2 km smoothed grid.

D. Summary

The energy balance equation for random surface gravity waves, including Bragg scattering (the lowest order resonant interactions between waves and bottom undulations), was re-derived for non-stationary conditions and multiple-scale bottom topography, combining Hasselmann's (1962) perturbation expansion of the wave energy, with a ray approximation for medium variations. The bottom topography is decomposed in a large scale topography, responsible for wave refraction and shoaling, and random undulations with smaller wavelengths (of the order of the surface wavelength), that cause Bragg scattering. The effects of the large-scale and small-scale bottom slopes, surface non-linearity, wave non-stationarity and non-uniformity are represented by five small parameters, β , η , ε , α , and γ , respectively. Using $\alpha \approx \beta \approx \gamma \approx \eta^2 \approx \varepsilon^2$, a closure of the fourth order energy yields a spectral energy balance equation in which refraction, shoaling, and Bragg scattering processes are all of the same order ε^4 .

The stochastic scattering theory was reconciled with a spectral application of deterministic theories for waves propagating over sinusoidal bars (Davies & Heathershaw, 1984; Mei, 1985; Dalrymple & Kirby, 1986). Agreement of the theories in the asymptotic limit of a large number of bars supports the present derivation of the Bragg scattering source term (3.48) which is a factor 8 and 4 smaller than expressions given by Hasselmann (1966) and Long (1973), respectively. Analysis of the detuning of wave-bottom interactions by the large scale bottom slope β shows that the present theory is valid only for small values of $\beta/\cos^3\theta$, where θ is the wave incidence direction relative to the bedform-normal. In the present application, wave-bottom interactions corresponding to θ larger than a cut-off value θ_{\max} are neglected.

The effect of bottom scattering on swell propagation was illustrated with a hindcast for the North Carolina continental shelf using the numerical wave model CREST with high resolution bathymetry and an efficient implicit scheme to evaluate the bottom scattering contribution to the energy balance. Back-scattering of waves towards the open ocean was found to be negligible in this region. However, forward scattering causes a diffusion of wave energy about the mean direction that results in a dramatic increase of the directional spread of the wave spectrum on the inner shelf. This weak back-scattering and strong forward scattering is caused by the sharp roll-off of the bottom elevation spectrum at high wavenumbers. The directional broadening of the swell spectrum predicted in shallow water is qualitatively consistent with field measurements.

IV. OBSERVATIONS OF WAVE-GENERATED RIPPLES

This chapter was submitted for publication, with part of chapter I, in the *Journal of Geophysical Research* (Ardhuin, Drake & Herbers, submitted manuscript). It describes observation of bedforms in relation to wave measurements.

A. Experiment

Wave, bedform and sediment data were collected off the coast of Duck, North Carolina, from September to December 1999, as part of the SHOaling Waves EXperiment (SHOWEX) a multi-institution effort to improve the understanding of the transformation of waves in shallow water. The experiment site is a wide sandy continental shelf, exposed to North Atlantic swells. The bottom slopes gently from 20 m depth, 5 km from shore, to 40 m, over a distance of 60 km (figure 4.1), and is characterized by the presence of sand ridges with spacings and heights ranging from about 1–10 km and 1–10 m, respectively (Green, 1986; Wright, 1995; figure 3.7). The larger-scale ridges are oriented along a south-north axis (figure 4.1).

Six Datawell Directional Waverider buoys, named X1 to X6, were deployed from September 13 to December 13, 1999, along a cross-shelf transect. Buoys X1 through X5 span the shelf from 21 m to 39 m depth, and buoy X6 was located on the shelf break in 193 m depth. Wave frequency spectra and directional moments (mean propagation direction and directional spread) as functions of frequency were computed internally by the buoys at 30 minute intervals, and transmitted continuously to shore by buoys X1 to X4 using HF radio. Buoys X5 and X6, situated farther offshore, were equipped with internal data loggers. The significant wave height $H_{1/3}$ (four times the root-mean-square surface displacement) and spectral peak frequency f_p observed at X1 and X3 are shown in figure 4.2 for energetic periods preceding three cruises when side-scan sonar images of the bottom were acquired. Figure 4.2 also displays the mean wave direction $\theta_E(f)$, defined as the direction of the first moment vector of the frequency directional surface elevation spectrum $E(f, \theta)$

$$(a_1(f), b_1(f)) = \int_0^{2\pi} (\cos \theta, \sin \theta) E(f, \theta) d\theta \quad (4.1)$$

The large, long-period waves (peak frequencies ranging from 0.06 to 0.08 Hz) originated from three category 4 hurricanes: Dennis looped offshore of the buoy transect (August 29 – September 5) before coming ashore farther south, Floyd swept through the region, with the eye passing a few tens of kilometers inland on September 15, and Gert remained more than 1200 km away from the experiment site, sending swell along the buoy transect (September 20 to 23). The month of December was marked by a strong northeaster (December 1 and 2). The observed strong attenuation of wave energy between X3 and X1, particularly for low frequency waves when $H_{1/3}$ is in the range 1–2 m, is consistent with previous observations and the large bottom roughness predicted for wave-formed ripples (Herbers *et al.*, 2000; Ardhuin *et al.*, 2001).

Bedforms were surveyed with an EG&G model DF1000 side-scan sonar, towed from the R.V. *Cape Hatteras* at night during cruises for buoy deployment, maintenance, and recovery. The first survey (S1) took place between the passages of hurricanes Dennis and Floyd from September 10 to 13. A second survey (S2) was conducted two weeks later (September 24–26), after swells from Gert and a coincident Northeasterly wind sea, had subsided. Repeating most of the tracks from survey S1, the objective of S2 was an assessment of changes in bedforms after hurricanes Floyd and Gert. The final survey (S3) took place as buoys were being recovered (December 12–15), after

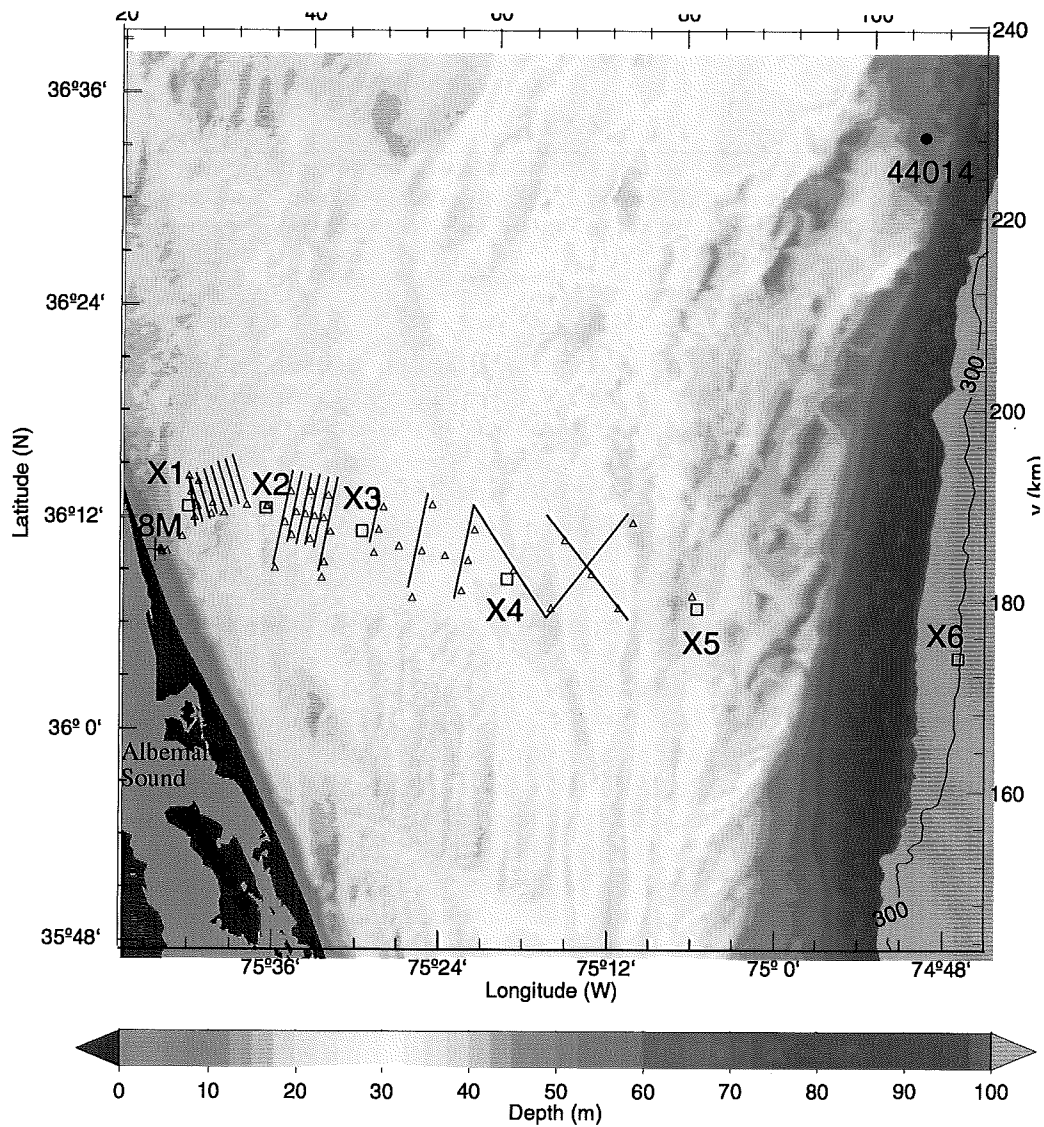


Figure 4.1. Topography and SHOWEX sidescan sonar surveys. Squares numbered X1 to X6 indicate the positions of Directional Waverider Buoys deployed during SHOWEX, the large filled circle indicates the National Data Buoy Center buoy 44014, and the + symbol indicates the Field Research Facility 8 m depth pressure sensor array (8M). Solid lines represent ship tracks for the sidescan sonar surveys, and triangles indicate the locations where surficial sediments were sampled.

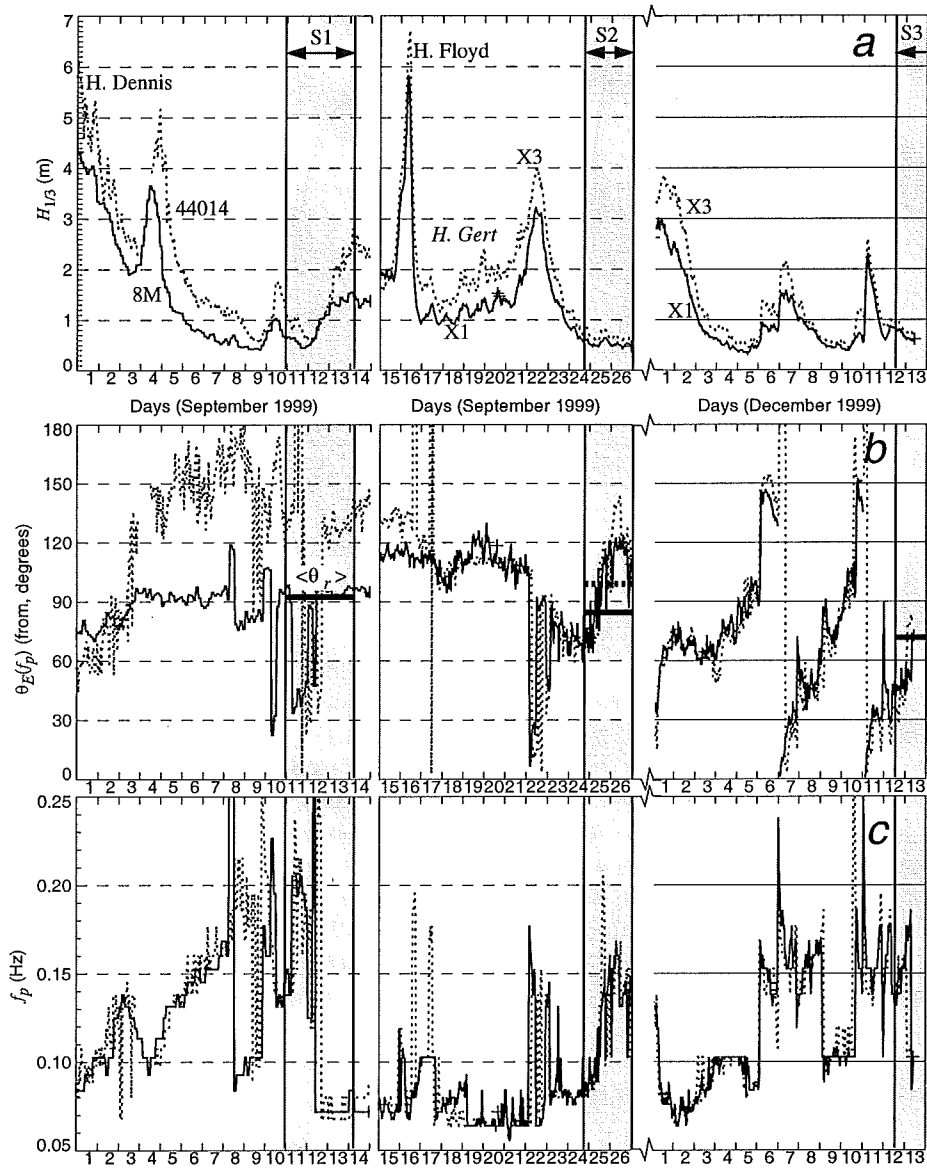


Figure 4.2: SHOWEX observed wave conditions and ripples

(a) Evolution of significant wave height $H_{1/3}$, (b) mean wave direction at the peak frequency $\theta_E(f_p)$, and (c) peak frequency f_p . Observations at buoys X1 (solid) and X3 (dotted) are shown, spanning the inner shelf. Before survey S1 (conducted during the buoy deployment cruise), data from 8M and 44014 are shown. During Hurricane Dennis $\theta_E(f_p)$ at X1 is estimated to be 0–10° larger than $\theta_E(f_p)$ measured at 8M, owing to refraction. For each survey the average of crest-normal ripple directions θ_r observed in the vicinity of X1 is indicated with a solid horizontal bar. The dashed bar indicates a more southerly average θ_r of ripples observed close to X3 during survey S2.

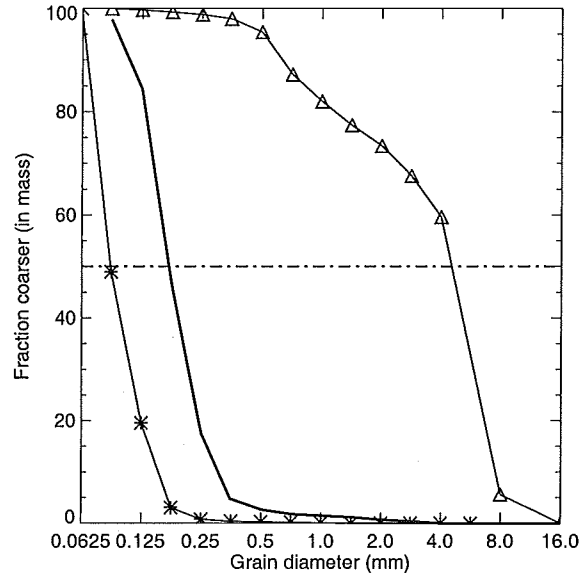


Figure 4.3: Example grain size distributions

A typical distribution (solid thick), and the distributions with the finest (asterisks) and coarsest (triangles) sediments are shown.

a series of northeasters. The same tracks were repeated again, and a few additional regions were surveyed (all ship survey tracks for S3 are shown in figure 4.1).

The dual frequency sonar (100 and 500 kHz), was towed 2–3 m above the bottom in the shallower regions and 10–15 m in regions deeper than 30 m, at a speed of about 2.3 m s^{-1} . The 100 kHz frequency was used throughout for larger area coverage, at the expense of poorer resolution. All back-scatter sonograms, covering a 100-m wide swath along a total track length of 420 km were both recorded in a digital format and printed on paper scrolls. In selected regions where ripples were clearly visible, the digital data was transformed into GEO-TIFF mosaics, fully corrected for slant range and speed, with a resolution of 5 or 10 pixels per meter. Surficial sediments were collected with a Shipek grab (46 samples), and by divers (5 samples), at locations indicated in figure 4.1.

B. Surficial sediments

The continental shelf between Cape Hatteras and the entrance to the Chesapeake Bay (Cape Henry) is believed to be covered by fine quartz sand (Milliman *et al.*, 1972; Swift and Sears, 1974), with occasional coarser sands and gravel in fluvial paleochannels flooded by Holocene sea-level rise (Swift *et al.*, 1972). The Albemarle river paleochannel coincides with the buoy transect (figure 4.1). Very fine sands with a silt and clay content of 10 to 26% are found between 8 and 18 m depth (Field *et al.*, 1979; Wright, 1993; Madsen *et al.*, 1993), their origin can be traced to old lagoonal deposits (Wright, 1995).

The samples gathered during the three cruises confirm this pattern. Most samples consisted of fine sand with a median diameter D_{50} of about 0.2 mm (figure 4.3). Samples occasionally contained shell hash, particularly around X1 (figure 4.1). Grain sizes at neighboring sample sites can be significantly different (figure 4.4a, suggesting strong variability of sediment properties on scales less than a few kilometers, in particular on the inner shelf between X1 and X2. For example, the finest sand ($D_{50} = 0.09 \text{ mm}$, asterisks in figure 4.3) was found offshore of the Field Research Facility pier

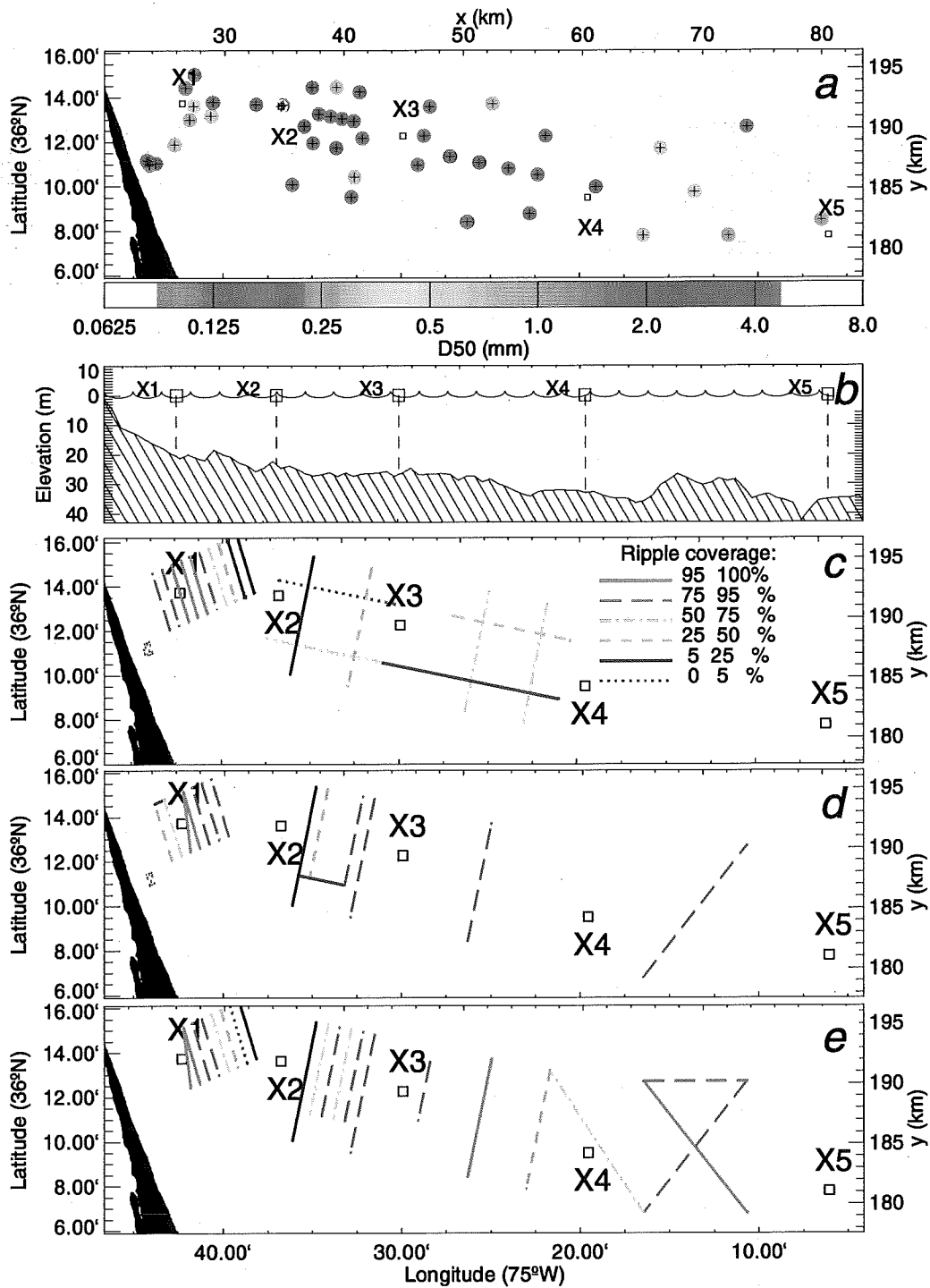


Figure 4.4: Spatial variations of D_{50} and ripple coverage
 (a) Geographical distribution of the median grain size D_{50} , (b) depth profile along the instrumented transect, and (c,d,e) fraction of sonar surveyed regions visibly covered by ripples for surveys S1, S2 and S3, respectively.

in 12 m depth, and the coarsest sample, a mixture of sand and small gravel with $D_{50} = 4$ mm (triangles in figure 4.3), was found in the vicinity of X1, in 19 m depth. All samples taken near X2 were fine-medium sand, except for one coarse sample collected by divers within 300 m of X2 that contained pebbles several centimeters in diameter.

The variability of sediment properties also is evident in the side-scan sonograms. For the range of grain sizes found in the samples, a stronger reflectivity (dark shades in the sonograms) usually corresponds to coarser sands. A large portion of the regions surveyed between X1 and X2 show alternating light and dark bands (the coarsest sand found in the samples came from one of these dark bands), a few hundred meters wide, with sharp transitions (e.g. figure 4.6a, discussed below). Offshore of X2 some dark bands are still present, although they contrast less with their lighter surroundings. This alternating pattern is similar to the one found by Green (1986) in a side-scan sonar survey conducted in 1984, 6 km south of X1. Green (1986) identified dark bands lying in the troughs between ridges oriented north-south (with approximate heights and spacings of 5 and 500 m, respectively) as the pre-Holocene 'basement' underlying the finer Holocene sand ridges. In the surveys presented here the dark regions also correspond to relatively low-lying areas, at least inshore of X3 where high-resolution multibeam sonar surveys were conducted in December 1999 (submitted manuscript).

C. Sidescan sonar images of bedforms

In addition to qualitative information on sediment grain sizes, the sidescan sonar images document the presence and characteristics of bedform patterns. A qualitative inspection of the entire sonar data set for the three surveys (figure 4.4c-e) reveals the predominance of long-crested ripples with wavelengths between 0.4 and 3 m, and crests approximately parallel to the coastline, consistent with the scales and orientation of vortex ripples formed by large low-frequency surface gravity waves propagating across the shelf. In cross-shore surveys ripple marks are generally faint or absent, probably because the alongshore orientation of the sonar beams (perpendicular to the ship track) was at a grazing angle relative to the ripple crests, usually oriented alongshore. Images from part of the surveys were blurred by excessive wave-induced towfish motion. In regions where ripples were not detected, the bottom may be smooth, as a result of the shallow nature of the sediment cover or some other unknown phenomenon, or the bottom may be covered with ripples that are too small to be resolved. For example at a site in 12 m depth high-resolution mapping instruments located on a bottom-mounted frame show the presence of short wavelength (10–20 cm) ripples (T. Stanton, Naval Postgraduate School, personal communication, 2000) in fine sediments ($D_{50} = 0.09$ mm, asterisks in figure 4.3) that were not resolved in the sidescan sonar surveys. The absence of ripples in alongshore ship tracks usually correspond to regions with finer surficial sediments. Assuming that vortex ripples, for which the wavelength scales with the near-bed wave orbital diameter, are formed by wave action during a storm and become relic when the near-bed velocity decreases, ripples generated on finer sand are 'frozen' later, when the waves are smaller, and thus are expected to have shorter wavelengths (i.e. not resolved by the sonar) than ripples in coarse sand. A quantitative analysis was performed for surveyed regions with clearly visible bedforms and relatively uniform bedform geometry and sound reflectivity. For each region a representative 100 m by 100 m image was processed. In some cases with faint ripples a smaller image with clear ripple crests was analyzed. Although spectral analysis is well suited to characterize regular ripples, bidimensional variance spectra computed from sonar images exhibit multiple peaks in many cases, either as the result of excessive sidescan towfish motions (along-track modulations of ripple patterns on the sonar images), or because of the presence of many defects in the ripple patterns. Therefore a different procedure was used that is less sensitive to ripple defects and image artifacts (figure 4.5). For each image, after subtracting a piecewise bilinear fit to the pixel values, we computed the zero-

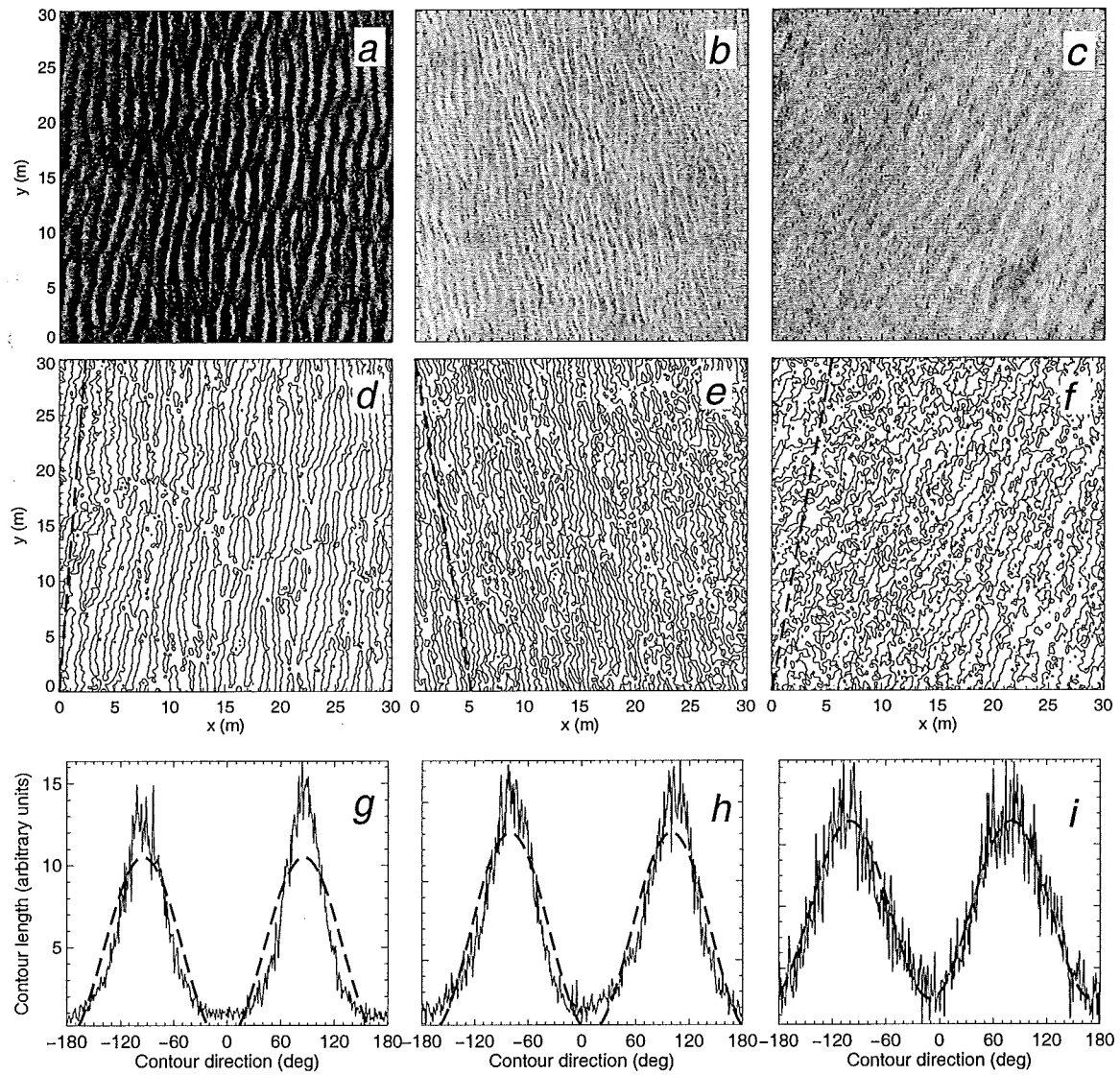


Figure 4.5: Extraction of ripple parameters from sidescan images
 (a, b, c) example images from the sites where samples 111, 114 and 207 were collected (see table 4.1),
 (d, e, f) corresponding zero-crossing contours with an indication of the mean crest orientation θ_c
 (thick dashed line), and (g,h,i), histogram of contour direction with fitted cosine distribution (thick
 dashed line).

crossing contours of the image intensity, and formed a histogram of the contour length as a function of its orientation, at one degree intervals, using the trigonometric (right-handed) convention.

A function $p(\theta) = a_0 + a_2 \cos[2(\theta - \theta_c)]$ was fitted to this histogram in a least-squares sense, and θ_c was interpreted as the mean orientation of the ripple crests. The ratio a_2/a_0 gives an indication of the presence, long-crestedness, and regularity of ripples. For high contrast ripples with long crests and few pattern defects $a_2/a_0 > 1$ (e.g. figure 4.5a,b). For faint ripples or ripples with short or brick-patterned crests $a_2/a_0 < 0.5$. An example of marginally detectable and non-uniform ripples, with $a_2/a_0 = 0.8$, is shown in figure 4.5c. Once θ_c was determined, standard one-dimensional Fourier spectra were computed for east-west image lines (usually within 30° of the crest-normal direction). The spectra were then averaged over all lines, and the peak wavenumber k_p was determined. The average wavelength of the ripples λ was then taken to be $2\pi \sin \theta_c / k_p$, and the crest-normal direction, using the (left-handed) nautical convention, was given by $\theta_r = 180(1 - \theta_c/\pi)$. In cases with $a_2/a_0 < 0.4$, this procedure failed to determine θ_r and λ unambiguously, and the bed was presumed featureless.

In most images with visible ripples the dominant bedforms are regular long-crested ripples with an apparently sinusoidal profile (figure 4.5). Spatial variations observed in the backscatter sonar intensity and ripple patterns are the result of non-uniformities in sediment properties (e.g. variations in grain size (figure 4.6a) or small-scale (unresolved) ripples or both). A few regions reveal intricate bedform patterns with second harmonic ripples (figure 4.6b) that may be the result of decreasing wave forcing conditions. Earlier observations and numerical modeling studies have shown that when the mean wave direction is constant, ripple wavelengths gradually increase with increasing wave orbital diameter $d_{1/3}$, but the converse is not true: when $d_{1/3}$ decreases the ripple wavelengths typically remain unchanged. For decreasing $d_{1/3}$, if the Shields number threshold for sediment motion is still exceeded, secondary ripple crests may appear in the troughs, reducing the wavelength by half (Forel, 1894; Traykovski *et al.*, 1999; Andersen, 1999). Other ripple patterns include superpositions of two ripple systems (e.g. figure 4.6c,d) similar to previous observations (e.g. Forel, 1894; Swift *et al.*, 1972). As discussed below, these patterns are likely caused by successive wave events with different wave directions. The wavelengths in some of these ripple systems can be as large as 4 m, of the order of the wavelengths of long-crested features observed in this region and called ‘megaripples’ by Green (1986). The variety of observed bedform patterns underscores the important effects of past bedform evolution on their present state in the relatively mild forcing conditions prevalent during these surveys.

Temporal changes in ripple direction θ_r and wavelength λ are examined in figure 4.7 using repeated survey track lines close to X1. All surveys reveal widespread ripple coverage with typical wavelengths λ of 0.5–2 m, and ripple crest-normal directions θ_r between 60° and 120° (shore-normal is 70°). Changes observed between surveys S1 and S2 (figure 4.7a,b) are small, with a slight shift of the average value of θ_r from 91° to 85° . A larger change in ripple orientation is observed in S3 with an average θ_r of 73° (figure 4.7c).

This observed change in bedforms is related to a change in wave conditions, from hurricane-generated waves from east to south-east propagation directions in September, to northeasterly waves in December. The average values of θ_r in surveys S1, S2 and S3 (indicated by thick horizontal bars in figure 4.2) correspond to the wave directions of preceding large wave events on September 4–5 (Hurricane Dennis), September (22–23) (Hurricane Gert), and December 1–2 (northeaster), suggesting that the observed ripples were formed in these periods. The large oblique ripples observed in S2 ($\lambda = 2.0$ m, $\theta_r = 105^\circ$) and S3 ($\lambda = 2.0$ m, $\theta_r = 132^\circ$) close to the northern end of the surveyed region are notable exceptions. The corresponding sidescan image of the anomalous ripples in S2, shown in figure 4.6c, indicates that the estimated λ and θ_r are averages of two superposed ripple systems: $\lambda = 2.0$ m, $\theta_r = 120^\circ$, probably generated during the passage of Hurricane Floyd, and $\lambda = 0.8$ m, $\theta_r = 85^\circ$ probably generated during the arrival of swell from Hurricane Gert. Within 200 m of these ripples, a similar but smaller patch of large ripples was observed in survey S3 (figure 4.7c) with a more oblique angle $\theta_r = 132^\circ$ that does not match the wave directions of any energetic

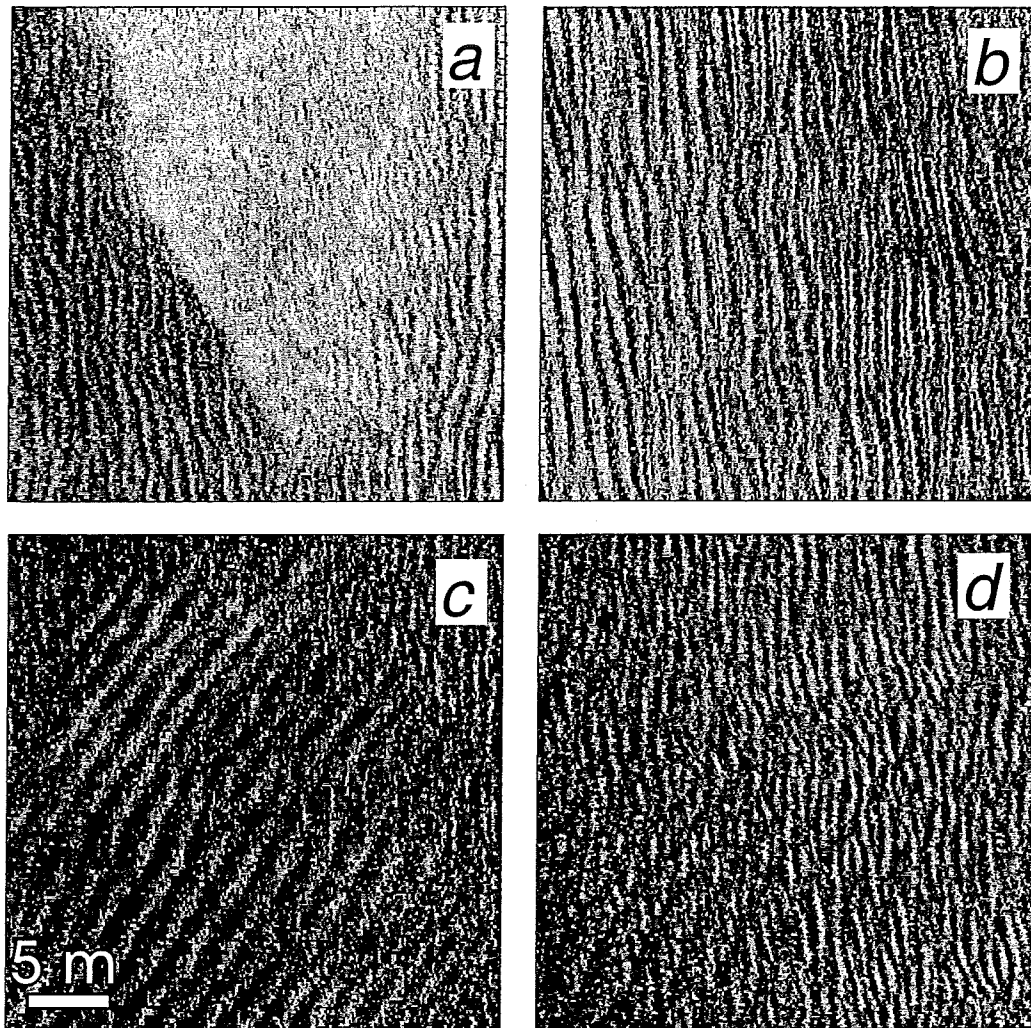


Figure 4.6: Examples of unusual ripple patterns
(a) sharp transition in sediment properties, (b) second harmonic ripples, and (c and d) superposition of ripple patterns (see text).

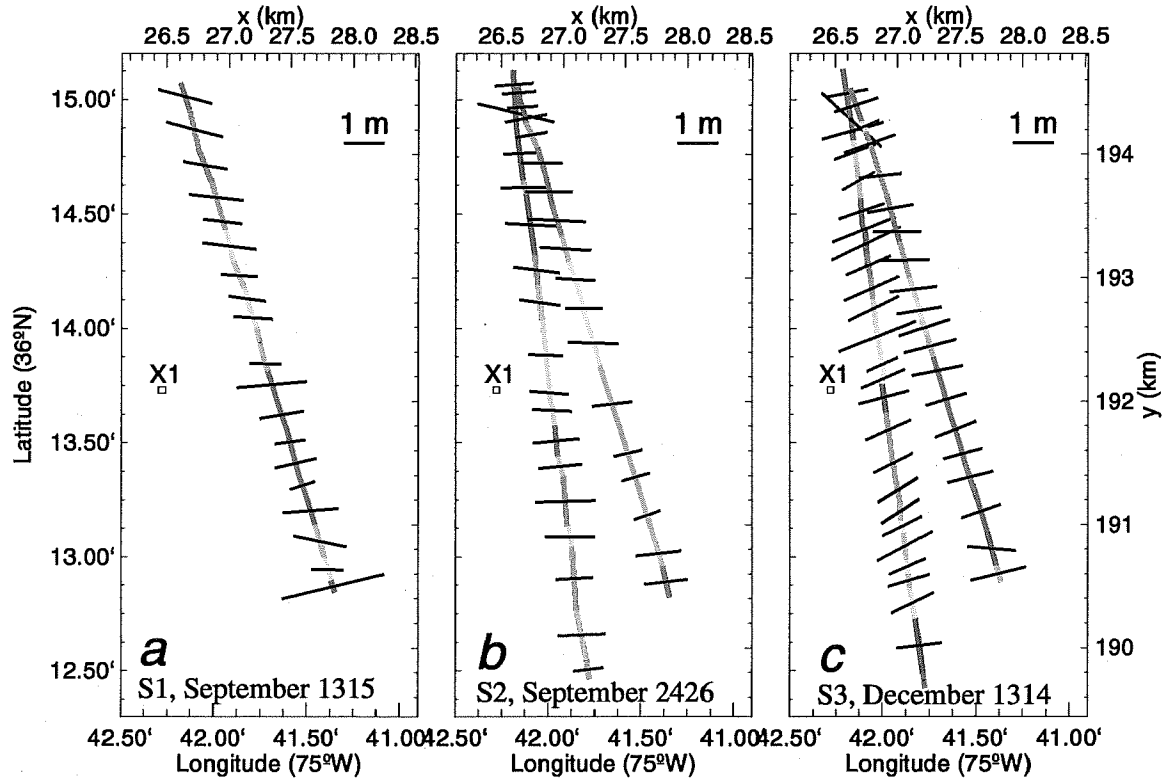


Figure 4.7: Time evolution of ripple directions and wavelengths (a) for survey S1, (b) S2, and (c) S3. The thick bars indicate the crest-normal ripple direction θ_r and the ripple wavelength λ with a scale given in the upper right corner of each panel. Each bar is drawn in the middle of the survey segment for which the ripple parameters are representative. The colors along the survey line indicate the average back-scatter strength of the sidescan sonar images: red is strong (generally coarse sand) and blue is weak (generally very fine sand). Surveyed regions without a bar indicate the absence of ripples or a failure of the analysis procedure to determine θ_r and λ .

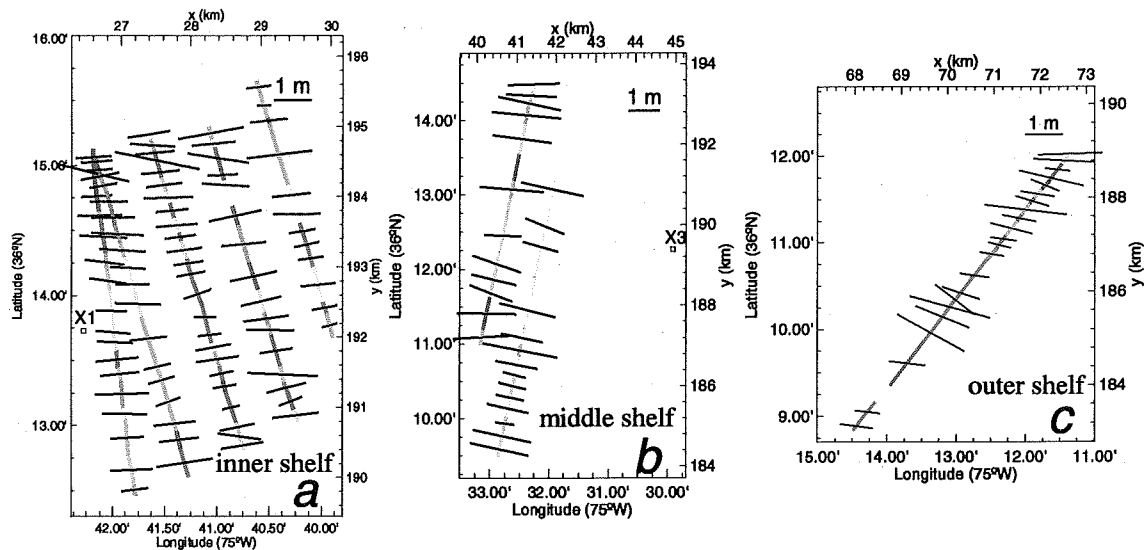


Figure 4.8: Cross-shelf distribution of ripple directions and wavelengths Same as figure 4.7, for survey S2 only, at different locations across the shelf.

wave event observed during the three months between surveys S2 and S3 that would be capable of moving bottom sediments in that region, suggesting that these ripples also were formed during Floyd and persisted throughout the experiment.

Spatial variations in θ_r and λ across the shelf during survey S2 are shown in figure 4.8. Observations on the middle and outer shelf show more southerly θ_r angles than observations on the inner shelf (figures 4.8b,c and 4.8a). Some spatial variation of ripple directions is expected associated with the refraction of the swell that probably generated the bedforms. However, observed differences in wave direction θ_E between X3 and X1 are small compared with the 15° difference between the average θ_r around X3 and X1. Temporal changes of the wave forcing conditions also may have contributed to the θ_r variations. In deeper regions where the wave motion is more attenuated over the water column, ripples may have become relic at an earlier stage when the swell was more energetic and arrived from a more southerly angle (figure 4.2a,b). Indeed the average θ_r values of 100° and 85° near X3 and X1, respectively (dashed and solid horizontal bars in figure 4.2b), are close to mean wave directions on September 22 and 23, respectively. Large variations of θ_r and λ also are observed over much shorter distances, with estimates varying by as much as 30° and a factor 2, respectively, within 1 km. These differences are caused primarily by the superposition of ripple patterns (figures 4.8b and 4.8c), some of which are barely resolved in our images. The relation between observed ripple geometry and changing wave forcing conditions is analyzed in the next section.

D. Evaluation of ripple parameterizations

Bedforms observed in the sonar images usually are not related to the instantaneous wave forcing (surveys were performed in relatively calm conditions), but are the result of earlier wave events that were sufficiently energetic to move the sediments. Here, the ripple properties observed in surveys S2 and S3 are compared with the wave forcing history estimated at the nearest buoy. Neglecting variations in the wave forcing conditions over the 1–5 km distance separating the locations of the wave and ripple measurements, we computed a ‘significant’ Shields number $\psi_{1/3}$ from (1.4), using a range of D_{50} values for the grain size, and $u_{1/3}$ defined as two times the root-mean-square

velocity near the sea bed, determined from the surface elevation frequency spectrum with linear wave theory. The skin friction factor f_w' was obtained with Grant and Madsen's (1979, 1982) parameterization, based on a linear profile of the eddy viscosity (see also the review by Tolman, 1994). We assumed a threshold of ripple formation $\psi_{1/3} = \psi_c$ (Traykovski *et al.*, 1999), where ψ_c is the threshold of sediment motion under sinusoidal waves. Madsen and Grant (1976) give a review of values of ψ_c determined experimentally for well-sorted sand. Here we use a piece-wise fit to the experimental data of Wallbridge *et al.* (1999) for mixed sands under combined wave-current flow, that we apply to the median grain size,

$$\psi_c = 0.1 \exp[(S_* - 2) \ln(0.35)/10] \quad \text{for } 2 < S_* < 12, \quad (4.2)$$

$$S_* = D_{50} [(s - 1)gD_{50}]^{1/2} / (4\nu), \quad (4.3)$$

where ν is the kinematic viscosity of water. These values of ψ_c are slightly larger than those given by Shields (1936) or Soulsby and Whitehouse (1997) for unidirectional and combined wave-current flows (about 30 % larger in the range $3 < S_* < 12$), but follow the same trend, decreasing with increasing grain size. Based on these assumptions, all but the coarsest surficial sediments have moved on 22 September, and during the 1–2 December northeaster, after which ripples became relic and remained unchanged until surveys S2 and S3, respectively (figure 4.9a).

The interpretation of survey S2 is complicated by cross seas observed on September 22 (when the wave height was maximum). Different definitions of a representative wave forcing direction yield different ripple predictions depending on the relative importance they give to motions with higher and lower frequencies. Here the bulk mean directions of the near-bed orbital velocity θ_u and displacement θ_d are defined as the directions of the first spectral moment vectors are defined as

$$(a_u, b_u) = \int \frac{2\pi f}{\sinh^2(kH)} \int_0^{2\pi} (\cos \theta, \sin \theta) E(f, \theta) d\theta df, \quad (4.4)$$

$$(a_d, b_d) = \int \frac{1}{\sinh^2(kH)} \int_0^{2\pi} (\cos \theta, \sin \theta) E(f, \theta) d\theta df, \quad (4.5)$$

where the angle θ is defined with the nautical convention. The superposition of a local wind sea traveling at right angles to swell from Hurricane Gert caused θ_u to veer to the north from 85° to 50° and then back to the east, whereas θ_d shifted gradually from 95° to 70° (figure 4.9b). Although the high frequency seas contributed significantly to the near-bed velocity variance and Shields number $\psi_{1/3}$ (equal contributions from the 0.05–0.11 and 0.11–0.25 Hz frequency ranges when $\psi_{1/3}$ is maximum), the orbital displacement direction θ_d remained aligned with the lower frequency swell. Observed ripple crest-normal directions θ_r are closer to θ_d than θ_u at possible freezing times ($\psi_{1/3} \simeq \psi_c$, figure 4.9a). These observations suggest that the mean direction of the orbital displacement θ_d , which is less influenced by high frequency (wind sea) motion, may describe better the relation between wave direction and ripple orientation (figure 4.9b). The $\psi_{1/3} = \psi_c$ ripple freezing threshold yields values of θ_d that are still $5\text{--}10^\circ$ to the south of θ_r . Several factors may contribute to this difference: a reorientation of the ripple pattern may require a larger forcing ($\psi_{1/3}$) than the initiation of sediment motion (ψ_c) (Werner & Kocurek, 1997), the time of adjustment of the bedforms in conditions close to the threshold may be larger than the time scale of the wave height decrease, θ_r may not be simply related to θ_d , or the values of ψ_c are not well predicted by (4.2)–(4.3). Such 'early freezing' of ripples in conditions of decreasing forcing also was observed by Traykovski *et al.* (1999) with frozen bedform patterns occurring for $\psi_{1/3}$ as large as $2\psi_c$. Although the exact threshold for the cessation of ripples evolution is uncertain, the wavelength λ are generally close to $0.7d_{1/3}$ when $\psi_c < \psi_{1/3} < 3\psi_c$ for representative grain sizes (figure 4.9a,c), suggesting that the observed ripples are probably of the 'vortex ripple' type, similar to those observed by Traykovski *et al.* (1999).

Analysis of bedforms at sites that coincide with the location of sediment samples shows that the ratio λ/D_{50} varies from 300 to 8100 (table 4.1), extending the range of previously observed

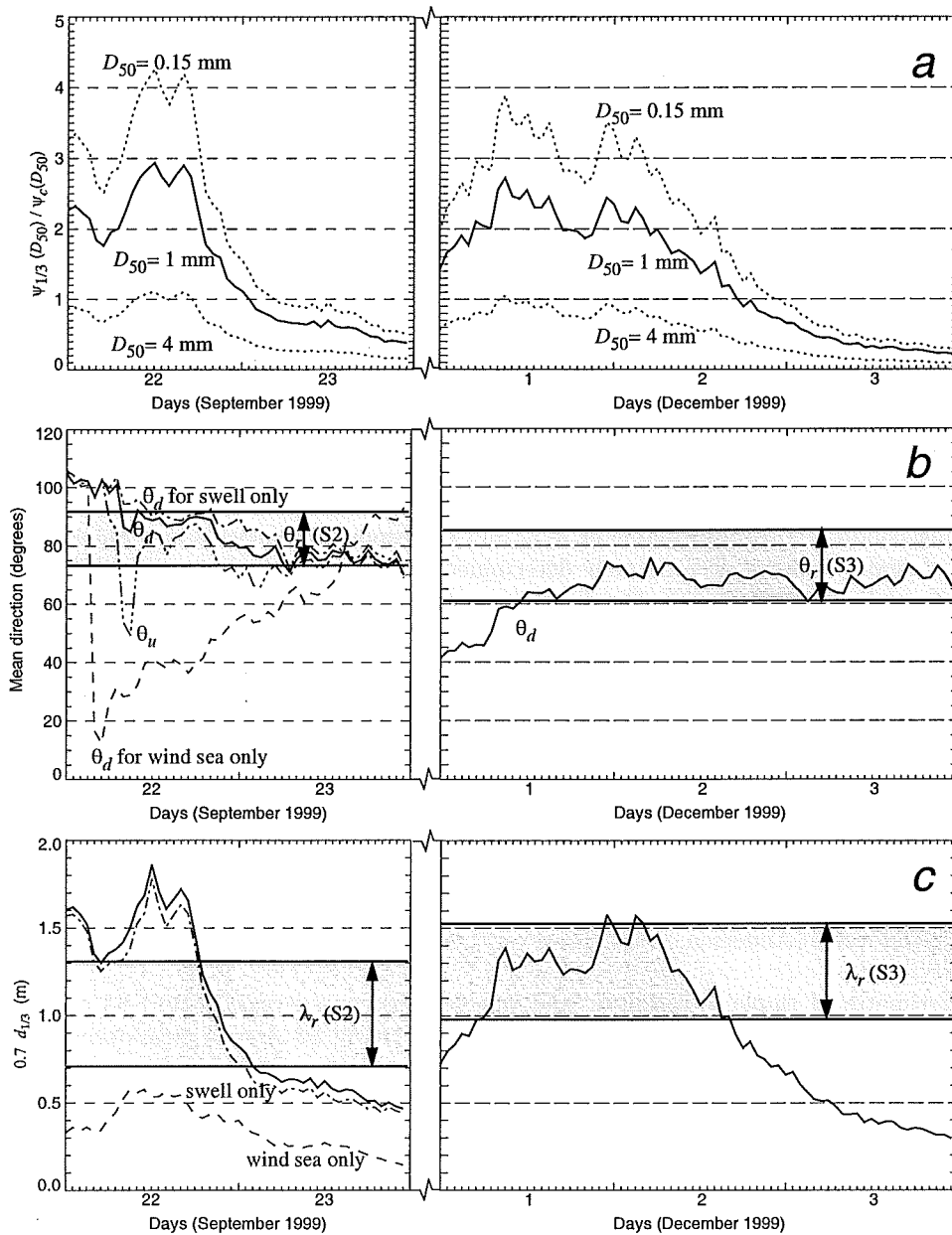


Figure 4.9: Wave forcing conditions during ripple formation

(a) $\psi_{1/3}/\psi_c$ computed at X1 using the full wave spectrum and various values of the median grain size D_{50} . (b) Corresponding values of the mean direction of the orbital displacements at the top of the wave bottom boundary layer θ_d . For the complex September 22–23 wave conditions the mean direction of the near-bed orbital velocity θ_u is also indicated, as well as θ_d estimates for swell (0.05–0.11 Hz) and wind sea (0.11–0.25 Hz) only. (c) Corresponding values of predicted ripple wavelength $0.7d_{1/3}$ for vortex ripples, where $d_{1/3}$ is the significant diameter of the orbital displacement at the top of the wave bottom boundary layer. The gray band in (b,c) represent the mean value of the crest-normal ripple direction θ_r and wavelength λ_r , respectively, plus or minus one standard deviation, observed in the vicinity of X1 (figure 4.7b,c).

Sample number	111	110	114	11	207	212	206	205
Nearest buoy	X1	X1	X1	X1	X3	X3	X3	X3
Depth (m)	22.3	19.7	20.7	21.2	22.7	27.6	26.3	27.4
D_{50} (mm)	4.71	0.98	0.32	0.15	0.28	0.19	0.17	0.15
D_{85} (mm)	7.30	2.29	0.48	0.28	0.68	0.28	0.25	0.24
θ_r	94°	85°	80°	88°	101°	99°	n.a.	n.a.
λ (m)	1.25	1.20	0.77	1.22	1.30	1.37	n.a.	n.a.
$d_{1/3}$ (m)	2.55	1.85	1.34	1.60	2.73	2.34	n.a.	n.a.
$u_{1/3}$ (m s ⁻¹)	0.58	0.48	0.37	0.42	0.67	0.55	n.a.	n.a.
$\psi_{1/3}/\psi_c$	0.90	2.00	1.33	3.54	3.4	3.0	n.a.	n.a.
$w_s/u_{1/3}$	0.50	0.25	0.10	0.03	0.08	0.04	n.a.	n.a.
$\lambda/d_{1/3}$	0.49	0.65	0.58	0.76	0.48	0.59	n.a.	n.a.
$d_{1/3}/D_{50}$	540	1900	4200	10700	9800	12300	n.a.	n.a.
λ/D_{50}	270	1200	2400	8133	4600	7200	n.a.	n.a.

Table 4.1: Ripples at sites of sediment sample collection

The forcing conditions (orbital diameter $d_{1/3}$ and corresponding velocity and Shields number) at the time of ripple ‘freezing’ were crudely determined by matching the bottom orbital displacement direction θ_d at the nearest buoy to the direction normal to the ripple crests θ_r (see text).

values (Wiberg & Harris, 1994), in particular for vortex ripples. Crude estimates of active ripple forcing conditions can be obtained from the preceding wave records by determining the most recent time when ripples and wave crests were aligned ($|\theta_d - \theta_r| < 5^\circ$), while surficial sediments were still in motion (assuming $\psi_{1/3} > 0.8\psi_c$). This analysis gives values of $\psi_{1/3}/\psi_c$ between 0.9 and 3.5, and values of $\lambda/d_{1/3}$ from 0.5 to 0.76 (table 4.1). Although these estimates have a large uncertainty and should be considered with caution, they are consistent with accurate measurements by Traykovski *et al.* (1999) who observed that λ is close to $0.76d_{1/3}$ under moderate forcing conditions. These estimates are also qualitatively consistent with the values of λ/d predicted in numerical simulations with sinusoidal waves (Andersen, 1999). However there is no clear increase of λ/d with the normalized fall velocity w_s/u .

Estimates of ripple direction θ_r and wavelength λ in surveys S2 and S3 are summarized in figure 4.10 for the region around X1. The observations in S2 show a clear trend of increasing wavelength corresponding to more southerly angles (figure 4.10a). This trend is consistent with the freezing of the largest ripples shortly after the peak of the event (September 22), and a later freezing in finer sediments where the ripple patterns gradually adjusted to the more northerly angles, and small orbital diameters of the waves observed on September 23. Observations in S3 (figure 4.10b) do not indicate a clear relation between θ_r and λ , possibly because the wave direction remained steady when the storm subsided on December 2. However, with the exception of apparent ‘Floyd survivors’ ($\theta_r = 132^\circ$, $\lambda = 2$ m), the longer ripples ($\lambda > 1.5$ m) in S3 consistently have crest-normal directions at large northerly angles ($60^\circ < \theta_r < 75^\circ$), suggesting they became relic on December 1 and early December 2 when wave directions were similar, and the orbital diameter $d_{1/3}$ was maximum.

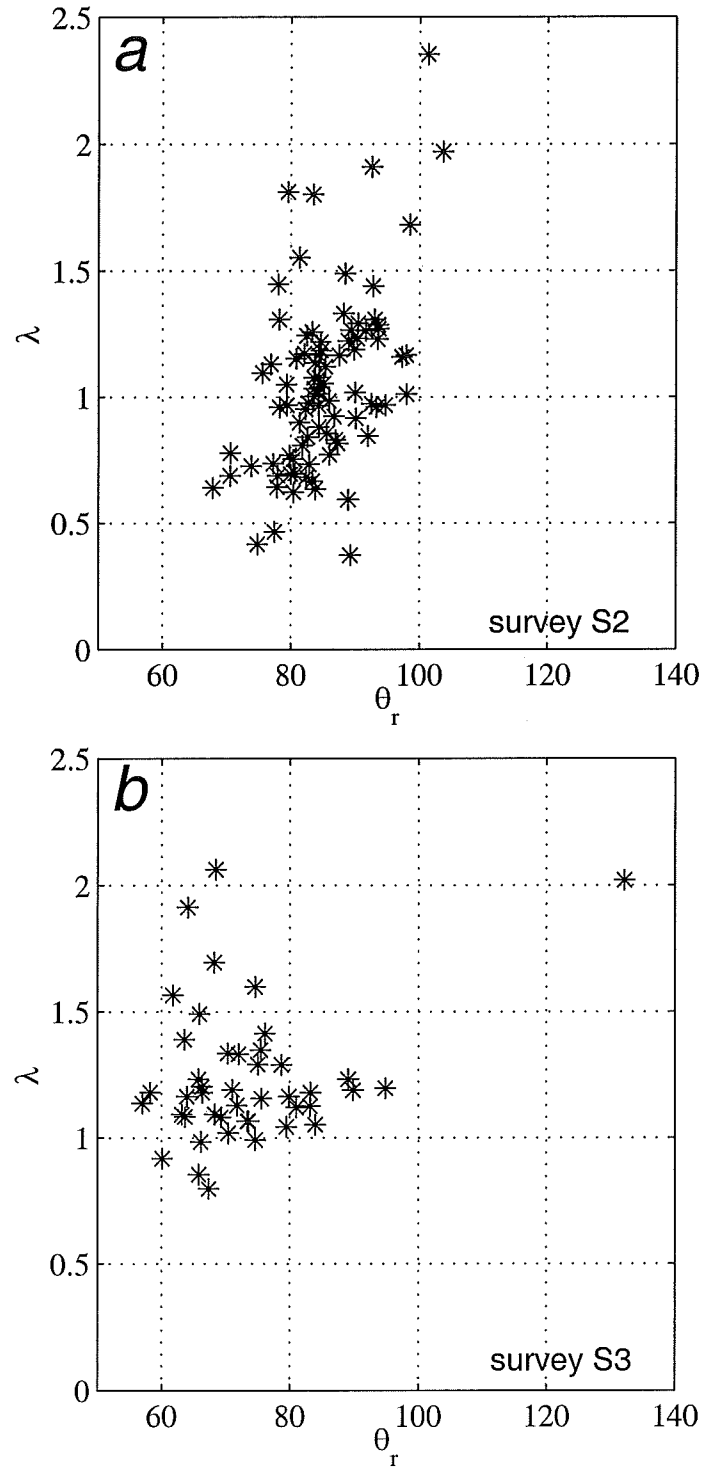


Figure 4.10: Ripple wavelength λ versus crest-normal ripple direction θ_r . λ versus θ_r for ripples observed on the inner shelf in (a) survey S2 (figure 4.7b), and (b) survey S3 (figure 4.7c).

E. Summary and discussion

Widespread formation and evolution of sand ripples on the North Carolina continental shelf, observed in side-scan sonar surveys, were examined in relation to time-series of directional wave measurements. Sediment samples confirm the ubiquitous presence of very fine to fine quartz-dominated sand, with significant variability in the grain sizes over distances less than 1 km, in particular in regions shallower than 25 m. Side-scan sonar surveys reveal the presence of ripples in most surveyed areas, with wavelengths between 0.5 and 3 m, and crest-normal directions within 30 degrees of the west-east axis. The apparent absence of any bedforms in some regions with finer sediments may be caused by their close spacing (less than 40 cm) not resolved by the sonar images.

The ripple crest-normal directions θ_r are aligned approximately with the direction of the near-bed orbital displacement θ_d when the ripples became relic. Although the precise time of cessation of sediment motion is uncertain, estimated ripple wavelengths λ and forcing conditions (the orbital diameter $d_{1/3}$) are consistent with previous observations of vortex ripples ($\lambda/d_{1/3} \simeq 0.5-0.76$), even for large values of $d_{1/3}/D_{50}$ and λ/D_{50} .

The present observations extend the range of previous field observations of vortex ripples (e.g. Traykovski *et al.*, 1999) to larger adimensional orbital diameters $d_{1/3}/D_{50}$, but equally moderate Shields numbers $1 < \psi_{1/3}/\psi_c < 3$, for which similar vortex ripples ($\lambda/d \approx 0.8$ with λ/D_{50} up to 2×10^4) have been observed in the laboratory (Southard *et al.*, 1990). Both the present observations and these earlier laboratory and field studies do not support parameterizations of the ripples based on the grain size only (e.g. Wiberg & Harris, 1994), but rather support a need for more complete parameterization of the physical processes responsible for ripple formation, including a dependence of ripples characteristics on the Shields number and possibly the sediment fall velocity (e.g. Nielsen, 1981; Andersen & Fredsøe, 1999).

The widespread presence of vortex ripples on the continental shelf lends support for a dominant role of these rough bedforms in the strong attenuation of swells observed in this and other coastal experiments, during periods of moderate to strong wave forcing conditions (Hasselmann *et al.*, 1973; Young and Gorman, 1995; Herbers *et al.*, 2000), when ripples should be generated (Ardhuin *et al.*, 2001).

V. VALIDATION OF THE ENERGY BALANCE EQUATION

A. Introduction

As described in chapter I many processes affect the evolution of gravity waves propagating at the surface of oceans, marginal seas or lakes, particularly in shallow water. Winds directly force the high frequency ('wind sea') part of the wave spectrum, actively generating waves with phase speeds slower than the wind speed, and a large fraction of this energy input is immediately lost through wave breaking (whitecaps). The low-frequency ('swell') part, with larger phase speeds, is influenced by local winds indirectly through nonlinear wave-wave interactions. In water shallower than the surface wavelength additional wave-bottom interactions become important. As local winds dominate the wave climate in marginal seas such as the North Sea, investigations of the spectral energy balance of waves often have to deal with the full complexity of air-sea-bottom interactions (e.g. Bouws and Komen, 1983; Weber, 1988; Johnson and Kofoed-Hansen, 2000). However, outside the surf zone and in the absence of a wind-sea or strong currents, the steepness of swell is generally too small to induce wave breaking, and the propagation distances across continental shelves are typically too short for significant nonlinear transfers of energy in the spectrum. Hence swell transformation across the shelf is a much simpler problem controlled primarily by wave-bottom interactions, and thus more tractable. Nevertheless, few studies of swell evolution in shallow water have been presented (e.g. Hasselmann *et al.*, 1973; Young and Gorman, 1995; Herbers *et al.*, 2000; chapter II).

Swell is modified by a wide range of bottom topography and roughness scales, from the large scales (1–10 km) causing refraction and shoaling, and intermediate scales responsible for wave-bottom Bragg scattering, to small scales (0.1–10 m) enhancing the bottom roughness and wave energy dissipation, (figure 1.2). In earlier chapters a process-based approach was used to estimate the dissipation of wave energy across the shelf (chapter II), related to the widely observed formation of sand ripples under waves (chapter IV), and to evaluate numerically the directional diffusion of waves, predicted by Bragg scattering theory for random waves and irregular topography (chapter III). Here we propose to combine these processes in general swell cases, and test the closure of the spectral energy balance of swell with hindcasts of all swell-dominated periods observed during the experiments DUCK94 and SHOWEX. A comprehensive statistical analysis of the results is presented to evaluate different source term formulations. This work will hopefully lead to more accurate operational swell forecasts on open ocean coastlines, and is a first step towards closing the energy balance in more complex cases with wind forcing. An expanded version of the present chapter will be submitted as a two-part paper to the *Journal of Physical Oceanography* (co-authors: T. H. C. Herbers, P. F. Jessen, and W. C. O'Reilly).

We propose to test the following energy balance equation for the evolution of swell spectra

$$\frac{dE(\mathbf{k})}{dt} = S_{\text{fric}}(\mathbf{k}) + S_{\text{Bragg}}(\mathbf{k}), \quad (5.1)$$

where E is the wave energy spectral density, S_{fric} and S_{Bragg} are source terms representing bottom friction and wave-bottom Bragg scattering (3.48). Equation (5.1) incorporates the combined effects of all the scales of the bottom topography on a random wave field. The Lagrangian time derivative on the left hand side follows a wave component along its ray trajectory predicted by linear refraction theory (e.g. Mei, 1989). For $S_{\text{fric}} = 0$ energy is conserved and (5.1) is identical to (3.47) derived in chapter III from the equations of motion assuming irrotational flow. S_{fric} , based on Tolman's (1994) movable bed parameterization of wave-bedform coupling over a sandy bottom, is introduced heuristically in the energy balance as a sink term. A formal derivation of (5.1) with bottom friction may be performed by adding a rotational motion, following the approach of Weber (1991), to the

irrotational flow determined in §III.A, but other source terms may arise as the result of the coupling of the rotational and irrotational flows. The bottom friction source term used here is further simplified by assuming a narrow wave spectrum (see for example Weber, 1991; Madsen, 1994).

We integrate (5.1) in time from deep water to the shore with the Coupled Rays with Eulerian Source Terms (CREST) wave model (chapter II), and the results are compared to wave measurements acquired during DUCK94 and SHOWEX on the North Carolina continental shelf. The wave data collected during the experiments, and the reduction of the data set to swell cases are described in §V.B, while the model set-up is detailed in §V.C. The results of hindcasts are given in §V.D, in the form of a statistical analysis of all observed swell events, followed by a discussion and summary in §V.E, where practical advice is given for swell forecasting in shallow areas.

B. Swell observations during DUCK94 and SHOWEX

1. Instruments and data analysis

During the DUCK94 (August–December 1994) and SHOWEX (September–December 1999) experiments extensive wave measurements were collected across the wide shelf of the Mid-Atlantic Bight, in the region between Cape Hatteras and the entrance to the Chesapeake Bay (figure 5.1). Bottom mounted pressure sensors were used during DUCK94 (Herbers et al., 2000; chapter II), and replaced by surface-following Datawell Directional Waverider buoys in SHOWEX. For the periods covered by both experiments wave data is also available from National Data Buoy Center (NDBC) 3-m pitch and roll discus buoy number 44014, in 49 m depth, and a coherent array of bottom pressure sensors and a Waverider buoy, in 8 and 15 m depth respectively, both maintained by the US Army Corps of Engineers Field Research Facility (FRF), in Duck, North Carolina. In addition to these instruments, the Diamond Shoals (DSL7) and Chesapeake Lighthouse (CHLV2) C-MAN stations, operated by NDBC, were equipped with infrared laser wave gauges at the time of SHOWEX. The locations of the instruments are indicated in figure 5.1, and their basic characteristics are summarized in table 5.1.

The dataset includes both directional (buoys and coherent pressure array) and non-directional (single pressure, buoy, and laser gauges) measurements. Although some instruments are ideally equivalent (e.g. directional Waveriders and 3 m discus buoys), different sampling frequencies, record lengths, and response characteristics, introduce some variations in quality. The model-data comparisons presented in §V.D are restricted to bulk spectral moments (significant wave height, H_s , mean direction and directional spread at the spectral peak, θ_p and $\sigma_{\theta,p}$) that can be reliably estimated from the short records of routine wave measurement systems. These parameters are determined from the wave frequency spectra $E(f)$, and the standard lowest order Fourier moments of the directional spectrum $a_1(f)$, $b_1(f)$, $a_2(f)$, and $b_2(f)$, computed for all directional instruments. For the high-resolution 8M array the full frequency-directional spectra $E(f, \theta)$ were estimated and offshore propagating waves were excluded from the directional moments. $E(f, \theta)$ spectra also were estimated from the directional moments at X6 and/or 44014 using the Maximum Entropy Method (Lygre & Krogstad, 1986), in order to initialize the model at the offshore boundary. All spectra and directional parameters were interpolated on a common frequency grid, also shared by the numerical model CREST in the hindcasts described below. These parameters were averaged over 2–3 hour periods for the DUCK94 experiment (variable length data records were collected every 3 hours), and 1 hour periods for SHOWEX (continuous data collection). The statistical parameters computed below from observations and model results are weighted accordingly, on an record length basis.

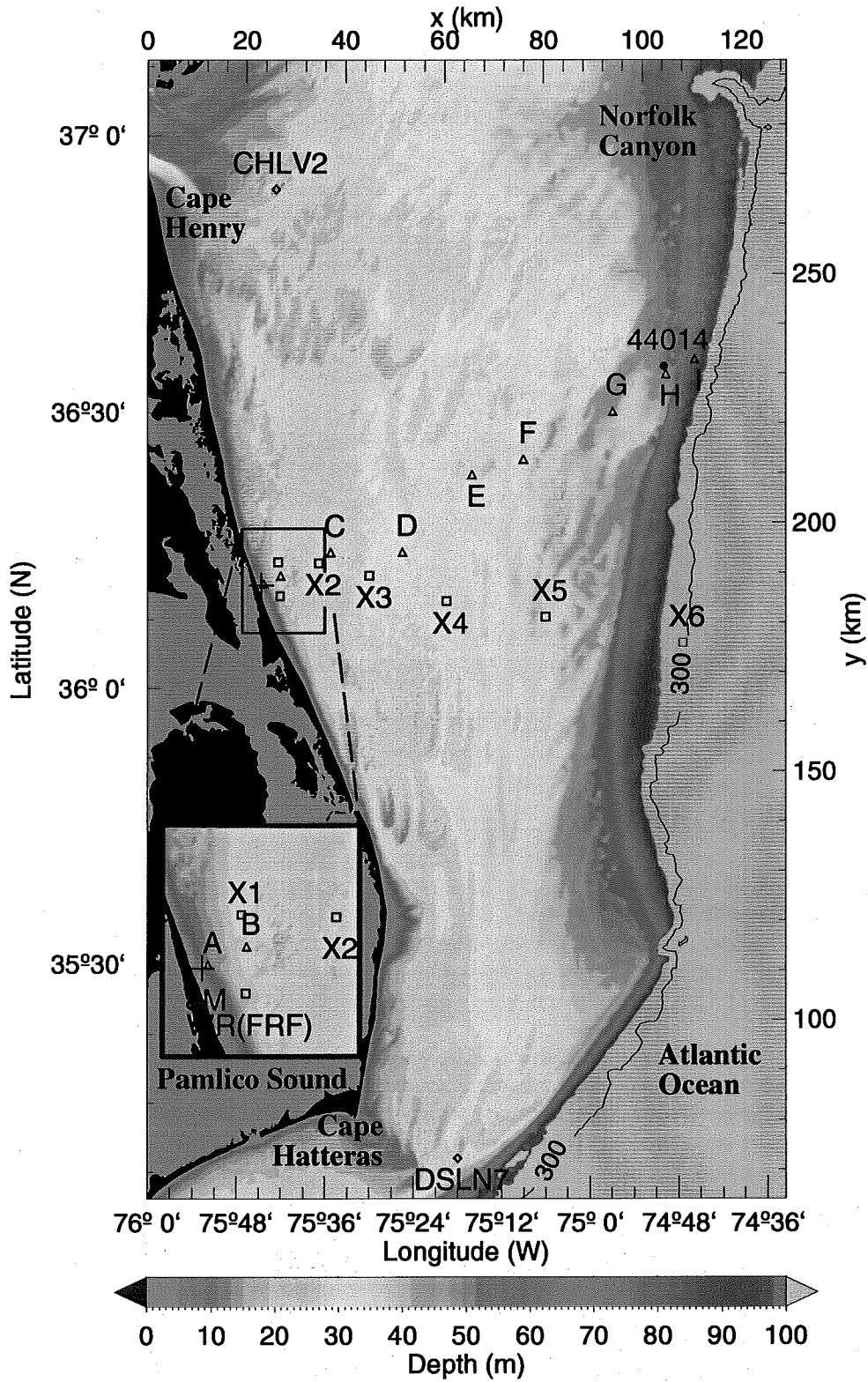


Figure 5.1: Bathymetry and instrument locations during DUCK94 and SHOWEX. (see text and table 5.1 for instrument description)

Name	water depth	directional	data availability	Operated by
8M	8.0 m	yes	02/1987 – present	FRF
WR(FRF)	17.0 m	no	10/80 – 11/96	FRF
WR(FRF)	17.0 m	yes	11/96 – present	FRF
44014	49 m	yes	10/90 – present	NDBC
CHLV2	15 m	no	9/84 – present	NDBC
DSLN7	18 m	no	11/88 – present	NDBC
A	12 m	no	DUCK94 until 17/11/94	NPS
B	21 m	no	DUCK94 until 17/11/94	NPS
C	26 m	no	DUCK94	NPS
D	34 m	no	DUCK94	NPS
E	35 m	no	DUCK94	NPS
F	33 m	no	DUCK94	NPS
G	46 m	no	DUCK94	NPS
H	49 m	no	DUCK94	NPS
I	87 m	no	DUCK94	NPS
X1	21 m	yes	SHOWEX	NPS
X2	24 m	yes	SHOWEX	NPS
X3	26 m	yes	SHOWEX	NPS
X4	33 m	yes	SHOWEX	NPS
X5	39 m	yes	SHOWEX	NPS
X6	193 m	yes	SHOWEX	NPS

Table 5.1: Wave-measuring instruments during DUCK94 and SHOWEX. DUCK94 covers 1/8/1994 – 30/11/1994, and SHOWEX spans 13/9/1999 – 13/12/1999. Occasional instrument failure or maintenance causing loss of data is not indicated

2. Wave conditions

The dominant wave events in the mid-Atlantic bight are generally the result of tropical storms and hurricanes in the summer–early fall, that follow a curved path to the northwest along the coast, or Northeaster storms that develop over North America and move offshore into the North Atlantic. 1994 was a moderate hurricane season, with only one major hurricane (Gordon, 15-19 November, figure 5.2) that remained for a long period in the Atlantic, south of Cape Hatteras, causing overwash of the barrier islands, and a maximum observed wave height of 9 m at 44014. Other significant events observed during DUCK94 were Northeaster storms (figure 5.3). In contrast 1999 was a very active Hurricane season in the Atlantic. SHOWEX was delayed by a few days due to category 4 Hurricane Dennis (30 August to 5 September) causing overwash in Hatteras Island. Instruments had just been deployed when category 4 Hurricane Floyd made landfall south of Cape Hatteras, with maximum significant wave heights H_s of 6.75 m at 44014, 9 m at X6, and 12.5 m at NDBC buoy 41004 ($34^{\circ}30' N$, located off Charleston, S.C., and not shown), and peak frequency $f_p = 0.11$ Hz (at X6). A maximum sustained wind speed $U_{19.5} = 34$ m s⁻¹ was recorded at the end of the FRF pier. Floyd was immediately followed by Hurricane Gert (category 4) that remained far offshore, sending large amplitude swell over the shelf (f_p about 0.07 Hz, H_s up to 3 m at X6, 3.4 m at 44014). and Hurricane Irene, that crossed the Florida peninsula from the Gulf of Mexico into the Atlantic and passed 100 km offshore of Cape Hatteras, moving to the northeast. Hurricane Jose followed a track close to that of Gert (figure 5.2), sending only small amplitude swell to the instrument sites. SHOWEX was also marked by Northeaster storms, with a particularly severe storm on 1 December (figure 5.4).

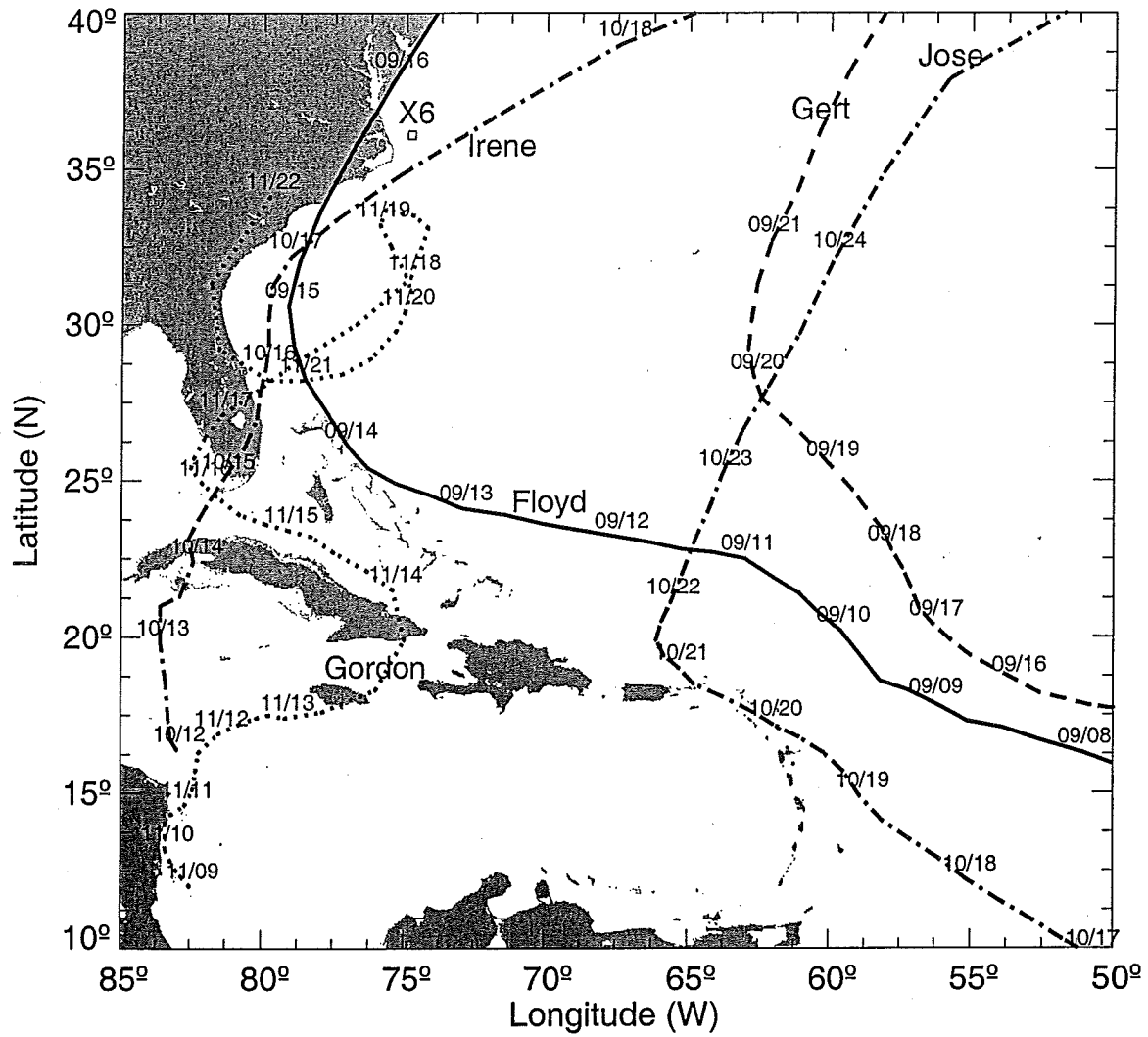


Figure 5.2: Tracks of North Atlantic hurricanes
 The dates indicate the position of the eye of the storms (Gordon during DUCK94, Floyd, Gert, Irene, and Jose during SHOWEX), at 12:00 EST every day, after reaching the tropical depression stage.

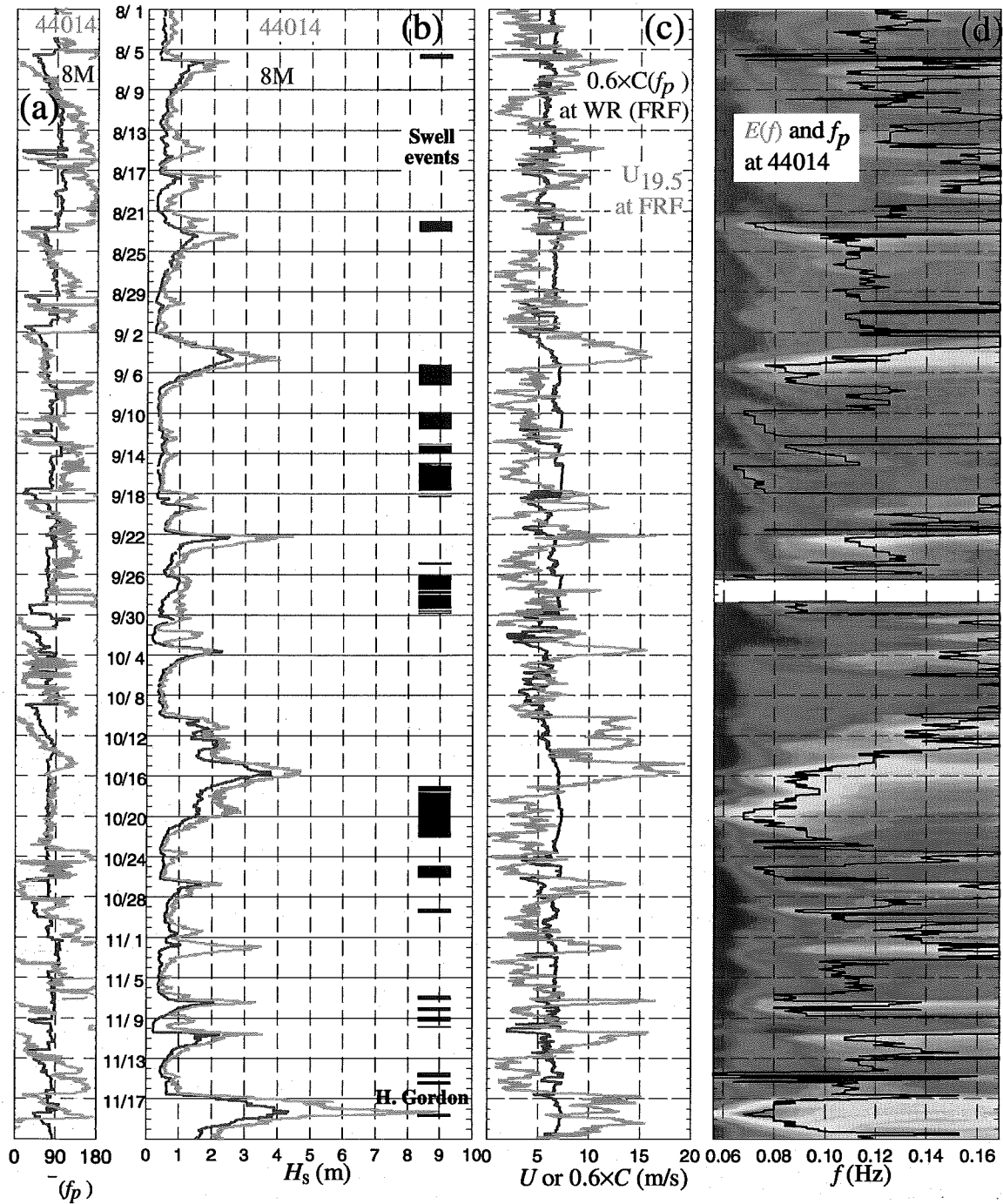


Figure 5.3: Wind and wave conditions during DUCK94.

(a) Mean direction at the peak frequency f_p , and (b) significant wave height, for buoy 44014 and the 8M array. Dark bands in (b) indicate swell-dominated conditions, defined here as periods when (c) the wind speed at 19.5 m is less than 60% of the wave phase speed at the peak frequency on the inner shelf. (d) Frequency spectrum (high densities in red, low densities in purple, with a normalized logarithmic scale), and f_p at buoy 44014.

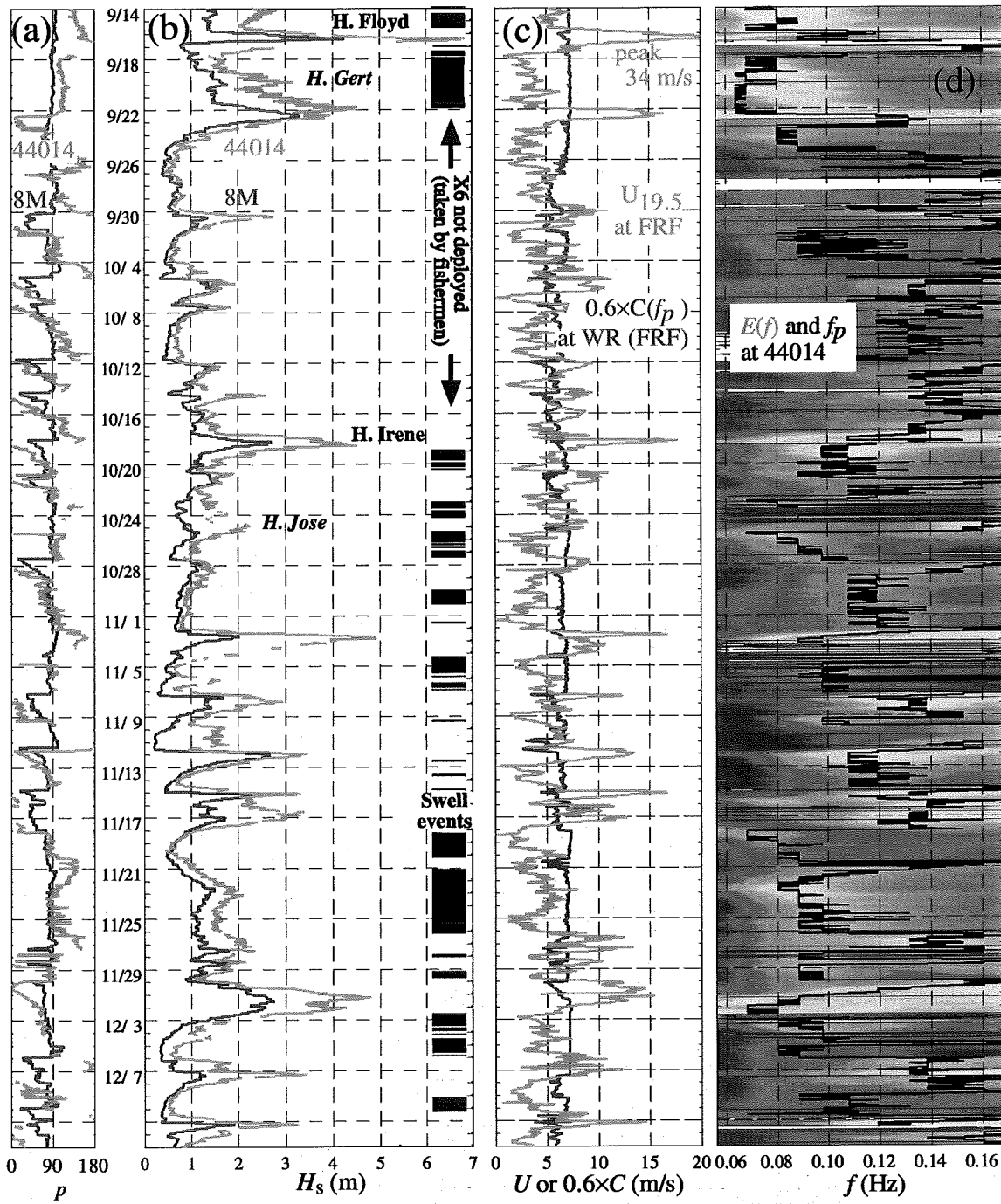


Figure 5.4: Wind and wave conditions during SHOWEX. Same format as figure 5.3.

3. Dataset reduction

In order to restrict the present analysis to swell-dominated conditions in which the effects of wind and wave breaking can be neglected, the following criteria were applied to select hindcast periods:

- a peak frequency f_p less than 0.12 Hz (reduced to 0.10 Hz for DUCK94, to avoid potentially large errors in the depth correction of high frequency bottom pressure)
- a maximum wind speed less than 0.6 times the linear wave phase speed at the peak frequency $C(f_p)$.

The latter condition was chosen to exclude low-frequency wind-waves generated on the shelf in high wind conditions, such as the Hurricane Floyd landfall. The estimate of $C(f_p)$ are based on data from the Waverider buoy WR(FRF), on the inner shelf, and the wind speed is taken as the maximum of 1-hour averaged values $U_{19.5}$ measured at 19.5 m above sea level at the end of the FRF pier (close to the 8M array) and U_5 measured at 5 m above sea level on board NDBC buoy number 44014. These instruments functioned with very few interruptions during both experiments. Wind speeds measured at the FRF pier and 44014 are generally close, in spite of the difference in anemometer height, except for a time lag due to the motion of the weather systems and they are expected to bracket wind speeds at 5 m height over the entire shelf. The wave phase speed estimated in 15 m depth give a lower bound for wave speeds on the shelf. Hence these criteria are expected to yield a conservative selection of swell dominated conditions. The swell criteria were applied not only for the selected data record, but also during the preceding 3 hours, a period that corresponds to the propagation time of 0.08 Hz waves across the shelf. These swell-dominated time periods (indicated in black on figures 5.3b,5.4b) are generally associated with distant storms or the early arrival of low-frequency waves from approaching storms (figures 5.3d,5.4d).

C. Hindcasts organization

1. The CREST wave model

CREST is a hybrid Eulerian-Lagrangian spectral wave model described in chapter II, and § III.C, that uses finite frequency-direction bands, and an unstructured geographical grid. The spectral energy balance equation is solved in its Lagrangian form (5.1), a simple one-dimensional advection equation, by advecting the k-space spectral densities of the wave energy along precomputed ray trajectories, from the model domain boundary to each point of the geographical grid. The source terms in (5.1) are determined in Eulerian form from the spectrum at each grid point and interpolated in space and directions on the rays to give Lagrangian source terms. For each grid point and finite band of frequency and arrival direction at that point (5.1) is integrated in time using a first order Euler scheme (§II.A) with a fixed 10-minute timestep.

2. Bathymetry and model grid

In order to encompass the instrumented sites in both experiments, and allow for oblique swell arrivals, the model domain was set to cover the North Carolina and Virginia shelf region, extending 400 km between 34°30' N, south of Cape Hatteras, and 38° N, at the Virginia-Maryland border on Assateague Island (figure 5.5). The National Ocean Service (NOS) database of depth soundings in that region generally has a resolution better than 200 m, with finer details resolved around shoals dangerous for navigation. A large gap in this dataset, off Duck between X2 and X5, was filled with soundings acquired during instrument deployment, maintenance, and recovery, and

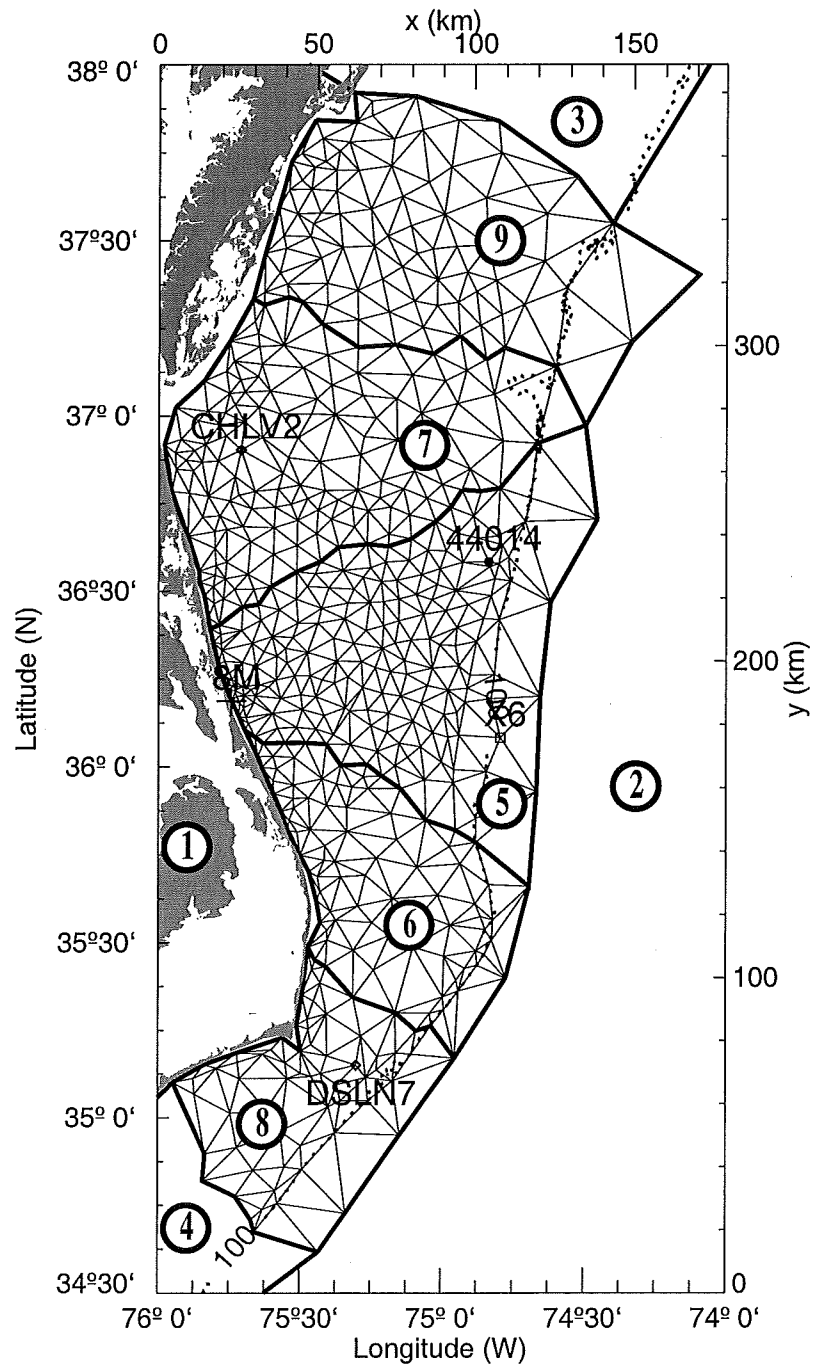


Figure 5.5: Model grid.

The grid points from which rays are computed and where the source terms are evaluated are the nodes of the triangular mesh. A linear interpolation is applied in each triangle to approximate the source terms along the rays. The entire model domain is divided into subdomains, numbered 1 through 9, separated by thicker lines. The locations of some instruments are added for geographical reference, and a dotted line marks the 100 m depth contour.

dedicated cruises on board R/V Cape Hatteras, together with multibeam sonar surveys acquired on board the Canadian hydrographic vessel Frederick G. Creed (figures 2.5, 3.7). This composite dataset was gridded with 6" resolution in latitude and longitude (180 and 150 m, respectively). Before computing wave rays the bathymetry was smoothed with an isotropic tapered filter with a radius equal to 5 times the local wavelength (adapted to the wave frequency and local water depth), in order to remove smaller scale topographic features that are represented in a stochastic form in the wave-bottom Bragg scattering source term (see § III.B.4). The unstructured model grid was constructed starting from the instrument positions. Points were added along the 8, 15, 20, 25, 30, 40, 60, 100, and 1500 m isobaths, increasing spacings away from the coast and away from the instrumented transects. This ensemble of points was complemented by gradually introducing points at the centers of the corresponding Delaunay triangles, until all sides of these triangles were shorter than 2 to 20 km (depending on the water depth and the alongshore location). The model uses 29 frequency bands from 0.05 to 0.15 Hz, and 76 direction bands regularly spaced at 5-degree intervals. For each of these finite bands, bundles of rays were traced from all grid points. The grid was subdivided into nine subdomains (numbered 1 to 9 on figure 6) coupled at their mutual boundaries, where the ray computations are stopped, as described in § II.A.1.

3. Boundary conditions

At the external boundaries bordering domains 1 (land), 2 (offshore), 3 and 4 (north and south model limits) the following conditions were applied. The offshore frequency-direction wave spectrum is interpolated from the MEM-estimated spectra at X6 and 44014 (back-refracted to deep water, assuming parallel bottom contours). To examine the sensitivity to offshore boundary conditions, results are also presented using only X6 data. Although the offshore conditions generally varied slowly on time scales of several hours, the deep water spectra are computed at 10-minute intervals, in order to match the model time step Δt , using a linear interpolation. Time lags based on the deep water group speed of linear waves are applied between the boundary grid points and the measurement location for each frequency-directional band, assuming uniform conditions along wave crests. This procedure was also used for the lateral boundary conditions (between subdomains 4 and 8, 9 and 3, see figure 5.5), crudely accounting for refraction of the offshore spectrum by assuming parallel depth contours and applying Snell's law. This treatment of the lateral boundaries does not represent accurately the propagation of waves across shelf regions outside the model domain, but avoids artificial shadow regions created by closed lateral boundaries (a problem encountered in chapter II). At the boundaries with domain 1 (land) a zero incoming flux was prescribed, corresponding to the absence of wave reflection from the beach and surf zone.

4. Bottom sediments and small scale topography.

Qualitative inspection of 20 core samples collected in 1997 on the inner shelf (Rebecca Beavers, Duke University, personal communication, 1999), and quantitative grain size analysis of 50 samples gathered during SHOWEX (see also § IV.B), give a good description of the surficial sediments in a narrow (20 km wide) region around the 8M-X5 transect (figure 5.6). The median grain diameter D_{50} varies between 0.09 and 4 mm. The average value of D_{50} (binned as a function of distance from shore) is 0.22 mm, slightly coarser than the average of D_{50} for the inner shelf (0.15 mm) used in chapter II. In order to extrapolate these observations away from the 8m-X5 transect a 5th order polynomial was fitted to the distribution of D_{50} as a function of the logarithm of the distance from shore (figure 5.6). This fitted distribution is used in model hindcasts, although very similar results obtained with a uniform value $D_{50} = 0.22$ mm suggest that the model is insensitive to the weak spatial variations in median grain size.

The small-scale bottom topography is generally well resolved in the NOS bathymetric

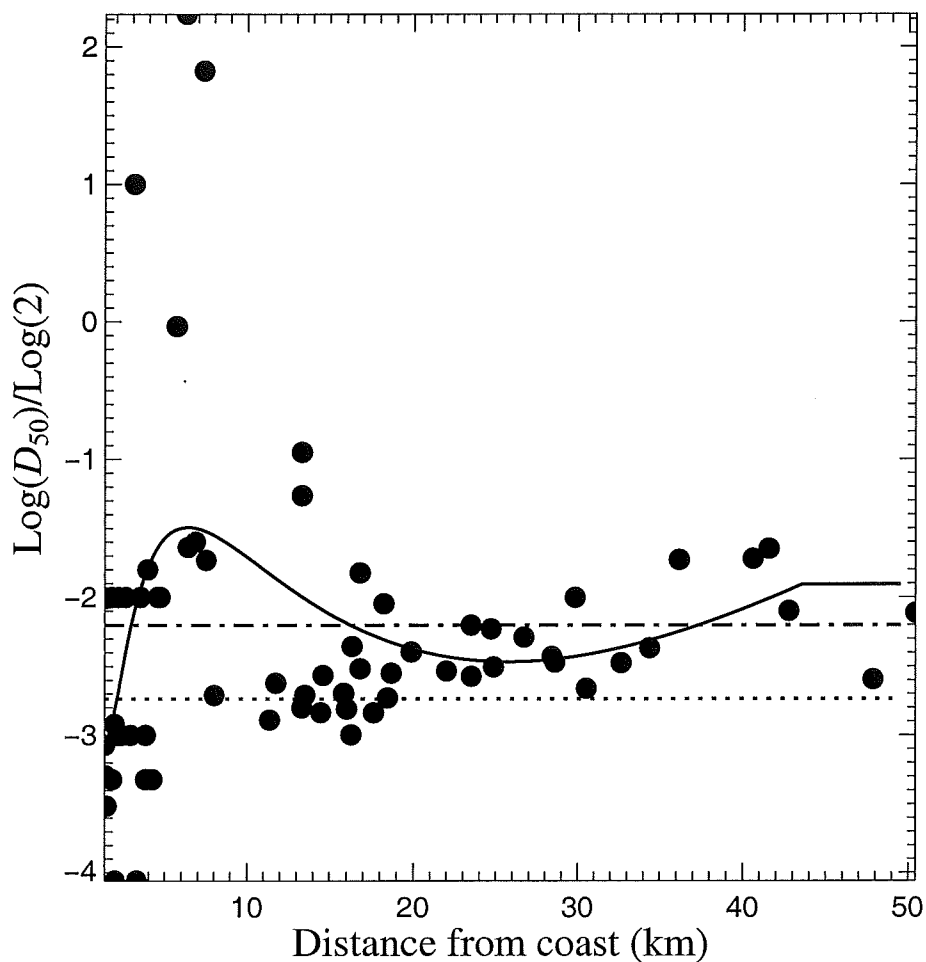


Figure 5.6: Distribution of median grain sizes.

D_{50} as a function of distance from the coast, for surficial sediments in vibracore samples collected in the period 1994-1997 (Rebecca Beavers, Duke University, personal communication, 1999) and Shipek grab samples collected during SHOWEX (figure 4.4a). The dotted line indicates $D_{50} = 0.15$ mm, used in II. The average grain size $D_{50} = 0.22$ mm is indicated by the dash-dotted line, and the solid line is a polynomial fit used for hindcasts in the present chapter.

database, for water depths between 10 and 30 m, and wavelengths larger than 300 m. Estimates of bottom elevation spectra from a region with shoals on the inner shelf south of the instrument transects, and a deeper (20–40 m) mid-shelf region to the south-east of X2, give direction-integrated spectra with a slope close to k^{-3} , and spectral levels decreasing by a factor 3 from the shoals to the middle shelf (dotted lines in figure 5.7b). The corresponding two-dimensional wavenumber spectra are not isotropic and show larger variance along a north-west to south-east axis, (e.g. figure 5.7a). For wavelengths under 300 m, the topography is only resolved in the multibeam surveys conducted in small regions, in 20 and 25 m, giving the two spectra F_1^B and F_2^B , respectively (figure 3.8), and represented as direction-integrated spectra in figure 5.7 (dashed lines). Other regions surveyed only along individual tracks, with the EM1000 multibeam system or a ISIS100 sonar (data acquired and provided by J. McNinch, FRF) gave unidirectional spectra comparable to these direction-integrated spectra. All spectra decrease approximately as k^{-3} (not shown), with variance levels between those of F_1^B and F_2^B .

In the model the topographic features that contribute to wave-bottom Bragg scattering (with horizontal scales smaller than five times the wavelength, see §III.B.4) are assumed to be statistically uniform on the entire shelf. A representative composite bottom elevation spectrum at these scales was generated from spectra computed from the 6" resolution bathymetry grid, ensemble averaging over regions with water depths between 10 and 30 m (figure 5.7a, and solid line in figure 5.7b). The variance at large scales is lower than for the two spectra determined from regions well-resolved in the NOS database (dotted lines in figure 5.7b), possibly due to the coarse resolution of the bathymetry data in some regions. At higher wavenumbers, not resolved by the grid, the variance densities were taken from the small-scale spectrum with the larger variance (F_1^B in figure 3.8). Computations of the Bragg scattering source term using this spectrum may therefore overestimate scattering by the smaller scales ($l/2\pi > 0.002$) and possibly underestimate scattering by the larger scales ($l/2\pi < 0.002$). To investigate this effect the model was also run with a similar composite spectrum in which the small scale part was replaced by F_2^B (figure 3.8).

5. Source terms

The wave-bottom Bragg scattering source term S_{Bragg} is estimated using a uniform bottom elevation spectrum and integrated with a semi-implicit scheme, taking advantage of the linear relation between $E(f, \cdot)$ and $S_{\text{Bragg}}(f, \cdot)$ (§III.C). Implementation of the bottom friction source term S_{fric} is made more complex by the empirical parameterizations of the bottom Nikuradse roughness k_N . In the present chapter we generalize Tolman's (1994) decomposition of k_N in a ripple roughness k_r and sheet flow roughness k_s ,

$$k_r = a_b \times A_1 \left(\frac{\psi}{\psi_c} \right)^{A_2}, \quad (5.2)$$

$$k_s = 0.57 \frac{u_b^{2.8} a_b^{-0.4}}{[g(s-1)]^{1.4} (2\pi)^2}, \quad (5.3)$$

where a_b and u_b are the r.m.s. amplitude of the bottom wave orbital displacement from the equilibrium position (half of the orbital diameter) and velocity at the top of the boundary layer, s is the sediment specific density and g is the gravity acceleration. While Tolman (1994) used values of the empirical coefficients A_1 and A_2 determined by Madsen et al. (1990), we will examine if adjustments to these coefficients improve hindcasts of waves on the North Carolina shelf (figure 5.8).

When the wave motion is not strong enough to generate vortex ripples, i.e. for values of the Shields number less than a threshold ψ_{rr} , k_N is given by a relic ripple roughness k_{rr} . Madsen et al. (1990) proposed

$$\psi_{\text{rr}} = A_3 \psi_c, \quad (5.4)$$

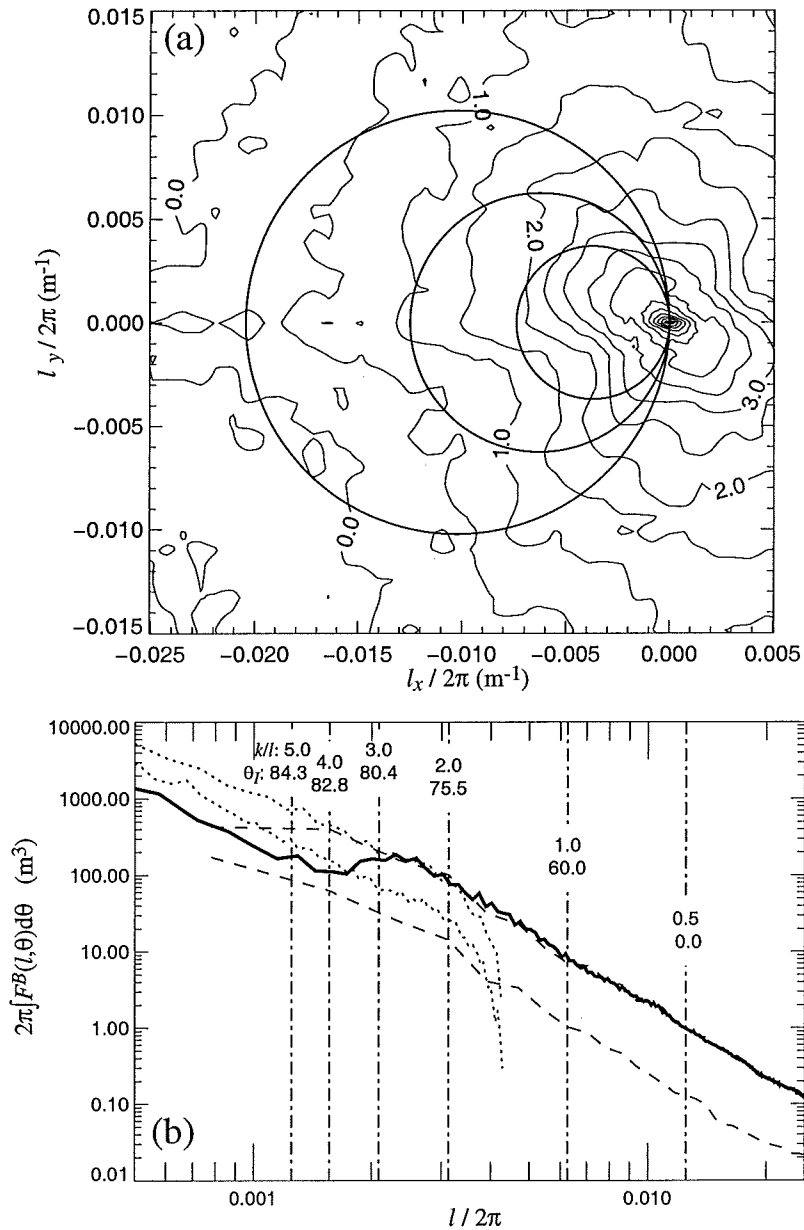


Figure 5.7: Bottom elevation spectra

(a) Composite two-dimensional bottom elevation spectrum F^B , based on 10–30 m depth bathymetry in the entire model domain, and high-resolution multibeam bathymetry in a 5 km × 5 km region in 20 m depth. Contour values are $\log_{10}(4\pi^2 F^B)$ with F^B in $\text{m}^4 \text{rad}^{-2}$, at 0.5 intervals. Circles indicate the bottom components that interact in 20 m depth with waves from the east with frequencies 0.05 (inner circle), 0.12 (middle circle) and 0.25 Hz (outer circle). Axes units are reciprocal wavelengths $l_x/(2\pi)$ and $l_y/(2\pi)$. (b) Corresponding direction-integrated spectrum (solid) and other spectra estimated from high-resolution multibeam bathymetry (dashed), and well resolved regions in the NOS database (dotted). The vertical lines indicate the bottom scales responsible for scattering 0.08 Hz swell, for different incidence angles θ_I .

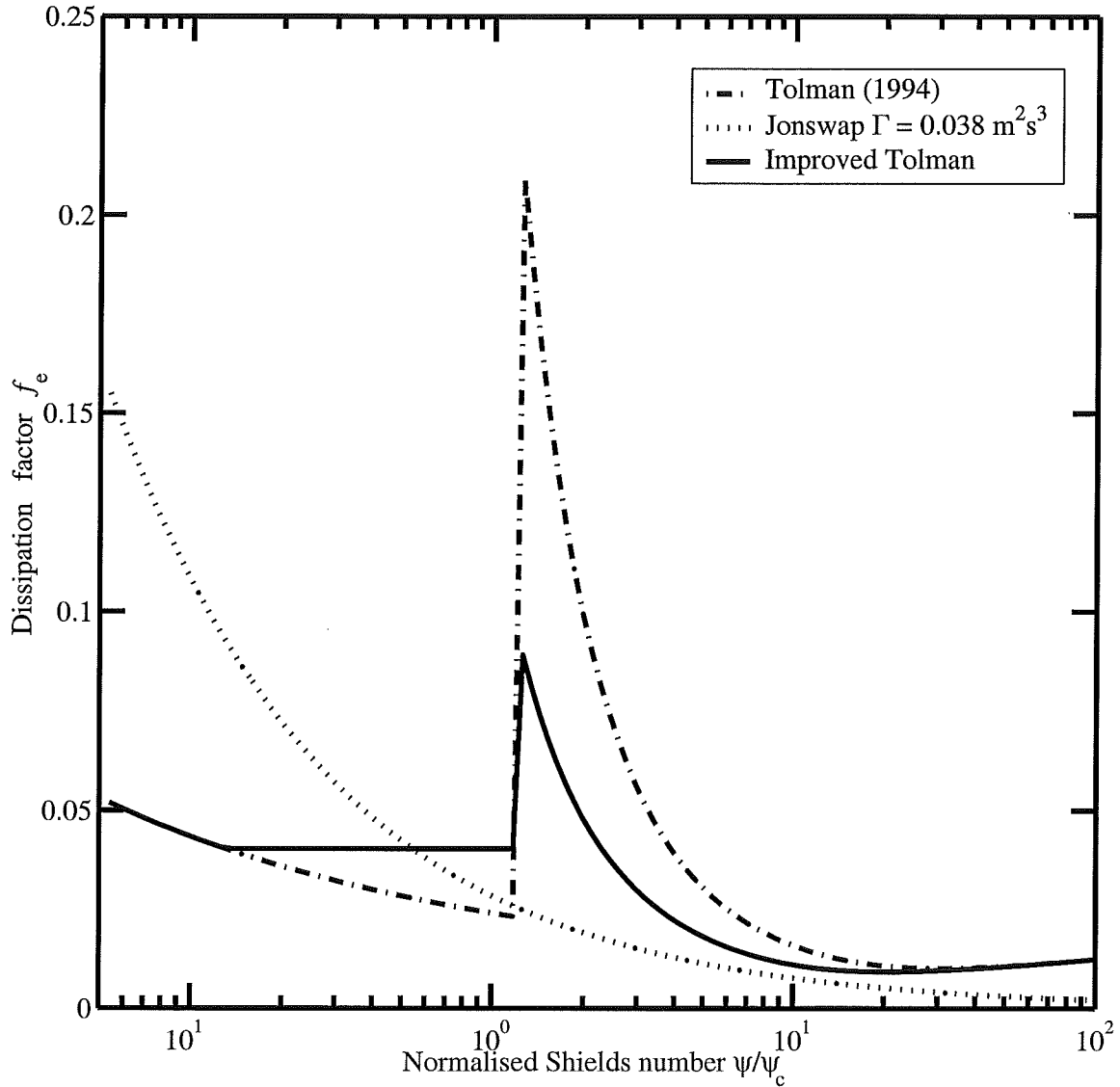


Figure 5.8: Dissipation factors

f_e as a function of the Shields number ψ normalized by its critical value ψ_c for sediment motion. The original parameterization proposed by Tolman (1994) using Madsen *et al.* (1990) ripple roughness, is compared to the JONSWAP linear damping source term, and an improved roughness parameterization is given by $A_1 = 0.4$, $A_2 = -2.5$, $A_3 = 1.2$ and $A_4 = 0.05$, and it is used below in the source term $S_{fric,I}$, giving better hindcast results, for the Shields number covered by the present data set (at X3: $0.03 < \psi/\psi_c < 6.5$).

with $A_3 = 1.2$ determined empirically, and ψ_c the critical Shields number for the initiation of sediment motion on a flat bed and under sinusoidal waves. ψ_c should be a known property of the sediment. In the absence of any data, the relic ripple roughness k_{rr} was first proposed to be equal to the grain size diameter by Graber & Madsen (1988), which is appropriate for a flat bed, but Tolman (1994) suggested a larger value to account for relic bedforms and bioturbation, and proposed a constant value $k_{rr} = 0.01$ m. Our earlier hindcast study showed that this constant value yields good wave height predictions for very small waves (§II.D.1), but the dissipation is so weak that different roughness values could yield similar wave heights. For larger forcing conditions (but still in the relic ripple regime), recent experiments suggest that k_{rr} actually decreases with ψ on a smooth cohesive bed (Alex Babanin, University of South Australia, analysis of Lake George experimental data, personal communication, 2001). However hindcasts of waves on the North Carolina shelf (dominated by non-cohesive sand) presented in this chapter, suggest that the roughness may increase with the forcing, possibly due to the presence of relic bedforms that are more likely to be intercepted by larger orbital diameters. We therefore propose to use

$$k_{rr} = \max \{0.01\text{m}, A_4 a_b\} \text{ for } \psi < \psi_{rr}. \quad (5.5)$$

A_1 , A_2 , A_3 and A_4 define the response of the bed roughness to the wave forcing and the resulting wave energy dissipation, $A_1 = 1.5$, $A_2 = -2.5$, $A_3 = 1.2$ and $A_4 = 0$ corresponds to the original Tolman (1994) parameterization.

In this parameterization, the critical value ψ_c must be known beforehand. It is usually determined experimentally as a function of the sediment physical properties. Although recent experimental results for mixed sands suggest values of ψ_c larger by about 30% (Wallbridge et al., 1999), we use an analytical fit to Shields' (1936) laboratory data:

$$\psi_c = \frac{0.3}{1 + 1.2D_*} + 0.055 [1 - \exp(-0.02D_*)], \quad (5.6)$$

$$D_* = D_{50} \left[\frac{g(s-1)}{\nu^2} \right]^{1/3}, \quad (5.7)$$

where ν is the kinematic viscosity of water. This expression was proposed by Soulsby (1997), and includes the correction for very fine grain sizes by Soulsby and Whitehouse (1997) intended to limit ψ_c to values less than 0.3. It is consistent with the laboratory data reviewed by Madsen & Grant (1976), and the ripple roughness parameterization of Madsen et al. (1990).

The critical Shields number ψ_c actually depends on the flow conditions and bed geometry. Knowledge of the exact threshold under irregular waves is not critical for the present work, and ψ_c is better interpreted as a well-defined sediment property defined for a flat bed and given flow conditions (e.g. steady flow). In contrast, the parameterization of the equivalent ripple roughness k_r , that also depends on the flow conditions and bed geometry, should be valid in field conditions. The laboratory experiments of Madsen et al. (1990) do not include all the properties of natural boundary layers, thereby giving a parameterization that may not be general enough. In particular it has been observed that ripples in the field are usually less sharp than ripples in the laboratory, perhaps as a result of the directional spreading of waves. This effect can be expected to reduce k_r and may be parameterized by decreasing A_1 or increasing A_2 . The results of other local effects are not so clear, such as the impact of biological benthic activity (Fries et al., 1999). The detailed composition of mixed sands may also have some effect on the empirical parameters A_1 , A_2 and A_3 , and using the median grain diameter D_{50} in (5.6) may not give the best value ψ_c . k_N for $\psi \simeq \psi_{rr}$ should also be a function of the time varying properties of turbulence in the bottom boundary layer, as only the largest waves in a wave group may be able to generate vortices (responsible for the form drag and the very development of ripples, see Ayrton, 1910), but it should also depend on the past history of the bed morphology as relic ripples may determine if the vortices can be generated.

In addition to these complications, due to the local properties of natural environments, the practical use of bedform roughness parameterizations is hindered by spatial variations of the water depth and sediment grain size (see for example Green, 1986; figure 4.4a), on scales not resolved by operational wave prediction models. The adaptation of the local parameterization to a larger scale (of the order of 0.1 to several kilometers), was envisaged by Tolman (1995), and performed in chapter II using the known statistics of depth variations, and ignoring the variations of D_{50} , because of insufficient data. This representation of subgrid variations in the properties of the bottom boundary layer is used here. Additional representation of subgrid variations of median grain sizes, assuming a Gaussian distribution, did not give significantly different results.

A widely used alternative to this physics-based bottom friction source term assumes S_{fric} to be a linear function of the bottom velocity spectrum, with a proportionality coefficient Γ/g^2 . Γ is an empirical constant with dimensions of m^2s^{-3} . This formulation emerged after the wave data analysis in the JOint North Sea WAve Project (JONSWAP), as variations in the cross-shore energy flux were examined in terms of Γ , an attenuation coefficient. This linear dissipation can only be justified by assuming that the wave orbital velocities are weak compared to the mean (tidal) currents, but this should cause a modulation of Γ by the current that was not observed. However observations showed large variations of Γ (from 0.0019 to 0.160 m^2s^{-3}). Nevertheless this parameterization, with the averaged value $\Gamma = 0.038 \text{ m}^2\text{s}^{-3}$ observed during JONSWAP, has encountered some success (Bouws and Komen, 1983), and replaced quadratic drag formulations proposed previously (Hasselmann and Collins, 1968). This ‘JONSWAP’ bottom friction source term, $S_{\text{fric,J}}$, may yield good results over sand because the corresponding dissipation factors f_e decreases as a function of the Shields number, following the movable-bed model for relic roughness and sheet flow conditions (figure 5.8). However values of f_e in the active ripple regime ($\psi > \psi_{\text{tr}}$) are significantly smaller than those observed over ripples, and $S_{\text{fric,J}}$ fails to reproduce the observed strong attenuation of waves when active ripples are present (§ II.D.1). Fortunately for operational wave models, these active ripple conditions occur only in a small range of wave conditions, although these may be dominant in some regions.

It must be emphasized that no parameterization has been tested for very large Shields numbers $\psi/\psi_c > 5$, for which very little laboratory or field data is available, but these conditions occur in large storms that are most important for navigation safety or coastal engineering. It is expected that a physics-based parameterization performs better than the JONSWAP empirical formulation calibrated in very different conditions.

S_{fric} parameterizations used in the present chapter include $S_{\text{fric,T}}$, given by Tolman (1994) (i.e. $A_1 = 1.5$, $A_2 = -2.5$, $A_3 = 1.2$ and $A_4 = 0$), and an improved movable bed parameterization $S_{\text{fric,I}}$ for which the values of the empirical parameters have been adjusted to increase the overall hindcast skills: $A_1 = 0.4$ and $A_2 = -2.5$, $A_3 = 1.2$, and $A_4 = 0.05$. Although no physical interpretation can be given for the JONSWAP source term $S_{\text{fric,J}}$, it is used here for reference.

D. Model-data comparisons

To objectively assess the accuracy with which the energy balance equation (5.1) describes the evolution of swell across the North Carolina continental shelf, a statistical analysis of hindcast results for the entire data set is presented here, based on 528 1-hour swell-dominated records (22 days) of SHOWEX observations and 121 three-hour swell-dominated records (15 days) of DUCK94 observations, out of the 2100 SHOWEX observation records (87 days), and 725 DUCK94 records (91 days). Fewer records were available for some instruments, in particular A, B and WR(FRF) which failed during the 1994 Hurricane Gordon, and X6 which malfunctioned at the peak of the 1999 Hurricane Floyd. The period in September and October 1999 when X6 was not deployed was entirely excluded.

The directional properties of the waves, influenced primarily by refraction and Bragg scattering (chapter III), are discussed first using only SHOWEX data. This is followed by an analysis of

the wave heights, predominantly influenced by refraction and bottom friction using both DUCK94 and SHOWEX hindcasts. For all parameters the model errors generally grow across the shelf towards the shore. The ‘initial’ model errors, at the instruments located close to the offshore boundary, are discussed separately in § V.D.4.

1. Mean direction

A mean direction θ_p at the peak frequency f_p was computed for each instrument, using an energy-weighted average over a finite bandwidth of $0.15f_p$ centered at f_p . Following standard conventions (e.g. Kuik *et al.*, 1988), θ_p is defined as the direction of the moment vector (a_1, b_1) , with

$$(a_{1,p}, b_{1,p}) = \int_{0.925f_p}^{1.075f_p} \int_0^{2\pi} (\cos \theta, \sin \theta) E(f, \theta) d\theta df \quad (5.8)$$

f_p was determined from the measured frequency spectra at X1, so that the modeled and observed directions correspond to the exact same frequency band. θ_p is well predicted by the model with no source terms or bottom friction only, with a maximum root mean square (r.m.s.) error of 8–10 degrees on the inner shelf, that decreases onshore as refraction narrows the incoming spectra toward 70° , the beach-normal direction (figure 5.9). The conditions summarized here contain many events with large oblique angles that are well reproduced by the model, such as swell from Hurricane Floyd with offshore directions of 160° refracted to 90° at 8M. The relatively large bias at 8M is not observed in similar hindcasts of DUCK94 swells (-1.6° bias, and r.m.s. error 6.9°) and may be related to a change in bottom topography not represented in the bathymetry grid used for ray computations. Errors at X5 are anomalously larger. In particular θ_p at X5 was observed to oscillate between 90° and 140° , whenever the offshore direction at X6 was slowly varying between 110° and 130° , for all frequencies between 0.05 and 0.14 Hz. This suggests that the wave rays are bent by refraction, over bottom features not resolved in the sparse bathymetric surveys conducted on the outer shelf (Herbers *et al.*, 2000). However, the errors are generally small compared to the changes in θ_p across the shelf (up to 70° for the southerly swell from Hurricane Floyd), and are of the order of the model directional resolution (5°).

The addition of Bragg scattering in the model biases the mean direction further to the north. This additional bias is due to the anisotropy of the bottom elevation spectrum used in the hindcasts, at wavelengths ($2\pi/l$) less than 500 m, in combination with refraction by the large scale topography. These scattering bottom undulations have crests preferentially aligned with a south-west to north-east direction and have a strongest effect on waves propagating along that direction. The model bias and r.m.s. error added by Bragg scattering is partially cancelled by bottom friction (compare runs 3 and 4 in figure 5.9). Indeed the scattered waves propagating at larger angles relative to the depth contours propagate on the shelf for a longer time, over which the cumulated effect of bottom friction is larger. A weaker variance in the bottom elevation spectrum for $2\pi/l < 500$ m clearly reduces this effect (run 5 in figure 5.9).

2. Directional spread

The directional spread at the peak frequency $\sigma_{\theta,p}$ was computed for each instrument, as was the mean direction θ_p , for a finite frequency band around the peak of the measured frequency spectrum at X1. $\sigma_{\theta,p}$, defined in radians, as

$$\sigma_{\theta,p} = [2(1 - a_{1,p} \cos \theta_p - b_{1,p} \sin \theta_p)]^{1/2} / \int_{0.925f_p}^{1.075f_p} \int_0^{2\pi} E(f, \theta) d\theta df, \quad (5.9)$$

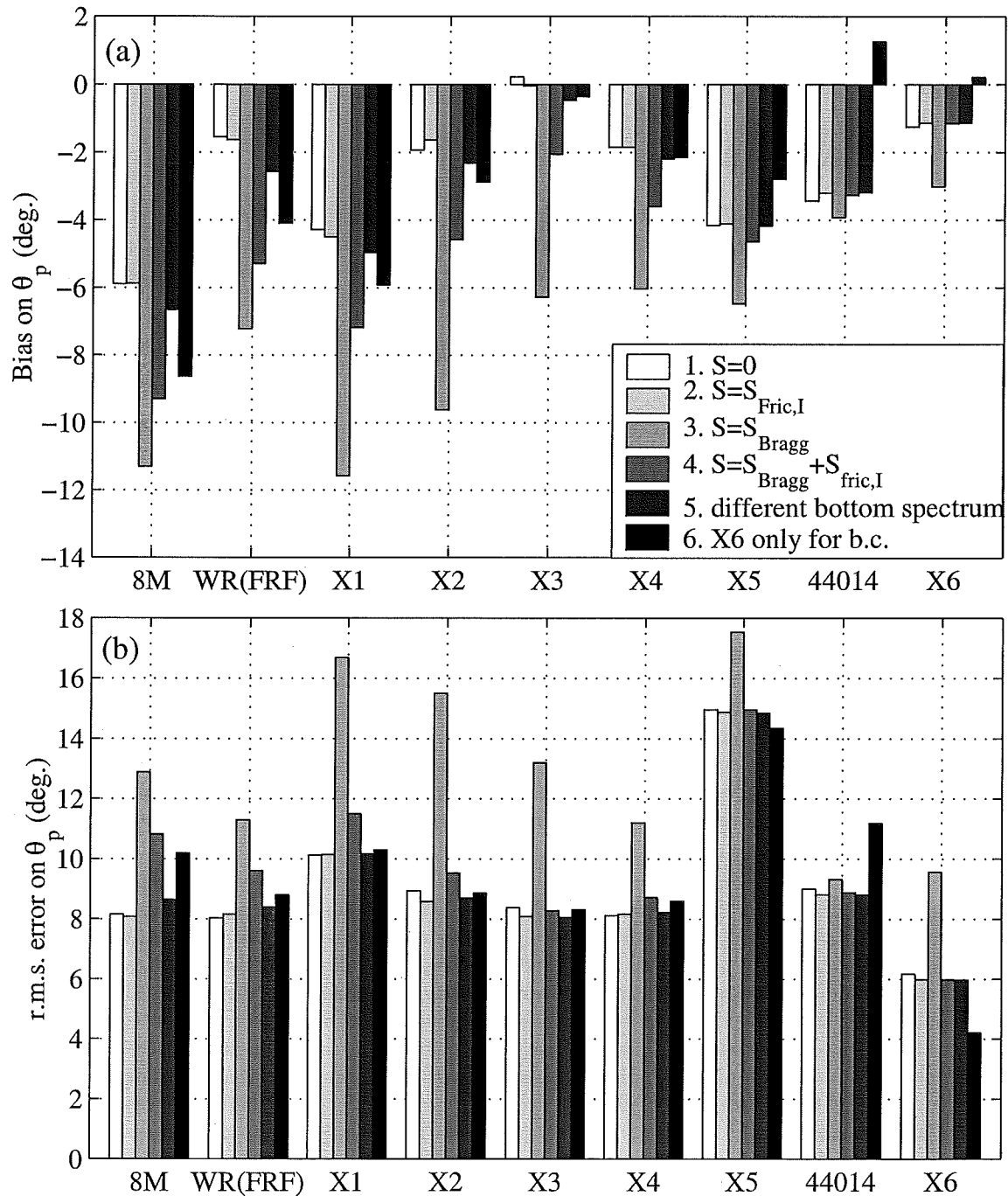


Figure 5.9: Model errors on the mean direction θ_p at the peak frequency
 (a) Model bias and (b) r.m.s. error for swell-dominated periods observed during SHOWEX. Runs 1–4 use different sets of source terms in (5.1). Source terms in runs 5 and 6 are identical to those in run 4, but run 5 uses a different bottom elevation spectrum that has a lower variance at small scales (F_2^B , figure 3.8b). Run 6 is forced with X6 data at the offshore boundary instead of the interpolation of X6 and 44014 data used in all other runs. Positive values in (a) correspond to a clockwise bias.

is an estimate of the standard deviation of the directional distribution of wave energy, and thus can be loosely interpreted as the half-width of the directional spectrum. For an isotropic spectrum $\sigma_{\theta,p}$ is $2^{1/2}$ radians, that is 81° .

Observed directional spreads are, in general, relatively uniform across the shelf, decreasing slightly towards the coast. Observations at X6 range from 10 to 55° with typical values between 30 and 40° , whereas observations at 8M vary between 12 and 27° with typical values of 15 – 25° (figure 5.10). However, when the offshore directional spectrum is very narrow ($\sigma_{\theta,p}(X6) < 20^\circ$), $\sigma_{\theta,p}$ increases towards the shore. This observation is contrary to the general belief that waves become one-directional in shallow water, as expected from depth-refraction. Indeed model calculations that incorporate refraction, as well as bottom friction (in order to provide reasonable wave heights) give directional spreads much narrower than the observations (figure 5.10). This bias, largest at 8M and on the inner shelf, can be observed throughout the shelf.

Statistics from model runs with different source terms (figure 5.11) demonstrate how bottom friction and wave-bottom Bragg scattering contribute to $\sigma_{\theta,p}$. Run 1, without source terms, clearly underestimates $\sigma_{\theta,p}$ and only contains the narrowing effect of refraction as waves approach the shore. Run 2 includes bottom friction that narrows the spectrum further: waves propagating at larger angles relative to the depth contours are more exposed to dissipation, because of their longer propagation time across the shelf. Wave-bottom Bragg scattering opposes these two narrowing effects by diffusing the energy around the mean direction (see § III.C). While Bragg scattering alone tends to give spectra that are too broad in the middle of the shelf (figure 5.11, run 3), the addition of Bragg scattering to bottom friction generally yields good agreement across the shelf (figure 5.11, run 4), reducing the scatter index from 0.51 (run 2) to 0.25 (run 4) at 8M, with comparable improvement on the inner shelf (figure 5.11).

However, results are sensitive to the choice of the bottom elevation spectrum. Run 5 using a different spectrum with the small-scale variance taken from F_2^B (figure 3.8b, representative of smoother regions of the shelf) only partially accounts for the observed increase of $\sigma_{\theta,p}$ (figure 5.11, run 5). Bragg scattering most strongly affects narrow spectra, and reproduces well the observed broadening of very narrow offshore spectra (figure 5.10). For broad offshore spectra ($20 < \sigma_{\theta,p}(X6) < 40$) the observed spectra at 8M are still 5 – 10° broader than the predicted spectra. The predicted scattering effect is also strongest for waves with low peak frequencies (figure 5.12), but the narrowest offshore spectra tend to coincide with the ones with the lowest peak frequency, so that the influence of the spectral width and peak frequency cannot be clearly separated.

As the effect of Bragg scattering increases with the bottom elevation variance, it is likely that the bottom spectrum used in run 4, with relatively large small-scale variance, represents an upper bound on the true effect of wave-bottom Bragg scattering across this continental shelf. The remaining negative bias of $\sigma_{\theta,p}$ predictions in run 4 suggests that other processes are important. Higher order Bragg scattering, among others, may be the cause of further directional spreading.

The bottom friction source term was somewhat arbitrarily assumed to be isotropic. A quadratic drag law gives a difference between the major and minor principal axes of the directional dissipation source term that is up to a factor 2 for unidirectional waves (Hasselmann & Collins, 1968). This type of anisotropy would cause more dissipation for waves with directions along the mean direction, and less dissipation in the perpendicular directions, therefore increasing the directional spread. The absence of wave reflection from the beach in the model is another likely cause for the negative bias. Even though the offshore traveling waves are removed in the directional spectrum estimates and $\sigma_{\theta,p}$ at 8M, they contribute to the $\sigma_{\theta,p}$ estimates at other sensors.

3. Wave heights

For the analysis of wave height predictions the SHOWEX data set is augmented with the DUCK94 data. Statistics given below combine results at SHOWEX and DUCK94 instruments located nearby or in similar water depths. Changes in the peak frequency across the shelf are

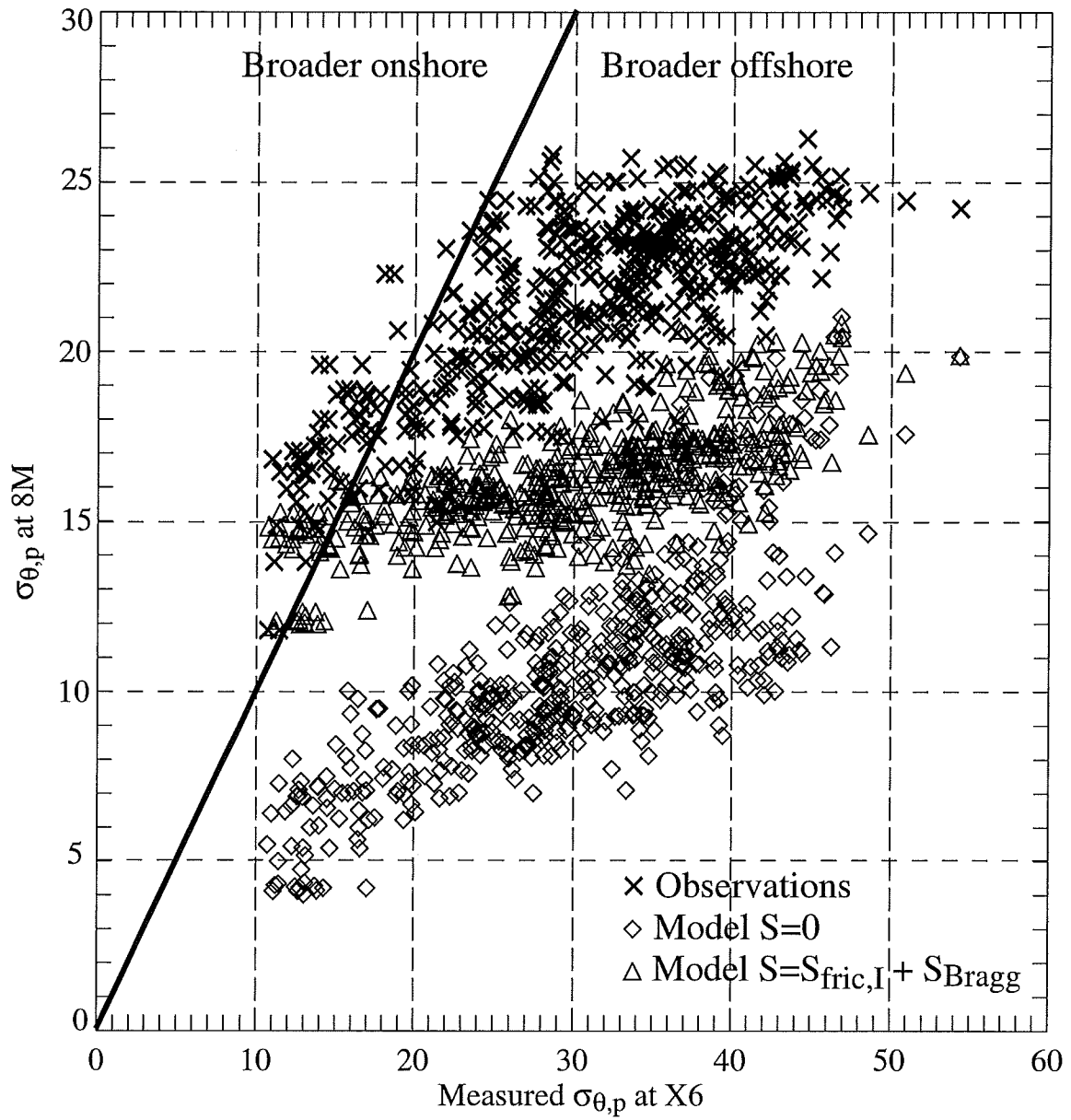


Figure 5.10: Nearshore versus offshore directional spread

Directional spread at the peak frequency $\sigma_{\theta,p}$ at 8M, as a function of the offshore directional spread measured at X6. The solid line separates spectra that are broader in the nearshore and spectra that are broader offshore.

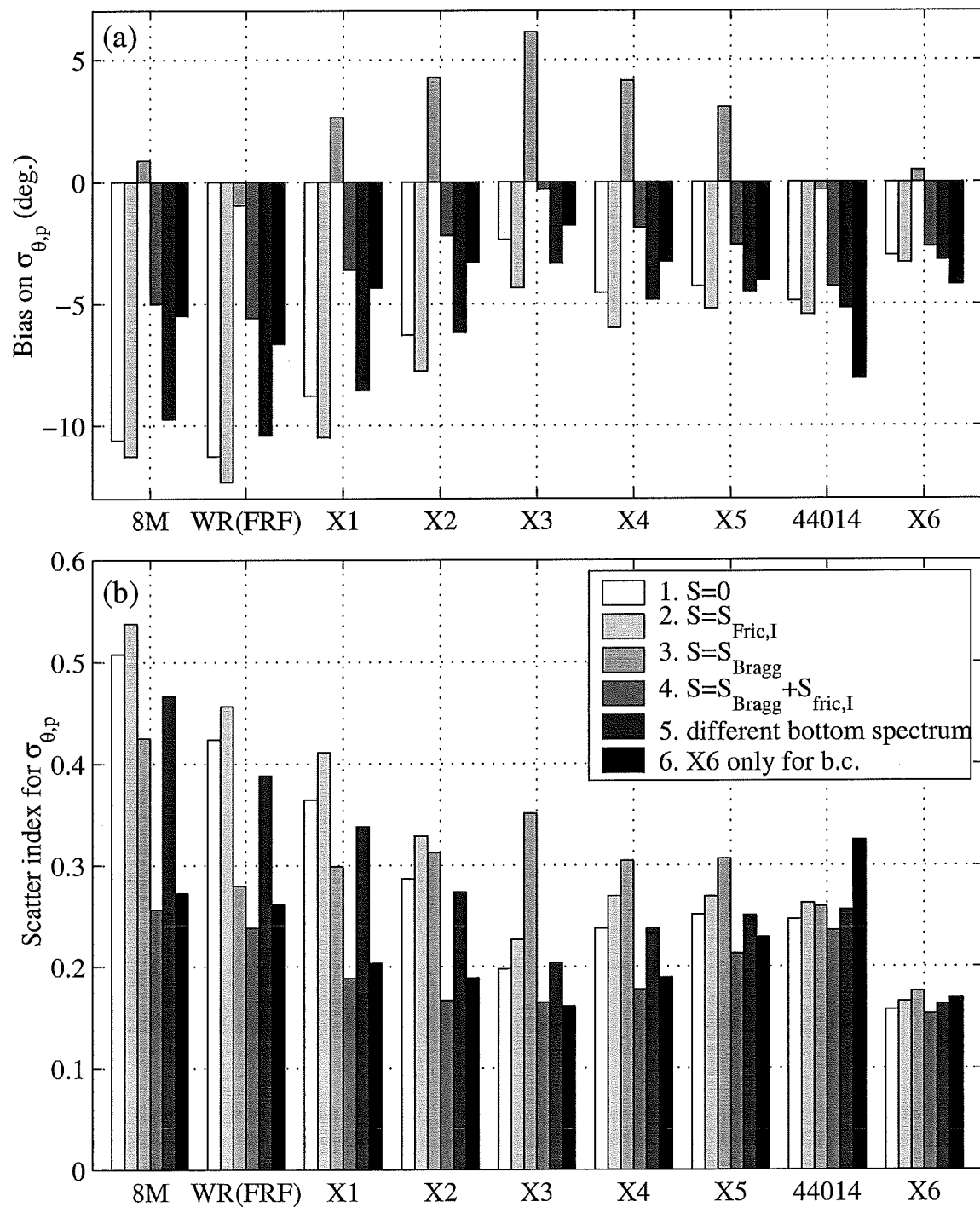


Figure 5.11: Model errors on the directional spread $\sigma_{\theta,p}$ at the peak frequency. Same format as figure 5.9. The r.m.s. error is replaced by a scatter index defined as the ratio of the r.m.s. error and the r.m.s. value.

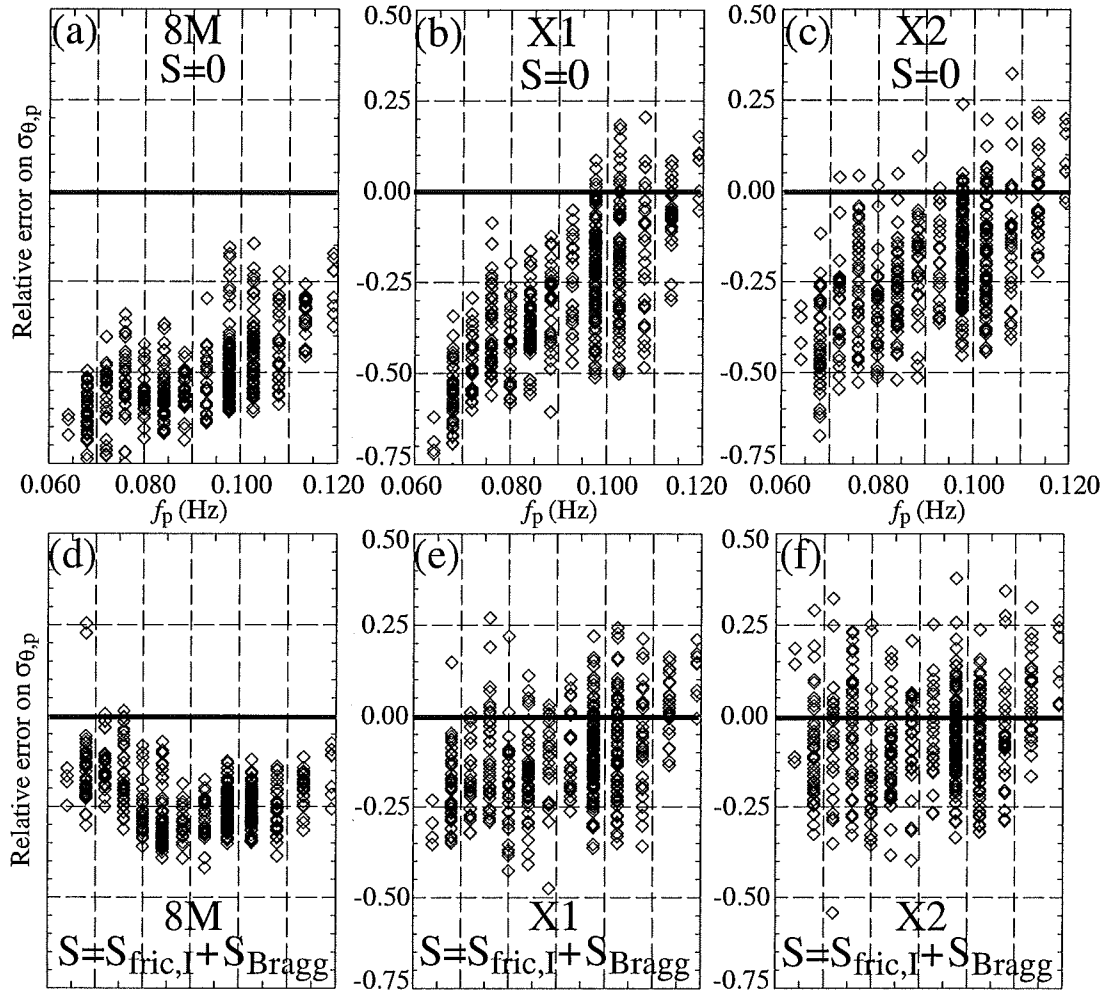


Figure 5.12: Relative error on the directional spread $\sigma_{\theta,p}$ as a function of the peak frequency. Relative errors of 1 or 0.5 represent an overprediction or underprediction by a factor 2, respectively.

negligible, but the significant wave height H_s generally decreases from offshore to the nearshore with observed H_s at 8M about half of the observed values at X6 for moderate-energetic swell, and a generally smaller reduction ($\approx 25\%$) in benign conditions ($H_s(X6) < 1.5m$). This effect is explained only in part by refraction that reduces the wave heights of waves that propagate onshore at large oblique angles relative to the depth contours. Indeed the model without source terms (figure 5.13, run 1), that accounts only for the effects of refraction and shoaling, overpredicts wave heights with a typical bias of 0.2 m on the inner shelf, and gives an overall (for all sensors) scatter index of 0.26 for H_s . Adding Bragg scattering slightly increases model errors: the increased directional spread translates into a larger cross-shelf propagation time (on average), which, in the absence of dissipation, increases the wave height, giving an overall scatter index of 0.29 (figure 5.13, run 3).

Including bottom friction dramatically reduces the model errors. Run 4b, using the Tolman movable-bed source term, based on laboratory data without any empirical tuning to field conditions, reduces the overall scatter index of H_s predictions from 0.29 to only 0.15 (figure 5.13). This result supports the hypothesis that the formation of vortex ripples (observed in chapter IV) and their feedback on the waves through enhanced bottom roughness, are the primary mechanisms for wave attenuation across a sandy continental shelf. However, a negative bias of -9 cm at 8M indicates a model tendency to overestimate dissipation, already noted in chapter II.

On average the empirical JONSWAP bottom friction source term performs about equally well (figure 5.13, run 4a), giving an overall scatter index of 0.16. However, this source term gives poor results at CHLV2, a site located down wave of shallow shoals (but not shallow enough for depth-induced breaking), with a scatter index of 0.53 and a positive bias of 20 cm. This bias is the result of large model-data discrepancies during the arrival of swell from Hurricane Gert (17–21 September 1999). Observed wave heights at CHLV2 during this event are 70% smaller than predicted by refraction and shoaling, which corresponds to a dissipation of 84% of the incident wave energy flux. This strong dissipation is probably the result of active ripple generation on the shoals offshore of CHLV2 (figure 5.1), and the JONSWAP source term grossly underpredicts bottom friction in active ripple conditions (figure 5.8). The improved Tolman source term $S_{\text{fric,I}}$ (using a modification of Madsen *et al.*'s (1990) empirical parameters, designed to reduce the model errors) gives an overall scatter index of 0.13, with a maximum of 0.20 at X2 (run 4c in figure 5.13).

The distribution of model errors as a function of the Shields number, estimated from waves measured at representative inner shelf sites X3 (SHOWEX) and C (DUCK94), is shown in figure 5.14. The largest errors of a non-dissipative model (run 1) clearly occur for large values of the Shields number when the presence of active ripples is expected. A model using the JONSWAP friction source term also gives the largest errors in this regime. It should be noted that the two largest Shields numbers correspond to DUCK94 3-hour records in the afternoon of 18 November 1994, after the peak of Hurricane Gordon (see figure 2.10), as the eye hurricane was moving back to the south (figure 5.2). This is the only data available for large hurricane-swell forcing conditions, with near-sheet flow conditions (the sheet flow conditions indicated in figure 2.12 correspond to the peak of the storm a few hours earlier, on the morning of 18 November). In the strongest forcing conditions the JONSWAP source term largely overestimates the wave height. As the dissipation factor is expected to *increase* with the onset of sheet flow, the JONSWAP source term, with a *decreasing* dissipation factor, may systematically overpredict wave heights in sheet flow conditions.

In contrast the standard Tolman source term $S_{\text{fric,T}}$ significantly underestimates wave height in active ripple conditions (figure 5.14g–i). If the ripples (observed on most of the shelf, chapter IV) had been as rough than those in Madsen's (1990) laboratory experiments, $S_{\text{fric,T}}$ should give reasonable wave heights. The observed discrepancies suggest that ripples in the field are significantly smoother than in the laboratory. This may be due to the directional spreading of natural waves, as well as the initial bed configuration. Both may increase the shape of the ripple crests and the number of defects in the ripple pattern, and modify the equilibrium bed configuration. A reduction of the maximum ripple roughness by a factor 4 gives better agreement with the DUCK94 and SHOWEX data (run 4c, using $S_{\text{fric,I}}$, figure 5.14j–l).

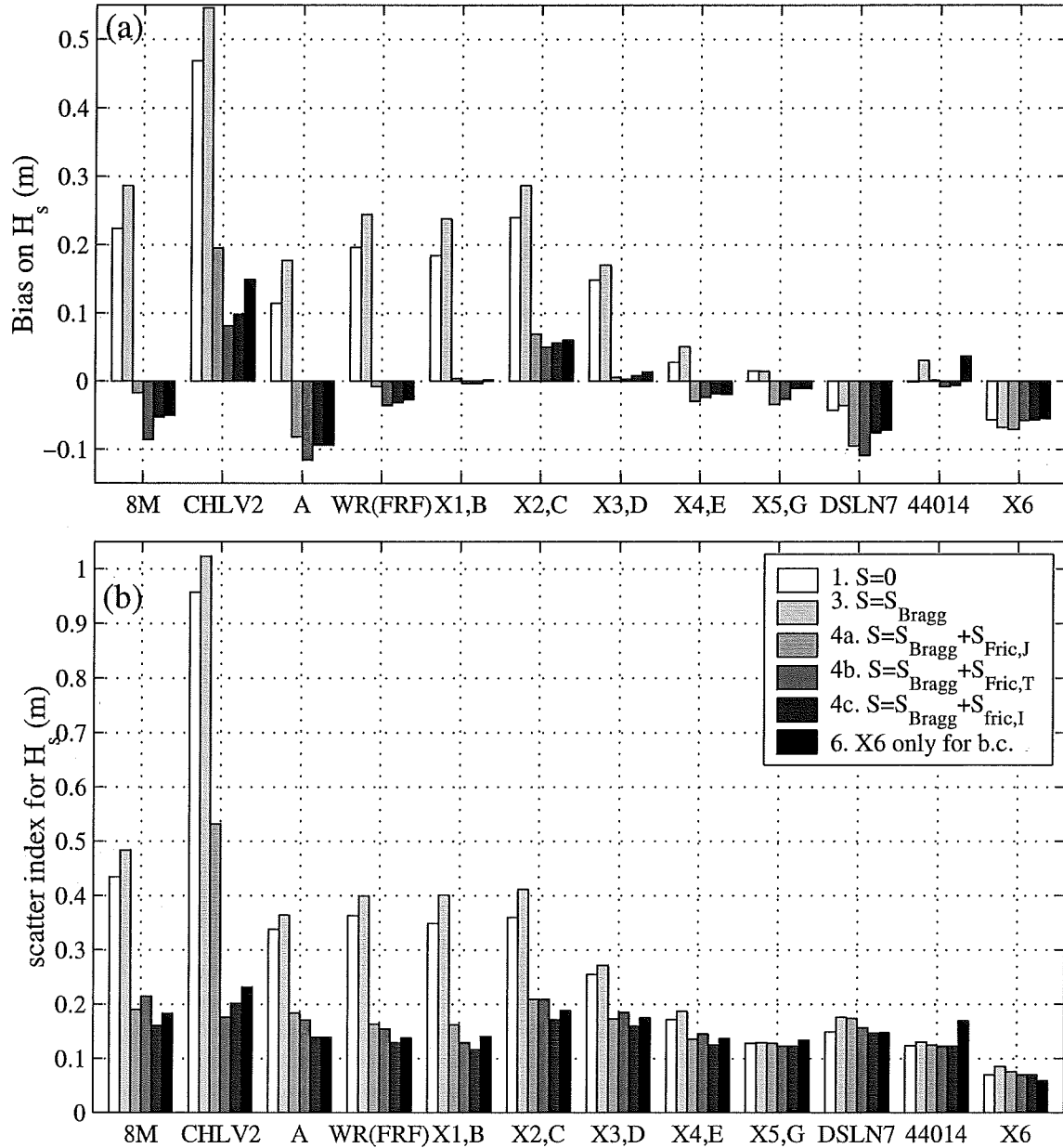


Figure 5.13: Model errors in predictions of the significant wave heights H_s .

(a) Model bias and (b) scatter index (ratio of r.m.s. error and r.m.s. value) for H_s , in swell-dominated periods observed during SHOWEX and DUCK94. Run 1 includes no source terms (refraction and shoaling only), run 3 includes wave-bottom Bragg scattering, and different friction source terms are added in runs 4a (JONSWAP) 4b (Tolman) and 4c (improved Tolman). Source terms in run 6 are identical to those in run 4c, but only X6 data is used for the offshore boundary condition in SHOWEX cases instead of a linear interpolation of X6 and 44014 data. For DUCK94 cases the offshore boundary condition is obtained from 44014.

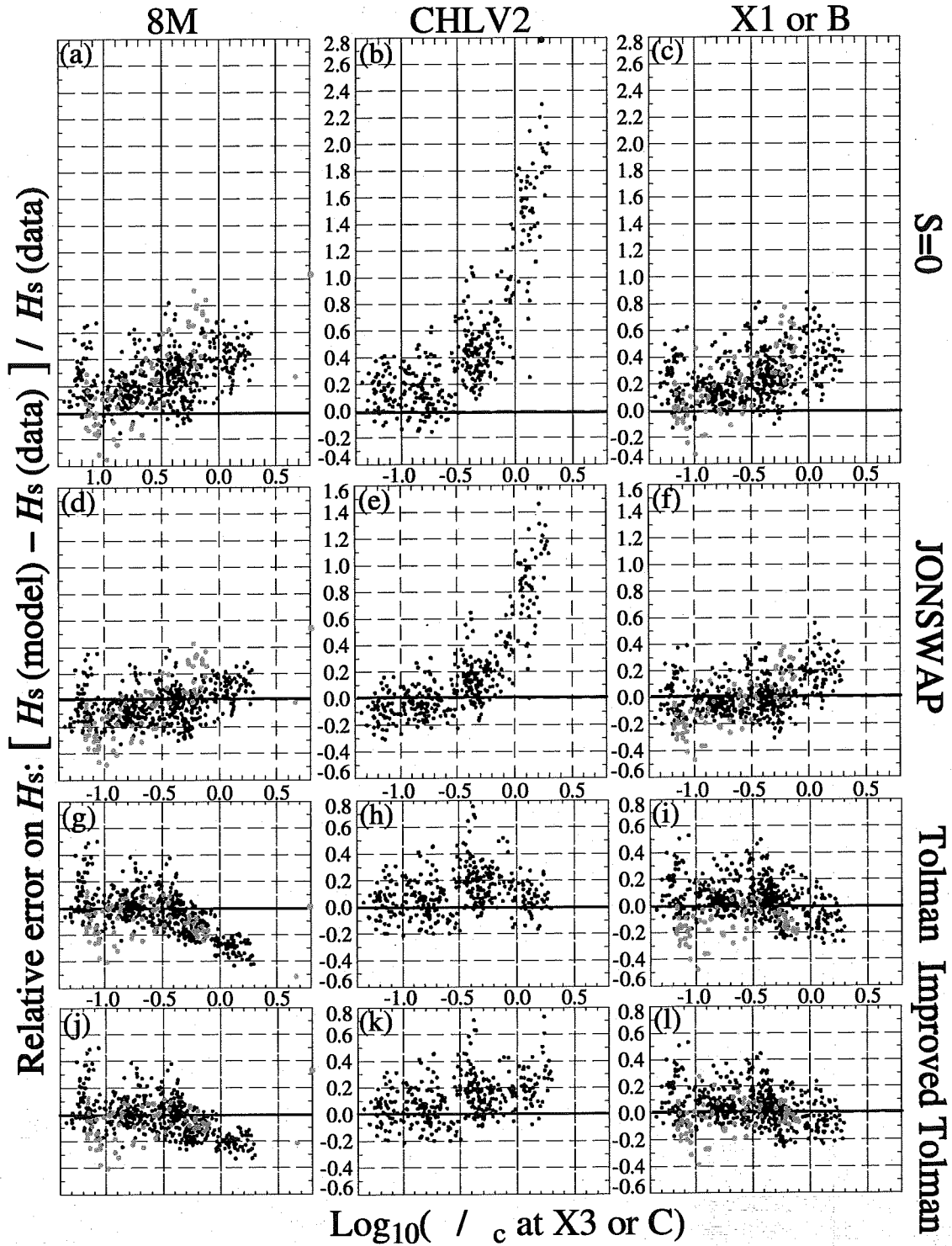


Figure 5.14: Relative error of H_s predictions as a function of the Shields number. Errors are computed at different sensors indicated at the top of each column, for different source terms, (a-c) $S = 0$, (d-f) $S = S_{\text{fric},J} + S_{\text{Bragg}}$, (g-i) $S = S_{\text{fric},T} + S_{\text{Bragg}}$, (j-l) $S = S_{\text{fric},I} + S_{\text{Bragg}}$. Larger red dots correspond to 3-hour DUCK94 records and smaller black dots correspond to 1-hour SHOWEX records.

The present dataset is too limited to address effects of past history of the bedforms, and there is no clear indication that the ripple roughness should be different between wave events with increasing, stable, or decreasing forcing conditions. The behavior of $S_{\text{fric,T}}$ and $S_{\text{fric,I}}$ seems acceptable in the strong forcing conditions prevailing during the Hurricane Gordon event, although more data would be needed for a more quantitative assessment.

4. Model errors and offshore boundary

Errors are not zero at the buoy (X6 and/or 44014) used to provide the offshore boundary condition, as only incoming waves are used for the forcing whereas the outgoing waves are radiated by the model. Errors are also introduced by the numerical propagation and interpolation between the buoy and the grid boundary.

Errors at X6, when the boundary condition is determined from X6 data only (run 6), are entirely the result of the difference between outgoing waves predicted by the model and caused by refraction and back-scattering, and those estimated from the buoy data using the Maximum Entropy Method. Since this method is only constrained to fit the first four Fourier components of the directional spectra, it may give significant errors for these outgoing waves that usually carry very little energy, compared to the incoming waves. The corresponding r.m.s. error on the mean direction is 5° , and the scatter indices for $\sigma_{\theta,p}$ and H_s are 0.18 and 0.06, respectively.

For this same run 6, errors at 44014 are enhanced (11° r.m.s. for θ_p , and scatter indices for $\sigma_{\theta,p}$ and H_s of 0.33 and 0.17, respectively) possibly due to propagation errors across the shelf break, but also likely caused by spatial variations in the offshore wave field, over the 60 km separating X6 and 44014. These offshore variations may be caused in part by wave-current refraction in the Gulf Stream and its eddies (Holthuijsen & Tolman, 1991), often seen along the shelf break in sea surface temperature satellite images. This effect should be strongest at high frequencies and could explain the fact that the energy difference between X6 and 44014 for remotely generated swells is either constant or increases with increasing frequency. The errors on the directional spread $\sigma_{\theta,p}$ may also be influenced by differences in the response between a Waverider buoy (X6) and a 3-m discus pitch and roll buoy (44014), the latter giving generally larger directional spreads (O'Reilly *et al.*, 1996).

These errors in run 6 give an order of magnitude for the model errors due to the treatment of the boundary condition in all other runs. The imperfect knowledge of the variations in the wave field along the shelf break is probably a major source of errors in runs 4a-c. Based on errors at 44014 and X6, contribution to the scatter indices resulting from boundary condition errors is estimated to about 0.1 for H_s and 0.15 for $\sigma_{\theta,p}$. In view of this high background error in the treatment of boundary conditions, the energy balance (5.1) gives a good description of swell evolution.

E. Summary and practical implications

The numerical model CREST was implemented on a large portion of the North Carolina-Virginia continental shelf for a comprehensive hindcast of all swell-dominated conditions observed during the experiments DUCK94 and SHOWEX. The model integrates the energy balance (5.1) from deep water (1500 m depth) to the inner shelf (8 m depth), with little numerical diffusion, allowing detailed comparison of measured wave parameters with results obtained using various sets of source terms. The effect of the small-scale (comparable to the surface wavelength) shelf topography, was represented by a wave-bottom Bragg scattering source term, assuming uniform statistics determined from high-resolution bathymetric surveys, explains most of the observed broadening of the wave spectrum towards the shore, that occasionally balances the narrowing caused by refraction over the quasi-plane large-scale bathymetry. Predicted directional spectra are nevertheless still too narrow on the inner shelf (by about 20% compared to 50% for hindcasts without Bragg scattering), maybe as a result of wave reflection from the beach, anisotropy in the bottom friction source term, and/or

higher order wave-bottom Bragg scattering, that are not represented in the present model. The strong attenuation of large swells (inferred dissipation up to 84% of the incident wave energy flux) is well reproduced by Tolman's (1994) bottom friction source term, that accounts for the generation of sand ripples by waves and their feedback on the waves. Including this source term into the spectral refraction model reduces the scatter index for the significant wave heights H_s from 0.27 to 0.15. A large fraction of the remaining error may be due to the imperfect knowledge of the offshore boundary condition which may cause a scatter of 0.1 on the outer shelf, in predictions of H_s by a perfect model.

The widely used JONSWAP source term gives slightly larger errors on average (overall scatter index equal to 0.16), but occasionally causes much larger errors than the Tolman source term, because it does not account for large increases in bottom roughness under active ripple conditions. Tolman's (1994) movable bed model tends to overestimate dissipation in strong forcing conditions, suggesting that ripples in the field are significantly smoother than in Madsen *et al.*'s (1990) laboratory experiments, that were used to calibrate the empirical ripple roughness. The reason for this difference between laboratory and field conditions is not clear but may be caused by the universal presence of relic bedforms in the field, and the directional spreading of natural waves. An ad hoc reduction of the ripple roughness by a factor 4 improves the hindcast results and reduces the overall scatter index for the wave heights from 0.15, for Tolman's (1994) source term, to 0.13.

Overall the energy balance (5.1) with a bottom friction source term, dissipating swell energy, and a wave-bottom Bragg scattering source term (chapter III), broadening the directional spectrum in the cases presented here, provides a good description of swell evolution across the North Carolina continental shelf. In addition to the direct local effects of each source term, the numerical integrations of (5.1) reveal indirect effects coupling the source terms as waves propagate over a finite distance. Bottom friction reduces the directional spread since obliquely traveling waves are more exposed to dissipation as they propagate for a longer distance (and time) across the shelf, while Bragg scattering lengthens the average propagation distance. In the absence of dissipation this longer propagation may yield larger wave heights, in a way similar to shoaling waves propagating straight towards the shore: the onshore energy flux is conserved, but the average onshore group speed is reduced by scattering into obliquely traveling components, so that the wave height must increase. However, in the presence of dissipation the opposite happens: the wave height is reduced because these obliquely propagating waves have more time to be dissipated.

VI. CONCLUSIONS AND PERSPECTIVES

The work presented in the previous chapters focused on the physical processes and numerical prediction of the evolution of swell in shallow water, using new high-quality field data from the North Carolina continental shelf.

A new numerical wave model named CREST (Coupled Rays with Eulerian Source Terms) was presented in chapter II, that integrates in time an energy balance equation for the evolution of the wave frequency-directional spectrum. The novelty of this model resides in its hybrid numerical scheme. It couples inverse ray trajectories adopted from Lagrangian models, tracing back the paths followed by wave groups, and a modification of the wave energy along these paths using a spectral source term. The source term, evaluated on the Eulerian grid from which the rays are traced, and interpolated onto these rays, prescribes how the energy of each component changes in time based on the entire wave spectrum and environmental factors such as the bottom sediment nature and the wind speed. This hybrid method essentially eliminates the numerical diffusion of finite difference schemes, allowing accurate and high-resolution predictions of the wave spectrum. We demonstrated that this numerical method can be applied to a large area (100 km \times 400 km for the North Carolina-Virginia continental shelf) and implemented it on a modern workstation, because the grid, on which source terms are evaluated, can be much coarser than the bathymetry grid used for the ray computations. Although detailed comparisons have still to be made, it can be expected that the computational cost of the Lagrangian advection scheme in its present form is comparable to or larger than the cost of a finite-difference scheme, which uses higher resolution grids to resolve scales responsible for depth refraction. However the new model is expected to be more efficient for the prediction of the generation and non-linear evolution of wind sea spectra, because the costly source term computation in finite difference models is performed on the same high-resolution grid as the advection, while it is done on a coarse source term grid in the present model. CREST may therefore be used as a research community tool for hindcasting wind seas with exact calculations of the quartet wave-wave interaction source term. The computational cost of CREST may be reduced by adopting so-called 'piecewise ray' methods that use rays ray segments over single time steps (e.g. the TOMAWAC model, Benoit *et al.*, 1996). Practical trade-off criteria should be determined for choosing intermediate schemes with ray advection over several time steps, reducing the numerical cost at the expense of numerical diffusion. These cost-saving measures may promote an operational or engineering use of the code as computers keep getting faster. However, the hybrid Eulerian-Lagrangian scheme, in its present form, cannot handle time-varying depth and strong variable currents that are important for wave evolution in macrotidal coastal regions (e.g. the North Sea, the English Channel, or the French Atlantic continental shelf), where ray trajectories vary in time.

Complementing earlier wave observations made on the North Carolina continental shelf during the DUCK94 experiment, a new experiment, SHOWEX, provided high-quality directional wave measurements across the same region, over a three-month period with a wide range of wave conditions. CREST was implemented on the North Carolina continental shelf and produced hindcasts of swell observed during both experiments, used to quantitatively evaluate wave-bottom interactions in the absence of currents. The evolution of swell in moderately shallow water is essentially influenced by the bottom topography at all scales. The field data and model results confirmed that large features with horizontal dimensions much larger than the wavelength cause well-known refraction and shoaling effects, such as increased wave heights around headlands, and provided new insights into the effects of smaller scale bottom topography and roughness.

Bottom undulations with horizontal scales comparable to the surface wavelengths cause directional scattering of waves through a Bragg resonance. In a spectral description this wave-bottom interaction can be represented, at the lowest order in the bottom and surface slopes, as interactions among triads of two wave components with the same frequency, exchanging energy,

and a bed undulation with the difference vector wavenumber that makes this exchange possible. The evolution of the wave spectrum caused by this triad interaction was derived in the form of a spectral source term S_{Bragg} by Hasselmann (1966), using a Hamiltonian formalism, and Long (1973) showed that it could cause significant back-scattering (i.e. reflection) of swell towards deeper waters for a realistic bottom elevation spectrum. Here the theory was extended to slowly varying random waves and bottom elevations on a sloping shelf, and a correction of the coupling coefficient was given. Hindcasts of swell transformation across the North Carolina shelf, marked by gentle sand ridges with spacings of 1 km or more, showed that back-scattering is insignificant, but 'forward scattering' (the interacting waves have almost the same direction) increases the directional spread of the wave spectrum. This unexpected effect, not considered in previous studies, opposes directional narrowing resulting from depth refraction. The combination of these two processes in CREST, a numerical model with little numerical diffusion, yields directional spread hindcasts that agree well with directional wave measurements from SHOWEX. In 8–15 m depth the use of the Bragg scattering source term increases the predicted spread by a factor 2–3, in particular for low frequency swell. Applications to other regions where detailed bathymetric information and directional wave data is available should provide further verification of the wave-bottom Bragg scattering theory for random waves and topography. Such studies should encourage new work on the practical implications of higher order theories and effects of currents on the wave-bottom interactions. Wave-bottom Bragg scattering is the simplest resonant interaction involving surface gravity waves, but it shares some properties of the non-linear wave-wave interactions. Thus the ideas developed in chapter III on the detuning effects of the bottom slope on the resonant interactions may be applied to wave-wave interactions, providing practical guidelines for the use of resonant interaction theory in varying depth.

At scales smaller than the wave orbital motion, sand ripples and biogenic mounds on the seabed contribute to the bed roughness experienced by the waves. It is well-known that non-cohesive sediments are mobilized by sufficiently energetic wave conditions forming 'vortex ripples' that dramatically enhance dissipation of the wave energy. Widespread ripple marks were observed across the North Carolina using sidescan sonar (chapter IV). The combination of sonar surveys and time-series of wave observations established their 'vortex ripple' nature, consistent recent observations in shallower water. A parameterization for the dissipation source term S_{fric} of wave energy by bottom friction over these bedforms was proposed by Madsen *et al.* (1990), based on careful laboratory experiments. It was tested for the first time against field data from the DUCK94 experiment (chapter II). The model hindcasts reproduces well the observed swell attenuation across the shelf, but Madsen *et al.*'s (1990) parameterization tends to overestimate dissipation in ripple-forming conditions.

A comprehensive analysis of all swell-dominated conditions observed during DUCK94 and SHOWEX was conducted to objectively examine the performance of bottom friction parameterizations, and propose empirical adjustments (chapter V). The effect of Bragg scattering was included in the source term together with various bottom friction parameterizations. The widely used empirical 'JONSWAP' parameterization of the bottom friction gives average errors similar to Tolman's (1994) source term that uses Madsen *et al.*'s (1990) ripple roughness. However the JONSWAP source term grossly underestimates the swell decay in active ripple conditions.

A modification of Tolman's bottom friction source term, increasing the roughness of relic bedforms as a function of the wave forcing, and reducing the roughness of actively generated vortex ripples by a factor 4, improves the hindcast accuracy. These results suggest that natural ripples formed by a directionally spread wave field are less rough than those generated by uni-directional waves in wave flumes. Both Madsen *et al.*'s (1990) parameterization and the one presented here are based on dissipation rates inferred from observed wave attenuation. A true verification of the parameterization requires detailed measurements of the properties of the bottom boundary layer under waves in realistic conditions. Reynolds stress profiles measured by T. Stanton & E. Thornton during SHOWEX, should help constrain parameterizations of the ripple roughness and the directional properties of the bottom friction source term.

In addition to the direct local effects of bottom friction (dissipating swell energy) and Bragg scattering (broadening the directional spectrum), indirect effects couple these source terms as waves propagate over a finite distance. Bottom friction reduces the directional spread since obliquely travelling waves are more exposed to dissipation as they propagate for a longer distance (and time) across the shelf, while Bragg scattering lengthens the average propagation distance. In the absence of dissipation this longer propagation may yield larger wave heights. However, in the presence of dissipation the opposite happens: the wave height is reduced because these obliquely propagating waves have more time to be dissipated. This interaction of the source terms in the energy balance equation shows that one source term cannot be considered in isolation, unless all others are negligible. It also emphasizes the importance of the directional distribution of wave energy for nearshore wave height predictions.

Theories and parameterizations for wave-bottom interactions were examined here only for waves in the swell frequency band at a single site. The same interactions however also affect waves in the infragravity band (0.01–0.05 Hz) and the wind sea band (0.1–1 Hz). Extension and verification of the present work into these other frequency domains and other shallow water regions is needed for a comprehensive validation of S_{fric} and S_{Bragg} formulations. Incorporating these validated source terms in the wind sea energy balance may help improve parameterizations of other source terms: wind input, and dissipation due to deep-water wave breaking. In the absence of wind forcing, the present work establishes that the transformation of swell across a sandy continental shelf is well described by the energy balance equation

$$\frac{dE(\mathbf{k})}{dt} = S_{\text{fric}}(\mathbf{k}) + S_{\text{Bragg}}(\mathbf{k}), \quad (6.1)$$

where the bottom friction source term parameterizes movable bed processes: relic roughness, vortex ripple formation, and sheet flow. On the wide and shallow shelf of North Carolina, these effects are locally weak: energy dissipation is of the order of 0.1–10 W m⁻² compared to a typical energy flux of 10–100 kW m⁻¹, but they add up to a strong attenuation as waves propagate across the shelf, occasionally reducing the wave heights of large swells by more than 50 %. The formation of vortex ripples is therefore among the most important processes for the nearshore wave climate.



Figure 6.1: Singing sands, lake Huron, 28 April 2001
Sand ripples, waves, and capillary 'Wilton ripples'. From auto-organization to resonant wave-wave interactions. Photo by Fanny Girard-Arduin.

APPENDIX A: DERIVATION OF THE ENERGY BALANCE (3.47)

A. Derivation of $E_{2,2}(\mathbf{k})$

The governing equation (3.34) for $\Phi_{2,\mathbf{k}}^s(t)$ is an undamped forced harmonic oscillator with a resonant frequency ω given by the dispersion relation (3.28). Applying a Fourier decomposition to the right hand side forcing terms, (3.34) can be written as a linear superposition of equations of the type

$$\frac{d^2 f_1}{dt^2} + \omega^2 f_1 = e^{i\omega' t}. \quad (\text{A.1})$$

In order to specify a unique solution to (A.1), initial conditions must be prescribed. In the limit of large propagation distances the initial conditions contribute a negligible bounded term to the solution. Following Hasselmann (1962), we chose $f_1(0) = 0$ and $df_1/dt(0) = 0$, giving the solution

$$f_1(\omega, \omega'; t) = \frac{e^{i\omega' t} - e^{i\omega t} + i(\omega - \omega') \sin(\omega t) / \omega}{\omega^2 - \omega'^2} \quad \text{for } \omega'^2 \neq \omega^2, \quad (\text{A.2})$$

$$f_1(\omega, \omega'; t) = \frac{te^{i\omega' t}}{2i\omega'} - \frac{\sin(\omega t)}{2i\omega'\omega} \quad \text{for } \omega' = \pm\omega. \quad (\text{A.3})$$

$\Phi_{2,\mathbf{k}}^s(t)$ is given by

$$\Phi_{2,\mathbf{k}}^s(t) = \sum_{\mathbf{k}'} A(\mathbf{k}, \mathbf{k}') B_{\mathbf{k}-\mathbf{k}'} \widehat{\Phi}_{1,\mathbf{k}'}^s f_1(\omega, -s\omega'; t), \quad (\text{A.4})$$

where

$$A(\mathbf{k}, \mathbf{k}') = [k - \omega'^2 \tanh(kH)] \frac{\mathbf{k} \cdot \mathbf{k}'}{k}. \quad (\text{A.5})$$

The third-order energies $E_{1,2}$ and $E_{2,1}$ that result from the correlations between $\Phi_{1,s\mathbf{k}}^s$ and $\Phi_{2,-s\mathbf{k}}^s$ (A.4) are found to be bounded but the fourth order energy $E_{2,2}$ grows with time. Substituting (A.4) in (3.16) and taking the limit (3.17) to a continuous spectrum yields the solution for $E_{2,2}(t, \mathbf{k})$ as defined by (3.25):

$$E_{2,2}(t, \mathbf{k}) = \int_0^\infty \int_0^{2\pi} A(\mathbf{k}, \mathbf{k}') F^B(\mathbf{k} - \mathbf{k}') E_2(\tilde{t}, \mathbf{k}') |f_1(\omega, -\omega'; t)|^2 dk' d\theta' + \dots, \quad (\text{A.6})$$

where $\mathbf{k}' = k'(\cos\theta', \sin\theta')$, and the omitted terms (...) include bounded terms forced by surface non-linearity. Assuming that the frequency spectrum is continuous, the contribution of exact resonant interactions ($k' = k$) to (A.6) is negligible compared to contributions of near-resonant interactions ($k' \approx k$) that span a finite range of wavenumbers, and thus (A.2) can be substituted in (A.6). We now change the integration variable k' to ω' , given by the dispersion relation (3.28), and replace $|f_1|^2$ by the expansion in powers of $(\omega - \omega')$,

$$|f_1(\omega, -\omega')|^2 = \frac{2 - 2 \cos[(\omega - \omega')t] + O(\omega - \omega')}{4\omega^2 (\omega - \omega')^2} \quad (\text{A.7})$$

The leading term in this expansion is the real part of a function of the complex variable $z = (\omega - \omega')$, $(1 - e^{izt}) / (2\omega^2 z^2)$, which is differentiable with respect to z on the entire Argand-Cauchy plane, except at $z = 0$. The integral $\int_0^\infty |f_1|^2 d\omega'$ cuts through that singularity and its value $\pi t / (2\omega^2)$ can be

obtained by contour integration on the complex plane. Other terms in (A.6) are continuous so that they can be considered constant in a small region around the singularity and we obtain

$$E_{2,2}(t, \mathbf{k}) = t \int_0^{2\pi} \frac{4\pi\omega k^4 \cos^2(\theta - \theta')}{\sinh(2kH) [2kH + \sinh(2kH)]} F^B(\mathbf{k} - \mathbf{k}') E_2(\tilde{t}, \mathbf{k}') d\theta' + \text{bounded terms}, \quad (\text{A.8})$$

For large t the derivative of $E_{2,2}(t, \mathbf{k})$ with respect to t yields equation (3.35).

B. Derivation of $E_{3,1}^{\text{sc}}(\mathbf{k}) + E_{1,3}^{\text{sc}}(\mathbf{k})$

The particular solution ϕ_3^{sc} to (3.37)–(3.39) in the vicinity of $\mathbf{x} = \mathbf{0}$ can be written as

$$\phi_3^{\text{sc}}(\mathbf{x}, z, t) = \sum_{\mathbf{k}, s} \left[\Phi_{3,\mathbf{k}}^s(t) \frac{\cosh(kz + kH)}{\cosh(kH)} + \Phi_{3,\mathbf{k}}^{\text{si},s}(t) \frac{\sinh(kz + kH)}{\cosh(kH)} \right] e^{i\mathbf{k}\cdot\mathbf{x}}. \quad (\text{A.9})$$

The solution for the bound component $\Phi_{3,\mathbf{k}}^{\text{si},s}$ follows from substituting the second-order velocity potential (3.32) in the bottom boundary condition (3.38 with term V set to zero)

$$\Phi_{3,\mathbf{k}}^{\text{si},s}(t) = - \sum_{\mathbf{k}'} \frac{\mathbf{k} \cdot \mathbf{k}'}{k} B_{\mathbf{k}-\mathbf{k}'} \Phi_{2,\mathbf{k}}^s(t). \quad (\text{A.10})$$

Substitution of (A.10) in the surface boundary condition (3.39 with the right-hand side set to zero) yields the forced harmonic oscillator equation

$$\left(\frac{d^2}{dt^2} + \omega^2 \right) \Phi_{3,\mathbf{k}}^s = - \sum_{\mathbf{k}'} \frac{\mathbf{k} \cdot \mathbf{k}'}{k} B_{\mathbf{k}-\mathbf{k}'} \left[\left(k + \tanh(kH) \frac{d^2}{dt^2} \right) \Phi_{2,\mathbf{k}'}^s(t) \right]. \quad (\text{A.11})$$

Using (3.34) and (A.4) we have

$$\begin{aligned} \left(\frac{d^2}{dt^2} + \omega^2 \right) \Phi_{3,\mathbf{k}}^s &= - \sum_{\mathbf{k}'} A(\mathbf{k}, \mathbf{k}') B_{\mathbf{k}-\mathbf{k}'} \sum_{\mathbf{k}''} A(\mathbf{k}', \mathbf{k}'') B_{\mathbf{k}'-\mathbf{k}''} \hat{\Phi}_{1,\mathbf{k}''}^s f_1(\omega', -s\omega''; t) \\ &\quad - \sum_{\mathbf{k}'} \frac{\mathbf{k} \cdot \mathbf{k}'}{k} \tanh(kH) B_{\mathbf{k}-\mathbf{k}'} \sum_{\mathbf{k}''} A(\mathbf{k}', \mathbf{k}'') B_{\mathbf{k}'-\mathbf{k}''} \Phi_{1,\mathbf{k}''}^s(t), \end{aligned} \quad (\text{A.12})$$

where A is defined by (A.5). The only terms of (A.12) that force growing correlations with ϕ_1 are those that have a product of two factors A and equal wavenumbers $\mathbf{k}'' = \mathbf{k}$. Other terms force bounded correlations and can be neglected. Therefore (A.12) can be regarded as a linear combination of forced oscillator equations of the form

$$\frac{d^2 f_2}{dt^2} + \omega^2 f_2 = f_1(\omega', -s\omega, t). \quad (\text{A.13})$$

The solution of (A.13) for $\omega'^2 \neq \omega^2$ and initial conditions $f_2(0) = df_2/dt(0) = 0$ is

$$f_2(\omega, \omega', s; t) = - \frac{te^{i\omega t} - \sin(\omega t)/\omega}{2is\omega(\omega'^2 - \omega^2)} - \frac{(\omega' + \omega)e^{i\omega' t} + (\omega' - \omega)e^{-i\omega' t} - 2\omega'e^{i\omega t}}{2\omega'(\omega'^2 - \omega^2)^2}. \quad (\text{A.14})$$

Following the steps of § A.A, we obtain

$$E_{3,1}^{\text{sc}}(t, \mathbf{k}) + E_{1,3}^{\text{sc}}(t, \mathbf{k}) = -t \int_0^{2\pi} \frac{4\pi\omega k^4 \cos^2(\theta - \theta')}{\sinh(2kH) [2kH + \sinh(2kH)]} F^B(\mathbf{k} - \mathbf{k}') E_2(\tilde{t}, \mathbf{k}) d\theta' + \text{bounded terms}. \quad (\text{A.15})$$

Taking the derivative of (A.15) with respect to t yields equation (3.41).

C. Derivation of $E_{3,1}^{\text{NS}}(\mathbf{k}) + E_{1,3}^{\text{NS}}(\mathbf{k})$

In the vicinity of $\mathbf{x} = \mathbf{0}$, ϕ_3^{NS} can be written in the form

$$\phi_3^{\text{NS}} = \sum_{\mathbf{k},s} \frac{\cosh(kz + kH)}{\cosh(kH)} \Phi_{3,\mathbf{k}}^s(t) e^{i\mathbf{k}\cdot\mathbf{x}},$$

where $\Phi_{3,\mathbf{k}}^s$ satisfies

$$\left(\frac{d^2}{dt^2} + \omega^2\right) \Phi_{3,\mathbf{k}}^s = 2is\omega \frac{\partial \widehat{\Phi}_{1,\mathbf{k}}^s}{\partial t} e^{-is\omega t}, \quad (\text{A.16})$$

With the solution given by eq. (A.3):

$$\Phi_{3,\mathbf{k}}^s(t) = -t \frac{\partial \widehat{\Phi}_{1,\mathbf{k}}^s}{\partial t} e^{-is\omega t}. \quad (\text{A.17})$$

This solution is correlated with the first order velocity potential, giving the energy contribution at $\tilde{\mathbf{x}} = \mathbf{0}$

$$E_{3,1}^{\text{NS}}(t, \mathbf{k}) + E_{1,3}^{\text{NS}}(t, \mathbf{k}) = -t \frac{\partial E_2(\tilde{t}, \mathbf{k})}{\partial t} + \text{bounded term}. \quad (\text{A.18})$$

Taking the derivative of (A.18) with respect to t yields (3.42).

D. Derivation of $E_{3,1}^{\text{he}}(\mathbf{k}) + E_{1,3}^{\text{he}}(\mathbf{k})$

Terms I and II in (3.37) can be written as

$$\begin{aligned} \text{I} + \text{II} &= \sum_{\mathbf{k},s} \frac{e^{i\mathbf{k}\cdot\mathbf{x}}}{\cosh(kH)} \{ \cosh(kz + kH) (\nabla \cdot \mathbf{k}_r + 2\mathbf{k} \cdot \nabla) \\ &\quad + 2[(z + H) \sinh(kz + kH) - H \tanh(kH) \cosh(kz + kH)] \mathbf{k} \cdot \nabla k_r \\ &\quad + 2[k \sinh(kz + kH) - k \tanh(kH) \cosh(kz + kH)] \mathbf{k} \cdot \nabla H \} \Phi_{1,\mathbf{k}}^s(t). \end{aligned} \quad (\text{A.19})$$

In the vicinity of $\mathbf{x} = \mathbf{0}$ we can write the solution to (3.37) as

$$\begin{aligned} \phi_3^{\text{he}} &= \sum_{\mathbf{k},s} \frac{\cosh(kz + kH)}{\cosh(kH)} \left[(z + H)^2 \Phi_{3,\mathbf{k}}^{\text{coz},s}(t) + (z + H) \Phi_{3,\mathbf{k}}^{\text{coz},s}(t) + \Phi_{3,\mathbf{k}}^s(t) \right] e^{i\mathbf{k}\cdot\mathbf{x}} \\ &\quad + \frac{\sinh(kz + kH)}{\cosh(kH)} \left[(z + H) \Phi_{3,\mathbf{k}}^{\text{siz},s}(t) + \Phi_{3,\mathbf{k}}^{\text{siz},s}(t) \right] e^{i\mathbf{k}\cdot\mathbf{x}}, \end{aligned} \quad (\text{A.20})$$

where

$$\begin{aligned} \Phi_{3,\mathbf{k}}^{\text{siz},s}(t) &= \frac{-i}{2k} (\Phi_{1,\mathbf{k}}^s(t) \nabla \cdot \mathbf{k}_r + 2\mathbf{k} \cdot \nabla \Phi_{1,\mathbf{k}}^s(t)) \\ &\quad + i \frac{\Phi_{1,\mathbf{k}}^s(t)}{k} \mathbf{k} \cdot \left\{ \left[H \tanh(k_r H) + \frac{1}{2k} \right] \nabla k_r + k \tanh(kH) \nabla H \right\} \end{aligned} \quad (\text{A.21})$$

$$\Phi_{3,\mathbf{k}}^{\text{coz},s}(t) = -i \Phi_{1,\mathbf{k}}^s(t) \frac{\mathbf{k} \cdot \nabla k_r}{2k}, \quad (\text{A.22})$$

$$\Phi_{3,\mathbf{k}}^{\text{coz},s}(t) = -i \Phi_{1,\mathbf{k}}^s(t) \mathbf{k} \cdot \nabla H, \quad (\text{A.23})$$

and the remaining two terms follow from the bottom and surface boundary conditions. Substituting (A.20)–(A.23) in the bottom boundary condition (3.38, with III and IV set to zero) gives

$$\Phi_{3,\mathbf{k}}^{\text{si},s}(t) = 0. \quad (\text{A.24})$$

Substituting (A.20)–(A.24) in the surface boundary condition (3.39 with VI set to zero) yields a forced harmonic oscillator equation for $\Phi_{3,\mathbf{k}}^s(t)$:

$$\begin{aligned} \left(\frac{d^2}{dt^2} + \omega^2 \right) \Phi_{3,\mathbf{k}}^s(t) &= isge^{-is\omega t} \left\{ \left[\frac{\tanh(kH) + kH [1 - \tanh^2(kH)]}{k} \right] \right. \\ &\times \left[\nabla \cdot \mathbf{k}_r + \mathbf{k}_r \cdot \nabla + 2\mathbf{k} \cdot \left[\left(H \tanh(kH) + \frac{1}{2k} \right) \nabla k_r + k \tanh(kH) \nabla H \right] \right] \\ &\left. + \frac{H}{k} \mathbf{k} \cdot \nabla k_r + \mathbf{k} \cdot \nabla H \right\} \hat{\Phi}_{1,\mathbf{k}}^s. \end{aligned} \quad (\text{A.25})$$

(A.25) is of the same form as (A.1) with only resonant forcing terms ($\omega' = \pm\omega$) and a solution given by (A.3). The covariance of $\Phi_{3,\pm\mathbf{k}}^\pm$ and the first order potential, defined by (3.16), is given by

$$\begin{aligned} F_{3,1,\mathbf{k}}^{\Phi,\text{he}} &= -t \frac{C_g}{2k} \nabla \cdot (\mathbf{k}_r F_{1,1,\mathbf{k}}^\Phi) \\ &+ t \frac{C_g}{k} \mathbf{k} \cdot \left[\left(H \tanh(kH) + \frac{1}{2k} \right) \nabla k_r + k \tanh(kH) \nabla H \right] F_{1,1,\mathbf{k}}^\Phi \\ &- \frac{t\omega}{k^2 \tanh(kH)} \mathbf{k} \cdot (H \nabla k_r + k \nabla H) F_{1,1,\mathbf{k}}^\Phi + \text{bounded term}, \end{aligned} \quad (\text{A.26})$$

where C_g is the group speed

$$C_g = \frac{\omega}{k_r} \left[\frac{1}{2} + \frac{k_r H}{\sinh(2k_r H)} \right], \quad (\text{A.27})$$

and the bounded term is given by the initial conditions (the second right hand side term in A.3). From the dispersion relation (3.28) we find

$$\nabla H = -\frac{2kH + \sinh(2kH)}{2k^2} \nabla k_r, \quad (\text{A.28})$$

and

$$\frac{\nabla [C_g \tanh(k_r H)]}{k \tanh(kH)} = -\frac{\omega}{2k^3} \left\{ 3 + \frac{2kH}{\sinh(2kH)} - 2kH \tanh(kH) \right\} \nabla k_r. \quad (\text{A.29})$$

Using (A.28),(A.29), and the definition of the Lagrangian energy spectrum $E_2(\mathbf{k}_r)$ (3.45), (A.26) reduces to

$$[E_{3,1}^{\text{he}}(\mathbf{k}) + E_{1,3}^{\text{he}}(\mathbf{k})] \Delta k_{r,x} \Delta k_{r,y} = -t \nabla \cdot (C_g E_2(\mathbf{k}_r) \Delta k_{r,x} \Delta k_{r,y}) + \text{bounded terms} \quad (\text{A.30})$$

Writing C_g as $(C_g \cos \theta, C_g \sin \theta)$, where θ is the local ray direction, the divergence term in (A.30) can be expressed in terms of intrinsic coordinates:

$$\nabla \cdot [C_g E_2(\mathbf{k}_r) \Delta k_{r,x} \Delta k_{r,y}] = \frac{\partial [C_g E_2(\mathbf{k}_r) \Delta k_{r,x} \Delta k_{r,y}]}{\partial r} + C_g E_2(\mathbf{k}_r) \Delta k_{r,x} \Delta k_{r,y} \frac{\partial \theta}{\partial n} \quad (\text{A.31})$$

where r and n are the local along-ray and ray-normal coordinates. Longuet-Higgins (1957, equations 6, 10 and 21) showed that (A.31) can be simplified using ray theory. Defining the small separation p of two rays that are parallel in the vicinity of $\tilde{\mathbf{x}} = \mathbf{0}$, we have

$$\frac{\partial \theta}{\partial n} = \frac{1}{p} \frac{\partial p}{\partial r} \quad (\text{A.32})$$

and

$$\frac{\partial (pC_g \Delta k_{r,x} \Delta k_{r,y})}{\partial r} = 0 \quad (\text{A.33})$$

Substituting (A.32) and (A.33) in (A.31), and taking the limit $|\Delta \mathbf{k}_r| \rightarrow 0$, we have

$$E_{3,1}^{\text{he}}(\mathbf{k}) + E_{1,3}^{\text{he}}(\mathbf{k}) = -tC_g \frac{\partial E_2(\mathbf{k}_r)}{\partial r} + \text{bounded term} . \quad (\text{A.34})$$

Finally the derivative of (A.34) with respect to t yields (3.43).

LIST OF REFERENCES

- AGNON, Y. & SHEREMET, A. 2000 Stochastic evolution models for nonlinear gravity waves over uneven topography. In *Advances in coastal and ocean engineering, vol. 6* (ed. P. L. F. Liu), pages 103–131. World Scientific, Singapore.
- ANDERSEN, K. H. 1999 The dynamics of ripples beneath surface waves and topics in shell models of turbulence. PhD thesis, Det Naturvidenskabelige Fakultet Københavns Universitet, [<http://mail.isva.dtu.dk/ken/Thesis.html>].
- ANDERSEN, K. H. 2001 A particle model of rolling grain ripples under waves. *Phys. of Fluids* **13** (1), 58–64.
- ANDERSEN, K. H. & FREDSSØE, J. 1999 How to calculate the geometry of vortex ripples. In *Proceeding of the Coastal Sediments conference*, pp. 78–93. ASCE.
- ARDHUIN, F., DRAKE, T. G. & HERBERS, T. H. C. 2001*a* Observations of wave-generated vortex ripples on the North Carolina continental shelf. *J. Geophys. Res.* **107**, submitted manuscript.
- ARDHUIN, F. & HERBERS, T. H. C. 2001 Bragg scattering of random surface gravity waves by irregular sea bed topography. *J. Fluid Mech.* In press.
- ARDHUIN, F., HERBERS, T. H. C. & O'REILLY, W. C. 2001*b* A hybrid Eulerian-Lagrangian model for spectral wave evolution with application to bottom friction on the continental shelf. *J. Phys. Oceanogr.* **31** (6), 1498–1516.
- ATHANASSOULIS, G. A. & BELIBASSAKIS, K. A. 1999 A consistent coupled-mode theory for the propagation of small amplitude water waves over variable bathymetry regions. *J. Fluid Mech.* **389**, 275–301.
- AYRTON, H. 1910 The origin and growth of the ripple mark. *Proc. Roy. Soc. of London* **A84**, 285–310.
- BAGNOLD, R. A. 1946 Motion of waves in shallow water, interaction between waves and sand bottoms. *Proc. Roy. Soc. of London* **A187**, 1–15.
- BELZONS, M., GUAZZELLI, E. & PARODI, O. 1988 Gravity waves on a rough bottom: experimental evidence of one-dimensional localization. *J. Fluid Mech.* **186**, 539–558.
- BELZONS, M., REY, V. & GUAZZELLI, E. 1991 Subharmonic bragg resonance for surface water waves. *Europhysics Letters* **16** (2), 189–194.
- BENJAMIN, T. B., BO CZAR-KARAKIEWICZ, B. & PRITCHARD, W. G. 1987 Reflection of water waves in a channel with corrugated bed. *J. Fluid Mech.* **185**, 249–274.
- BENNEY, D. J. & SAFFMAN, P. G. 1966 Nonlinear interactions of random waves in a dispersive medium. *Proc. Roy. Soc. Lond. A* **289**, 301–380.
- BENOIT, M., MARCOS, F. & BECQ, F. 1996 Development of a third generation shallow-water wave model with unstructured spatial meshing. In *Proceedings of the 25th international conference on coastal engineering*, pp. 465–478. ASCE.
- BLONDEAUX, P. 1990 Sand ripples under sea waves part 1. ripple formation. *J. Fluid Mech.* **218**, 1–17.

- BOOIJ, N., RIS, R. C. & HOLTHUIJSEN, L. H. 1999 A third-generation wave model for coastal regions. 1. model description and validation. *J. Geophys. Res.* **104** (C4), 7,649–7,666.
- BOUWS, E. & BATTJES, J. A. 1982 A Monte-Carlo approach to the computation of refraction of water waves. *J. Geophys. Res.* **87** (C8), 5,718–5,722.
- BOUWS, E. & KOMEN, G. J. 1983 On the balance between growth and dissipation in an extreme depth-limited wind-sea in the southern North Sea. *J. Phys. Oceanogr.* **13**, 1653–1658.
- BRETHERTON, F. P. & GARRETT, C. J. R. 1969 Wavetrains in inhomogeneous moving media. *Proc. Roy. Soc. of London* **A302**, 529–554.
- CARESS, D. W. & CHAYES, D. N. 1995 New software for processing sidescan data from sidescan-capable multibeam sonars. In *Proceedings of the IEEE Oceans 95 Conference*, pp. 997–1000. IEEE.
- CARTWRIGHT, D. E. & SMITH, N. D. 1964 Buoy techniques for obtaining directional wave spectra. In *Buoy technology, transactions of the International Buoy technology symposium, Washington, D. C.*, pp. 111–136. National Academy of Sciences, Marine Technology society.
- CAVALERI, L. & MALANOTTE-RIZZOLI, P. 1981 Wind wave prediction in shallow water: theory and applications. *J. Geophys. Res.* **86** (C5), 10,961–10,975.
- CLIFTON, H. E. 1976 Wave-formed sedimentary structures: a conceptual model. In *Beach and nearshore sedimentation* (ed. R. A. Davis, Jr & R. L. Ethington), pp. 126–148. SEPM.
- DALRYMPLE, R. A. & KIRBY, J. T. 1986 Water waves over ripples. *J. of Waterway, Port Coast. Ocean Eng.* **112**, 309–319.
- DARWIN, G. H. 1883 On the formation of the ripple-mark in sand. *Proc. Roy. Soc. of London* **A36**, 18–43.
- DAVIES, A. G. 1979 The potential flow over ripples on the seabed. *J. Mar. Res.* **37**, 743–757.
- DAVIES, A. G. & HEATHERSHAW, A. D. 1984 Surface-wave propagation over sinusoidally varying topography. *J. Fluid Mech.* **144**, 419–443.
- DAVIS, R. E. & REGIER, L. A. 1977 Methods for estimating directional wave spectra from multi-element arrays. *J. Mar. Res.* **35** (3), 453–478.
- DEVILLARD, P., DUNLOP, F. & SOUILLARD, B. 1988 Localization of gravity waves on a channel with a random bottom. *J. Fluid Mech.* **186**, 521–538.
- DINGLER, J. R. 1974 Wave-formed ripples in nearshore sands. PhD thesis, University of California, San Diego.
- DOBSON, R. S. 1967 Some applications of a digital computer to hydraulic engineering problems. *Tech. Rep.* 80. Department of Civil Engineering, Stanford University.
- DONELAN, M. A., DRENNAN, W. M. & MAGNUSSON, A. K. 1996 Nonstationary analysis of the directional properties of propagating waves. *J. Phys. Oceanogr.* **26**, 1901–1914.
- DUGAN, J. P., SUZUKAWA, H. H., FORSYTH, C. P. & FARBER, M. S. 1996 Ocean wave dispersion surface measured with airborne IR imaging system. *IEEE Transactions on Geoscience and Remote Sensing* **34** (5), 1282–1284.
- ELGAR, S. & GUZA, R. T. 1985 Shoaling gravity waves: comparisons between field observations, linear theory, and a nonlinear model. *J. Fluid Mech.* **158**, 45–70.

- ELGAR, S., HERBERS, T. H. C. & GUZA, R. T. 1994 Reflection of ocean surface gravity waves from a natural beach. *J. Phys. Oceanogr.* **24** (7), 1,503–1,511.
- EWING, J. A. & PITT, E. G. 1982 Measurements of the directional wave spectrum off South Uist. In *Proceedings of wave and wind directionality with applications to the design of structures*, p. 573. Editions Technip, Paris.
- FARACI, C. & FOTI, E. 2001 Evolution of small scale regular patterns generated by waves propagating over a sandy bottom. *Phys. of Fluids* **13** (6), 1624–1634.
- FIELD, M. E., MEISBURGER, E. P., STANLEY, E. A. & WILLIAMS, S. J. 1979 Upper quarternary peat deposit on the Atlantic inner shelf of the United States. *Geological Society of America Bulletin* **90**, 618–628.
- FOREL, F.-A. 1883 Rides formées à la surface du sable déposé au fond de l'eau. *Archives des sciences physiques et naturelles* **9**, 256.
- FOREL, F.-A. 1998 *Le Léman*, , vol. II. Geneva: Slatkine Reprints, first published in 1894.
- FREILICH, M. H. & GUZA, R. T. 1984 Nonlinear effects on shoaling surface gravity waves. *Phil. Trans. Roy. Soc. London* **A311**, 1–41.
- FRIES, J. S., BUTMAN, C. A. & WEATCROFT, R. A. 1999 Ripples formation induced by biogenic mounds. *Marine Geology* **159**, 287–302.
- GALLAGHER, E. L., ELGAR, S. & THORNTON, E. B. 1998 Megaripple migration in a natural surf zone. *Nature* **394** (6689), 165–168.
- GELCI, R., CAZALÉ, H. & VASSAL, J. 1957 Prévision de la houle. la méthode des densités spectroangulaires. *Bulletin d'information du Comité central d'Océanographie et d'Etude des Côtes* **9**, 416–435.
- GRABER, H. C., BEARDSLEY, R. C. & GRANT, W. D. 1989 Storm-generated surface waves and sediment resuspension in the East China and Yellow seas. *J. Phys. Oceanogr.* **19**, 1039–1059.
- GRABER, H. C. & MADSEN, O. S. 1988 A finite-depth wind-wave model. part 1: model description. *J. Phys. Oceanogr.* **18**, 1,465–1,483.
- GRANT, W. D. & MADSEN, O. S. 1979 Combined wave and current interaction with a rough bottom. *J. Geophys. Res.* **84**, 1797–1808.
- GRANT, W. D. & MADSEN, O. S. 1982 Movable bed roughness in unsteady oscillatory flow. *J. Geophys. Res.* **87** (C1), 469–481.
- GREEN, M. O. 1986 Side-scan sonar mosaic of a sand ridge field: southern Mid-Atlantic Bight. *Geo-Marine Letters* **6**, 35–40.
- HARA, T. & MEI, C. C. 1987 Bragg scattering of surface waves by periodic bars: theory and experiment. *J. Fluid Mech.* **178**, 221–241.
- HASSELMANN, K. 1962 On the non-linear energy transfer in a gravity wave spectrum, part 1: general theory. *J. Fluid Mech.* **12**, 481–501.
- HASSELMANN, K. 1966 Feynman diagrams and interaction rules of wave-wave scattering processes. *Review of Geophysics* **4** (1), 1–32.

- HASSELMANN, K., BARNETT, T. P., BOUWS, E., CARLSON, H., CARTWRIGHT, D. E., ENKE, K., EWING, J. A., GIENAPP, H., HASSELMANN, D. E., KRUSEMAN, P., MEERBURG, A., MÜLLER, P., OLBERS, D. J., RICHTER, K., SELL, W. & WALDEN, H. 1973 Measurements of wind-wave growth and swell decay during the Joint North Sea Wave Project. *Deut. Hydrogr. Z.* **8** (12), 1-95, suppl. A.
- HASSELMANN, K. & COLLINS, J. I. 1968 Spectral dissipation of finite depth gravity waves due to turbulent bottom friction. *J. Mar. Res.* **26**, 1-12.
- HEATHERSHAW, A. D. 1982 Seabed-wave resonance and sand bar growth. *Nature* **296**, 343-345.
- HERBERS, T. H. C. & BURTON, M. C. 1997 Nonlinear shoaling of directionally spread waves on a beach. *J. Geophys. Res.* **102** (C9), 21,101-21,114.
- HERBERS, T. H. C., ELGAR, S. & GUZA, R. T. 1999 Directional spreading of waves in the nearshore. *J. Geophys. Res.* **104** (C4), 7683-7693.
- HERBERS, T. H. C. & GUZA, R. T. 1990 Estimation of directional wave spectra from multicomponent observations. *J. Phys. Oceanogr.* **20**, 1703-1724.
- HERBERS, T. H. C., HENDRICKSON, E. J. & O'REILLY, W. C. 2000 Propagation of swell across a wide continental shelf. *J. Geophys. Res.* **105** (C8), 19,729-19,737.
- HERTERICH, K. & HASSELMANN, K. 1980 A similarity relation for the non-linear energy transfer in a finite-depth gravity-wave spectrum. *J. Fluid Mech.* **97**, 215-224.
- HOLTHUIJSEN, L. H. & TOLMAN, H. L. 1991 Effects of the Gulf Stream on ocean waves. *J. Geophys. Res.* **96** (C7), 12755-12771.
- HUNT, A. R. 1882 On the formation of the ripplemark. *Proc. Roy. Soc. of London* **34**, 1-18.
- HWANG, P. H., WANG, D. W., WALSH, E. J., KRABILL, W. B. & SWIFT, R. N. 2000 Airborne measurement of the wavenumber spectra of ocean surface waves. part ii: directional distribution. *J. Phys. Oceanogr.* **30**, 2768-2787.
- JACKSON, F. C., WALTON, W. T. & BAKER, P. L. 1985 Aircraft and satellite measurement of ocean wave directional spectra using scanning-beam microwave radars. *J. Geophys. Res.* **90**, 987-1004.
- JOHNSON, H. K. & KOFOED-HANSEN, H. 2000 Influence of bottom friction on sea surface roughness and its impact on shallow water wind wave modeling. *J. Phys. Oceanogr.* **30** (7), 1743-1756.
- JONSSON, I. G. 1980 A new approach to oscillatory rough turbulent boundary layers. *Ocean Eng.* **7**, 109-152.
- KAJIURA, K. 1968 A model of the bottom boundary layer in water waves. *Bull. Earthquake Res. Inst. Univ. Tokyo* **46**, 75-123.
- KELLER, J. B. 1958 Surface waves on water on non-uniform depth. *J. Fluid Mech.* **4**, 607-614.
- KIRBY, J. T. 1986a A general wave equation for waves over rippled beds. *J. Fluid Mech.* **162**, 171-186.
- KIRBY, J. T. 1986b On the gradual reflection of weakly nonlinear stokes waves in regions with varying topography. *J. Fluid Mech.* **162**, 187-209.

- KIRBY, J. T. 1988 Current effects on resonant reflection of surface water waves by sand bars. *J. Fluid Mech.* **186**, 501–520.
- KIRBY, J. T. 1993 A note on bragg scattering of surface waves by sinusoidal bars. *Phys. of Fluids* **5** (2), 380–386.
- KOMEN, G. J., CAVALERI, L., DONELAN, M., HASSELMANN, K., HASSELMANN, S. & JANSSEN, P. A. E. M. 1994 *Dynamics and modelling of ocean waves*. Cambridge: Cambridge University Press.
- KRASITSKII, V. P. 1994 On reduced equations in the Hamiltonian theory of weakly nonlinear surface waves. *J. Fluid Mech.* **272**, 1–20.
- KUIK, A. J., VAN VLEDDER, G. P. & HOLTHUIJSEN, L. H. 1988 A method for the routine analysis of pitch-and-roll buoy wave data. *J. Phys. Oceanogr.* **18**, 1020–1034.
- LAVRENOV, I. V. & ONVLEE, J. R. A. 1995 A comparison between the results of wave energy propagation of the WAM model and the interpolation-ray method. *Russian Meteorology and Hydrology* (3), 29–42.
- LENTZ, S., GUZA, R. T., ELGAR, S., FEDDERSEN, F. & HERBERS, T. H. C. 1999 Momentum balances on the North Carolina inner shelf. *J. Geophys. Res.* **104** (C8), 18,205–18,226.
- LI, M. Z. & AMOS, C. L. 1998 Predicting ripple geometry and bed roughness under combined waves and currents in a continental shelf environment. *Continental Shelf Research* **18**, 941–970.
- LI, M. Z. & AMOS, C. L. 1999 Sheet flow and large wave ripples under combined waves and currents: field observations, model predictions and effect on boundary layer dynamics. *Continental Shelf Research* **19**, 637–663.
- LIU, Y. & YUE, D. K. P. 1998 On generalized bragg scattering of surface waves by bottom ripples. *J. Fluid Mech.* **356**, 297–326.
- LONG, R. B. 1973 Scattering of surface waves by an irregular bottom. *J. Geophys. Res.* **78** (33), 7,861–7,870.
- LONG, R. B. 1980 The statistical evaluation of directional spectrum estimates derived from pitch/roll buoy data. *J. Phys. Oceanogr.* **10**, 944–952.
- LONG, R. B. & HASSELMANN, K. 1979 A variational technique for extracting directional spectra from multi-component wave data. *J. Phys. Oceanogr.* **9**, 373–381.
- LONGUET-HIGGINS, M. S. 1957 On the transformation of a continuous spectrum by refraction. *Proceedings of the Cambridge philosophical society* **53** (1), 226–229.
- LONGUET-HIGGINS, M. S., CARTWRIGHT, D. E. & SMITH, N. D. 1963 Observations of the directional spectrum of sea waves using the motions of a floating buoy. In *Ocean Wave Spectra, proceedings of a conference, Easton, Maryland*, pp. 111–136. National Academy of Sciences, Prentice-Hall.
- LUO, W. & MONBALIU, J. 1994 Effects of the bottom friction formulation on the energy balance for gravity waves in shallow water. *J. Geophys. Res.* **99** (C9), 18,501–18,511.
- LYGRE, A. & KROGSTAD, H. E. 1986 Maximum entropy estimation of the directional distribution in ocean wave spectra. *J. Phys. Oceanogr.* **16**, 2,052–2,060.

- MADSEN, O. S. 1994 Spectral wave-current bottom boundary layer flows. In *Proceedings of the 24th international conference on coastal engineering*, pp. 384-397. ASCE.
- MADSEN, O. S. & GRANT, W. D. 1976 Quantitative description of sediment motion by waves. In *Proceedings of the 15th international conference on coastal engineering, Honolulu, Hawaii*, , vol. II, pp. 1093-1112. ASCE.
- MADSEN, O. S., MATHISEN, P. P. & ROSENGAUS, M. M. 1990 Movable bed friction factors for spectral waves. In *Proceedings of the 22nd international conference on coastal engineering*, pp. 420-429. ASCE.
- MADSEN, O. S., POON, Y.-K. & GRABER, H. C. 1988 Spectral wave attenuation by bottom friction: theory. In *Proceedings of the 21th international conference on coastal engineering*, pp. 492-504. ASCE.
- MADSEN, O. S., WRIGHT, L. D., BOON, J. D. & CHISHOLM, T. A. 1993 Wind stress, bed roughness and sediment suspension on the inner shelf during an extreme storm event. *Continental Shelf Research* **13**, 1303-1324.
- MATHISEN, P. P. & MADSEN, O. S. 1999 Wave and currents over a fixed rippled bed. 3. bottom and apparent roughness for spectral waves and currents. *J. Geophys. Res.* **104** (C8), 18,447-18,461.
- MEI, C. C. 1985 Resonant reflection of surface water waves by periodic sandbars. *J. Fluid Mech.* **152**, 315-335.
- MEI, C. C. 1989 *Applied dynamics of ocean surface waves*, 2nd edn. Singapore: World Scientific, 740 p.
- MILLIMAN, J. D., PILKEY, O. H. & ROSS, D. A. 1972 Sediments of the continental margin off the eastern United States. *Geological Society of America Bulletin* **83**, 1315-1333.
- MITRA, A. & GREENBERG, M. D. 1984 Slow interaction of gravity waves and a corrugated sea bed. *J. Applied Mech.* **51**, 251-255.
- MOGRIDGE, G. R., DAVIES, M. H. & WILLIS, D. H. 1994 Geometry prediction for wave-generated bedforms. *Coastal Eng.* **22** (C11), 255-286.
- MUNK, W. H. & TRAYLOR, M. A. 1947 Refraction of ocean waves: a process linking underwater topography to beach erosion. *Journal of Geology* **LV** (1), 1-26.
- NEWELL, A. C. & AUCOIN, P. J. 1971 Semidispersive wave systems. *J. Fluid Mech.* **49**, 593-609.
- NIELSEN, P. 1979 Some basic concepts of wave sediment transport. *Tech. Rep.* 20. ISVA, Danish Technical University, Copenhagen.
- NIELSEN, P. 1981 Dynamics and geometry of wave-generated ripples. *J. Geophys. Res.* **86** (C7), 6,467-6,472.
- NIELSEN, P. 1992 *Coastal bottom boundary layers and sediment transport*. World Scientific Publishing.
- O'REILLY, W. C. & GUZA, R. T. 1991 Comparison of spectral refraction and refraction-diffraction wave models. *J. of Waterway, Port Coast. Ocean Eng.* **117** (3), 199-215.

- O'REILLY, W. C. & GUZA, R. T. 1993 A comparison of two spectral wave models in the Southern California Bight. *Coastal Eng.* **19**, 263–282.
- O'REILLY, W. C., HERBERS, T. H. C., SEYMOUR, R. J. & GUZA, R. T. 1996 A comparison of directional buoy and fixed platform measurements of Pacific swell. *J. Atmos. Ocean Technol.* **13**, 231–238.
- OSBORNE, A. R., SERIO, M., BERGAMASCO, L. & CAVALERI, L. 1998 Solitons, cnoidal waves and nonlinear interactions in shallow-water ocean surface waves. *Phys. D* **123** (1-4), 64–81.
- PAWKA, S. S. 1983 Island shadows in wave directional spectra. *J. Geophys. Res.* **88**, 2579–2591.
- PIERSON, JR, W. J. & MOSKOWITZ, L. 1964 A proposed spectral form for fully developed wind seas based on the similarity theory of S. A. Kitaigorodskii. *J. Geophys. Res.* **69** (24), 5181–5190.
- PRESS, W. H., TEUKOLSKY, S. A., VETTERLING, W. T. & FLANNERY, B. P. 1992 *Numerical Recipes*, 2nd edn. Cambridge University Press.
- PRIESTLEY, M. B. 1965 Evolutionary and non-stationary processes. *J. Roy. Statist. Soc. Ser. B* **27**, 204–237.
- PRIESTLEY, M. B. 1981 *Spectral analysis and time series*. London: Academic Press, 890 p.
- RAO, P., HOLMES, S., ANDERSON, R., WINSTON, J. & LEHR, P. 1990 *Weather Satellites: Systems, Data, and Environmental Applications*. Boston: American Meteorological Society.
- REICHARDT, H. 1951 Vollständige Darstellung der turbulenten Geschwindigkeitsverteilung. *Z. angew. Math. Mech.* **31** (7), 208–219.
- RICHTER, K., SCHMALFELDT, B. & SIEBERT, J. 1976 Bottom irregularities in the North Sea. *Deut. Hydrogr. Z.* **29** (1), 1–10.
- SHEMDIN, O. H., HSIAO, S. V., CARLSON, H. E., HASSELMANN, K. & SCHULZE, K. 1980 Mechanisms of wave transformation in finite depth water. *J. Geophys. Res.* **89** (C9), 5012–5018.
- SHERER, M. A., MELO, F. & MARDER, M. 1999 Sand ripples in an oscillating annular sand-water cell. *Phys. of Fluids* **11** (1), 58–67.
- SHIELDS, A. 1936 Anwendung der Ähnlichkeits-Mechanik und der Turbulenz-forschung auf die Geschiebebewegung. *Preussische Versuchsanstalt für Wasserbau und Schiffbau* **26**, 524–526, translated as California Inst. Technol. W. M. Keck Lab. for Hydraulic Water Res. Report 167.
- SOBEY, R. J. 1986 Wind-wave prediction. *Annu. Rev. Fluid Mech.* **18**, 149–172.
- SOULSBY, R. 1997 *Dynamics of marine sands, a manual for practical applications*. London: Thomas Telford Publications.
- SOULSBY, R. L. & WHITEHOUSE, R. J. S. W. 1997 Threshold of sediment motion in coastal environments. In *Proceedings of the Pacific coasts and ports 1997 conference*, pp. 149–154. University of Canterbury, New Zealand.
- SOUTHARD, J. B., LAMBIE, J. M., FEDERIC, D. C., PILE, H. T. & WIEDMAN, C. R. 1990 Experiments on bed configurations in fine sands under bidirectional purely oscillatory flow, and the origin of hummocky cross-stratification. *J. Sediment. Petrol.* **60**, 1–17.

- SVERDRUP, H. U. & MUNK, W. H. 1947 Wind, sea, and swell: theory of relations for forecasting. *Tech. Rep.* 601. U. S. Hydrographic Office.
- SWAMP GROUP 1984 *Ocean wave modelling*. New York: Plenum Press.
- SWIFT, D. J. P., KOFOED, J. W., SAULSBURY, F. P. & SEARS, P. 1972 Holocene evolution of the shelf surface, central and southern Atlantic shelf of North America. In *Shelf sediment transport: process and pattern*, chap. 23, pp. 499–574. Wiley & Sons.
- SWIFT, D. J. P. & SEARS, P. 1974 Estuarine and littoral depositional patterns in the surficial sand sheet central and southern Atlantic shelf of North America. *Mémoires de l'Institut Géologique du Bassin Aquitain* **7**, 171–189.
- TING, C., LIN, M. & KUO, C. 2000 Bragg scattering of surface waves over permeable rippled beds with current. *Phys. of Fluids* **12** (6), 1382–1388.
- TOLMAN, H. L. 1994 Wind waves and moveable-bed bottom friction. *J. Phys. Oceanogr.* **24**, 994–1,009.
- TOLMAN, H. L. 1995 Subgrid modeling of moveable-bed bottom friction in wind wave models. *Coastal Eng.* **26**, 57–75.
- TRAYKOVSKI, P., HAY, A. E., IRISH, J. D. & LYNCH, J. F. 1999 Geometry, migration, and evolution of wave orbital ripples at LEO-15. *J. Geophys. Res.* **104** (C1), 1,505–1,524.
- VINCENT, C. E. & OSBORNE, P. D. 1993 Bedform dimensions and migration rates under shoaling and breaking waves. *Continental Shelf Research* **13** (11), 1267–1280.
- VITTORI, G. & BLONDEAUX, P. 1990 Sand ripples under sea waves part 2. finite-amplitude development. *J. Fluid Mech.* **218**, 19–39.
- WALLBRIDGE, S., VOULGARIS, G., TOMLISON, B. N. & COLLINS, M. B. 1999 Initial motion and pivoting characteristics of sand particles in uniform and heterogeneous beds: experiment and modelling. *Sedimentology* **46**, 17–32.
- WAMDI GROUP 1988 The WAM model - a third generation ocean wave prediction model. *J. Phys. Oceanogr.* **18**, 1,775–1,810.
- WEBER, N. 1991a Bottom friction for wind sea and swell in extreme depth-limited situations. *J. Phys. Oceanogr.* **21**, 149–172.
- WEBER, S. L. 1988 The energy balance of finite depth gravity waves. *J. Geophys. Res.* **93**, 3,601–3,607.
- WEBER, S. L. 1991b Eddy-viscosity and drag-law models for random ocean wave dissipation. *J. Fluid Mech.* **232**, 73–98.
- WERNER, B. T. & KOCUREK, G. 1997 Bed-form dynamics: does the tail wag the dog? *Geology* **25** (9), 771–774.
- WHITHAM, G. B. 1974 *Linear and nonlinear waves*. New York: Wiley, 636 p.
- WIBERG, P. L. 1995 A theoretical investigation of boundary layer flow and bottom shear stress for smooth, transitional and rough flow under waves. *J. Geophys. Res.* **100** (C11), 22,667–22,679.
- WIBERG, P. L. & HARRIS, C. K. 1994 Ripple geometry in wave-dominated environments. *J. Geophys. Res.* **99** (C1), 775–789.

- WILLEBRAND, J. 1975 Energy transport in a nonlinear and inhomogeneous random gravity wave field. *J. Fluid Mech.* **70**, 113–126.
- WILLIS, D. H., DAVIES, M. H. & MOGRIDGE, G. R. 1993 Laboratory observations of bedforms under directional irregular waves. *Revue canadienne de génie civil* **20**, 550–563.
- WILSON, K. C. 1989 Friction of wave-induced sheet flow. *Coastal Eng.* **12**, 371–379.
- WRIGHT, L. D. 1993 Micromorphodynamics of the inner continental shelf: a Middle Atlantic Bight study. *Journal of Coastal Research* **15**, 93–130.
- WRIGHT, L. D. 1995 *Morphodynamics of inner continental shelves*. Boca Raton, Florida: CRC Press.
- YOUNG, I. R. 1988 A shallow water spectral wave model. *J. Geophys. Res.* **93** (C5), 5,113–5,129.
- YOUNG, I. R. & GORMAN, R. M. 1995 Measurements of the evolution of ocean wave spectra due to bottom friction. *J. Geophys. Res.* **100** (C6), 10,987–11,004.
- ZHUKOVETS, A. M. 1963 The influence of bottom roughness on wave motion in a shallow body of water. *Izv. Acad. Sci. USSR Geophys. Ser.* **10**, 1561–1570.

